Numerical modelling and simulation of the drying of failed fuel rods

Clément Loiseau

UNIVERSITÉ PARIS-EST

ÉCOLE DOCTORALE 531: Sciences, Ingénierie & Environnement

Dissertation

submitted to Université Paris-Est Marne-la-Vallée for the degree of doctor in Fluid Mechanics

by

Clément LOISEAU

Numerical modelling and simulation of the drying of failed fuel rods

presented on October 17th 2024

Committee in charge:

Mr. CHENIER, Eric	Professor	MSME - Marne-la-Vallée	Jury chairman
Mr. JOSSERAND, Christophe	Professor	LadHyX - Saclay	Reviewer
Ms. ROIG, Véronique	Professor	IMFT - Toulouse	Reviewer
Ms. CHOUIPPE, Agathe	Doctor	UNISTRA - Strasbourg	Examiner
Mr. COLOMBET, Damien	Doctor	LEGI - Grenoble	Examiner
Mr. VINCENT, Stéphane	Professor	MSME - Marne-la-Vallée	Research Director
Mr. MIMOUNI, Stéphane	Expert Research Engineer	EDF R&D and MSME	Research Co-Director
Mr. COLMONT, Dider	Expert Research Engineer	EDF R&D - Chatou	Industrial Supervisor

Remerciements

La rédaction de ce manuscrit, ainsi que l'obtention des résultats présentés dans cette thèse, n'auraient pas été possibles sans le soutien, tant technique que moral, de nombreuses personnes rencontrées tant dans un contexte professionnel que personnel, et que je tiens ici à remercier chaleureusement.

Je souhaite tout d'abord exprimer ma gratitude aux membres du jury pour le temps qu'ils ont consacré à la lecture de mon manuscrit et pour s'être déplacés, parfois de loin, afin d'assister à ma soutenance. En particulier, un grand merci à Eric Chénier, président du jury, pour ses questions stimulantes lors de la soutenance et pour les discussions enrichissantes qui en ont découlé. Mes remerciements vont également aux deux rapporteurs, Christophe Josserand et Véronique Roig, pour la relecture de mon manuscrit. Je tiens aussi à remercier Agathe Chouippe et Damien Colombet pour leur participation active à mon jury, ainsi que pour les échanges fructueux que nous avons eus lors de nos rencontres en congrès et au LEGI.

Je souhaite ensuite remercier très sincèrement Stéphane Mimouni, qui fut d'abord mon encadrant de stage en 2021, puis mon encadrant industriel et co-directeur de thèse. Stéphane, ta disponibilité constante, ton intérêt pour mon travail, ainsi que ton soutien indéfectible, ont été des éléments clés dans l'avancement de cette recherche. Tes conseils, tes idées, et ta double vision académique et industrielle du travail scientifique chez EDF R&D m'ont permis d'atteindre les résultats que je présente aujourd'hui dans ce manuscrit. Sur un plan plus personnel, merci aussi pour ton humour, que ce soit au travers de tes blagues franchouillardes ou de tes histoires surprenantes qui ont égayées nos échanges !

Je tiens également à adresser toute ma reconnaissance à Didier Colmont, mon encadrant industriel et chef du lot transport de combustible. J'ai bénéficié de ton expertise précieuse en matière d'emballages de transport et de modélisation thermique. Ta bonne humeur constante a été des plus appréciables, et j'ai hâte de poursuivre notre collaboration dans mon nouveau poste chez EDF R&D.

Mes remerciements vont aussi à Stéphane Vincent, mon directeur de thèse. Ta maîtrise des aspects scientifiques, tant sur les plans numériques que de modélisation, a été un véritable atout dès ma première année de doctorat. Grâce à toi, j'ai pu acquérir de solides bases et développer de nouveaux modèles dans neptune_cfd.

Je tiens également à remercier Damien Colombet, membre de mon jury de thèse mais surtout encadrant pendant mes deux mois de campagne expérimentale au LEGI. Damien, tes explications et conseils m'ont permis d'appréhender pleinement les enjeux de l'expérimentation, de la conception des expériences aux défis de mesure en passant par la calibration. Ta patience et ta pédagogie ont été pour moi une véritable chance. Merci encore !

Je suis également reconnaissant envers les managers et chefs de projets d'EDF qui m'ont accompagné : Laurent Charpin, ancien chef de groupe I8B, Ludovic Idoux, chef de projet PRETING, dont la confiance dans mon travail a permis le financement de la campagne expérimentale au LEGI, ainsi que Carole Vit, qui a su m'orienter durant ma dernière année de doctorat et a contribué à mon recrutement à EDF R&D. Merci aussi à l'équipe Neptune, notamment Nicolas Mérigoux, Jérôme Lavieville et Chaï Koren, toujours disponibles pour répondre à mes questions techniques sur le code.

Je ne saurais conclure sans exprimer toute ma gratitude envers mes parents, qui m'ont constamment soutenu dans mes études et mes choix, et qui m'ont encouragé à me lancer dans cette thèse.

Enfin, je remercie mes collègues d'EDF qui ont grandement enrichi ces années par leur amitié et leur présence. Vous avez fait de cette expérience un moment inoubliable, que ce soit sur site lors des

pauses café, autour de la table de tennis de table, au tennis, à la musculation (merci Julien pour tes programmes et conseils !), à la ludothèque ou encore en dehors lors de nos afterworks. En premier lieu, mes collègues doctorants d'I8B, Matthieu Barcet, avec qui j'ai partagé mon bureau durant deux ans, ainsi que Théo Lasseur et Gaétan Pierre, compagnons de route durant trois ans. Merci aussi aux collègues d'I8B Antoine Morente, Fanny Beltran, Benjamin Pyryt, Antoine Sicot, Léo Deperne, Mathis Boiteau, et William Benguigui, que j'ai eu le plaisir de connaître plus tardivement, mais avec qui j'ai toujours apprécié échanger, tant sur le plan professionnel que personnel. Mes remerciements vont aussi aux autres stagiaires et doctorants d'EDF avec qui j'ai partagé de nombreux moments agréables : Luc, Hector, Guilhem, Jacques, Federico, Li, Arthur, Elisa, Audrey, Clément, et Abraham.

Et enfin, un merci tout spécial à Corina Sanz Souhait, rencontrée au cours de ma thèse à EDF, pour avoir rendu mes derniers mois de thèse bien moins stressants qu'ils n'auraient dû l'être.

Contents

List of Figures

List of Tables

Nomenclature

Superscripts

AM	Added Mass
D	Drag
k	at iteration k
L	Lift
n	Current time step

Subscripts

0	in the initial state
$\underline{\underline{X}}$	tensor X
$\underline{x}$	vector x
b	bubble
d	dispersed
d	droplet
f	in the final state
g	gas
int	at the interface
k	phase k
l	liquid
m	mean
max	maximum
min	minimum
out	at the outlet

pl in the plenum

sat at saturation

tot total

vap vapour

$wall$ or w at the wall

Abbreviations

ASN Autorité de Sûreté Nucléaire

CEA Commissariat à l'Énergie Atomique et aux Énergies Alternatives

CFD Computational fluid dynamics

EDF Électricité de France

GEMMA GEneralized Multiphase Modelling Approach

GLIM Generalized Large Interface Model

IAEA International Atomic Energy Agency

IRSN Institut de Radioprotection et de Sûreté Nucléaire

LEGI Laboratoire des Écoulements Géophysiques et Industriels

LIM Large Interface Model

LS Level-Set

Mucellphage MUltiphase cutCELL PHase chanGE

PWR Pressurized Water Reactor

R&D Research and Development

RTE Réseau de Transport d'Électricité

U.S.NRC U.S. Nuclear Regulatory Commission

VOF Volume Of Fluid

Greek symbols

α Volume Fraction []

χ Thermal conductivity [W.m^{-1}.K^{-1}]

ϵ Thermal emissivity []

Γ Interfacial mass transfer rate [kg.m^{-3}.s^{-1}]

κ Curvature [m^{-1}]

λ Thermal conductivity [W.m^{-1}.K^{-1}]

μ Dynamic viscosity [Pa.s]

Φ Total heat flux [W]

Π Bulk interfacial heat transfer rate [W.m^{-3}]

Π' Sensible bulk interfacial heat transfer rate [W.m^{-3}]

ρ Density [kg.m^{-3}]

σ Surface tension [N.m]

φ Heat flux [W.m^{-2}]

Roman symbols

ΔT Superheat [°C]

Δt Time step [s]

Δx Grid size [m]

$\mathcal{P}$ Perimeter [m]

Boil Boiling number []

Bo Bond number []

Ca Capillary number []

Fr Froude number []

Kn Knudsen number []

Nu Nusselt number []

Po Poiseuille number []

Pr Prandtl number []

Re Reynolds number []

Sc Schmidt number []

Sh Sherwood number []

We Weber number []

θ Contact angle [°]

$\underline{\underline{S}}$ Viscous stress tensor [s^{-1}]

$\underline{n}$ Normal vector to the interface []

A Area [m^2]

a_i Interfacial area concentration [m^{-1}]

b Crack radial length [m]

C_D Drag coefficient []

C_L Lift coefficient []

C_p Specific heat [J.kg^{-1}.K^{-1}]

C_{AM} Added mass coefficient []

d Diameter [m]

D_h Hydraulic diameter [m]

E Energy [J]

e Crack width [m]

f Fanning friction factor []

f_D Modified drag coefficient [kg.m^{-3}.s^{-1}]

g Gravity acceleration [m.s^{-2}]

H Total enthalpy [K.kg^{-1}]

h Heat transfer coefficient [W.m^{-2}.K^{-1}]

h_{lat} Enthalpy of vaporization [J.mol^{-1}]

I Average interfacial momentum transfer contribution [kg.m^{-2}.s^{-2}]

j Superficial velocity [m.s^{-1}]

K Permeability [m^2]

L Channel length [m]

L_c Characteristic length [m]

M Molar mass [kg.mol^{-1}]

n Amount of substance [mol]

N_A Avogadro number []

P Pressure [Pa]

Q Residual heat power [W]

Q_v Volumetric flow rate [m^3.s^{-1}]

R Radius [m]

R_{gas} Specific gas constant [J.K^{-1}.mol^{-1}]

TS Momentum source term [Pa.m^{-1}]

T Temperature [°C]

t Time [s]

T_{ONB} Wall superheat required for the onset of nucleate boiling [°C]

V Volume [m^3]

w Width [m]

x	vapour quality []
y_{vap}	Vapour mass fraction []
erf	Error function []
u	mean velocity [m.s^{-1}]

Résumé

Avant de transporter le combustible nucléaire usé, il est nécessaire de s'assurer que la quantité d'eau résiduelle dans l'emballage est presque nulle. Cependant, la gaine des crayons combustibles, des tubes cylindriques contenant de l'uranium, peut parfois être endommagée, permettant à l'eau de s'infiltrer dans les fissures. Dans ces situations, il est nécessaire d'estimer la vitesse de séchage de ces crayons endommagés.
Pour atteindre cet objectif, la thèse se concentre sur la modélisation des écoulements bouillants dans des micro-canaux de moins de 100 µm. Des modèles numériques ont été développés dans le code multi-champs neptune_cfd pour intégrer les phénomènes physiques propres à la microfluidique, comme l'ébullition interfaciale et la mouillabilité.
En parallèle, une étude expérimentale sur les écoulements diphasiques en micro-canaux a été réalisée en partenariat avec le LEGI pour valider les hypothèses de la thèse. Ces approches numériques et expérimentales ont permis de développer un modèle 1D par upscaling, capable de simuler une situation industrielle en un temps raisonnable.
Enfin, un tableau destiné à l'ingénierie d'EDF a été élaboré. Ce tableau indique le temps de séchage en fonction de la taille des fissures et de la puissance résiduelle des assemblages combustibles.

Mots-clefs: Crayons inétanches, Microfluidique, Ébullition interfaciale, Mouillabilité, Remontée d'échelle

Abstract

Before transporting spent nuclear fuel, it is necessary to ensure that the residual water content in the packaging is almost zero. However, the cladding of fuel rods, which are cylindrical tubes containing uranium, can sometimes be damaged, allowing water to seep into the cracks. In these situations, it is essential to estimate the drying rate of these damaged rods.
To achieve this goal, the thesis focuses on modeling boiling flows in microchannels less than 100 µm in size. Numerical models were developed in the multi-field code neptune_cfd to incorporate the physical phenomena specific to microfluidics, such as interfacial boiling and wettability.
In parallel, an experimental study on two-phase flows in microchannels was conducted in partnership with LEGI to validate the thesis hypotheses. These numerical and experimental approaches led to the development of a 1D model through upscaling, capable of simulating an industrial situation within a reasonable time frame.
Finally, a table was developed for EDF engineering. This table indicates the drying time based on the crack size and the residual power of the fuel assemblies.

Keywords: Failed rods, Microfluidics, Interface boiling, Wettability, Upscaling

Introduction

Summary

This chapter presents the context and the industrial challenges for EDF behind the thesis. Notably, it explains what a failed fuel rod is, and why the nuclear industry needs to dry these failed rods. The importance of modelling accurately two-phase flows in microchannels for this application is then discussed. Notably, the limitations of the current scientific knowledge are highlited. Finally, the methodology employed in the thesis is described.

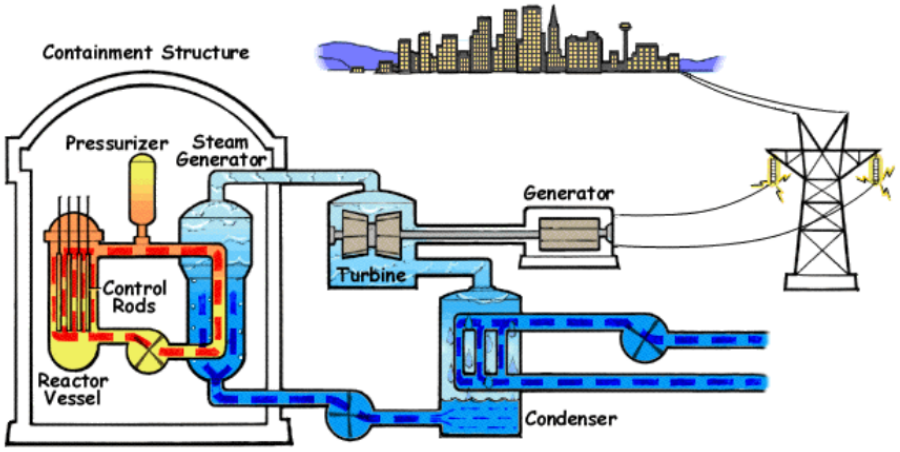

Figure 1: Schematic view of a pressurized water reactor from U.S.NRC. (a). The primary loop is in yellow and red and the secondary loop is in blue.

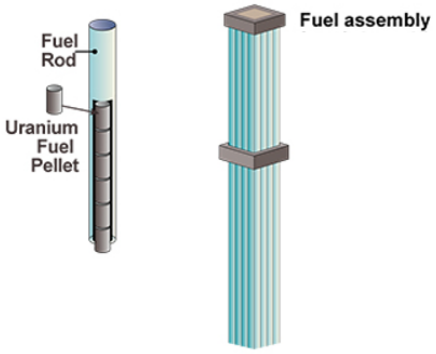

Figure 2: Schematic view of a fuel rod (left) made of a 265 UO_2 uranium pellets contained in a zirconium cladding, and of a fuel assembly (right) composed of 264 fuel rods. Picture from U.S.NRC. (b).

0.1 Industrial context

0.1.1 Pressurized Water Reactors and fuel

Nuclear energy constitutes the majority of France's electricity production, with approximately 70% of the electricity production (70.6% in 2019 and 67.1% in 2020, as reported by RTE). The backbone of France's nuclear energy infrastructure consists of 56 pressurized water reactors (PWR). The operational principle of PWR is depicted in Figure 1. In this design, heat is extracted from the nuclear fuel through pressurized water circulating in the primary loop. Subsequently, the heated water enters the steam generator, initiating the boiling process in the secondary loop. Finally, the generated vapour from the secondary loop powers turbines to produce electricity.
The amount of nuclear fuel in French reactors varies depending on their power, with between 157 and 205 fuel assemblies. These assemblies take the form of 20 cm wide square parallelepipeds, incorporating 264 fuel rods, control rods, and instrumentation tubes. Each fuel rod, depicted in Figure 2, is a 4-meter-long cylinder containing 265 UO_2 pellets. These pellets are securely enveloped by a zirconium-alloy cladding, with an external diameter of 9.5 mm and a thickness of 0.57 mm.

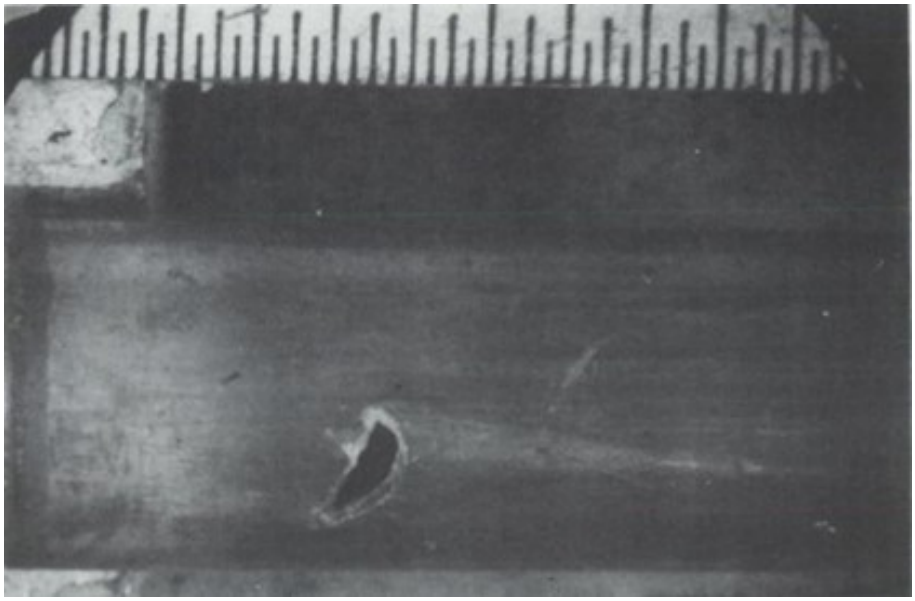

Figure 3: Hole in the cladding of a failed fuel rod. Picture from Kohli (1986).

0.1.2 Fuel element failure

During the normal operation of a PWR, the degradation of the cladding of fuel rods can happen, leading to the development of cracks and to the loss of its watertight integrity. Several mechanisms can cause this problem. The two most common causes are by far the interaction between cladding and debris in the coolant flow (40-45% of the failure cases) and the fretting of fuel rod claddings under the spacer grid (40-45%) (IAEA (International Atomic Energy Agency) (2002)). Figure 3 shows a typical breach in a failed fuel rod. The failure of a fuel rod currently happens on average for one fuel assembly out of 1000, which represents between five and ten failed assemblies every year in France.
During their stay in the primary circuit and in the pool of the fuel building, water can penetrate the failed rods, flow through the microscopic cracks of the irradiated uranium pellets (illustrated in Figure 4) and occupy all the free volumes of the failed rod. Later, during the evacuation of the failed assembly, this water can vaporize and dissociate into hydrogen by radiolysis, or pressurize the transport cask, leading to a hydrogen or a mechanical risk if there is too much vapour. To prevent such a risk, the French safety authority (ASN) limits the volume of liquid water in a transport cask to 300 cm^3. However, with the current knowledge, it is unclear how much water remains in a failed rod after the vacuum drying of the transport cask, and EDF must make penalizing assumptions on this liquid volume.
Hence, the thesis aims to investigate the drying process of failed rods, considering the phenomena arising from two-phase flow within microscopic cracks. The objective is to offer quantitative insights and, ideally, enable more informed and less conservative assumptions in future assessments.

0.2 Presentation of the French vacuum drying process and description of the geometry of failed rods

Remark 0.2.1. Modelling the drying of failed rods requires a clear understanding of the industrial drying process (section 0.2.1) as well as a comprehensive understanding of the geometry of the failed rods (sections 0.2.2 and 0.2.3). The objective of this section is to provide this information, which will serve as initial and boundary conditions for the numerical simulations presented in this manuscript.

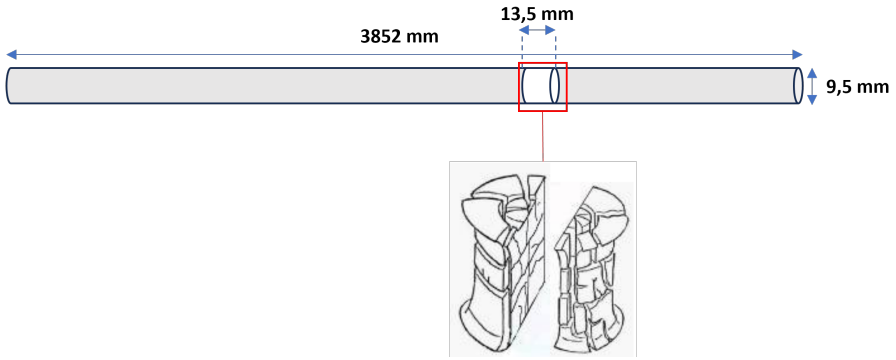

Figure 4: Schematic view of a fuel rod (top), and of an irradiated cracked pellet (bottom).

0.2.1 The industrial vacuum drying process

After spending several years in the storage pool of PWRs, used fuel assemblies, whether they are failed or not, are transferred to the reprocessing plant at La Hague (France). To comply with regulations and safety measures (radiation protection, heat dissipation, mechanical resistance to accidents, etc.), these assemblies are transported in shipping casks. In France, these casks contain 12 assemblies.
The transport casks undergo a vacuuming process that lasts for several hours until the pressure in the cask reaches a value between 7 and 10 mbar. Subsequently, a drying test is conducted: the vacuum system is stopped for 10 minutes, and the pressure must not increase by more than 1 mbar during this period. If the test is successfully passed, the vacuum drying process is stopped.

Remark 0.2.2. If liquid water is still present in the transport cask, it will evaporate due to the low pressure and the residual heat power of the 12 assemblies. This vaporization will result in a pressure increase, which can be predicted by the ideal gas law:

$$\Delta P = \frac{R_{gas} T_{sat}(P)}{M_{H_2 0} V} \Delta m_l \tag{1}$$

ΔP represents the pressure increase, $R_{gas} = 8.314$ J.K^{-1}.mol^{-1} is the ideal gas law constant, $T_{sat}(P)$ is the saturation temperature at the pressure $P = 10$ mbar. $M_{H_2 0} = 18$ g.mol^{-1} is the water molar mass, $V = 2.8$ m^3 is the free volume of a transport cask, and Δm_l is the mass of water evaporated during these 10 minutes.
Using this formula, the test fails if more than $\Delta m_l = 1.5$ g evaporates during these 10 minutes.
This test can prove the absence of a significant quantity of liquid water in the transport cask, but it is not sufficient to conclude that there is no remaining water in the failed rods.

Remark 0.2.3. During the vacuum drying process, no external heat source is used. All the heat comes from the residual power of the assemblies.

0.2.2 Free volumes in fuel rods

Several studies, including those conducted by Ambard (2013), Montgomery and Morris (2019), Rondinella et al. (2015), and Desgranges (2001), have employed a double gas expansion test to measure the free volumes in irradiated rods (see Appendix A for more information about the test). These comprehensive experiments, including 196 measurements, have determined that the free volume of an irradiated fuel rod typically falls within the range of 9 to 21 cm^3, with an average free volume of

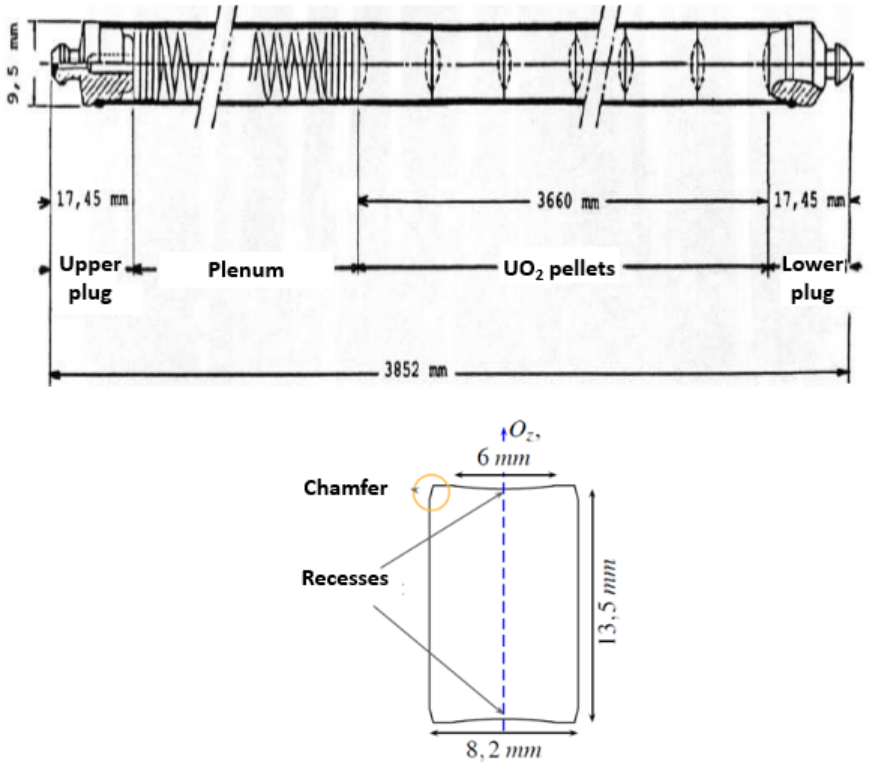

Figure 5: Schematic view of a fuel rod (top), and of a UO_2 pellet (bottom).

14.3 cm^3. Figure 5 presents a schematic view of a fuel rod, and of a UO_2 pellet, which show the different free volumes.
The overall free volume is composed of five volumes.

1. **Plenum:** This represents a free volume at the top of a rod, partially filled with a spring to accommodate the deformation of uranium pellets. The authors note that the plenum often accounts for approximately 50% of the total free volume.

2. **Pellet-Cladding Gap:** Initially substantial (several cm^3), this volume corresponding to the gap diminishes with irradiation. The authors report that it tends to be completely closed for a burnup exceeding 50 MWd/kgU.

3. **Cracks in Uranium Pellets:** Estimating this volume is challenging, given its dependence on the specific rod under consideration.

4. **Chamfers between Pellets:** Chamfers are expected to partially close up during the irradiation of the fuel.

5. **Recesses between Pellets:** Similar to chamfers, recesses are anticipated to partially close up during irradiation.

Remark 0.2.4. In summary, the free volume within a failed rod averages $V_{free} = 14.3$ cm^3. However, the value $V_{free} = 20$ cm^3 will be used in this manuscript as a conservative estimate. Most of this free volume is located at the top of the rod, in an area known as the plenum.

0.2.3 Crack width in failed fuel rods

0.2.3.1 Visual observation

The direct measurement of crack width in uranium pellets has been conducted in a limited number of experiments, primarily due to the challenges posed by the size of these cracks. One notable study, carried out by Aubrun and Chatelet (2011), involved the measurement of crack width on approximately 10 pellets from different irradiated rods. The results, illustrated in Figures 6 and 7, indicated that crack widths ranged from 5 µm to 50 µm.
It is important to note that these observations are localized and cannot be extrapolated to the entire rod. A typical rod is made of 300 pellets, and the observed variations in crack width on a limited number of pellets may not represent the overall distribution across the entire rod.

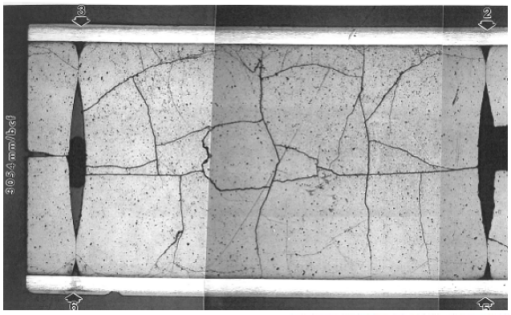

Figure 6: Longitudinal cut of an irradiated pellet from Aubrun and Chatelet (2011). White represents the cladding, grey the UO_2, and black the holes (cracks, chamfers, and recesses).

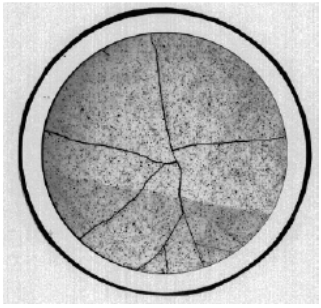

Figure 7: Radial cut of an irradiated pellet from Aubrun and Chatelet (2011). White represents the cladding, grey the UO_2, and black the holes (cracks, chamfers, and recesses).

0.2.3.2 Gas flow measures

For more quantitative assessments of crack width, researchers have employed permeability measurements on fuel rods. Several studies, including Jernkvist (2022), Dagbjartsson et al. (1977), Desgranges (2001), Turnbull and White (2002), Castelier and Obry (2015), Rondinella et al. (2015), Montgomery and Morris (2019), and Verwerft et al. (2019), have used a rod puncturing method to measure the permeability of failed rods.
In the rod puncturing technique, a fuel rod is punctured at its top (in the plenum) and bottom. Subsequently, a gas flow rate is imposed between these two points, and the pressure difference is measured as illustrated by Figure 8. By applying Darcy's law, these two values can be correlated using an empirical coefficient, denoted as K. This approach provides a means to assess crack characteristics and permeability within the fuel rod.

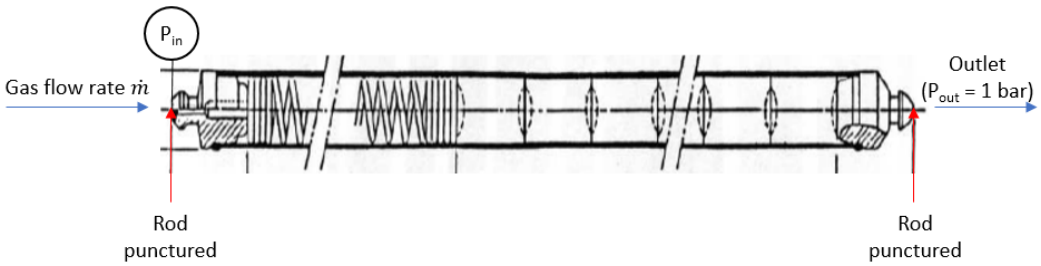

Figure 8: Schematic view of a gas flow measure. The rod is punctured in the top and bottom plugs, and a gas flow rate is imposed at the top plug (in the plenum). The pressure difference between the two plugs is then measured.

Remark 0.2.5. The permeability K is an empirical coefficient defined in the Darcy law for non-compressible fluids (equation 2), or in the Darcy-Poiseuille law (equation 3) for ideal gases.

$$\dot{m} = \rho \frac{KA}{\mu L}(P_{pl} - P_{out}) \tag{2}$$

$$\dot{m} = \frac{KA}{2\mu L}\frac{M}{R_{gas}T}(P_{pl}^2 - P_{out}^2) \tag{3}$$

$\dot{m}$ is the gas mass flow rate through the cracks, A is the cross section of the rod, L is the length of the rod, P_{pl} is the pressure of the plenum (at the top of the rod), P_{out} is the pressure at the bottom of the rod. ρ, μ, M, and T are the density, the viscosity, the molar mass, and the temperature of the gas used for the measure.

It is important to highlight that the cited studies may employ different values for the cross-section. Additionally, some authors define a hydraulic radius instead of permeability. To avoid potential confusion caused by distinct units and formulas used for permeability computation, the analytical Poiseuille formula for gas flow between two infinite planes is adopted to characterize the crack width (equation 4). This choice aims to provide consistency and facilitate comparisons across various studies.
Additionally, visualizing the physical meaning of permeability can be challenging, especially given its very small values for irradiated rods, typically ranging between 10^{-12} and 10^{-14} m^2. In contrast, crack width carries a stronger physical meaning.

$$\dot{m} = \frac{e^3 b}{24\mu L}\frac{M}{RT}(P_{pl}^2 - P_{out}^2) \tag{4}$$

In this expression, the cracks in the uranium pellets are merged into an equivalent crack. Here, e represents the crack width, and b is the radial length of the equivalent crack. Using the radial cuts from Aubrun and Chatelet (2011), as depicted in Figure 7, we visually estimate that a uranium pellet is typically crossed by three full radial cracks. Considering the diameter of a pellet is 8.2 mm, the radial length of the equivalent crack is $b = 25$ mm. A schematic view of this simplification is presented in Figure 9.

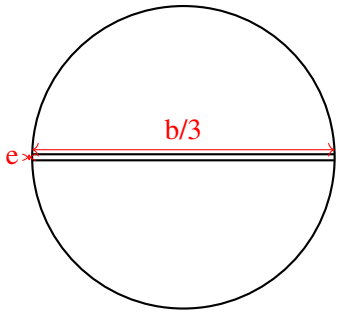

Figure 9: Schematic view of a simplified irradiated pellet. A crack is represented across a pellet. On average, a pellet is composed of three radial cracks.

Remark 0.2.6. An identification between equation 4 and equation 3, gives the expression of the crack width e as a function of the permeability K, the rod cross section A, and the radial length of the equivalent crack b.

$$e = \left(\frac{KA}{12b}\right)^{1/3} \tag{5}$$

Figure 10, drawn during the PhD, illustrates the equivalent crack width as a function of burnup based on data from the aforementioned research groups. Two noteworthy observations are:

- The equivalent crack width demonstrates a decrease with burnup. This might seem counterintuitive since the pellets are not initially cracked, and irradiation induces crack formation. However, there exists an initial gap of approximately 60 µm between the pellets and the cladding. This gap decreases during irradiation, ultimately closing completely after the second irradiation cycle (burnup of 25 MWd/kgU).
- For highly irradiated rods, the equivalent crack width ranges from 6.3 to 30 µm.

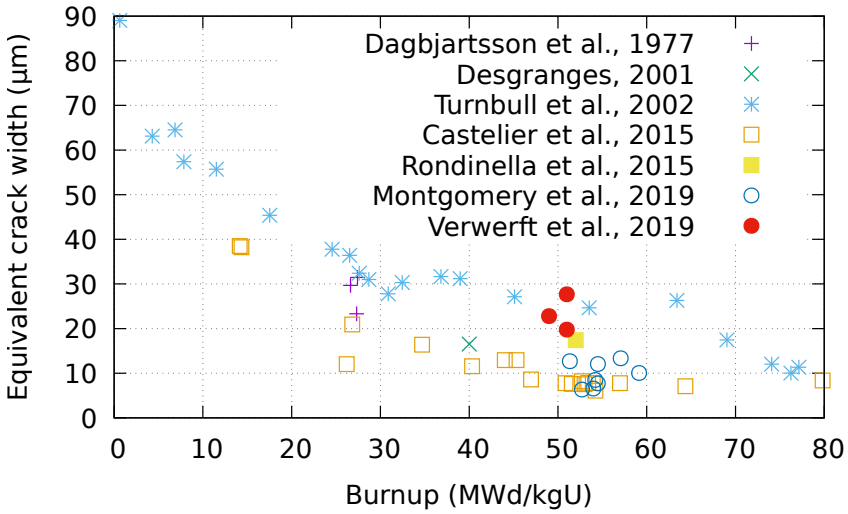

Figure 10: Equivalent crack width as a function of the burnup.

Remark 0.2.7. At the micrometric scale, gas rarefaction effects are not always negligible, especially at low pressures. However, we show in Appendix B that the rarefaction effect is not significant for failed fuel rods.

Remark 0.2.8. In summary, the equivalent crack width e for highly irradiated rods ranges between 6.3 and 20 µm.
It is however important to note that the values presented in this section are equivalent crack widths. In the industrial situation, the uranium pellets are crossed by a complex networks of very small cracks, equivalent to a single larger cracks. This concept of equivalent crack width will be utilized in the subsequent sections and chapters of this manuscript to model the drying process of failed rods. Given the lack of experimental data on the actual crack networks within the uranium pellets, this approach is the most practical and feasible method for modelling and analysis.

0.3 Two-phase flow in microchannels

0.3.1 Specifity of microchannels

Two-phase flows in microchannels exhibit distinctions from that in regular channels due to unique physical phenomena. To delve into the reasons behind this disparity, it is insightful to examine dimensionless numbers associated with a characteristic length L_c, such as the Reynolds number Re,

the Weber number We, the Bond number Bo, and the wall superheat required for the onset of nucleate boiling T_{ONB}. For a magnitude estimate, these numbers will be calculated for water ($\rho_l = 1000$ kg.m^{-3}, $\rho_g = 0.6$ kg.m^{-3}, $\mu_l = 0.001$ Pa.s, $\sigma = 0.075$ N.m^{-1}), with a characteristic length L_c = 100 µm, and a velocity u = 1 m.s^{-1}.

$$\mathrm{Re_l} = \frac{\rho_l u L_c}{\mu_l} \tag{6}$$

Remark 0.3.1. The Reynolds number (Re) characterizes the transition between laminar and turbulent flows. In microchannels, Re is significantly smaller compared to regular channels, because of the reduced characteristic length. Additionally, the importance of linear head losses tends to result in lower velocities (for instance, $u = 1$ m.s^{-1} is considered high in a microchannel). In the given example, Re equals 100, explaining why turbulence is almost never observed in microchannels.

$$\mathrm{We_g} = \frac{\rho_g u^2 L_c}{\sigma} \tag{7}$$

Remark 0.3.2. The Weber number (We) quantifies the balance between inertia and surface tension forces, crucial in predicting the shape of bubbles or droplets during motion. In this instance, $\mathrm{We}_g = 0.0008$. This implies that for a vapour bubble, inertia is negligible, and the bubble will remain spherical in the flow. In contact with a wall however, wettability effects will determine its shape.

$$\mathrm{Bo} = \frac{(\rho_l - \rho_g) g L_c^2}{\sigma} \tag{8}$$

Remark 0.3.3. The Bond number (Bo) represents the ratio of gravity to surface tension forces. In this specific scenario, $\mathrm{Bo} = 0.0013$ indicating that gravity has a negligible impact compared to surface tension. Consequently, when simulating two-phase flows in microchannels, gravity can be neglected.

Finally, the wall superheat required to initiate nucleation is much higher in microchannels. Kandlikar (2002) combined the correlations of Hsu and Graham (1961) and Sato and Matsumura (1964) for nucleate boiling and obtained equation 9 for the onset of nucleate boiling (ONB).

$$T_{ONB} - T_{sat} = \frac{8\sigma T_{sat}\,\mathrm{Nu}}{\rho_l L_c h_{lat}} \tag{9}$$

Nu is the Nusselt number. T_{sat} is the saturation temperature. $h_{lat}0 = 2257$ kJ.kg^{-1} is the enthalpy of vaporization.

Remark 0.3.4. Using this expression, Kandlikar (2002) found that the wall superheat required to initiate nucleation is small for conventional channels, but can be significant for microchannels. For instance, he assessed that a 4 °C wall superheat is required to initiate nucleation for a channel with a 100 µm diameter, while a 40 °C superheat is required for a channel with a 10 µm diameter. This phenomenon accounts for the rare occurance of nucleate boiling in microchannels, as most of the heat from the walls is transferred to heat the liquid. Boiling then primarily occurs at the interface between the liquid and existing bubbles.

0.3.2 Flow regimes in microchannels

Due to the unique characteristics of microchannels outlined in the previous subsection, the criteria used to define various flow regimes differ from those applicable to conventional channels. Numerous experiments and studies have investigated diverse flow regimes in microchannels. Noteworthy examples include the work of Feng and Serizawa (2000), who identified six distinct flow regimes — bubble flow, slug flow, liquid ring flow, liquid lump flow, and droplet/mist flow — observed during air-water flow in a 50 µm circular channel. Notably, they identified the liquid ring flow regime as unique to microchannels, attributed to the instability of the liquid between two slugs. These flow regimes are illustrated in Figure 11.

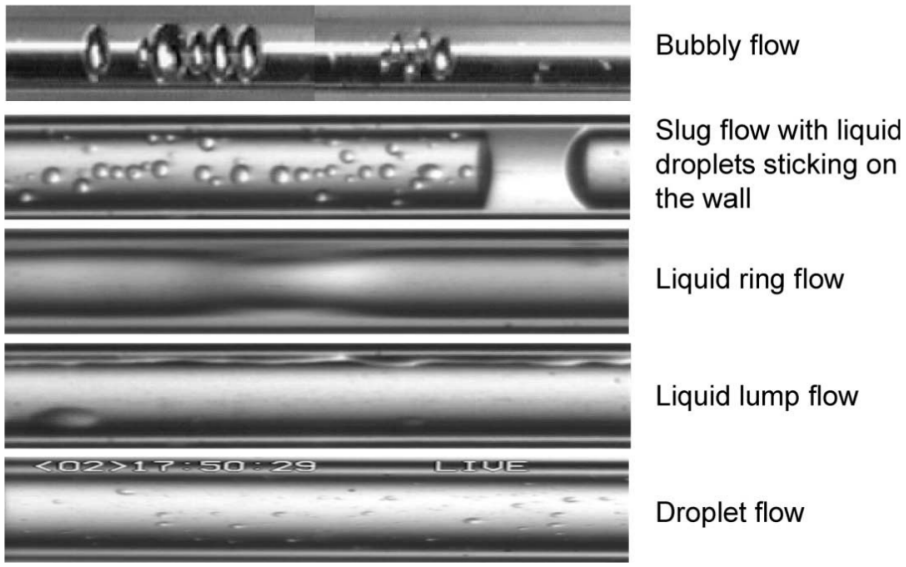

Figure 11: Flow regimes in a 100 µm quartz tube. Figure from Feng and Serizawa (2000). The bubbly flow consists of a liquid flow with dispersed bubbles. The slug flow consists of large bubble with a length greater than the channel diameter, in some cases liquid droplets are observed on the wall - but not always. The liquid ring flow appears at higher gas velocities when the liquid slug between two bubbles disappears leading to a coalescence of the gas slugs. For even higher gas velocities, the gas entrains the liquid phase and creates liquid lumps on the wall. Finally, for very low liquid fractions, a droplet/mist flow is observed.

Similarly, Kawahara et al. (2002) examined air-nitrogen adiabatic flow in a 50 µm circular channel, varying superficial liquid velocities from 0.02 m/s to 6 m/s and superficial gas velocities from 0.1 to 60 m/s. Their observations diverged from conventional flow regimes, with the absence of bubbly flow. They identified patterns such as liquid alone, liquid ring flow and slug flows. According to the authors, the absence of turbulence in 50 µm channels explained the lack of bubbly and churn flow.
After a series of experiments, the authors constructed a flow regime map based on superficial liquid and gas velocities, comparing it with maps from other researchers such as Fukano and Kariyasaki (1993), Triplett et al. (1999), and Zhao and Bi (2001). This map is illustrated in Figure 12 for a 100 µm microchannel.

Remark 0.3.5. The superficial liquid velocities considered in the microchannel cases presented in this manuscript are consistently low, typically around 0.1 m/s or less. Consequently, the regime of interest in this thesis is predominantly slug flow (Figure 12).

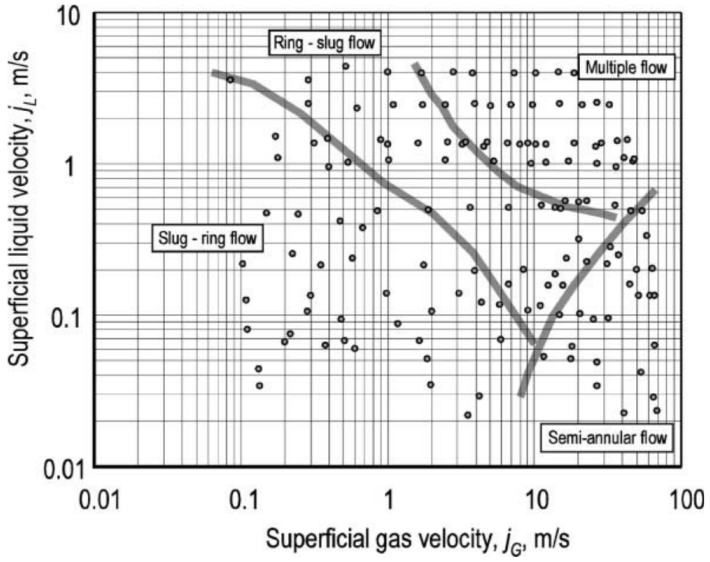

Figure 12: Two-phase flow regime map for a 100 µm microchannel (from Kawahara et al. (2002)).

0.3.3 Literature review on microchannels

Before the advent of computer science, studies on microchannels primarily relied on experiments, leading to the development of 1D correlations for head losses and/or heat transfer. These correlations will be presented in this section, but cannot be used reliably due to their poor accuracy, or their narrow domain of application. In recent times, Computational Fluid Dynamics (CFD) has emerged as a powerful tool, enabling precise 3D simulations of two-phase flow and flow boiling in microchannels. It now stands as a key instrument for understanding flow boiling phenomena in microchannels. The main drawback of these 3D simulations is their very high computational cost.
This section will present these different models and explain why they cannot be used to solve the industrial drying of failed rods.

0.3.3.1 1D correlations for head losses

Three common 1D approaches are employed in the literature to compute the pressure drop in microchannels. The homogeneous model assumes that the pressure drop can be predicted using single-phase flow formulas applied to an equivalent fluid. The Lockhart-Martinelli model, on the other hand, posits that the two-phase pressure drop comprises three terms: the single-phase gas pressure drop, the single-phase liquid pressure drop, and a term representing the two-phase effects. Lastly, the Friedel model is a correlation that utilizes dimensionless numbers to estimate the pressure drop.

0.3.3.2 Homogeneous model

The most natural method to compute head losses in microchannels is the homogeneous model. In this model, single-phase formulas are applied to a homogeneous fluid. The physical properties of this homogeneous fluid depend on the properties of the liquid and gas phases. For laminar flow, the head losses are computed as:

$$-\frac{dP}{dx} = \frac{64/\,\mathrm{Re}_m\,\rho_m u_m^2}{2D_h} \tag{10}$$

$\frac{dP}{dx}$ is the pressure loss in the channel, $\mathrm{Re}_m = \frac{\rho_m u_m D_h}{\mu_m}$ is the homogeneous Reynolds number, D_h is the hydraulic diameter of the channel, ρ_m is the average density, computed as the density of the

homogeneous fluid, and u_m is the velocity of the homogeneous fluid.

$$\rho_m = \left(\frac{x}{\rho_g} + \frac{1-x}{\rho_l} \right)^{-1} \tag{11}$$

where $x = \dfrac{\dot{m}_g}{\dot{m}_g + \dot{m}_l}$ is the vapour quality.

$$u_m = \frac{Q_g + Q_l}{A} \tag{12}$$

where Q_g and Q_l are the volumetric gas and liquid flow rates, and A is the area of the cross section.
The primary challenge in this approach is determining the correct value for the equivalent viscosity. Various correlations have been proposed, and some of these are provided in Table 1.

Authors	Correlation
Einstein (1906)	$\mu_m = \mu_l(1 + 2.5\alpha_g)$
McAdams (1954)	$\mu_m = \left(\dfrac{x}{\mu_g} + \dfrac{1-x}{\mu_l} \right)^{-1}$
Davidson et al. (1943)	$\mu_m = \mu_l \left(1 + x\dfrac{\rho_l - \rho_g}{\rho_g} \right)$
Cicchitti et al. (1959)	$\mu_m = x\mu_g + (1-x)\mu_l$
Owens (1961)	$\mu_m = \mu_l$
Dukler et al. (1964)	$\mu_m = \alpha_g\mu_g + \alpha_l\mu_l$
Beattie and Whalley (1982)	$\mu_m = \alpha_g\mu_g + \alpha_l(1 + 2.5\alpha_g)\mu_l$
Lin et al. (1991)	$\mu_m = \dfrac{\mu_l\mu_g}{\mu_g + x^{1.4}(\mu_l - \mu_g)}$
Garcia et al. (2003)	$\mu_m = \mu_l\dfrac{\rho_m}{\rho_l}$
Awad and Muzychka (2007)	$\mu_m = \dfrac{2\mu_g + \mu_l - 2(\mu_g - \mu_l)(1-x)}{2\mu_g + \mu_l + (\mu_g - \mu_l)(1-x)}$

Table 1: Correlations giving the homogeneous viscosity.

Chen et al. (2001) observed that these models were exclusively validated for water-air flows and proved ineffective for R-401A flows. They proposed that these discrepancies could be attributed to surface tension effects and introduced a correction factor accounting for the Bond and Weber numbers. This correction factor is defined as in equation 13. Unfortunately, this model has not undergone extensive testing by various research groups, making it challenging to draw definitive conclusions about its applicability.

$$\Omega_{\text{hom}} = \begin{cases} 1 + (0.2 - 0.9\exp(-\text{Bo})) & \text{if Bo} < 2.5, \\ 1 + (\text{We}^{0.2} \,/\, \exp(\text{Bo}^{0.3})) & \text{else.} \end{cases} \tag{13}$$

$$\frac{dP}{dx} = \left(\frac{dP}{dx} \right)_{\text{hom}} \Omega_{\text{hom}} \tag{14}$$

Several literature reviews on microchannels have compared various correlations with experimental data. For instance, Asadi et al. (2014) compared the correlations by McAdams (1954), Owens (1961), Cicchitti et al. (1959), Dukler et al. (1964), Beattie and Whalley (1982), Lin et al. (1991) and Myuztchka using data from 10 experiments. These experiments involved various fluids (though predominantly water) and hydraulic diameters ranging from 100 µm to 1 mm. The conclusion was that none of these correlations could consistently predict head losses accurately across all experiments. This comparison is illustrated in Figure 13. The most accurate correlation is that of Dukler, although it has an average error of 33% on the data set considered. Similarly, Chung and Kawaji (2004), Ali et al. (1993), and Salim (2018) conducted studies with the same conclusion: Dukler's correlation is the most suitable for microchannels with hydraulic diameters less than 100 µm, but the error remains significant.

	Mc Adams	Owens	Cicchitti	Dukler	Beattie and Whalley	Lin	Awad and Myuztchka
Choi and Kim [212], D_h = 490 µm	40.81	352.1	300.7	66.84	30.69	111.99	107.87
Choi and Kim [212], D_h = 141 µm	169.87	709.07	650.12	42.1	43.5	346.56	298.29
Cioncolini et al. [186]	43.6	40.0	26.6	47.7	39.2	–	27.8
Lee and Mudawar [134]	28.26	–	15.98	30.61	26.79	26.44	–
Yue et al. [214], D_h = 528 µm	19.31	244.38	221.14	–	–	67.54	–
Yue et al. [214], D_h = 333 µm	18.15	201.92	187.96	–	–	76.91	–
Kawahara et al. [136], distilled water	28.00	40.5	40.3	33.9	49.0	39.2	–
Kawahara et al. [136], ethanol 4.8 wt%	59.1	114.9	113.6	27.7	55.2	101.6	–
Kawahara et al. [136], ethanol 49 wt%	46.6	99.9	99.3	10.4	95.1	90.9	–
Kawahara et al. [136], ethanol 100 wt%	71.2	110.9	110.1	8.3	93.4	104.5	–
Average	52.4	212.62	196.2	33.43	54.11	107.29	144.65

Figure 13: Mean deviation between experimental data and homogeneous flow models (from Asadi et al. (2014)).

0.3.3.3 Lockhart-Martinelli model

The most widely used approach to compute the pressure drop in multiphase flows is the Lockhart and Martinelli (1949) model. In this model, the two-phase pressure drop is defined as the sum between the liquid pressure drop, the gas pressure drop, and a two-phase term as in equation 15.

$$\left(\frac{dP}{dx}\right)^2 = \left(\frac{dP_l}{dx}\right)^2 + \left(\frac{dP_g}{dx}\right)^2 + C\left(\frac{dP_l}{dx}\right)\left(\frac{dP_g}{dx}\right) \tag{15}$$

The single-phase pressure drops $\left(\frac{dP_l}{dx}\right)$ and $\left(\frac{dP_g}{dx}\right)$ are computed using the Fanning equation (equation 16), where f_k is the Fanning friction factor.

$$\frac{dP_k}{dx} = 2f_k\frac{\rho_k u_k^2}{D_h} \tag{16}$$

C (defined in equation 15) is the Chisholm parameter. Similar to the equivalent viscosity in the homogeneous model, dozen of correlations for this parameter have been developped. Most of these correlations depend on the hydraulic diameter D_h, the Reynolds number, and the Weber number. The most common correlations for microchannels are given in Table 2. The reader is refered to Asadi et al. (2014) for a more extensive review of the Lockhart-Martinelli correlations.

In his review, Asadi et al. (2014) showed that the Lockhart-Martinelli model outperforms the homogeneous model to predict annular and churn flows. Furthermore, he noted that correlations developed specifically for microchannels yield improved results. For instance, the correlation of Qu and Mudawar (2003) showed the best performance among the considered experiments (with an average error of 20% on the set of experiments). Following this, the models by Mishima et al. (1993) and Lee et al. (2012) also provided favorable results.
Other research groups, including Ma et al. (2010) and Salim (2018), tested Lockhart-Martinelli

Authors	Correlation
Mishima and Hibiki (1996)	$C = 21(1 - e^{-0.319 D_h})$
Hwang and Kim (2006)	$C = 0.227\,\mathrm{Re}_l^{0.452}\,X^{-0.32} N^{-0.82}$, with $N = \sqrt{\sigma / g(\rho_l - \rho_g) d_h^2}$
Chen et al. (2007)	$C = mx^n$
	$m = 5.55 - 0.758555 A^{-0.805} + 0.00439\,\mathrm{Re}_l$
	$n = 0.1001 + 0.0005 A^{0.895}$
Kawahara et al. (2009)	$C = 1.38\,\mathrm{Bo}^{0.04}\,\mathrm{Re}_l^{0.52}\,\mathrm{We}_g^{-0.12}$
Choi et al. (1991)	$C = 1732.95\,\mathrm{Re}^{-0.323}\,\mathrm{We}^{-0.24}$

Table 2: Most common Lockhart-Martinelli correlations.

correlations on microchannels but found that no correlation could predict pressure drop with average errors smaller than 20%.

0.3.3.4 Friedel model

Friedel (1979) proposed a correlation based on the Lockhart-Martinelli model where the parameters depend on dimensionless numbers. This correlation uses the Froude number $\mathrm{Fr} = \dfrac{u}{\sqrt{gL_c}}$ defined as the ratio of flow inertia and gravity, as well as the Weber number (equation 17).

$$\frac{dP/dx}{dP_l/dx} = A + 3.21 x^{0.78} (1-x)^{0.224} \left(\frac{\rho_l}{\rho_g}\right)^{0.91} \left(\frac{\mu_g}{\mu_l}\right)^{0.19} \left(1 - \frac{\mu_g}{\mu_l}\right)^{0.7} \mathrm{Fr}^{-0.0454}\,\mathrm{We}^{-0.035} \tag{17}$$

x is the vapour quality and A is defined as equation 18.

$$A = (1-x)^2 + x^2 \rho_l \lambda_g \left(\rho_g \lambda_l\right)^{-1} \tag{18}$$

The Friedel correlation is often mentioned in literature reviews, but rarely compared to experimental results, therefore it is difficult to assess its reliability.

0.3.3.5 Correlations for boiling and condensation in microchannels

Developing a universal correlation for heat transfer in microchannels is difficult because it depends heavily on the heat transfer mechanisms, which vary according to the flow regime. Thome and Consolini (2010) detailed the dominant heat transfer mechanisms for the most common flow regimes. This is also illustrated by Figure 14.

- **Bubbly flow:** In bubbly flows, heat transfer is dominated by nucleate boiling.
- **Slug flow:** In slug flows, heat transfer at the wall is dominated by single-phase liquid convection. The liquid superheat then leads to interface boiling.
- **Annular flow:** The heat transfer mechanism for annular flows is similar to slug flows.
- **Droplet flow:** In droplet flows, heat transfer at the wall is dominated by single-phase vapour convection. The vapour superheat then leads to interface boiling.

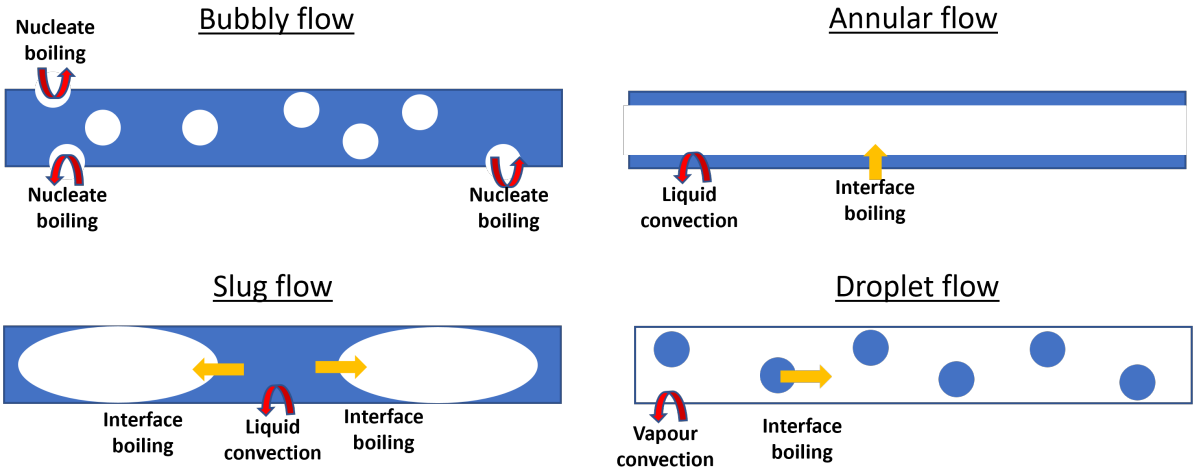

Figure 14: Dominant heat transfer mechanisms in bubbly, slug, annular, and droplet flows. The red arrows represent wall/fluid transfers, while the orange arrows represent liquid/gas transfers.

Similar to pressure drop computations, numerous correlations have been proposed for calculating the heat transfer coefficient in microchannels. Bertsch et al. (2008) conducted a comprehensive study testing 25 correlations on 1847 experimental data points in microchannels. The results indicated that none of the correlations could predict half of the measures with an error smaller than 30%. Notably, even correlations specifically developed for microchannels did not outperform conventional correlations. The conclusion drawn was that physical models need to be developed for predicting the heat transfer coefficient, as correlations exhibit poor reliability.

0.3.3.6 Conclusion about empirical models in microchannels

Remark 0.3.6. Numerous research groups have attempted to predict two-phase head losses in microchannels using 1D models, such as the homogeneous model, the Lockhart-Martinelli model, or the Friedel model. This is also true for correlations predicting the Nusselt number. The prevailing consensus is that no empirical correlation can reliably predict head losses or heat transfer coefficients in a general case. Consequently, many research groups now prefer the use of a 3D Computational Fluid Dynamics (CFD) approach over empirical methods as detailed in the next section.

0.3.3.7 CFD

The first 3D numerical studies on boiling flow in microchannels focused on the growth of a single vapour bubble in a superheated liquid. This approach makes sense because, as discussed in section 0.3.1, nucleate boiling is rare in microchannel and interface boiling is often the predominant phenomenon. For example, Mukherjee et al. (2011) used a Level-Set Method to simulate the growth of a vapour bubble in a microchannel and compared it with experimental results. This case is particularly crucial as it involves bubble growth in a superheated liquid, along with surface tension and wettability effects when the bubble reaches the channel walls. It will serve as a pivotal validation case for the models developed in this thesis. More recently, the researchers improved the interface capturing methods to gain accuracy or computational time. In his PhD, Magnini (2012) developed a height function algorithm to enhance the computation of the surface tension in VOF. Pan et al. (2016) developed a saturated-interface-volume phase change model to decrease the computational time, and also proposed a new method to limit spurious velocities at the interface in VOF. Some other authors, such as Ferrari et al. (2017), or Ling et al. (2015) decided to couple the VOF and the Level-Set methods to ensure mass conservation thanks

to the VOF algorithm while benefiting from the good accuracy of the Level-Set method on the interface curvature.
These progresses in numerical methods facilitated advanced sensitivity studies, revealing the fundamental importance of some parameters. For example, Munic chi et al. (2024) recently showed that the wall wettability can significantly affect the heat transfer coefficient (by a factor higher than 2). They also showed that the geometry of a rectangular microchannel (its height to width ratio) plays a role in the value of the heat transfer coefficient.
In recent years, Lattice-Boltzmann methods have also been employed for simulating flows in microchannels, as demonstrated in studies such as Li et al. (2024), Zhang et al. (2023), and Zhang et al. (2021). While there is growing interest in these methods, significant challenges persist in accurately simulating two-phase flows using Lattice-Boltzmann methods, and these methods are less mature than the 3D CFD methods. For instance, validation cases like the one by Mukherjee et al. (2011), which will be presented in Chapter 4, are commonly simulated using 3D Computational Fluid Dynamics (CFD) methods but not with Lattice Boltzmann Method (LBM) simulations.

Remark 0.3.7. In this short literature review, we showed that the existing 1D correlation for boiling flows in microchannels are highly inaccurate and cannot be used reliably to predict the drying of failed fuel rods. 3D CFD simulations on the other hand, are very precise and accurate. Their biggest drawback is their computational cost. Unfortunately, with the current numerical capabilities, it is unrealistic to simulate flow boiling in microchannels for more than a few seconds.

0.4 Methodology

The literature review detailed why it is currently impossible to simulate the drying of failed rods with a good accuracy and in a reasonable time. In fact, before this PhD thesis, it would have taken around 100,000 years to simulate one hour of drying of failed rod. The challenge of this thesis on the drying of failed rods therefore lies in finding a solution to limit the computational time. To do that, the manuscript will be split into three parts:

1. **3D numerical approach.** This first part aims to deepen the understanding of flow boiling in microchannels using a 3D CFD approach. Chapter 1 introduces the multifield software neptune_cfd used in this research, along with its governing equations. Chapters 2 and 3 describe new models implemented in neptune_cfd: chapter 2 introduces a drag force model to minimize spurious velocities, and chapter 3 presents an analytical interfacial phase change model validated against various cases. Chapter 4 details improvements to the wettability model applied to microchannels. The optimizations developed in this section reduce the computational time by a factor of 10 and underscore the role of wettability in drying. However, a simulation of one hour of drying would still require around 10,000 years, necessitating additional methods.

2. **Experimental approach.** Part II presents an experimental investigation into flow boiling in microchannels conducted in collaboration with LEGI. This study identifies various flow regimes and validates the Kreutzer law for pressure drop in the slug flow regime. The experiments provide essential validation data for the upscaling model discussed in part III.

3. **Upscaling.** The final section applies the insights from parts I and II to construct a 1D model (chapter 6) capable of simulating flow boiling in failed rods with reasonable accuracy and significantly reduced computational cost. While this 1D model requires several weeks to simulate an hour of drying, it reveals that two-phase effects are negligible for the drying process. Using this finding, a 0D model (chapter 7) was developed to simulate drying in under a minute, enabling the construction of a reference table for drying times based on the relevant parameters.

The gain in computational time through the thesis is presented in Figure 15.

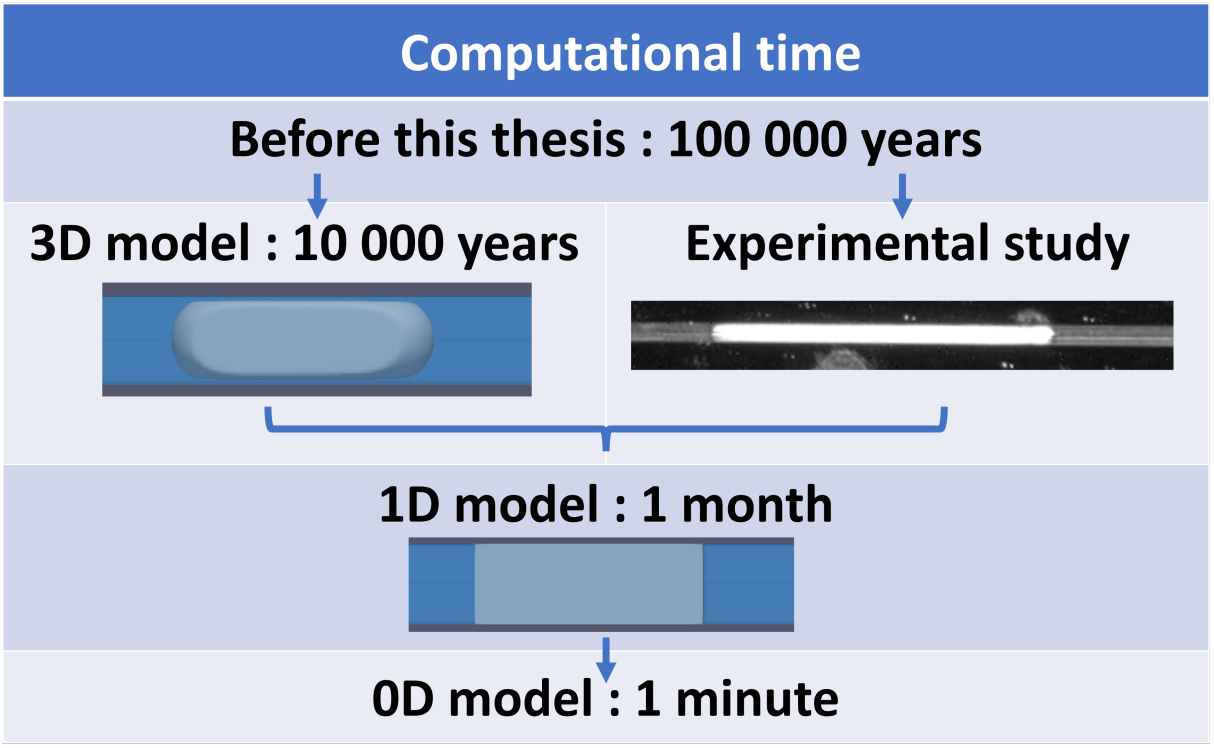

Figure 15: Gain in computational time simulating one hour of drying of failed rod through the thesis.

Part I

3D numerical study of flow boiling in microchannels

In the introduction, it was established that 3D CFD simulations are currently the only numerical method capable of accurately modelling flow boiling in microchannels. Prior to this study, the CFD software neptune_cfd, used in this thesis, could effectively represent large bubbles in adiabatic flows with excellent accuracy. However, existing phase change models within the software were insufficiently accurate, and the bubble-wall contact was not appropriately handled.

This section addresses these limitations to improve the modelling of flow boiling in microchannels. Chapter 1 introduces the neptune_cfd software and its governing equations. Chapter 2 presents a new drag force expression to reduce spurious velocities at the liquid-vapor interface, which will be applied throughout this thesis. Chapter 3 details the Mucellphage, a new analytical phase change model, and validates it against various analytical and experimental cases. Chapter 4 introduces enhancements to the existing wettability model to account for confinement effects. Following these four chapters, neptune_cfd is able to simulate bubble boiling in microchannels with near-perfect accuracy.

This work demonstrates the critical role of wettability in microchannels, paving the way for an upscaling model developed in part III.

CHAPTER 1

Governing equations and numerical methods

Summary

The 3D CFD solver neptune_cfd will be used in this thesis to model precisely the two-phase flow in the uranium cracks. This chapter presents the governing equations implemented in this software, as well as the standard models used in the following chapters.

1.1 The neptune_cfd software

The neptune_cfd software is developped by Électricité de France (EDF), Commissariat à l'Énergie Atomique et aux Énergies Alternatives (CEA), Institut de Radioprotection et de Sûreté Nucléaire (IRSN) and Framatome. It is a computational fluid dynamic code based on the two-fluid model of Ishii (1975) and Delhaye et al. (1981) for the modelling of two-phase flow in 3D. Density, viscosity, volume fraction and local velocity are defined for each field in each cell. The solver is implemented in the neptune_cfd environment (Guelfi et al. (2007), Mimouni et al. (2008)). It is based on a finite volume discretization, together with a collocated arrangement for all variables. A common pressure is assumed for all fields. A Semi-Implicit Method for Pressure-Linked Equations (SIMPLE) solver is used in the code neptune_cfd. An iterative coupling of these equations is applied to ensure mass conservation (and energy conservation for non-isothermal flows). More details about the numerical methods can be found in Fleau (2017).
Historically, neptune_cfd was mainly used with subgrid approaches, notably to model boiling crisis in nuclear reactors with a dispersed bubble model, and spray in the containment structure of nuclear power plants with a dispersed droplet model. More recently, models to represent and resolve "large interfaces" have been developed. These models are designed to capture the liquid/gas interface and are commonly used for free-surface flows, such as those in seas or rivers, or to model large bubbles with a surface tension force.

1.2 Governing equations

The mass, momentum, and enthalpy conservation equations are solved for all considered fields k. In this manuscript, two fields are utilized: a liquid field and a gas field. Employing the multi-field formulation, the conservation equations are represented by equation 1.1, equation 1.2, and equation 1.3 for mass, momentum, and enthalpy conservation, respectively. The method for deriving the multi-field balance equations from the Navier-Stokes equations is detailed in Appendix C.

Mass balance equation

$$\frac{\partial}{\partial t}(\alpha_k \rho_k) + \nabla.(\alpha_k \rho_k \underline{u}_k) = \Gamma_k \tag{1.1}$$

Momentum balance equation

$$\frac{\partial}{\partial t}(\alpha_k \rho_k \underline{u}_k) + \nabla.(\alpha_k \rho_k \underline{u}_k \otimes \underline{u}_k) = -\alpha_k \nabla P + \nabla.(\alpha_k \mu_k \underline{\underline{S_k}}) + \underline{I'_k} + \Gamma_k \underline{u^I_k} + \alpha_k \rho_k \underline{g} + \underline{F}_{ST,k} \tag{1.2}$$

$\underline{\underline{S_k}}$ is the viscous stress tensor. $\underline{u^I_k}$ is the interfacial velocity between the phases. $\underline{F}_{ST,k}$ is the surface tension force. It is detailed in section 1.4.3 for large interfaces and not modeled for dispersed approaches.

Enthalpy balance equation

$$\frac{\partial}{\partial t}(\alpha_k \rho_k H_k) + \nabla.(\alpha_k \rho_k H_k \underline{u}_k) = \nabla.(\alpha_k \lambda_k \nabla T_k) + \nabla.(\alpha_k \mu_k \underline{\underline{S_k}}.\underline{u_k}) + \alpha_k \frac{\partial P_k}{\partial t} + \alpha_k \rho_k \underline{g}.\underline{u_k} + \Pi_k + \varphi_{(wall->k)} \tag{1.3}$$

$\varphi_{(wall->k)}$ represents the heat exchanges with walls.

Remark 1.2.1. Turbulent terms are not modeled because section 0.3.1 showed that the flow is laminar in microchannels. Similarly, the gravity terms are neglected in the microchannel cases. However, it is essential to note that gravity is not negligible in some validation cases at larger scales. Therefore, the gravity terms are included in the momentum and enthalpy equations for those scenarios.

The physical parameters, such as the density ρ, the viscosity μ, or the conductivity λ are computed from the CATHARE tables. These tables give the value of these parameters for a high range of pressures and enthalpies.

Remark 1.2.2. Γ_k, I'_k, and Π_k are - respectively - the interfacial mass, momentum, and enthalpy transfers between the liquid and the gas phases. These transfers require specific models and closure laws which will be presented in the next sections. It should be noted that the interfacial enthalpy transfer Π_k can be split in two terms as in equation 1.4. The first term, Π'_k, is the sensible heat transfer, independent of mass transfer. The second term, $\Gamma_k h_{lat}$, is the latent heat transfer, related to the mass transfer between the two phases. h_{lat} is the enthalpy of vaporization [J.mol^{-1}].

$$\Pi_k = \Pi'_k + \Gamma_k h_{lat} \tag{1.4}$$

Using mass and enthalpy conservation ($\sum \Gamma_k = 0$ and $\sum \Pi_k = 0$), it is possible to express the interfacial mass transfer as a function of the interfacial sensible heat as in equation 1.5. For this reason, only I'_k and Π'_k require specific models.

$$\Gamma_l = -\Gamma_g = \frac{\Pi'_l + \Pi'_g}{h_{lat}} \tag{1.5}$$

1.3 Dispersed phase approaches

In the dispersed phase approaches, one field is treated as continuous and carries the dispersed field. In the bubble model, the gas phase is dispersed in the form of spherical bubbles, while in the droplet model, the liquid phase is dispersed in the form of spherical droplets. In both cases, the spherical hypothesis is done. These approaches yield relatively good results in many scenarios and do not require a fine mesh, as the droplets and bubbles are represented with subgrid models. The dispersed approaches are presented in this chapter to give an overview of the multi-field software neptune_cfd. However, they will not be used in part I, and the Large Interface Model presented in section 1.4 will be employed instead, because dispersed approaches are not able to capture microscale effects such as surface tension. Chapter 8 shows how dispersed approaches and large interface approaches can be combined to minimize computational time

Remark 1.3.1. In both the bubble and droplet models, an interfacial area concentration transport equation is solved (equation 1.6). The user can opt for a constant bubble/droplet diameter or choose more intricate models involving bubble/droplet growth, coalescence, and fragmentation of the dispersed field.

$$\frac{\partial a_i}{\partial t} + \nabla.(a_i \underline{u_d}) = \frac{2}{3}\frac{a_i}{\alpha_d \rho_d}\left(\Gamma_d - \alpha_d \frac{d\rho_d}{dt}\right) + \pi d_{NUC}^2 \Phi^{NUC} + \Phi^{CO} + \Phi^{BK} \tag{1.6}$$

In this section, the index d refers to the dispersed phase, while the index c refers to the continuous phase. $a_i = \dfrac{6\alpha_d}{d}$ is the interfacial area concentration. Φ^{NUC}, Φ^{CO} and Φ^{BK} are terms which account

for nucleation, coalescence and breakup respectively. These terms require specific models. Γ_d is the mass transfer source term from the continuous to the dispersed phase.

For dispersed fields, the interfacial momentum transfer I'_k can be split into three contributions as in equation 1.7.

$$\underline{I'}_d = \underline{F_d}^D + \underline{F_d}^L + \underline{F_d}^{AM} \tag{1.7}$$

Three interfacial forces are modeled: the drag force $\underline{F_d}^D$, the lift force $\underline{F_d}^L$, and the added mass force $\underline{F_d}^{AM}$. For droplets, only the drag force and the lift force are used. The expression of these three forces are given in equations 1.8, 1.9, 1.10. It is also possible to consider forces such as the turbulent dispersion force, but they are not considered in this PhD.

$$\underline{F_d}^D = \frac{1}{8} a_i \rho_c C_D \|\underline{u}_d - \underline{u}_c\| (\underline{u}_d - \underline{u}_c) \tag{1.8}$$

$$\underline{F_d}^L = -C_L \alpha_d \rho_c (\underline{u_d} - \underline{u_c}) \wedge (\nabla \wedge \underline{u_c}) \tag{1.9}$$

$$\underline{F_d}^{AM} = -C_{AM} \frac{1 + 2\alpha_d}{1 - \alpha_d} \alpha_d \rho_c \left[\left(\frac{\partial \underline{u_d}}{\partial t} + \underline{u_d}.\left(\nabla \underline{u_d}\right) \right) - \left(\frac{\partial \underline{u_c}}{\partial t} + \underline{u_c}.(\nabla \underline{u_c}) \right) \right] \tag{1.10}$$

Remark 1.3.2. C_D, C_L and C_{AM} are the drag, lift, and added mass coefficients respectively. These coefficients are given by empirical laws detailed in the following subsections.

The interfacial terms used for the dispersed fields are summarized in Table 1.1

	Bubble	Droplet
Drag	Ishii (1979)	Wen and Yu (1966)
Phase Change	Manon (2000) / Ranz-Marshall (1952)	Sherwood/Nusselt
Lift	Tomiyama (2002)	Baalbaki (2011)
Added mass	Zuber (1964)	-

Table 1.1: Interfacial momentum transfer terms for the bubble and the droplet models.

1.3.1 Bubble model

1.3.1.1 Interfacial momentum transfer

In the bubble model, the drag coefficient C_D is computed from the model of Ishii and Zuber (1979). The lift coefficient C_L is given by the correlation of Tomiyama et al. (2002), and the added mass coefficient C_{AM} is obtained from the model of Zuber (1964).

1.3.1.2 Interfacial enthalpy transfer for the gas

As for the interfacial enthalpy transfer, a "time-step return to saturation" model is used for the gas.

$$\Pi'_g = \alpha_l \alpha_g \frac{\rho_g c_{p,g}}{\tau_{relax}} (T_{sat} - T_g) \tag{1.11}$$

$\tau_{relax} = 10^{-2}$ s, is the time to saturation. $(T_{sat} - T_g)$ represents the superheat when $T_g > T_{sat}$.

1.3.1.3 Interfacial enthalpy transfer for the liquid

When the liquid is in a superheated state ($h_l > h_{sat}$), the correlation of Berne (1983) is used to model the flashing of the liquid. It is also based on a return to saturation model.

$$\Pi'_l = C_{berne} a_i (h_l - h_{sat}) y_{vap} \tag{1.12}$$

y_{vap} is the vapour mass fraction, a_i is the interfacial area computed from the bubble density and the bubble diameter, and C_{berne} is an empirical coefficient.

When the liquid is in a subcooled state ($h_l < h_{sat}$), the model of Manon (2000) is used for the interfacial enthalpy transfer (equation 1.13).

$$\Pi'_l = \frac{6\alpha_g \lambda_l}{c_{p,l} d_b^2} \mathrm{Nu} (h_{sat} - h_l) y_{vap} \tag{1.13}$$

The Nusselt number is computed from the Ranz-Marshal correlation ($\mathrm{Nu} = 2 + 0.6\,\mathrm{Re}^{1/2}\,\mathrm{Pr}^{1/3}$). d_b is the bubble diameter.

1.3.2 Droplet model

1.3.2.1 Interfacial momentum transfer

In the droplet model, the drag coefficient C_D is computed from the model of Wen and Yu (1966). The lift coefficient C_L is given by the correlation of Baalbaki (2011).

1.3.2.2 Interfacial enthalpy transfer

The interfacial enthalpy transfer term for droplets is computed using a semi analytical model presented in equations 1.14 and 1.15. The first term is the latent heat transfer. The second term is the sensible heat transfer.

$$\Pi'_g = \frac{6\alpha_l}{d^2_{droplet}} \mathrm{Nu}\, \lambda_g(T_m)(T_l - T_g) \tag{1.14}$$

$$\Gamma_g = \frac{6\alpha_l}{d^2_{droplet}} \mathrm{Sh}\, D(T_m)(\rho_{sat}(T_l) - \rho_g y_{vap}) \tag{1.15}$$

$D(T_m)$ is the diffusion coefficient computed from empirical correlations. The Sherwood number is computed from the Frossling correlation ($\mathrm{Sh} = 2 + 0.56\,\mathrm{Re}^{1/2}\,\mathrm{Sc}^{1/3}$), Sc is the Schmidt number. The Nusselt number is computed from the Ranz-Marshall correlation ($\mathrm{Nu}_g = 2 + 0.6\,\mathrm{Re}_g^{1/2}\,\mathrm{Pr}_g^{1/3}$). $\rho_{sat}(T_l)$ represents the saturation density at the liquid temperature. Pr is the Prandtl number.
This model is presented in more detail in Loiseau et al. (2023).

1.4 The Large Interface Model (LIM)

The Large Interface Model (LIM) was initially developed to represent the interface between a liquid and a gas when it significantly exceeds the size of a computational cell (Coste (2013)). This situation often arises in "free-surface flows" when liquid and gas are separated due to gravity.
Subsequently, in the works of Denèfle (2013) and Fleau (2017), this approach was extended to model large bubbles. In this extension, an alternative expression for the drag force is employed, an interface sharpening equation is solved at each time step to prevent the spread of the interface, and the surface-tension force is modeled. In this manuscript, references to the LIM will specifically denote this newer approach, rather than the "free-surface flow" application.

1.4.1 Interfacial momentum transfer

The interfacial momentum transfer term for the LIM is often referred to as a "drag force". Strictly speaking, it is not a drag force, as a drag force represents an integral force on an object, whereas the interfacial momentum transfer is a local force between the liquid and gas within a cell. Despite this distinction, for simplicity, this interfacial force will be referred to as a drag force in this manuscript.
The LIM drag force implemented in the code and employed before this PhD is a combination of the expression proposed by Coste (2013), and the expression proposed by Mimouni et al. (2017). The drag force $\underline{I'_k} = \underline{F_k^D}$ is computed using equation 1.8. The model of Coste gives the drag factor $f_d = \frac{3}{4}\rho_c \frac{\|\underline{u_c} - \underline{u_d}\|}{d_d} C_D$ in equation 1.16. The coefficient f_d is then employed to compute the coefficent C_D .

$$f_d = f_g + \theta(f_b - f_g) \tag{1.16}$$

$\theta = 1 - 0.5\cos(\pi\alpha_l)$ is a parameter used for numerical stability, f_b and f_g are given by equation 1.17:

$$\begin{cases} f_b = \dfrac{18\mu_l}{\alpha_l (dp_{\text{bubble, disp}})^2}(1 + 0.15\,\mathrm{Re}_g^{0.687}) \\ f_g = \dfrac{18\mu_g}{\alpha_g (dp_{\text{droplet, disp}})^2}(1 + 0.15\,\mathrm{Re}_l^{0.687}) \end{cases} \tag{1.17}$$

$dp_{bubble,disp}$ is taken equal to 5.10^{-3} m, and $dp_{droplet,disp}$ is taken equal to 10^{-3} m.

Remark 1.4.1. In the majority of cases presented in this manuscript, the value $f_D = 10^{12}$ will be used instead. This choice ensures that the relative velocity between the liquid and gas at the interface is close to 0, similar to the behavior in single-fluid approaches such as VOF and Level Set. This assumption is accurate for fine meshes and effectively mitigates spurious velocities at the interface (see section 2.1).

1.4.2 Interface sharpening

The numerical resolution of the equations presented in section 1.2 introduces artificial diffusion of the interface. This issue is well known within the multiphase flow community, and if left unaddressed, it can lead to nonphysical phenomena due to the diffusion of the interface across a large number of cells. For example, Fleau (2017) demonstrated that deactivating the interface sharpening in the Bhaga case (see chapter 2) resulted in significant qualitative differences in the bubble shape and a 27% relative error in the final velocity of the bubble.
To mitigate this numerical diffusion, one solution is to employ an interface sharpening method. The method used in neptune_cfd was initially proposed as a conservative level-set method for two-phase flow by Olsson and Kreiss (2005) and improved in Olsson et al. (2007).

Remark 1.4.2. In standard level set methods, the interface is captured and defined by the level set function Φ. This function corresponds to the signed distance to the interface, taking a value of 0 precisely at the interface between two fluids. It is positive on one side and negative on the other, as illustrated in Figure 1.1. At each time step, an advection equation (equation 1.18) is solved to capture the movement of the interface.

$$\frac{\partial \Phi}{\partial t} + \underline{u}.\nabla\Phi = 0 \tag{1.18}$$

The Level-Set (LS) method is relatively straightforward to implement compared to other methods such as Volume of Fluid (VOF). It enables accurate computation of the normal to the interface $\underline{n}$, and the curvature of the interface κ as in equations 1.19 and 1.20. Its biggest drawback is that the LS function needs to be reinitialized at each time step because the interface moves and consequently the isosurface

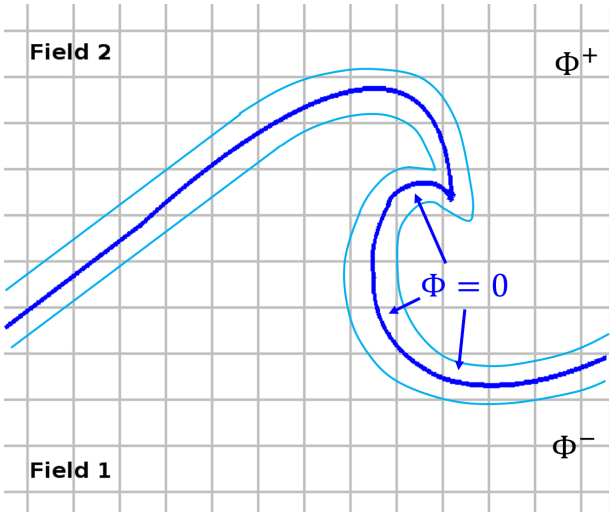

Figure 1.1: Schematic view of a Level-Set method on a moving interface. Picture from Fleau (2017).

$\Phi = 0$ also does. Unfortunately, most reinitialization methods introduce numerical errors, leading to the non-conservation of the area enclosed by the zero level set and, consequently, the non-conservation of the mass for each field.

$$\underline{n} = \frac{\nabla\Phi}{\|\nabla\Phi\|} \tag{1.19}$$

$$\kappa = -\nabla.(\underline{n}) \tag{1.20}$$

To avoid the mass conservation issues associated with the reinitialisation step, Olsson and Kreiss (2005) suggested replacing the LS function with a smeared Heaviside H function defined in equation 1.21. This new variable is spread over a thickness $2e$ (dependent on the grid size), ranging from 0 to 1. The interface is now defined by the isosurface $H = 0.5$.

$$H(\Phi) = \begin{cases} 0, & \text{if } \Phi < -e, \\ \frac{1}{2} + \frac{\Phi}{2e} + \frac{1}{2\pi}\sin\left(\frac{\pi\Phi}{e}\right), & \text{if } -e \leq \Phi \leq e, \\ 1, & \text{if } \Phi > e. \end{cases} \tag{1.21}$$

Remark 1.4.3. Equation 1.21 is presented by Olsson and Kreiss (2005) as an illustrative example for the variable change. In practice, this expression is not employed. Instead, the method described below is applied to a function H that is decorrelated from the Level-Set (LS) function Φ.

Olsson and Kreiss (2005) showed that this new function can be advected by equation 1.18 while conserving the area bounded by $H = 0.5$. The formulas for the normal to the interface and the curvature (equations 1.19 and 1.20) also hold true for the function H. They added an artificial compression to maintain the thickness of the interface equal to $2e$. It is given in equation 1.22. This method practically gives the same results as a conventional LS method, but it does conserve the mass of each field as the recompression equation is conservative - unlike the reinitialization step in conventional LS methods.

$$\frac{\partial H}{\partial \tau} + \nabla.(H(1-H)\underline{n}) = \epsilon\nabla.(\nabla H) \tag{1.22}$$

Remark 1.4.4. The term $\epsilon\nabla.(\nabla H)$ acts as a viscosity term, preventing discontinuities at the interface. The choice of the term $\nabla.(H(1-H)\underline{n})$ ensures that the recompression equation is only relevant near the interface (in areas where $H(1-H)$ is not equal to 0), and in the normal direction to the interface.
The parameters τ and ϵ set the thickness $2e$ of the interface. They are arbitrarily chosen, and may differ between codes.
Equation 1.22 is solved iteratively until a steady-state is reached (ie the volume fraction does not vary significantly after an iteration). The criterion used in neptune_cfd was specified by Fleau (2017) as:

$$\sum_{I}^{ncel} \delta\alpha_k^I |1-2\alpha_k^I|\Omega^I < \epsilon \sum_{I}^{ncel} \alpha_l^I \alpha_g^I \Omega^I \tag{1.23}$$

$\sum_I^{ncel} \alpha_l^I \alpha_g^I \Omega^I$ represents the volume occupied by the interface before solving the interface sharpening equation. The term $\delta\alpha_k^I|1-2\alpha_k^I|$ evaluates its variation after one iteration of the interface sharpening equation ($\delta\alpha_k$ represents the variation of α_k in a cell after one iteration). $\epsilon = 5 \times 10^{-4}$ is the convergence coefficient.

The interface sharpening model was implemented in neptune_cfd by Denèfle (2013) and Fleau (2017). The values picked for the coefficients ϵ and τ are given in equation 1.24, and correspond to an interface thickness of $5\Delta x$, with Δx the grid size.

$$\epsilon = \frac{\Delta x}{2} \quad \text{and} \quad \Delta\tau = \frac{\Delta x}{32} \tag{1.24}$$

The decision to use the volume fraction $\alpha_k = H$ as the conservative level-set function was motivated by its similar properties to H. Notably, it is bounded between 0 and 1, and the mass conservation equation (Equation 1.1) is an advection equation. Moreover, it allows the incorporation of mass transfer through the term Γ_k. This choice aligns with other research groups employing different codes, as seen in Štrubelj and Tiselj and Mathur et al. (2019).
Hence, equation 1.22 is applied to α_k at every time step.

Remark 1.4.5. With this approach α_k has two meanings. It represents the volume fraction in the balance equations, and the conservative level-set function because of the interface sharpening. The "physical" interface is represented by the isosurface $\alpha = 0.5$.

1.4.3 Surface tension

The surface tension force is modeled with the Continuum Surface Force (CSF) of Brackbill et al. (1992). In this model, the surface tension force is computed with a volume formulation. Notably, this means that the force is applied to five cells because the interface is spread on five cells with the interface sharpening method. This approach preserves the total surface tension force, and enhances the numerical robustness. This Continuum Surface Force is computed as:

$$\underline{F}_{ST,k} = \alpha_k \sigma \kappa \nabla \alpha_k \tag{1.25}$$

σ is the coefficient of surface tension of the fluid, and κ is the curvature computed with equation 1.26.

$$\kappa = -\nabla.(\underline{n_k}) = -\nabla.\left(\frac{\nabla\alpha_k}{\|\nabla\alpha_k\|}\right) \tag{1.26}$$

Remark 1.4.6. The computation of the curvature requires an approximation of the second order derivative of the conservative level set function α_k. To improve the accuracy of this approximation, α_k is diffused over multiple cells, similar to what is done with the smooth VOF method (Pianet et al. (2010)).
A fictive local function $\alpha_{diff,k}$ is constructed from α_k by incrementally solving equation 1.27. This equation conserves the normal vector, and diffuses α_k over several cells, depending on the value of $D\Delta\tau$ and on the number of iterations. For instance, $D\Delta\tau = 0.1$ and 10 iterations results in a diffusion of α_k over three cells.

$$\frac{\Delta\alpha_{diff,k}}{\Delta\tau} - \nabla.(D\nabla(\alpha_{diff,k})) = 0 \tag{1.27}$$

The surface tension force defined in equation 1.25 is then computed using $\alpha_{diff,k}$ instead of α_k.

1.4.4 Interfacial enthalpy transfer

Two interfacial enthalpy transfer models were available before this work for large interfaces in neptune_cfd: the LI3C model - an empirical return to saturation model, and the semi-analytical model of Fleau (2017) based on the gradient method. However, these models will not be used in this manuscript for reasons that will be explained later, and the new Mucellphage model presented in chapter 3 will be used instead.

CHAPTER 2

Adiabatic resolved flows in neptune_cfd

Summary

Simulating flows in microchannels necessitates modelling surface tension effects through the explicit resolution of the interface, rather than employing subgrid models. The interface sharpening approach, developed during the PhD work of Denèfle (2013) and Fleau (2017), is evaluated in this chapter for its effectiveness in modelling large bubble and slug flows. Additionally, an adjustment to the drag force formulation is proposed. The chapter begins with a simple verification case to quantify spurious velocities and validate the surface tension force. Subsequently, the velocity and deformation of a rising bubble under gravity are compared to experimental results.

2.1 Static bubble in a liquid

2.1.1 Description of the case

In this simple verification case, a bubble is placed in a stationary liquid with no gravity. Under these conditions, a spherical bubble is in equilibrium and should not move, as described by equation 2.1.

$$-\alpha_k \nabla P + \alpha_k \sigma \kappa \nabla \alpha_k = 0 \tag{2.1}$$

However, numerical methods, including CFD, do not compute the surface tension force, and in particular, the curvature, with a perfect accuracy. This results in an imperfect equilibrium, leading to small velocities and oscillations at the bubble interface. These instabilities, named "spurious velocities" or "spurious currents" have been studied extensively in the past 20 years. Several methods have been developped to reduce these spurious currents (Popinet (2009), Vincent et al. (2004), Magnini (2012), Abadie (2013) to name a few).
Before studying flows involving strong capillary effects, such as two-phase flows in microchannels, it is important to assess the impact of these spurious velocities on the numerical simulations.

2.1.2 Numerical case

The physical domain considered is a 5 mm $\times$ 5 mm square. Wall boundary conditions are set to the top, the bottom, and the side of this domain, and symmetry conditions are set to the two other boundaries. A 2D bubble with a radius R = 1 mm is initially placed in the middle of this domain. The density and the viscosity of both the liquid and the gas are set to ρ = 1000 kg.m^{-3} and μ = 0.001 Pa.s to avoid effects caused by a difference in physical properties. The case is summarized in Figure 2.1.
The simulation is run for 0.5 seconds with the meshes and time steps listed in Table 2.1. The Laplace pressure jump is computed as the difference between the average pressure in the gas cells, and the average pressure in the liquid cells. The spurious velocities are computed from equation 2.2.

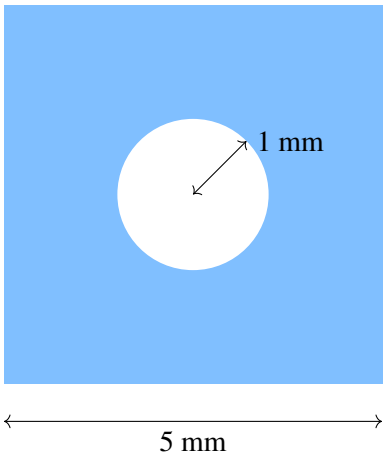

Figure 2.1: Schematic view of the static bubble case.

$$U_{spur} = \frac{\sum \alpha_g U_g}{\sum \alpha_g} \tag{2.2}$$

All the simulations are computed with an interface sharpening and the surface tension force. Two drag force models for large interfaces are compared: the LIM drag force presented in section 1.4.1, and an infinite drag force model ($f_d = 10^{12}$) proposed in this thesis.

Mesh	Cell size Δx (µm)	Time step (s)
Coarse	100	10^{-5}
Medium	50	5×10^{-6}
Fine	25	2.5×10^{-6}

Table 2.1: Cell size and time step according to the mesh for the static bubble case, three refinement levels: Coarse, Medium and Fine.

2.1.3 Numerical results

Figure 2.2 shows the norm of the spurious velocities with the two drag force models. It is clear that the infinite drag force induces less spurious velocities. This reduction occurs because some spurious velocities are introduced by the artificial relative velocity between the liquid and the gas. Furthermore, the figure demonstrates that using 20 cells per bubble diameter ensures that spurious velocities remain below 0.06 m/s. This level of resolution is sufficient to minimize the impact of numerical inaccuracies on the simulation results.

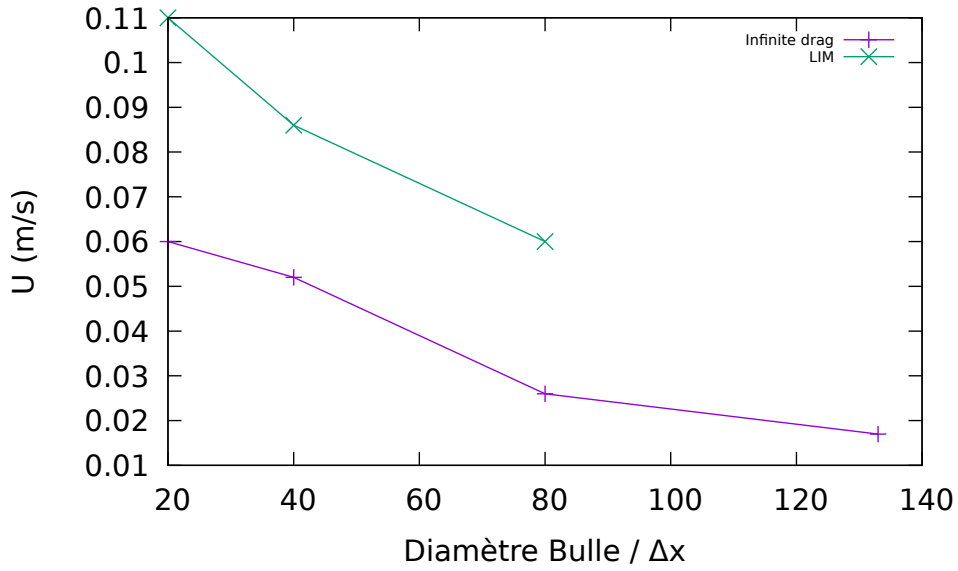

Figure 2.2: Norm of the spurious velocities as a function of the number of cells per bubble diameter. The green curve shows the results for the LIM drag force. The purple curve shows the results for the infinite drag force.

2.2 Rising bubble under gravity

2.2.1 Description of the case

The case of a rising bubble under gravity, also known as the case of Bhaga and Weber (1981), serves as a benchmark for validating the surface tension force in simulating moving bubbles. In this scenario, a bubble is initiated at the bottom of a water column and ascends due to buoyancy. Initially, the bubble maintains a spherical shape when its velocity is low. However, as it ascends, the increasing influence of inertia causes the bubble to flatten. Experimental data provide information about the bubble's shape and velocity as a function of time.

2.2.2 Numerical case

In this chapter, we focus on simulating case b of the experiment of Bhaga and Weber (1981). For simulations of other cases using neptune_cfd, readers are directed to Fleau (2017). The computational domain is a cuboid measuring 0.104 m $\times$ 0.104 m $\times$ 0.312 m in size. At the top of the domain, an outlet boundary condition at atmospheric pressure is applied, while the other boundary zones are treated as walls. The physical properties of the fluids used in the simulations are detailed in Table 2.2.

Phase	Density (kg.m^{-3})	Viscosity (Pa.s)
Liquid	1350	2.02
Gas	1.35	1.8×10^{-5}

Table 2.2: Physical properties in the Bhaga case (Bhaga and Weber (1981)).

An hydrostatic pressure is initially imposed in the column:

$$P = P_0 + \rho g(z_{max} - z) \tag{2.3}$$

$P_0 = 10^5$ bar is the atmospheric pressure, $z_{max} = 0.312$ m is the maximum height. The initial configuration places the bubble with a radius of $R = 1.3$ cm at a distance of $3R$ from the bottom of the water column. The Bhaga case is simulated using an adaptive time step determined by the Courant-Friedrichs-Lewy (CFL) condition Which the maximum allowed is set to 0.9.
A fine mesh with a regular cell size of $\Delta x = 500$ µm is used for the simulations. Previous studies have indicated that this resolution is adequate to achieve mesh convergence. Similar to the previous case, two drag force models are compared: the standard LIM drag force model, and the infinite drag force model.

2.2.3 Numerical results

Figure 2.3 shows the final shape of the bubble in the experiment of Bhaga. The numerical results correctly reproduce the ellipsoidal shape of the bubble, demonstrating that an infinite drag force obtains good qualitative results.

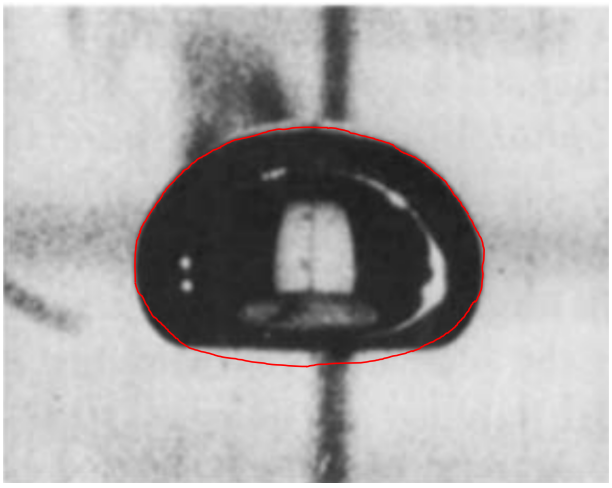

Figure 2.3: Comparison of the bubble shape in case b of the Bhaga experiment at $t = 0.6$ s. The picture is taken from the original article of Bhaga and Weber (1981). The red contour represents the bubble shape obtained with neptune_cfd. It was hand-drawn following the isosurface $\alpha = 0.5$.

As for the quantitative results, the final bubble velocity is compared to experimental results using both drag models in Figure 2.4. The results obtained with the LIM drag force exhibit a 20% overestimation

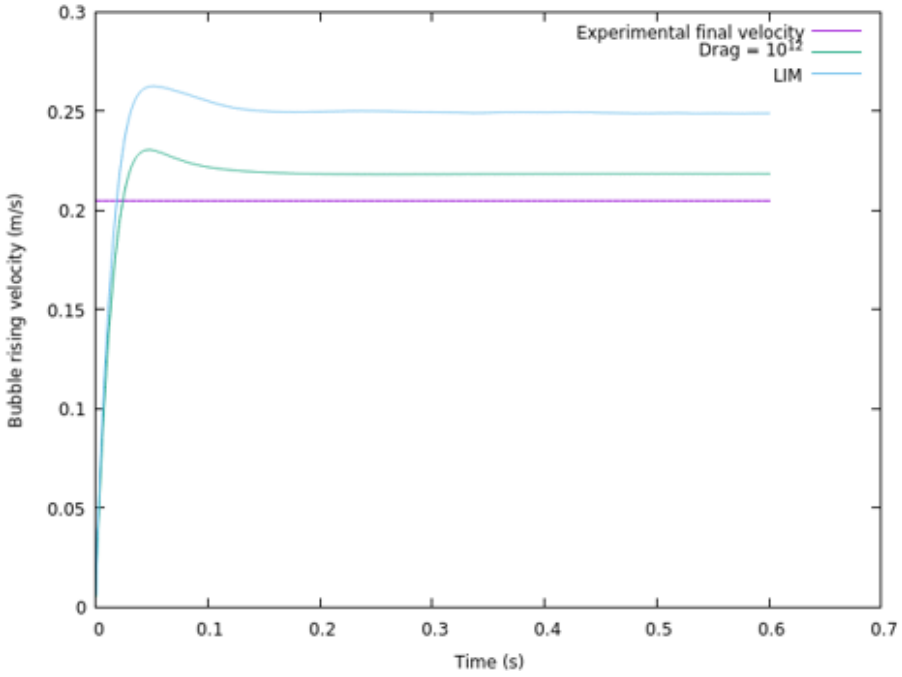

Figure 2.4: Evolution of the rising velocity of the Bhaga bubble over time. The purple curve represents the asymptotic velocity measured experimentally. The blue and green curves display the velocity of the bubble for the LIM and the infinite drag models respectively.

in velocity. This discrepancy is expected since the bubble experiences less deceleration from the liquid with the LIM drag force, due to the allowance of a relative velocity.

2.3 Conclusion

In this chapter, we evaluated the capability of neptune_cfd to simulate two straightforward adiabatic cases that involve modelling large interfaces using an interface sharpening approach: the case of the static bubble and the case of the ascendant bubble in a fluid at rest (Bhaga). Both cases demonstrated that an infinite drag force produces better results compared to the previous drag force model.
The study of a static bubble in a quiescent liquid revealed that applying an infinite drag force reduces the spurious velocities by 100%. Additionally, it indicated that using a grid resolution of 20 cells per bubble diameter effectively minimizes the spurious velocities at the interface between the liquid and the gas.
The Bhaga experiment, which involves the rise of a bubble in a water column under the influence of gravity, was simulated with very good accuracy. This simulation also showed that an infinite drag force yields slightly better quantitative results than the previous model. Therefore, this infinite drag force expression will be employed when using the LIM in the next chapters.

CHAPTER 3

The Mucellphage Model

Summary

In the previous chapter on adiabatic flows, the capability of neptune_cfd to model adiabatic flows involving large interfaces with good accuracy, employing an interface sharpening method and the surface tension force, was demonstrated.
However, to accurately model boiling flows involved in the drying of failed rods, it is crucial to calculate heat and mass transfer precisely. As discussed in section 0.3.1, bulk boiling takes precedence over nucleate boiling in microchannels, necessitating special attention to modelling heat and mass transfer at the interface between the liquid and the gas.
This chapter will present the most common models in the literature, along with those already available in neptune_cfd. Subsequently, a new model developed in this thesis will be detailed and validated against the usual verification and validation cases.

3.1 Available models in the literature and in neptune_cfd

3.1.1 Most common models in the literature

3.1.1.1 The gradient method

The most commonly used phase change model with an interface tracking approach is the gradient method. It has been used by numerous research groups such as Mukherjee and Kandlikar (2005), or Sato and Ničeno (2013). It is a semi-analytical method based on the Fourier law (equations 3.1 and 3.2). In this method, the interface is assumed to be at the saturation temperature T_{sat}. Therefore, the gradient of the temperature can be computed as $\underline{\nabla} T = \dfrac{T_i - T_{sat}}{d} \underline{n}$, with T_i being the temperature in an adjacent cell to the interface, and d the distance between this adjacent cell and the interface.

$$\varphi_l = -\lambda_l \underline{\nabla} T_l . \underline{n} \tag{3.1}$$

$$\varphi_{vap} = \lambda_{vap} \underline{\nabla} T_{vap} . \underline{n} \tag{3.2}$$

Remark 3.1.1. The gradient method shows very interesting mesh convergence towards analytical solutions. Its main drawback is that accurately locating the interface can be challenging to implement.

3.1.1.2 The Schrage model

The model of Schrage (1953) is another analytical model based on the classical evaporation theories of Hertz-Knudsen, which models the interaction of vapour molecules with a liquid interface. Kunkelmann (2011) reported that this model is less accurate at the same spatial resolution when compared to the gradient method. However, it does not require the reconstruction of an interface with a 0 thickness, which is why some research groups still use it.
In this model, the interface is represented as a heat resistance (equation 3.3). The coefficient R_{int} is defined by equation 3.4.

$$\varphi_k = \frac{T_k - T_{sat}}{R_{int}} \tag{3.3}$$

$$R_{int} = \frac{2 - \chi_e}{2\chi_e} \frac{\sqrt{2\pi R_{gas}} T_{sat}^{3/2}}{h_{lat}^2 \rho_v} \tag{3.4}$$

χ_e is the accommodation coefficient. It can be measured experimentally, but it is taken equal to 1 in most codes. R_{gas} is the specific gas constant.

Remark 3.1.2. To compute the total heat flux Φ_k [W] (or the volumic heat flux Π'_k [W.m^{-3}]) from the surface heat flux φ_k [W.m^{-2}], an approximation of the interface area A in each cell is necessary. Some researchers, like Hardt and Wondra (2008), have utilized equation 3.5 for this purpose, while others, such as Magnini (2012), have opted for the geometrically calculated interface area obtained through the reconstruction of the interface. Kunkelmann (2011) demonstrated that employing the expression provided in equation 3.5 necessitates a much finer resolution, while using a reconstructed interface reduces the mesh refinement requirements by a factor of 4.

$$\frac{A}{V_{cell}} = \|\nabla \alpha\| \tag{3.5}$$

V_{cell} is the volume of the cell considered.

3.1.1.3 The Lee model

The model of Lee (1980) is a relaxation model that keeps the temperature around the interface near saturation. The mass transfer rate is computed using Equation 3.6. Ω_k is an empirical coefficient.

$$\dot{m}_k = \frac{\Omega_k \rho_k \alpha_k (T_{sat} - T_k)}{T_{sat}} \tag{3.6}$$

Remark 3.1.3. The Lee model does not necessitate any information about the shape or position of the interface. Additionally, it exhibits low sensitivity to mesh refinement, making it effective on coarse meshes. However, the time to reach T_{sat} is dependent on the empirical coefficient Ω_k, and as a result, the model will introduce some error when compared to an analytical solution.

3.1.2 Models available in neptune_cfd

3.1.2.1 The LI3C model

In the LI3C model, the heat transfer terms used in neptune_cfd Π'_l and Π'_g are computed from a wall law model, as in Equations (3.7) and (3.8). h_{ge} and h_{le} are computed from empirical correlations, depending on multiple parameters, similar to what is done in the Lee model. The model of Jayatilleke (1966) is used for the gas coefficient. The heat transfer coefficient of the liquid h_{le} is taken from the Interface Sublayer Model (ISM) of Yao et al. (2005).

$$\Pi'_l = h_{le}(T_{sat} - T_l) \tag{3.7}$$

$$\Pi'_g = h_{ge}(T_{sat} - T_g) \tag{3.8}$$

Remark 3.1.4. The empirical LI3C model shares both the advantages and drawbacks of the Lee model. It is important to note that the empirical coefficients were calibrated to simulate free-surface flows. Consequently, this model is not suited for boiling at the interface between liquid and bubbles.

3.1.2.2 The Fleau model

Reconstructing the interface in each cell can be a challenging task, especially with the added complexity of the interface sharpening method, where the interface is smeared over multiple cells. To address this difficulty, Fleau (2017) developed a model based on the gradient method that does not require the explicit reconstruction of the interface. This model is inspired from the work of Nichita and Thome (2010) who developed a phase change model for Level Set codes.
This approach introduces a volume reformulation of the heat transfer term, similar to the method employed by Brackbill et al. (1992) for the surface tension force. The heat transfer term is distributed across multiple cells while maintaining the total heat transfer. The model is presented in equation 3.9.

$$\Pi'_k = -\alpha_g \lambda_k \nabla T_k . \nabla \alpha_k \tag{3.9}$$

∇T_k is computed as $\nabla T_k = \frac{T_{sat} - T_k}{\Delta x} \underline{n}_k$ where Δx is the cell size.

Remark 3.1.5. Being based on the gradient method, the Fleau model converges toward analytical solutions and was extensively validated in Fleau (2017). However, we will show in the next section that it suffers from a very slow mesh convergence.

3.2 Presentation of the new MUltiphase cutCELL PHase chanGE (Mucellphage) heat transfer model

3.2.1 The need for a new analytical model in neptune_cfd

3.2.1.1 Limit of the preexisting models

The Sublayer LI3C model is an empirical model, and as such, it tends to provide good qualitative results, but its quantitative accuracy is limited, particularly at atmospheric pressure. While its simplicity and low sensitivity to mesh refinement make it valuable for industrial applications with complex geometries, it does not achieve a high level of accuracy. This limitation becomes crucial when studying boiling phenomena in microchannels where precision is essential.
Regarding the Fleau model, while it converges toward analytical solutions, a comparison with the results obtained by other authors using the standard gradient method indicates that mesh convergence is notably worse with the Fleau model. To achieve comparable accuracy, the size of the interface cells must be three to five times smaller with the Fleau model. This discrepancy in mesh convergence is explained through semi-analytical considerations in the next section.

3.2.1.2 Comparison between the standard gradient method and the Fleau model

When a bubble is put in a superheated liquid, a thermal microlayer is formed around the bubble. In this thermal microlayer, the temperature increases from the temperature of the interface ($T^{int} = T_{sat}$) to the temperature of the superheated liquid far from the interface T_{max}.

Remark 3.2.1. Scriven (1958) found an analytical expression of the liquid temperature according to the distance from the interface for a bubble placed in a superheated liquid. It is given in Equation 3.10 (d represents the distance from the interface).

$$T_l(d) = T_{max} - 2\beta^2 \frac{\rho_v(h_{lat} + (c_{p,l} - c_{p,v}\Delta T))}{\rho_l c_{p,l}} \int_{1-\frac{R}{R+d}}^{\frac{1}{R}} \exp\left(-\beta^2((1-x)^{-2} - 2\left(1 - \frac{\rho_v}{\rho_l}\right)x - 1)\right)dx \tag{3.10}$$

T_{max} is the temperature of the liquid far from the interface. R is the radius of the bubble. β is a coefficient, it can be computed as $\beta = \sqrt{\frac{3}{\pi}} \frac{\Delta T}{\frac{\rho_v}{\rho_l}\left(\frac{h_{lat}}{c_{p,l}} + \frac{c_{p,l}-c_{p,v}}{c_{p,l}}\Delta T\right)}$ according to the approximation of Scriven (1958).

To better understand this complex expression, an illustrative example is provided. Let's consider a bubble with a radius $R_0 = 50$ µm in superheated water at $P = 1$ bar and $T = T_{sat} + 5$. Figure 3.1 depicts the evolution of the liquid temperature as a function of the distance from the interface. This temperature profile can be separated in 3 zones.

1. Close to the interface (less than two micrometers away), the temperature increases linearly in the linear thermal layer.
2. Further away, in the transition zone, the temperature keeps increasing until it reaches T_{max}, but the evolution is no longer linear.
3. Finally, far from the interface (d $>$ 4 µm), the temperature is constant and equal to T_{max}.

In the gradient method, the gradient of temperature at the interface, denoted as ∇T_l, is computed as $\nabla T_l = \frac{T_l - T_{sat}}{\Delta x}$, where Δx is the distance to the interface. Therefore, to accurately compute the

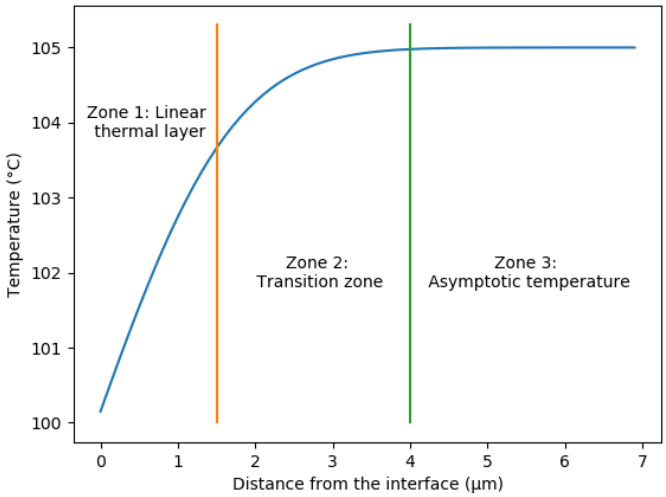

Figure 3.1: Liquid temperature as a function of the distance from the interface for a 50 µm bubble in a superheated liquid (from equation 3.10). The fluid considered is water at atmospheric pressure, and the liquid superheat is equal to 5°C.

analytical temperature gradient, the cell must be within the linear thermal layer. However, the heat transfer model of Fleau averages the heat transfer over 5 cells. Consequently, the length of 5 cells must be smaller than the linear thermal layer. Compared to methods like VOF or LS, where the interfaces are reconstructed, this results in a considerably slower mesh convergence toward the analytical solution.

3.2.2 Description of the Mucellphage model

To address the slow mesh convergence issues mentioned above, a new model compatible with the two-fluid approach and the interface sharpening method was developed. In this model, an interface with zero thickness is reconstructed from the conservative level-set function α_k. This enables the use of the gradient method with similar mesh convergence properties to the VOF and LS methods.
The reconstruction of the interface and the computation of the heat transfer with the gradient method requires 4 steps:

1. Locating the interface cells (i.e., the cells containing the zero-thickness interface).
2. Identifying the cell normal to the interface to compute the temperature gradient.
3. Computing the area of the interface within a cell, denoted as A_{int}.
4. Calculating the temperature gradient.

The interfacial heat transfer is finally computed as equation3.11.

$$\Pi'_k = -\lambda_k \nabla T_k \frac{A_{int}}{V_{cell}} \tag{3.11}$$

A step by step implementation of the Mucellphage model in neptune_cfd is provided in Appendix D.

3.2.2.1 Localisation of the interface

A cut-cell like method is used to locate the cells which contain a part of the interface, similar to what is done in Benguigui et al. (2018) for the immersed boundary method. The volume fraction is interpolated

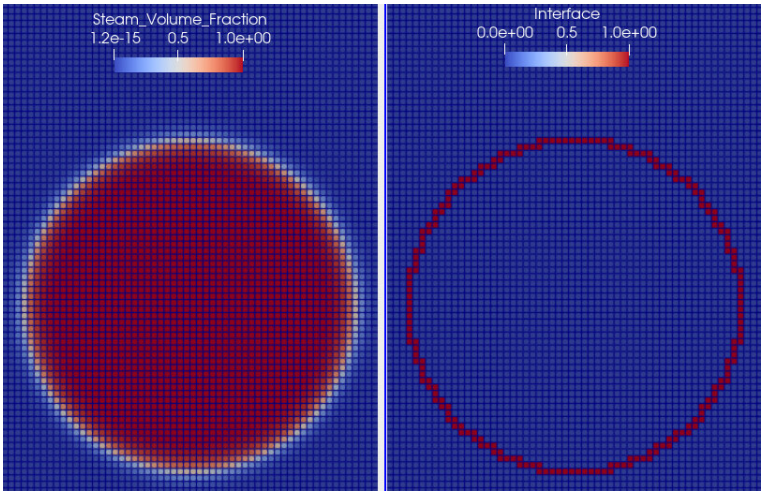

Figure 3.2: 2D bubble in a liquid. The left picture shows the gas volume fraction, which varies from 0 to 1 in 5 cells because of the interface sharpening algorithm. In the right picture, the interface cells are identified in red with the criteria detailed above.

from the center to the vertices of each cell. A cell is considered intersected by an interface if it has at least one vertex with $\alpha > 0.5$, and at least one vertex with $\alpha < 0.5$ (see Figure 3.5a).
For a 2D bubble, Figure 3.2 shows the volume fraction with an interface sharpening method on the left, and the interface cells (in red) on the right.

3.2.2.2 Identification of the normal cell to the interface

To compute the temperature gradient at the interface, it is necessary to identify the adjacent cell in the direction of the interface normal for each interface cell.
All cells sharing a vertex with the interface cell are considered, including those diagonal to the interface cell. The angle between the normal vector to the interface ($\underline{n} = \frac{\underline{\nabla}\alpha}{\|\underline{\nabla}\alpha\|}$ in Figure 3.3), and the line linking the interface cell to the adjacent cell (the green lines in Figure 3.3) is then computed. The normal cell to the interface is the one with the smallest angle between these two vectors.
Figure 3.4 shows the interface cells in white for a 2D bubble. The red arrows represent the vector going from the interface cells to the adjacent normal cells.

3.2.2.3 Computation of the area of the interface in a cell

The computation of the area A_{int} of the interface in a cell is carried out in three steps.

1. In the first step, two vertices with $\alpha - 0.5$ of opposite signs are selected. Using linear interpolation, the point that satisfies the condition $\alpha = 0.5$ between these two vertices is identified, as illustrated in Figure 3.5a.

2. In the second step, the interface is approximated by a plane. This plane is constructed using the interpolated point and the normal vector to the interface. The intersection between the interface plane and the edges of the cell forms a polyhedron as shown in Figure 3.5b (the normal vector was (1,1,1) in this example).

3. Finally, this polyhedron is divided into triangles, and the area of the interface in the cell is computed as demonstrated in Figure 3.5c.

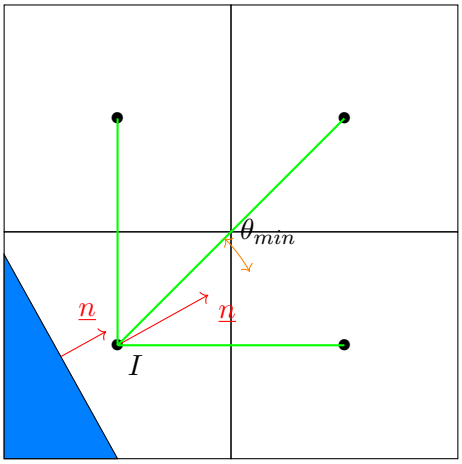

Figure 3.3: Identification of the normal cell. The normal to the interface $\underline{n}$ is in red. The green lines link the center of the interface cell to the adjacent cells. The normal cell is the cell with the smallest angle θ_{min}.

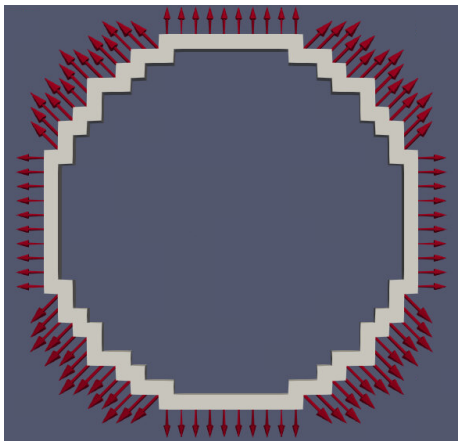

Figure 3.4: The interface cells are represented in white. The red arrows represent, for each interface cell, the vector going from the center of the cell to the center of the adjacent normal cell.

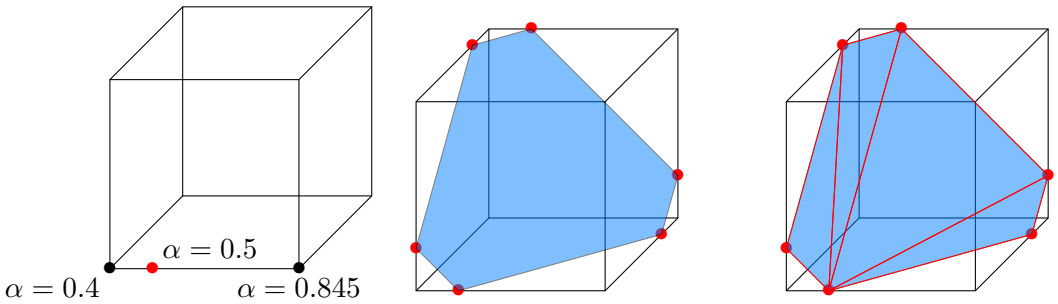

(a) Linear interpolation of a point verifying $\alpha = 0.5$ between two vertices of a cell.

(b) Construction of the plane approximating the interface using the interpolated point and $\underline{n}$.

(c) Splitting of the interface plane into triangles and computation of the interface area.

Figure 3.5: Interface plane construction and computation of the interfacial area.

Cell size (mm)	Time step (s)	Perimeter (cm)
Theory	-	6.3
1.56	7.5×10^{-5}	6.2
0.78	7.5×10^{-5}	6.4
0.52	3×10^{-5}	6.4
0.39	10^{-5}	6.4

Table 3.1: Perimeter of the circular bubble computed for different meshes.

Cell size (mm)	Time step (s)	Area (cm^2)
Theory	-	12.6
1.56	7.5×10^{-5}	11.4
0.78	7.5×10^{-5}	12.4
0.52	3×10^{-5}	12.5

Table 3.2: Surface area of the spherical bubble computed for different meshes.

This approach for computing the area of an interface was validated in 2D to calculate the perimeter of a circle, and in 3D to determine the surface of a sphere. In the 2D case, a circular air bubble with a radius $R = 1$ cm is initialized in an infinite liquid. The computation is run for 0.05 seconds on 4 square meshes using interface sharpening and surface tension. The size of the cells and the time step used for each mesh are given in Table 3.1.
In the 3D case, a spherical air bubble is initialized with a radius $R = 1$ cm in an infinite liquid. The computation is also run for 0.05 seconds using interface sharpening and surface tension on hexahedron cells. The size of the cells and the time step used for each mesh are provided in Table 3.2.
As shown in Tables 3.1 and 3.2, the algorithm detailed above predicts the interface area with good accuracy, with errors of less than 2% in both 2D and 3D once mesh convergence is reached.

Remark 3.2.2. Achieving mesh convergence requires a finer mesh in 3D than in 2D. This difference is due to the higher error caused by plane interpolation on the area of a sphere compared to linear interpolation on the perimeter of a circle.

The 3D case involving a spherical air bubble was also tested with a 2D axisymmetric approach. The results regarding the interface area were close to the 3D computations, but some oscillations in the surface area were observed, reaching up to 8%. These oscillations might be attributed to a less accurate computation of the surface tension force. Therefore, while this approach is also validated for 2D asymmetric cases, its accuracy is expected to be slightly lower.

3.2.3 Computation of the temperature gradient

In the Mucellphage model, the interface is supposed to be at the saturation temperature T_{sat}. The interface is described by a plane as explained in the previous sections. Thus, the distance between the center of the normal cell and the plane is represented as the orange line labeled "d" in Figure 3.6. The temperature gradient is computed using Equation 3.12.

$$\nabla T = \frac{T_{cell} - T_{sat}}{d} \tag{3.12}$$

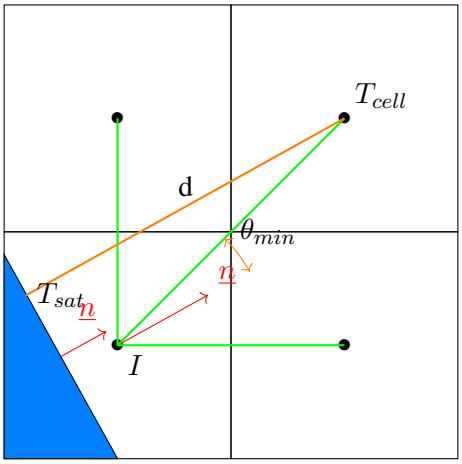

Figure 3.6: Computation of the temperature gradient. The interface is at the temperature T_{sat}. The orange line represents the distance d between the normal cell and the interface.

3.2.4 Diffusion of the mass source term

The mass source term calculated using the Mucellphage model can be substantial and may result in a significant rise in pressure or velocities in the interface cell, leading to numerical instabilities. To address this concern, a method akin to the one employed in Hardt and Wondra (2008) was implemented. The mass source term Γ_k computed at the interface is diffused over 3 cells using a diffusion equation. To do that, equation 3.13 is solved over 10 iterations with $D\Delta\tau = 0.1$.

$$\frac{\Delta\Gamma_k}{\Delta\tau} - \nabla.(D\nabla(\Gamma_k)) = 0 \tag{3.13}$$

Remark 3.2.3. In contrast to sharp interface methods like VOF, altering the volume fraction in cells located 3 cells away from the interface is not problematic due to the spreading of the interface over 5 cells. Consequently, there is no requirement for additional numerical treatments to reduce the interface thickness.

3.3 Verification of the Mucellphage model

In this section, the Mucellphage Model is compared with the analytical solutions of three verification cases, where mass transfer is the primary phenomenon: the 1D Sucking problem, the 1D Stefan problem, and a static bubble in a superheated liquid (also known as the case of Scriven (1958)). The sensitivity to the time step was checked for all cases. Therefore the analysis will focus on the mesh and model sensitivity.

3.3.1 The 1D Sucking problem

3.3.1.1 Description of the Sucking Problem

In the 1D Sucking Problem, a saturated vapour phase is in contact with a wall heated at the saturation temperature T_{sat}. The vapour is in contact with an infinite liquid initially at a temperature $T_{max} > T_{sat}$. In the Sucking case, the vapour remains at saturation, while the liquid boils at the interface, causing a displacement of the vapour/water interface. This scenario is summarized in Figure 3.7.

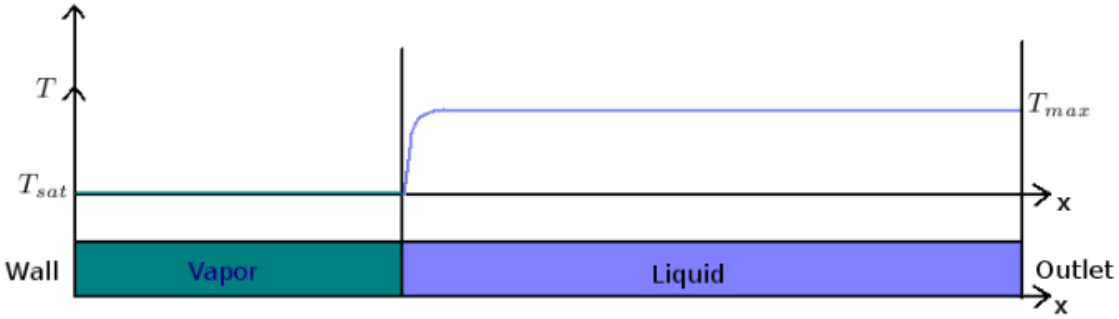

Figure 3.7: Description of the Sucking Problem (from Fleau (2017)).

	ρ (kg/m^3)	μ (Pa.s)	c_p (J/kg/K)	λ (W/m/K)	h_{lat} (J/kg)	σ (N/m)	T_{sat} (K)
Liquid	958	2.7×10^{-4}	4236	0.69	2.27×10^6	0.072	373.15
Gas	0.58	1.39×10^{-5}	1501	0.025	-	-	-

Table 3.3: Mean physical properties of water at 1 bar computed with CATHARE.

The theory of the Sucking Problem is given in Welch and Wilson (2000). The evolution of the interface position $X(t)$ is described analytically by Equation (3.14).

$$X(t) = \sqrt{\frac{2}{\pi}} \frac{\rho_l c_{p,l}}{\rho_v h_{lat}} (T_{max} - T_{sat}) \sqrt{2\chi_l t} \tag{3.14}$$

χ_l is the thermal diffusivity of the liquid phase. The fluid used in this section is water at 1 bar. The physical properties are given in Table 3.3.

Remark 3.3.1. Because it is a 1D problem, the sucking problem is a single-effect case involving only heat and mass transfer, whereas 3D cases are also affected by surface tension. It validates the interfacial heat transfer term Π_l' as the liquid is superheated.

3.3.1.2 Results on the Sucking Problem

Figure 3.8 illustrates the evolution of the interface position over time. The analytical solution is denoted by purple crosses, the results using the Mucellphage are represented with full lines, and the outcomes employing the Fleau model are depicted with dotted lines. This comparative analysis reveals that both models converge towards the analytical solution; however, the Mucellphage model achieves convergence with a significantly coarser mesh, as anticipated in section 3.2.1. Specifically, the Fleau model requires a cell size of $\Delta x = 12.5$ µm to reach the analytical solution, while the Mucellphage accomplishes the same accuracy with a cell size of $\Delta x = 5$ µm. Consequently, the Mucellphage can achieve the equivalent level of accuracy as the Fleau model with cells that are three times coarser.

Remark 3.3.2. If the mass transfer term is not spread over multiple cells employing the procedure detailed in section 3.2.4, this term becomes exceedingly large in the interface cells as the mesh is refined. In fact, without this numerical treatment, numerical instabilities emerge for cells smaller than $\Delta x = 25$ µm. However, with the mass source term diffusion, it is possible to achieve a mesh size as low as $\Delta x = 5$ µm without encountering these instabilities.

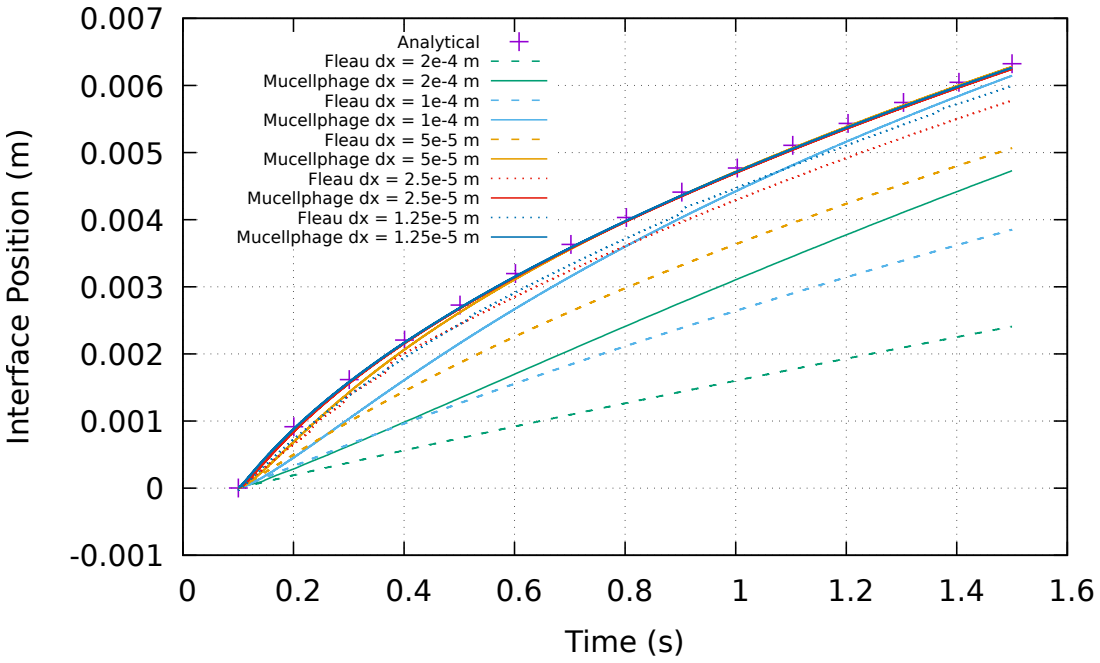

Figure 3.8: Evolution of the interface position over time for the sucking problem with different meshes. The purple crosses represent the analytical solution, the full lines represent the results using the Mucellphage model, and the dotted lines represent the results obtained with the model of Fleau.

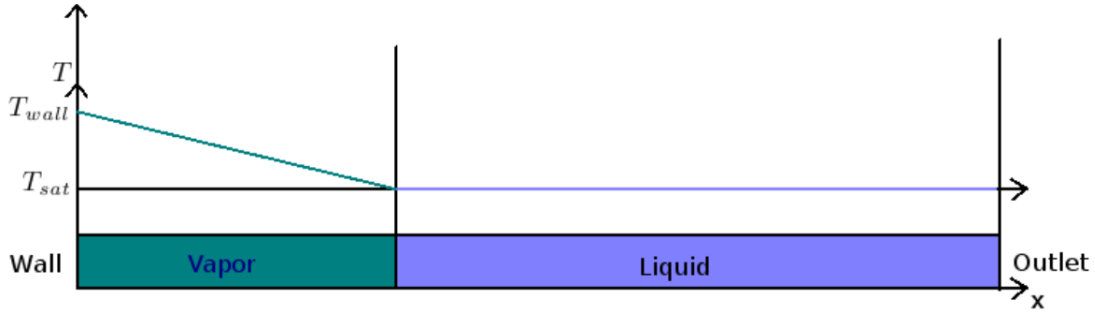

Figure 3.9: Description of the Stefan Problem (from Fleau (2017)).

3.3.2 The 1D Stefan problem

3.3.2.1 Description of the Stefan Problem

The 1D Stefan Problem is similar to the Sucking Problem, except that the temperature gradient is in the gas, rather than the liquid. In this scenario, a vapour phase is in contact with a wall heated at a temperature $T_{max} > T_{sat}$, while an infinite liquid is initially at saturation. As a result, the vapour is expected to heat the liquid and induce boiling at the interface. This case is illustrated by Figure 3.9.
The theory of the Stefan Problem is also given in Welch and Wilson (2000). The evolution of the interface position is given by Equation (3.15).

$$X(t) = 2\beta\sqrt{\chi_v t} \tag{3.15}$$

where β is the solution of equation 3.16. erf is the error function defined as $\text{erf}(z) = \frac{2}{\pi}\int_0^z e^{-t^2}\,dt$. χ_v is the thermal diffusivity of the vapour phase.

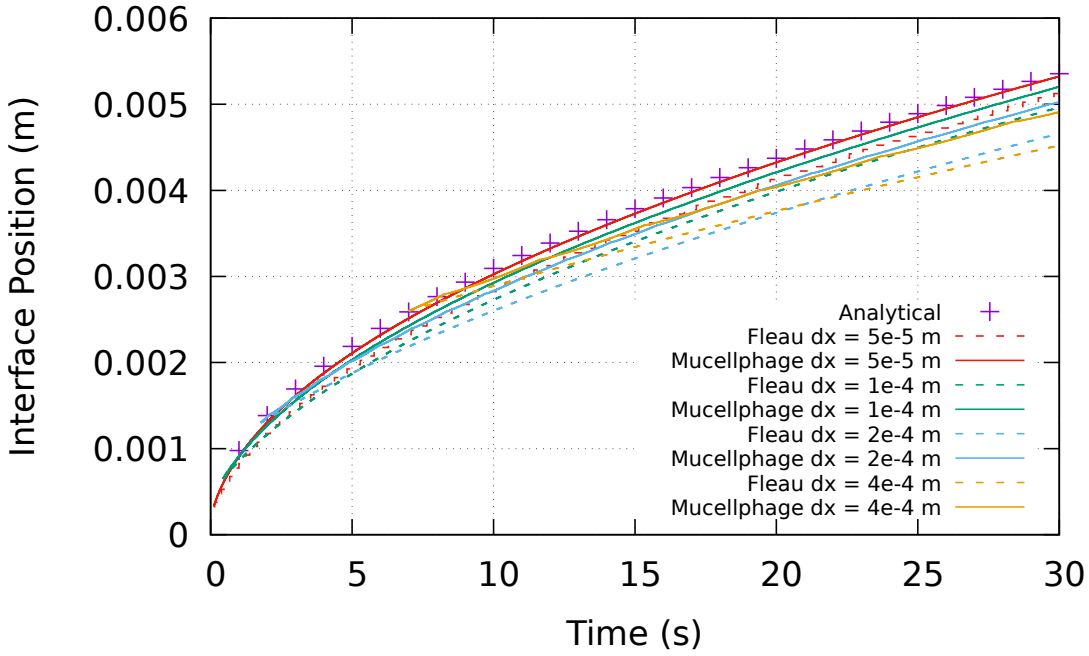

Figure 3.10: Evolution of the interface position over time for the Stefan problem with different meshes. The purple crosses represent the analytical solution, the full lines represent the results using the Mucellphage model, and the dotted lines represent the results obtained with the model of Fleau.

$$\beta \exp(\beta^2)\text{erf}(\beta) = \frac{c_{p,v}(T_{max} - T_{sat})}{\sqrt{\pi} h_{lat}} \tag{3.16}$$

The fluid used in the simulations is also water at P = 1 bar. Its physical properties are given in Table 3.3. This results in $\beta \approx 0.15$.

Remark 3.3.3. Like the sucking problem, the Stefan problem is a single-effect case involving only heat and mass transfer. It validates the interfacial heat transfer term Π'_g because this time the gas phase is superheated.

3.3.2.2 Results on the Stefan Problem

The results for the Stefan problem are displayed in Figure 3.10. Similar to what was observed for the sucking problem, the mesh convergence is significantly faster with the Mucellphage model.

3.3.3 Bubble in superheated liquid (Scriven case)

3.3.3.1 Description of the Scriven case

Unlike the Sucking and Stefan problems, the Scriven case is a 3D case. In the Scriven case, a saturated bubble is placed in an infinite superheated liquid resulting in boiling at the interface and the growth of the bubble. An analytical solution of this problem is provided in Scriven (1958). The evolution of the bubble radius can be approximated using Equation (3.17). More detail about how this equation is obtained is given in Appendix E

$$R(t) = 2\sqrt{\frac{3}{\pi}} \frac{\Delta T \sqrt{\rho_l c_{p,l} \lambda_l t}}{\rho_v h_{lat}} \tag{3.17}$$

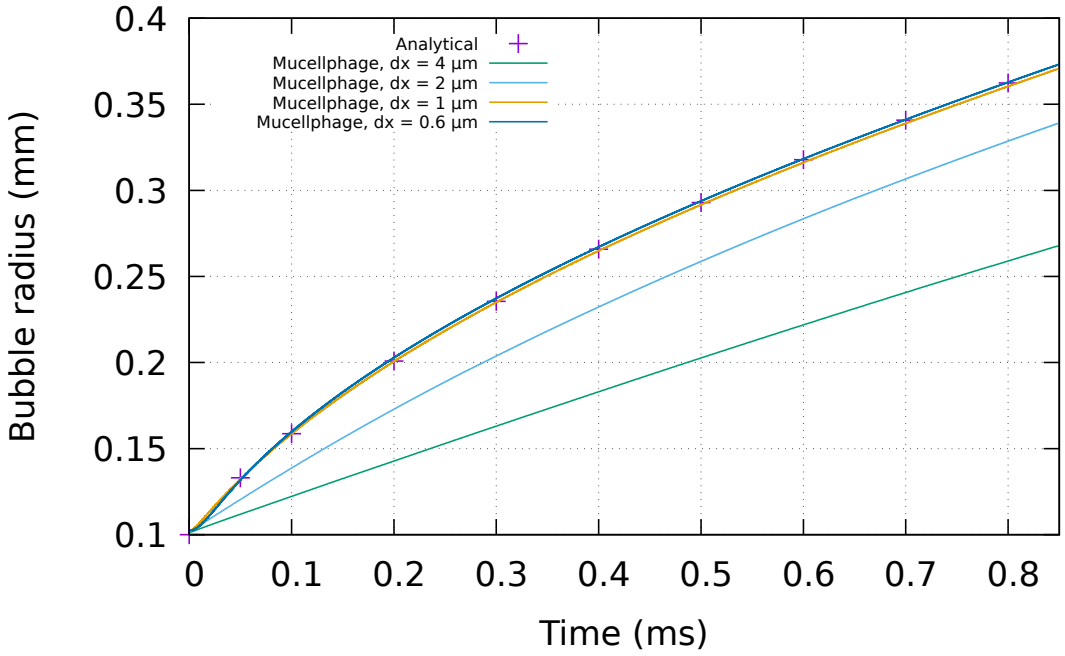

Figure 3.11: Evolution of the bubble radius over time with several 2D axisymmetric meshes and the Mucellphage model.

Like in the Sucking and Stefan problems, we consider water at $P = 1$ bar. The physical properties of the fluid are given in Table 3.3.

3.3.3.2 Results on the Scriven case

To reduce computational costs, the Scriven case was initially simulated using 2D axisymmetric meshes. The computational domain comprises a 2° portion of a cylinder with a radius $R = 400$ µm and a height $h = 400$ µm. A bubble with an initial radius of $R_0 = 100$ µm is introduced into water with a superheat ΔT = 5°C. The results for the 2D axisymmetric cases are presented in Figure 3.11, proving the mesh convergence toward the analytical solution.
Figure 3.12 shows the comparison between the three phase change models implemented in neptune_cfd, and the following observations can be made regarding the three compared models:

- The results obtained with the LI3C model do not converge toward the analytical solution of Scriven (heat transfer is overestimated and the computation eventually stops because the mass transfer term is too high).
- The Fleau model slowly converges toward the analytical solution; however, it fails to reach the analytical solution in this 2D case, even with the finest mesh. This represents a significant drawback caused by the slow mesh convergence of this approach.
- The Mucellphage model achieves convergence to the analytical solution with fine meshes. Similar to the 1D Sucking and Stefan cases, its mesh convergence appears to be approximately three times faster than that of the Fleau model.

Figure 3.13 compares the results of the Scriven model with the Mucellphage between 2D axisymmetric and 3D simulations conducted under identical conditions. The 3D computations also show convergence toward the analytical solution of Scriven, but this convergence appears to be slightly slower, especially at the beginning of the computation when the bubble radius is small. Several factors could account for this

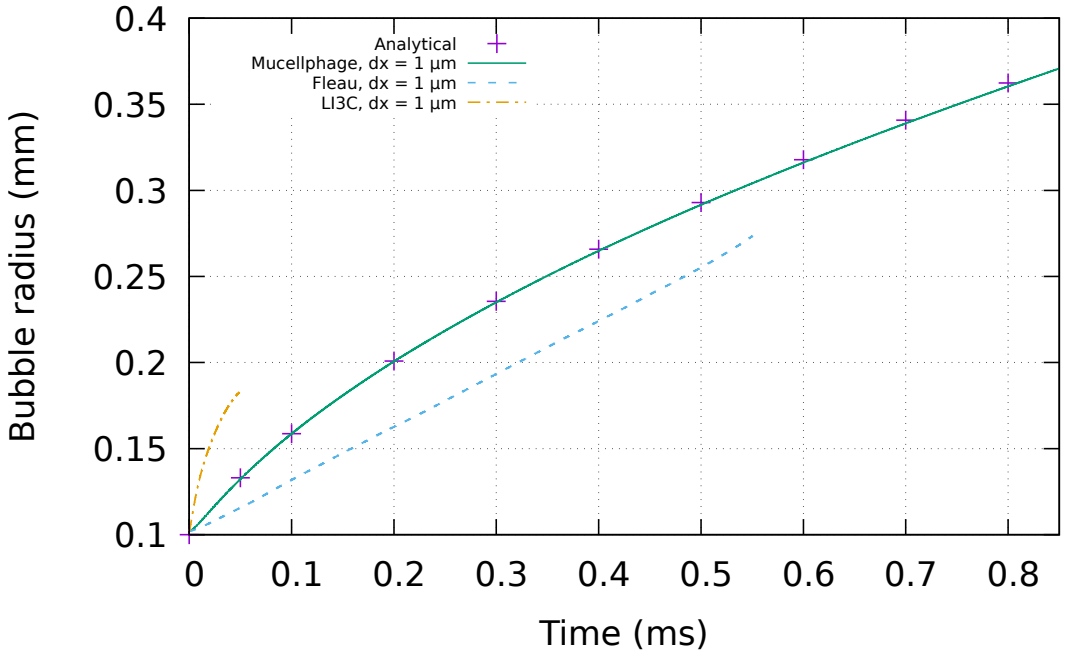

Figure 3.12: Evolution of the bubble radius over time with the three models implemented in neptune_cfd. The mesh is 2D axisymmetric with $\Delta x = 1$ µm.

minor difference, including the computation of the area of the interface in each cell, or the introduction of spurious velocities in 3D due to the surface tension force.

3.4 Validation of the Mucellphage model

The previous section demonstrated the ability of the Mucellphage model to converge toward analytical solutions on simple cases. In this section, an experiment conducted by Florschuetz et al. (1969) is simulated. In this experiment, a bubble is introduced into a superheated liquid, similar to the Scriven case. However, in this scenario, the bubble is in motion due to buoyancy effects. Because of this motion, the liquid temperature around the bubble differs from the Scriven case, leading to higher mass transfer than in the Scriven case. Additionally, the rise of the bubble leads to a flattening of the bubble (similar to what happens in the Bhaga case), which modifies the interfacial area between the bubble and the liquid, and therefore affects heat transfer. The goal of this section is to verify the accurate prediction of these combined effects.

3.4.1 Description of the Florschuetz case

Florschuetz et al. (1969) conducted a relatively large number of experiments on the growth of bubbles in superheated liquids under gravity. The experimental apparatus consists of a 8 mm × 8 mm × 20 mm cuboid initially filled with superheated liquid. Depending on the case, water, ethanol, or isopropanol was used as the working fluid. This section focuses on one experiment using ethanol (C_2H_6O). Ethanol is selected due to the larger thermal layer around the bubble, allowing for less refined meshes. The physical properties of ethanol at atmospheric pressure are computed with the REFPROP (Reference Fluid Thermodynamic and Transport Properties REFPROP) table, and their mean values are given in Table 3.4.
An ethanol bubble with a radius $R_0 = 210$ µm is put at a height $h_0 = 1$ mm from the bottom of the domain in the experiment. The equivalent bubble radius R_{eq} was measured over time experimentally and

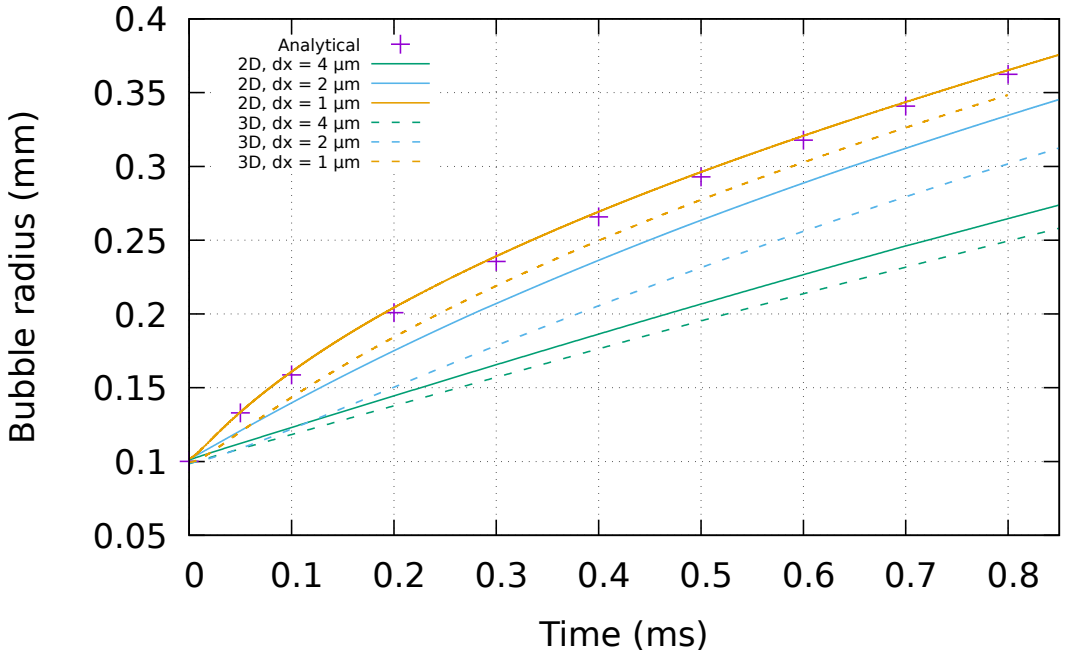

Figure 3.13: Evolution of the bubble radius over time in the Scriven case. The purple crosses represent the analytical solution, the full lines represent the 2D simulations, and the dotted lines represent the 3D simulations.

	ρ (kg/m^3)	μ (Pa.s)	c_p (J/kg.K)	λ (W/m.K)	h_{lat} (J/kg)	σ (N/m)	T_{sat} (K)
Liquid	733.4	4.2×10^{-4}	2963	0.154	8.5×10^5	0.018	351.6
Gas	1.65	1×10^{-5}	1719	0.021	-	-	-

Table 3.4: Mean physical properties of ethanol computed with REFPROP.

will serve as a comparison for the numerical results. This equivalent bubble radius represents the radius of the bubble if the bubble was perfectly spherical. It is defined by equation 3.18. Additionally, Sato and Ničeno (2013) provided numerical results on the bubble rising velocity over time, as well as the bubble shape and position over time. These results will also serve as a reference for comparison.

$$R_{eq} = \left(\frac{3}{4\pi}V\right)^{1/3} \tag{3.18}$$

V is the volume of the bubble.

3.4.2 Numerical modelling

Simulating this experiment with a 3D mesh would be extremely costly (between 30 and 50 million cells are required to reach mesh convergence). Consequently, a 2D axisymmetric approach was employed: instead of modelling the 8 mm $\times$ 8 mm $\times$ 20 mm cuboid, a portion of a cylinder with a 20 mm height and a 4 mm radius is used. This choice does not affect the results because the bubble remains far from the lateral walls. Wall boundary conditions with no heat flux are used for the lateral walls and the bottom of the cylinder. An outlet condition at atmospheric pressure is imposed at the top of the cylinder. The cell size used with this mesh is $\Delta x = 7.8$ µm, as Sato and Ničeno (2013) demonstrated that this is sufficient to reach mesh convergence.
A variable time step is used with a CFL number kept smaller than 0.5.

3.4.2.1 Numerical results

Figure 3.14 shows the position and the shape of the bubble at various time steps. Initially, when the bubble is small, its shape remains spherical due to the dominance of the surface tension force over gravity. However, as the bubble grows, it transitions into an ellipsoidal shape, as the influence of gravity becomes more pronounced in comparison to the surface tension force. Both neptune_cfd and the reference code yield excellent agreement regarding the bubble's shape and accurately capture these two stages.
In Figure 3.14, neptune_cfd predicts a slightly higher rise velocity, but the difference is not significant. Specifically, the difference on the vertical position at $t_f = 856$ ms after a 12 mm rise is only 0.5 mm.
Figure 3.15 provides a quantitative representation of the evolution of the equivalent bubble radius over time. In the experimental data, the radius initially follows the analytical solution proposed by Scriven (equation 3.17) when the influence of gravity is negligible. As the bubble gains velocity, the thermal layer surrounding it decreases, leading to a growth rate higher than that predicted by the Scriven solution. The numerical results obtained with the Mucellphage are in excellent agreement with the experimental data and accurately capture the increased growth rate due to velocity.

Figure 3.16 presents the evolution of the bubble rise velocity over time. It is important to note that this data was not measured experimentally, so the DNS of Sato and Ničeno (2013) are the only comparison data. Nevertheless, the results obtained with neptune_cfd are in excellent agreement with the results of Sato and Ničeno (2013). Both approaches predict an increase in the bubble rise velocity as the diameter of the bubble increases. Then, at $t = 50$ ms, the rise velocity decreases because the bubble shape changes from spherical to ellipsoidal, resulting in an increase in the interfacial area between the gas and the liquid.

3.5 Conclusions of the chapter

In this chapter, we introduced the Mucellphage Model, a novel approach for multi-field solvers that transforms the smeared interface in neptune_cfd into a zero-thickness interface using a cut-cell method. This transformation enables the application of analytical expressions for heat transfer through a large interface. We validated the Mucellphage Model using 1D problems such as the Sucking Problem and

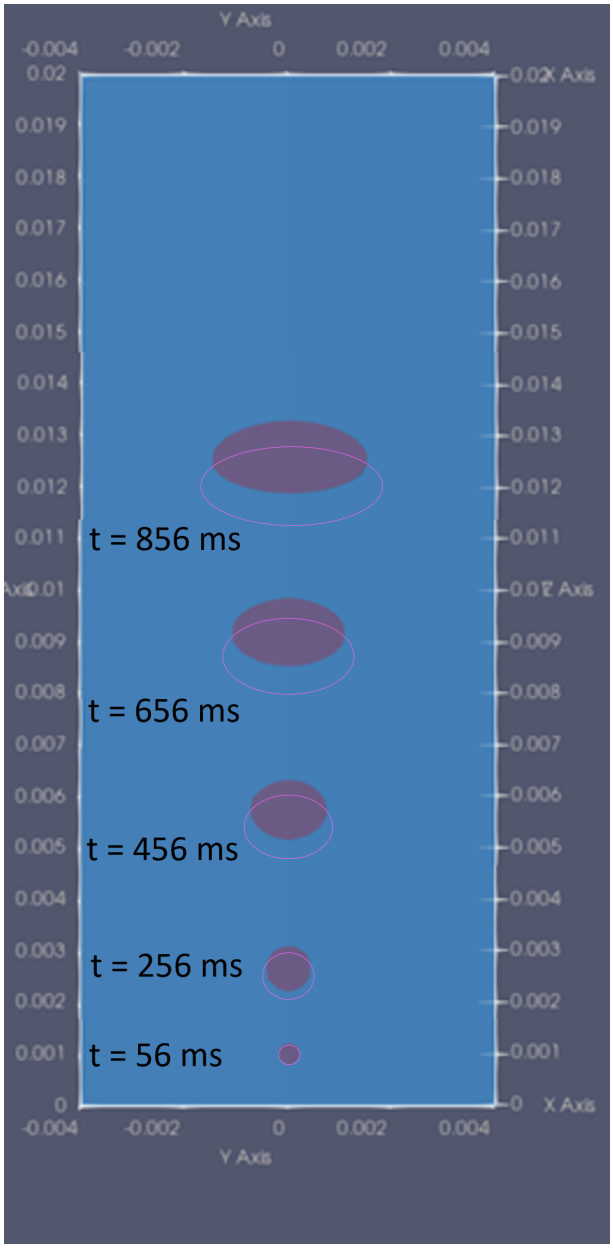

Figure 3.14: Evolution of the bubble shape and position over time. The length axis is in meters. The red bubbles represent the numerical results obtained with the Mucellphage Model on the fine mesh in 2D axisymetrical configuration (the symmetry was completed to give a full view). The pink shapes represent the numerical results of Sato and Ničeno (2013) in 3D with the finest grid (over 300 million cells).

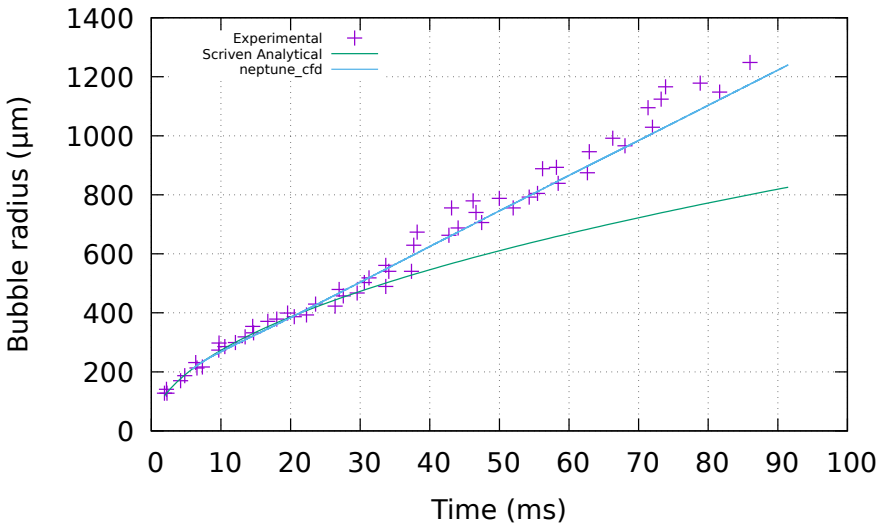

Figure 3.15: Evolution of the equivalent bubble radius over time. The crosses represent the numerical results of Sato and Matsumura (1964) in 3D with a fine mesh (30 million cells). The green curve gives the evolution of the rise velocity over time with neptune_cfd.

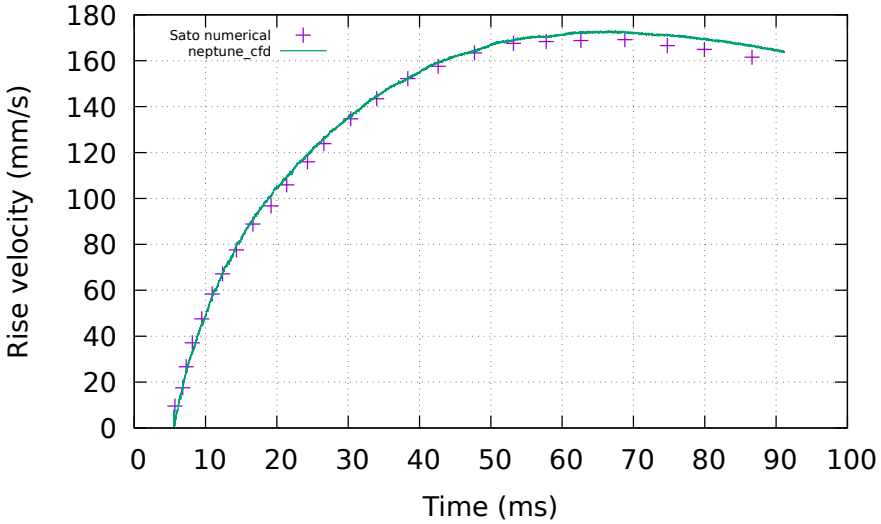

Figure 3.16: Evolution of the bubble rise velocity over time. The crosses represent the numerical results of Sato and Matsumura (1964) in 3D with a fine mesh (30 million cells). The green curve gives the evolution of the rise velocity over time with neptune_cfd.

the Stefan Problem, which revealed a significant improvement in mesh convergence compared to the previous model. This enhanced convergence was also observed in 3D simulations when studying bubble growth, demonstrating that the Mucellphage Model matches the performance of one-fluid approaches. Furthermore, we explored the behaviour of the model in scenarios involving the rising of a bubble in superheated liquid, showcasing its effectiveness even when the bubble has non-zero velocity. Appendix F also demonstrates the ability of the Mucellphage to predict heat and mass transfer in condensation cases, in cases involving non condensable gases, at high pressures, and on parallelepipedic meshes.
Through the use of interface sharpening, surface tension, and this model, neptune_cfd can accurately simulate boiling flows in microchannels, provided that bubbles remain at a distance from the channel walls, without experiencing confinement effects. In the upcoming chapter, the primary focus will be on wettability, allowing for the consideration of confinement effects within the modelling framework.

Model	LIM	Fleau	Mucellphage
Accuracy	$-$	$++$	$++$
Fast mesh convergence	$++$	$--$	$-$

Table 3.5: Summary of the advantages and drawbacks of the large interface models implemented in neptune_cfd.

CHAPTER 4

Wettability

Summary

The interface sharpening model, coupled with Brackbill's surface tension force, correctly characterizes bubble and slug flows within a conventional pipe with a good accuracy, as shown in the previous chapters. However, when bubbles interact with walls — a common occurrence in confined flows — wettability becomes a key factor, necessitating special numerical treatment to model the contact angle. This chapter delves into the wettability model integrated into neptune_cfd, along with a minor modification developed during the course of this thesis.

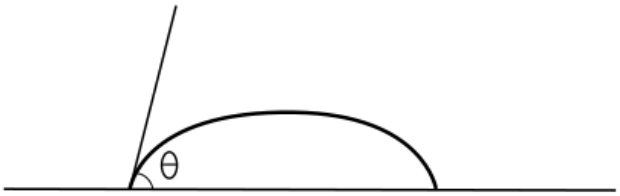

Figure 4.1: Contact angle for a liquid droplet on a solid surface (public domain by Ranjithsiji).

4.1 Wettability

Wettability refers to the capacity of a fluid to maintain contact with a solid surface, determined by a balance between adhesive and cohesive forces. This characteristic is quantified at a macroscopic scale by the contact angle, denoted as θ. Experimental measurement of this angle involves placing a droplet on a flat surface at the solid-liquid-vapour interface, as depicted in Figure 4.1. When the contact angle is less than 90°, the droplet tends to spread, indicating a "wetting" or "hydrophilic" surface. For example, water typically exhibits spreading on metallic surfaces with a contact angle around 30°. In contrast, if the contact angle is between 90° and 100°, the surface is considered "non-wetting" or "hydrophobic," commonly observed with water on plastic materials.

Remark 4.1.1. It is worth noting that the contact angle θ discussed here is a macroscopic measurement. For instance, Dupont and Legendre (2010) reported that the contact angle θ remains constant at an intermediate length scale (around 10 µm from the wall). However, as we approach the microscopic length scale, around 1 nm from the surface, intermolecular forces become predominant, and the angle approaches 0° regardless of the surface. Additionally, near the capillary length $L_c = (\sigma/\Delta\rho g)^{1/2} = 1$ mm, gravity becomes a significant factor, leading to modifications in the contact angle.
Therefore, the cell size at the wall should be at the intermediate length scale when using models where the contact angle is directly imposed.

4.2 Numerical model

Wetting is a phenomenon caused by capillary effects at the wall. Therefore, the vast majority of the wettability models are centered around the computation of the surface tension force at the wall. As explained in section 1.4.3, the surface tension force is computed as per equation 4.1. Computing $\nabla\alpha_k$, the gradient of the volume fraction at the wall, poses a challenge as the wall cells lack an adjacent cell. This issue is even worse for the computation of the curvature, a second order derivative of the volume fraction. The vast majority of wettability models address this challenge by incorporating ghost cells in the wall.

$$\underline{F}_{ST,k} = \alpha_k \sigma \kappa \nabla \alpha_k = -\alpha_k \sigma \nabla . \left(\frac{\nabla \alpha_k}{\|\nabla \alpha_k\|} \right) \nabla \alpha_k \tag{4.1}$$

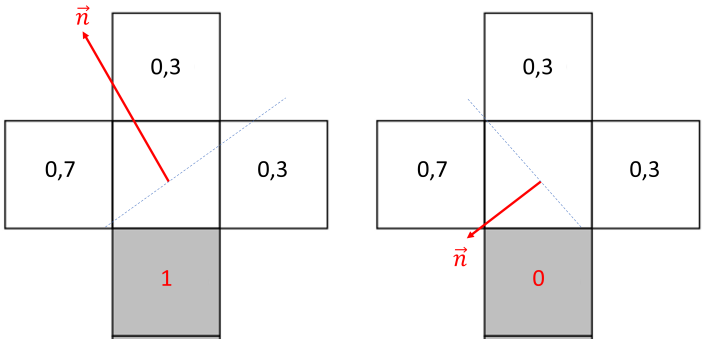

Figure 4.2: Normal vector to the interface as a function of the fictive volume fraction α_p. The blue dotted lines represent the shape of the bubble at the wall.

4.2.1 Existing models in the literature

Several approaches in the literature aim to model the wettability phenomenon using interface-capturing methods in Computational Fluid Dynamics (CFD) and Direct Numerical Simulation (DNS). The majority of these approaches involve modifying the normal vector at the wall during the computation of surface tension forces and curvature to geometrically impose the contact angle. For instance, techniques employed by Renardy et al. (2001) and Dupont and Legendre (2010) utilize a Volume-of-Fluid (VOF) method with a ghost cell in the wall. The color function in this cell is computed to enforce a normal vector at the interface that aligns with the specified contact angle.
Additionally, authors like Afkhami et al. (2009) impose a velocity-slip boundary condition at the triple line, arguing that the conventional no-slip condition is not justified at the contact line. Finally, certain research groups, such as Yin and Kuhn (2022), observed that the contact angle for a moving interface differs from the equilibrium contact angle (θ_e). They introduced a dynamic contact angle (θ_d) as a function of the Capillary number ($\mathrm{Ca} = \dfrac{\mu u_{cl}}{\sigma}$), where u_{cl} is the velocity at the contact line. In this model, the contact angle is modified when the interface is in motion ($\mathrm{Ca} > 0$).

These approaches where the contact angle is imposed geometrically yield very good results on the usual validation cases, and are well suited for DNS. However, they require a very fine mesh near the wall, which is penalizing for CFD.

4.2.2 The smooth boundary interface method

The method used in this manuscript is based on the work of Guillaument et al. (2015), and an initial version of this approach was implemented in neptune_cfd as detailed in Baconnier and Mimouni (2017). Instead of explicitly imposing the contact angle in the wall cells, by modifying the normal vector to the interface, this method imposes a fictive volume fraction α_p in these regions. If the volume fraction in the wall cells approaches 1, modifications are made to the normal vector and curvature, resulting in the spreading of the interface on the wall (wetting surface). Conversely, if the volume fraction in the wall cells approaches 0, the interface retracts, leading to a non-wetting surface. Figure 4.2 shows the normal vector at the interface depending on the value of α_p.
The initial implementation of this method in neptune_cfd directly imposed α_p within the wall cells. However, this initial implementation encountered numerical stability issues due to abrupt changes in the diffused volume fraction. To mitigate these challenges, the implementation was refined, incorporating ghost cells within the wall to achieve a smoother transition.
To implement this method in neptune_cfd, 3 ghost cells are added to the wall with an immersed boundary method (for more details about this method, the reader is referred to Benguigui et al. (2018)). This is illustrated by Figure 4.3 where the 3 cells in gray represent the ghost cells. The fluid volume fraction is

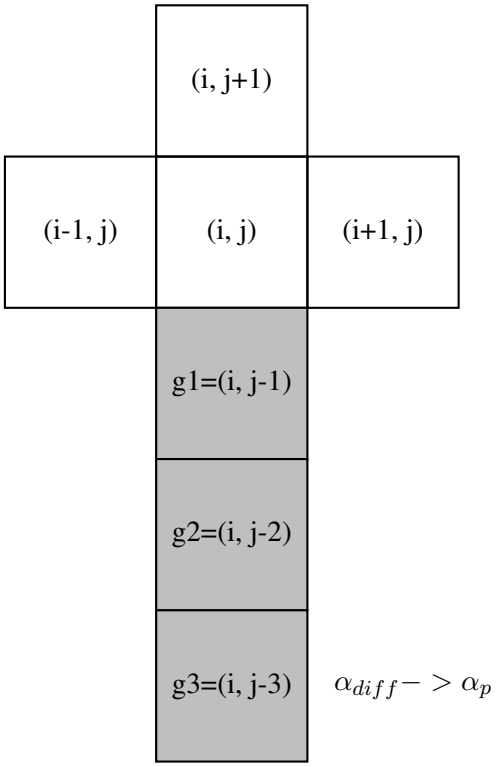

Figure 4.3: Ghost cells around the wall cell (i,j). The ghost cells are represented in gray and modeled with an immersed boundary method. They do not contain any fluid, and are used for the estimation of the normal vector and the curvature in the computation of the surface tension force.

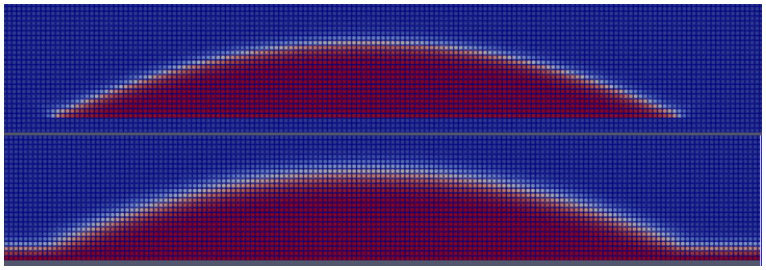

Figure 4.4: Top: Volume fraction α for a droplet spread on a hydrophilic surface ($\alpha_p = 1$). Bottom: diffused volume fraction α_{diff} for that same droplet.

set to 0 in these cells (meaning that these cells are solid), but a fictive volume fraction α_{diff} is defined in the ghost cells.
α_{diff} is initialized equal to α_p. Then, the diffusion equation for the volume fraction used to compute the curvature (equation 1.27) is modified into equation 4.2 when the wettability model is activated.

$$\frac{\Delta\alpha_{diff,k}}{\Delta\tau} - \nabla D \nabla\alpha_{diff,k} + B^S(\alpha^{n+1}_{diff,k} - \alpha_p) = 0 \tag{4.2}$$

The parameter α_p is given by the user and characterizes the contact angle. The parameter B^S, which acts as a penalty term, is set equal to 0 in the fluid cells, and equal to 10^{40} in the wall cell (g3 in Figure 4.3).

Remark 4.2.1. When $B^S = 0$, equation 4.2 is equivalent to equation 1.27, meaning that the standard diffusion equation on α_{diff} is solved in the fluid cells and in the first two ghost cells g1 and g2. When $B^S = 10^{40}$ (in the ghost cell g3), equation 4.2 simplifies to $\alpha^{n+1}_{diff,k} \approx \alpha_p$.
As a reminder, the surface tension force is computed as:

$$\underline{F}_{ST,k} = \alpha_{diff,k}\sigma\kappa\nabla\alpha_{diff,k} \tag{4.3}$$

The modification of $\alpha_{diff,k}$ near the wall thus leads to a modification in both the norm and the direction of the surface tension force.

Figure 4.4 shows the volume fraction α for a droplet on an hydrophilic surface ($\alpha_p = 1$), and the diffused volume fraction α_{diff} for that same droplet.
Since the smooth boundary interface method does not explicitly impose a contact angle θ, but sets a diffused volume fraction at the wall α_p, it is necessary to calibrate the model to establish a connection between these two parameters. This calibration process involves placing a half-droplet with a radius of $R_0 = 1$ mm on a wall. Simulations are conducted without gravity, utilizing a 2D axisymmetric mesh with $\Delta x = 2$ µm for various values of α_p until a steady state is attained. The contact angle is then measured. These simulations are performed with increased viscosity values ($\mu_l = 0.1$ Pa.s and $\mu_g = 0.001$ Pa.s) to significantly reduce spurious currents without affecting the steady state. Some computations were carried out on a finer mesh ($\Delta x = 1.5$ µm), and no notable differences in the contact angle were observed, indicating that the calibration is independent of the mesh at this scale.

Remark 4.2.2. Without gravity, the static shape of a drop is a circular cap that respects the contact angle with the wall (Dupont and Legendre (2010)), as in Figure 4.5. The height of the droplet e can be computed from equations 4.4.

$$e = R(1 - \cos(\theta)) \tag{4.4}$$

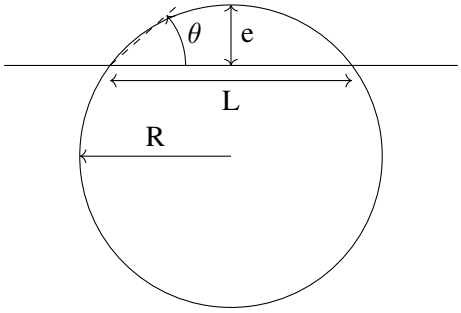

Figure 4.5: Droplet on a wall in the steady state under no gravity.

α_p	Direct measure: θ (°)	Droplet height method: θ (°)	Average: θ (°)
0.1	140	160	150
0.2	125	130	127.5
0.3	105	108	106.5
0.4	90	92	91
0.5	80	81	80.5
0.6	70	67	68.5
0.7	55	52	53.5
0.8	40	39	39.5
0.9	32	29	30.5
1	18	13	15.5

Table 4.1: Calibration of the smooth boundary interface method. α_p represents the diffused volume fraction at the wall, and θ represents the contact angle.

R, as defined in Figure 4.5, can be expressed as a function of R_0, the radius of the initial half droplet ($R_0 = 1$ mm) using equation 4.5.

$$R = R_0 \sqrt{\frac{\pi}{2(\theta - \sin(\theta)\cos(\theta))}} \tag{4.5}$$

This gives two methods to measure the numerical contact angle with the wall:

1. The direct measure of the contact angle.
2. The extrapolation of the contact angle from the droplet height using the formulas detailed above.

The calibration results are presented in Table 4.1. Both methods yield very similar results, except for cases with extremely high or low contact angles. In such instances, visual measurement of the contact angle becomes challenging due to rapid changes. An average value between the two methods was employed for the calibration. A view of spread droplets on hydrophilic, neutral and hydrophobic surfaces is given in Figure 4.6.
Equation 4.6 gives α_p as a function of the contact angle θ. This correlation is used at the beginning of a computation to set the value of α_p.

$$\alpha_p = 1.1394 - 0.0085\theta + 3 \times 10^{-6}\theta^2 + 4 \times 10^{-8}\theta^3 \tag{4.6}$$

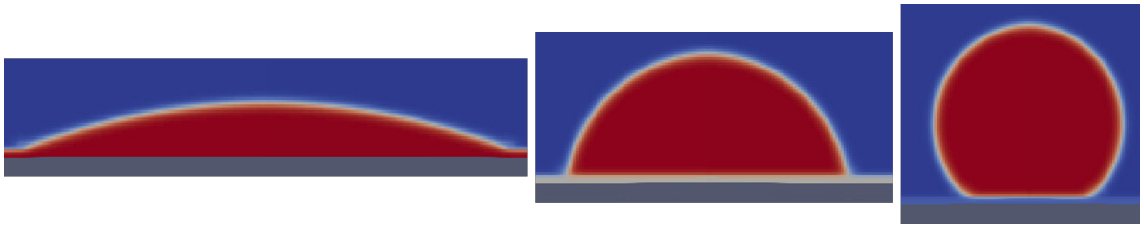

Figure 4.6: Spread droplets on hydrophilic, neutral and hydrophobic surfaces. The left picture corresponds to $\alpha_p = 1$ ($\theta = 15.5°$), the middle picture corresponds to $\alpha_p = 0.5$ ($\theta = 80.5°$), and the right picture corresponds to $\alpha_p = 0$ ($\theta = 159°$).

4.3 The coupled effect Mukherjee case

In industrial boiling scenarios within micro-channels, complex coupled phenomena occur, necessitating the modelling of boiling at the liquid-vapour interface, the impacts of surface tension on bubbles, and the wetting effects at the wall. In the case of Mukherjee and Kandlikar (2005) a vapour bubble is introduced in a superheated microchannel. This leads to bubble growth and significant wettability effects. The Mukherjee case offers both experimental and numerical data, and stands as a valuable validation case for assessing the coupled effects of the Mucellphage and wettability models.

4.3.1 Presentation of the case

4.3.1.1 Experiment

The experimental setup of Mukherjee and Kandlikar (2005) involves a rectangular microchannel with dimensions of $25400 \times 201 \times 266$ µm. A syringe pump was employed to enforce a constant flow rate of 0.41 mL/min at a temperature of $T_{in} = 102.1°$C, and the lower wall was maintained at the same temperature. The researchers observed a wall contact angle of 30°. Throughout the experiment, the bubble's position over time was documented through images, and the progression of the equivalent bubble diameter was recorded, providing essential data for the analysis.

4.3.1.2 Numerical modelling

In the numerical simulation, the domain takes the form of a rectangular microchannel measuring $1200 \times 207.5 \times 137.5$ µm. This includes the 3 ghost cells in the wall, required to take wettability effects into account. To save computational time, a symmetry boundary condition is enforced on the plane $z = 0$.
A constant cell size of $\Delta x = 2.5$ µm is adopted, consistent with what was done in Mukherjee and Kandlikar (2005), which demonstrated its sufficiency for achieving mesh convergence. The plane at $x = 0$ µm functions as an inlet, with an inlet velocity of u_{in} = 0.127 m/s and an inlet temperature $T_{in} = 102.1°$C, mirroring the conditions from the experiment. The plane at $x = 1200$ µm acts as an outlet for the water. Finally, the contact angle at the wall is set to $\theta = 30°$, like in the experiment.

4.3.2 Numerical results

Figure 4.7 provides a qualitative representation of the evolution of the bubble's shape and position over time. The results obtained with neptune_cfd exhibit strong congruence with both the experimental data and the numerical findings presented in Mukherjee et al. (2011). Notably, the onset of contact between the bubble and the wall occurs around $t = 1$ ms in all three cases. Furthermore, the quantitative results produced by neptune_cfd are highly accurate. Figure 4.8 illustrates that the difference between the experimentally measured equivalent bubble radius (defined in a previous section by equation 3.18) and

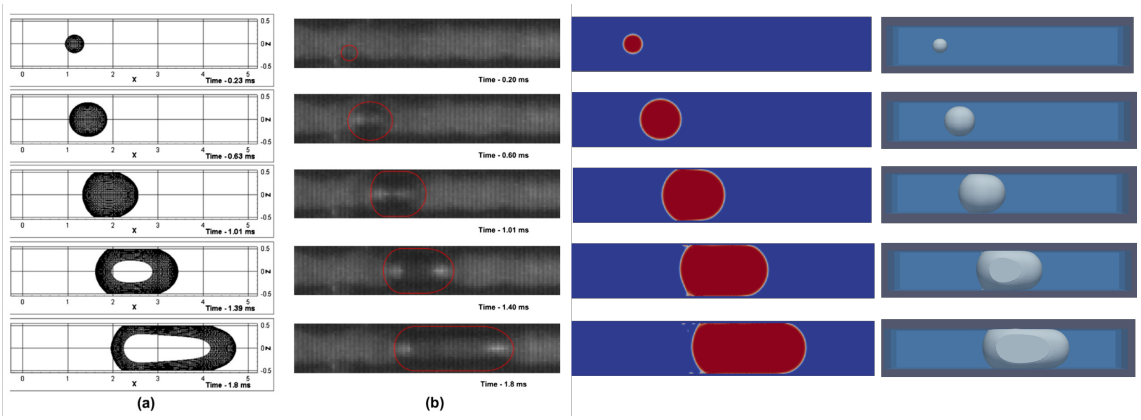

Figure 4.7: Visualisation of the bubble over time. Far left: Numerical results of Mukherjee et al. (2011) – Left: Experimental results of Mukherjee et al. (2011) – Right: 2D cut of the results with neptune_cfd (to compare with the experiment) – Far right: 3D view of the results with neptune_cfd (to compare with the numerical results). It should be noted that in Mukherjee et al. (2011), the computation domain is only 1000 µm long (1200 µm in the neptune simulation).

the computed bubble radius in neptune_cfd is minimal (less than 5%), indicating excellent quantitative results between the simulation and the experiment.

4.3.3 Importance of wettability on the Mukherjee case

Quantifying the influence of wettability on boiling flows can be challenging. In this section, we aim to assess the significance of wettability by comparing the numerical approach outlined earlier with an equivalent approach, without the inclusion of a wettability model. This comparative analysis seeks to provide insights into the relevance of accounting for wettability and confinement effects on boiling flows in microchannels.

Figure 4.9 illustrates the bubble shape in the Mukherjee case at $t = 1.3$ ms. The top image features a wettability model with a contact angle of $\theta = 30°$, while the bottom image has no wettability model, which is equivalent to a contact angle of $\theta = 90°$. The qualitative distinction between the two outcomes is striking, underscoring that the Mukherjee case cannot be adequately simulated without accounting for the contact angle. Turning to quantitative results, Figure 4.10 illustrates the evolution of the bubble radius over time in the Mukherjee case. The results are the same before the bubble comes into contact with the walls ($t < 1$ ms). However, once wettability comes into play, a contact angle of $\theta = 90°$ leads to a much smaller interfacial area between the superheated liquid and the bubble. This significantly underestimates the interfacial boiling, resulting in an error close to 50% in the bubble growth velocity.

4.4 Conclusions of the chapter

This chapter presented the wettability model used in the thesis. The model is based on a penalty method and was calibrated to set a contact angle at the wall between 15.5° and 150°. Validation against Mukherjee's case, which involves the growth of a vapour bubble in a superheated microchannel, demonstrated excellent results. The chapter also highlighted that in specific situations, such as the Mukherjee case, wettability significantly influences the accurate prediction of heat and mass transfer.

The numerical developments presented in this part led to a publication in International Journal of Multiphase Flow. This article is available in Appendix G.

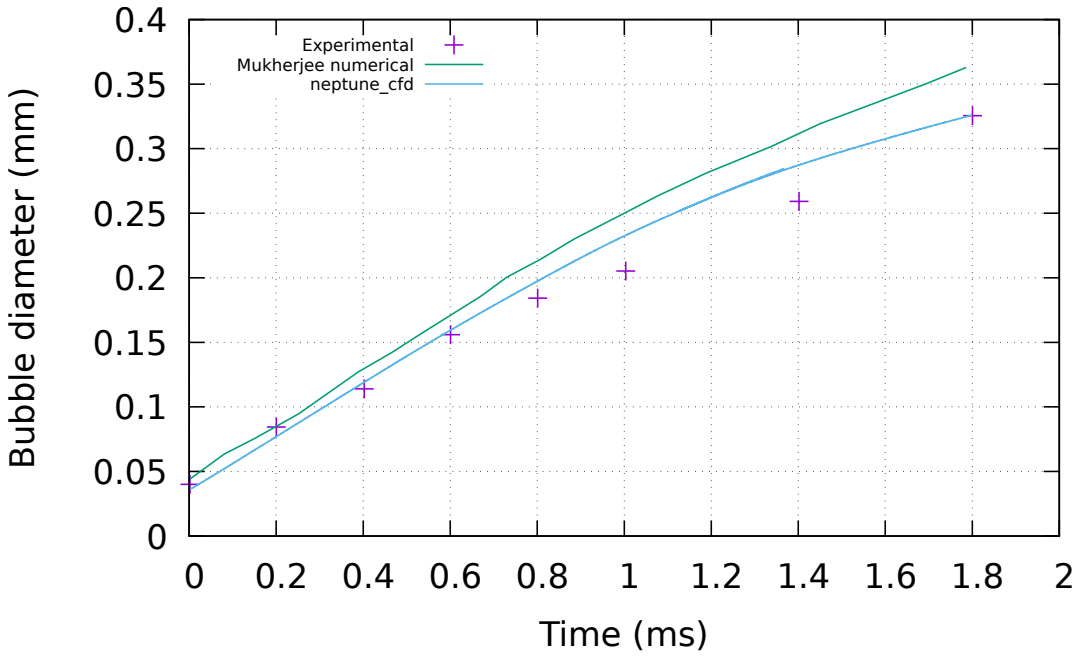

Figure 4.8: Evolution of the equivalent bubble diameter over time. The purple crosses represent the experimental results, the green line the numerical results obtained by Mukherjee et al. (2011), and the blue line represents the numerical results of the present work.

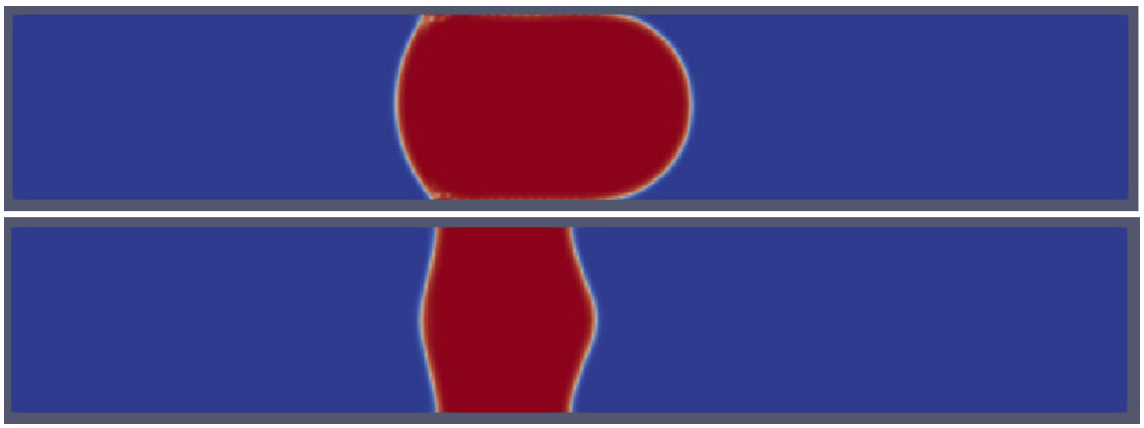

Figure 4.9: Bubble shape in the Mukherjee case at $t = 1.3$ ms. The top picture shows the results obtained with neptune_cfd taking wettability into account. The bottom picture shows the bubble without a wettability model (equivalent to a contact angle of 90°).

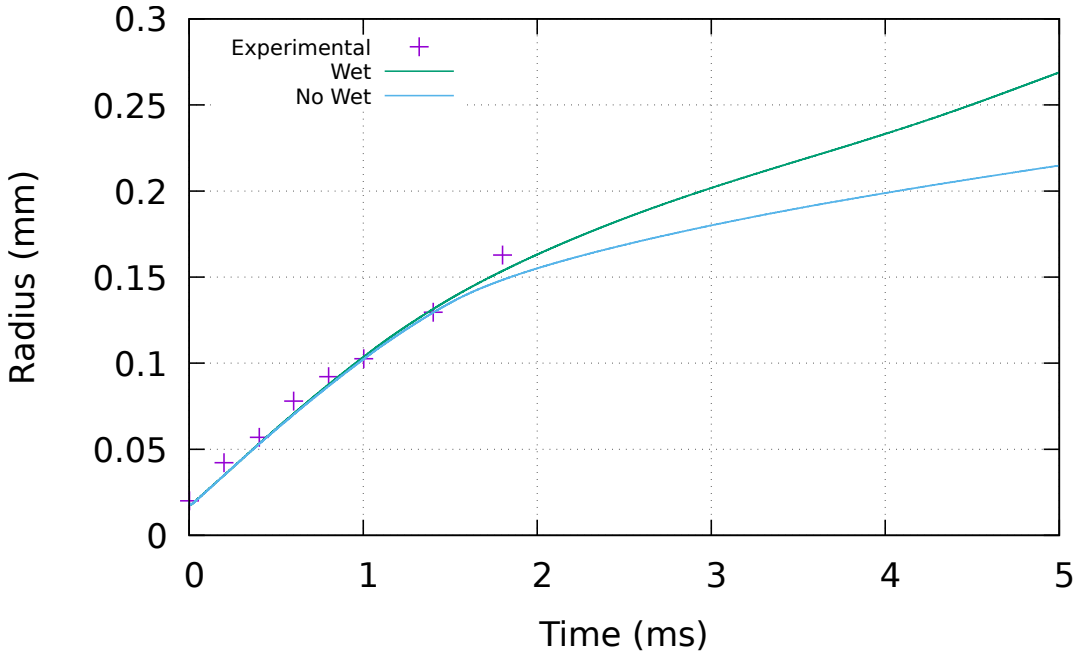

Figure 4.10: Evolution of the bubble radius over time on the modified Mukherjee experiment. The purple crosses represent the experimental results, the green line represent the numerical results with a wettability model, and the blue line represents the numerical results without a wettability model.

Part II

Experimental study of flow boiling in microchannels

Part I presented a numerical approach for simulating boiling flows in microchannels within the slug flow regime. While this method is highly accurate, it is computationally intensive and thus impractical for industrial applications. The goals of this part are to confirm that the slug flow regime is indeed the relevant regime during the drying of failed rods and to develop general correlations on flow boiling in microchannels to support an upscaling model in part III. Section 5.2 details the fabrication of microchannel samples by Damien Colombet at LEGI, while section 5.3 describes the experimental setup developed during this PhD research. Section 5.4 validates the microchannel geometry by comparing experimental and theoretical pressure losses in single-phase flow. Section 5.5 introduces and classifies the flow regimes observed experimentally. Section 5.6 explores two-phase pressure drop, specifically validating the simplified Kreutzer law for the slug flow regime under experimental conditions ($D_h < 140$ µm and $\mathrm{Re} < 100$). Finally, section 5.7 estimates the Nusselt number during slug flow regime experiments. This part provides a validated pressure loss law (the simplified Kreutzer law), essential for constructing the upscaling model in part III, along with valuable experimental data for model validation.

CHAPTER 5

Experimental study of flow boiling in microchannels

Summary

A partnership between EDF R&D and the LEGI (Laboratoire des Ecoulements Géophysiques et Industriels) was established during the PhD to conduct experiments on microchannels under the supervision of Damien Colombet, leveraging the expertise of the LEGI in this field.
Using microfabrication techniques on polished silicon wafers, several microchannels were machined with a geometry close to the cracks in uranium pellets (hydraulic diameter $D_h = 100$ µm, and channel length $L = 1$ m). Flow boiling in these microchannels was then studied both qualitatively and quantitatively to identify the different flow regimes, as well as the head loss and heat transfer laws associated to those regimes.

5.1 Introduction

5.1.1 The need for an experimental study

Identifying the correct flow regime in microchannels is fundamental to estimate the head losses in the cracks of failed rods. Unfortunately, experiments investigating boiling in microchannels are infrequent due to the complex fabrication process of microchannels, the difficulties associated with the measure of extremely small mass flow rates and with the visualization of microscopic areas.
While numerous experiments and data exist in the scientific literature for adiabatic flows in microchannels, such as those conducted by Salim (2018), Serizawa et al. (2002), or Kawahara et al. (2002), which proposed flow regime maps as a function of the liquid and gas superficial velocities (see Figure 12), these findings cannot be directly applied to boiling flows. This limitation arises because the concept of "superficial velocities" used in these studies is not applicable easily to thermally driven flows, such as those found in failed rods. Furthermore, it is not clear whether the bubble growth induced by boiling will affect the flows regimes.
Some research groups have conducted experiments specifically on flow boiling in microchannels, as seen in the works of Gamrat (2007) and Thome (2004). However, the focus of these experiments centered on characterizing heat transfer coefficients (Nusselt number), rather than investigating flow regimes and head losses. Finally, these experiments were conducted on short microchannels with a typical length of a few centimers, which is far from the conditions of cracks in failed fuel rods.
To address this scarcity of data, a cutting-edge exploratory experiment was conducted during the thesis in collaboration with the LEGI. This experiment utilized microchannels with a hydraulic diameter of approximately 100 µm and a total channel length of one meter to faithfully replicate the conditions encountered during the drying of failed rods.

5.1.2 Dimensionless study

Flow boiling in microchannels involves a multitude of physical parameters including the physical properties of both the liquid and the gas (density, viscosity, specific heat, thermal conductivity), the geometry (length and hydraulic diameter), and the flow characteristics (velocity, pressure, temperature). Additionally, it is influenced by two-phase properties like latent heat and surface tension. Table 5.1 provides a compilation of the most significant dimensionless numbers in this context.
In the experiments discussed in this section, water is used as the working fluid. Therefore, the density ratio, Prandtl number, and Jakob number remain unchanged compared to the conditions found in the cracks of failed rods. However, other dimensionless numbers are adjusted as follows:

- **Reynolds numbers:** According to Table 7.3, the industrial Reynolds number falls within the range of 1 to 25. In the experimental campaign, the pressure difference (ΔP) was kept small (between 1 and 4 bar in most experiments) to achieve Reynolds numbers ranging from 2 to 150, which is similar to the industrial case.

- **Weber numbers:** Maintaining both the industrial Reynolds and Weber numbers simultaneously was not feasible. Consequently, the Weber numbers in this experimental campaign are greater ($We_{l,exp} \approx 0.01$ while $We_{l,drying} \approx 10^{-6}$). However, the Weber numbers are extremely small in both cases because capillary forces dominate over inertia forces. Consequently, the bubbles remain symmetrical, with their deformation controlled by the channel diameter rather than by the flow in both cases.

- **Poiseuille number:** Similarly, preserving the Poiseuille number was not possible. However, this dimensionless number is only responsible for the total pressure loss, and does not alter the flow characteristics.

Dimensionless number	Expression	Characterized physical phenomenon
Density ratio	$\frac{\rho_g}{\rho_l}$	Bubble size
Reynolds liquid	$\frac{\rho_l u_l D_h}{\mu_l}$	Flow regime
Reynolds gas	$\frac{\rho_g u_g D_h}{\mu_g}$	Flow regime
Weber liquid	$\frac{\rho_l u_l^2 D_h}{\sigma}$	Impact of inertia on the droplet shape
Weber gas	$\frac{\rho_g u_g^2 D_h}{\sigma}$	Impact of inertia on the bubble shape
Poiseuille liquid	$\frac{2 D_h \Delta P}{\mu_l u_l L}$	Linear pressure loss
Prandtl liquid	$\frac{\mu_l c_{p,l}}{\lambda_l}$	Relative importance of momentum diffusivity compared to heat diffusivity
Prandtl gas	$\frac{\mu_g c_{p,g}}{\lambda_g}$	Relative importance of momentum diffusivity compared to heat diffusivity
Jakob number	$\frac{\rho_l c_{p,l} \Delta T}{\rho_g h_{fg}}$	Ratio between sensible and latent heat transfer

Table 5.1: Dimensionless numbers involved in two-phase flow in microchannels.

Sample	h (µm)	wt (µm)	wb (µm)	Mask
A	66	260	182	2
B	64	267	172	1
C	115	264	103	1
D	128	265	82	2

Table 5.2: Dimensions of the microchannels. The lengths are defined in Figure 5.3.

5.2 Microchannel samples

5.2.0.1 Sample fabrication

The microchannel samples were fabricated by Damien Colombet at the LEGI. These channels are etched into silicon and sealed using anodic bonding, employing the technology described in Ayela et al. (2017). The fabrication process involves the following steps, as depicted in Figure 5.1:

1. An UltraViolet sensitive photoresist layer (with a thickness of approximately 3 µm) and a non transparent mask are applied onto the Silicium wafer (first image in Figure 5.1).
2. The mask and the photoresist layer are irradiated to remove the portions of the photoresist layer that are not covered by the mask (second image in Figure 5.1).
3. KOH chemical etching is then carried out to create microchannels of uniform depth (third image in Figure 5.1).
4. Then, a pyrex cap is perforated to create inlet and outlet fluid connections.
5. Finally, the pyrex cap is anodically bonded onto the silicium channel (fourth image in Figure 5.1).

Four microchannels were fabricated using two different masks (mask 1 and mask 2). In mask 1, the channel length is slightly longer, but a portion of the channel is obscured by the inlet and outlet fluid connections, making flow visualization more challenging. On the other hand, in mask 2, the channel is not obscured by the inlet/outlet connectors, as illustrated in Figure 5.2. For both masks, the silicon sample size is 30×64 mm, with 1.2 mm square inlet and outlet connections, and a channel width of 250 µm. Each mask consists of 19 horizontal channels, 20 vertical channels, and 2 inlet/outlet channels. The length of the vertical channels is 1 mm for both masks. In mask 1, the length of the horizontal channels is 49.4 mm and 48 mm for the 2 inlet/outlet channels and regular channels, respectively, resulting in a total length of 1.03 m. For mask 2, the length of the horizontal channels is 45.4 mm and 40 mm for the 2 inlet/outlet channels and regular channels, respectively, corresponding to a total length of 0.87 m.
Four samples were fabricated (A, B, C, and D). Sample C was used as a test sample to set the experimental protocole. Samples A, B, and D were used for qualitative and quantitative results. Because of the fabrication process, their section is trapezoidal as depicted in Figure 5.3. The size of the four samples is given in Table 5.2. The height of the microchannels was measured with a profilometer dektakxt/bruker. Their width was measured with an optical microscope scopea1/axio/zeiss.

5.3 Experimental setup and flow visualizing

5.3.1 Experimental setup

The experimental setup is schematically represented in Figure 5.4, and a photograph of the experimental arrangement without the microscope is shown in Figure 5.5. Deionized water is stored in the supply tank and pressurized using a gas bottle. The inlet pressure is controlled by a manometer, and the inlet

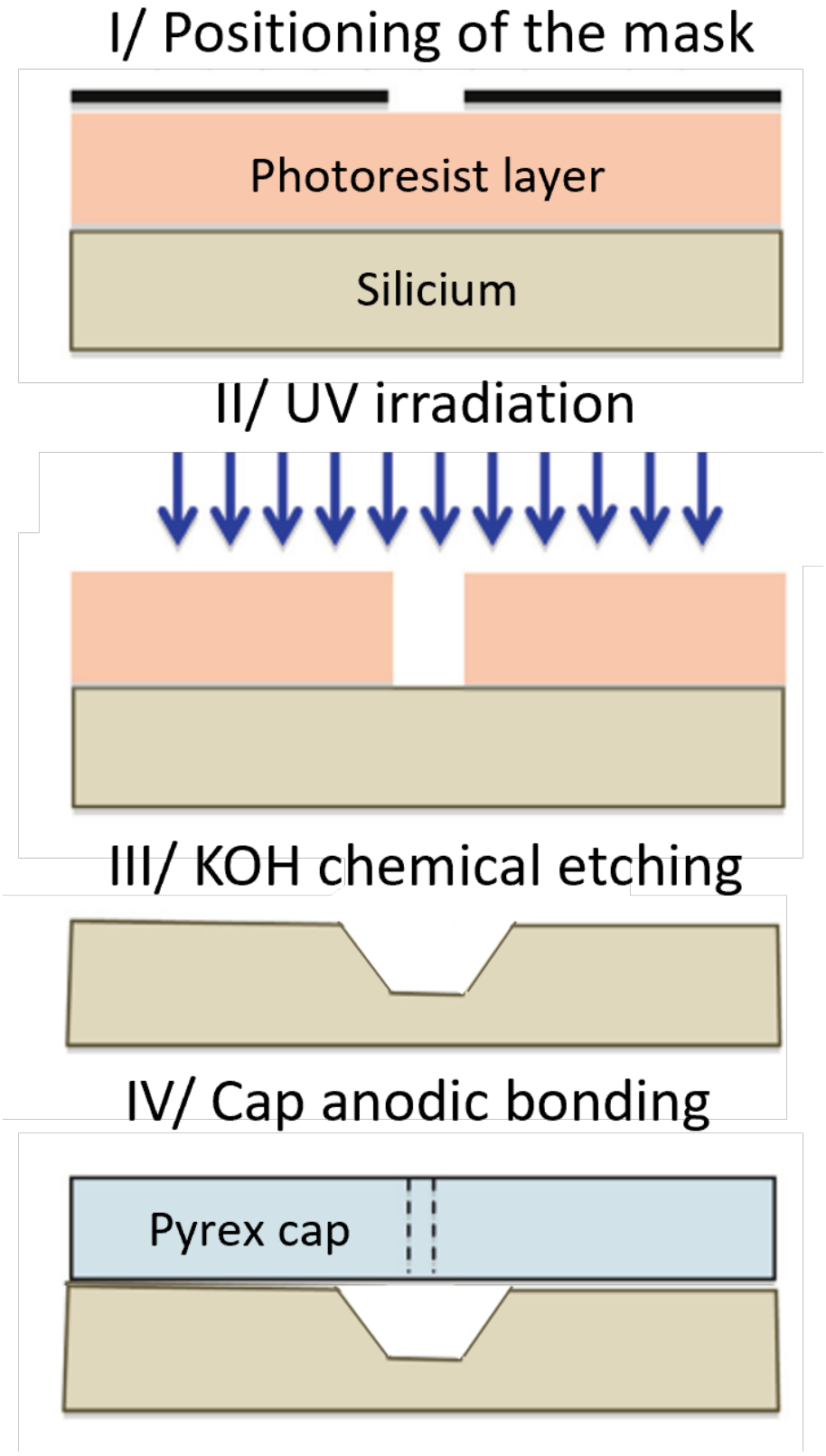

Figure 5.1: Fabrication of a silicium microchannel. From Ayela et al. (2017).

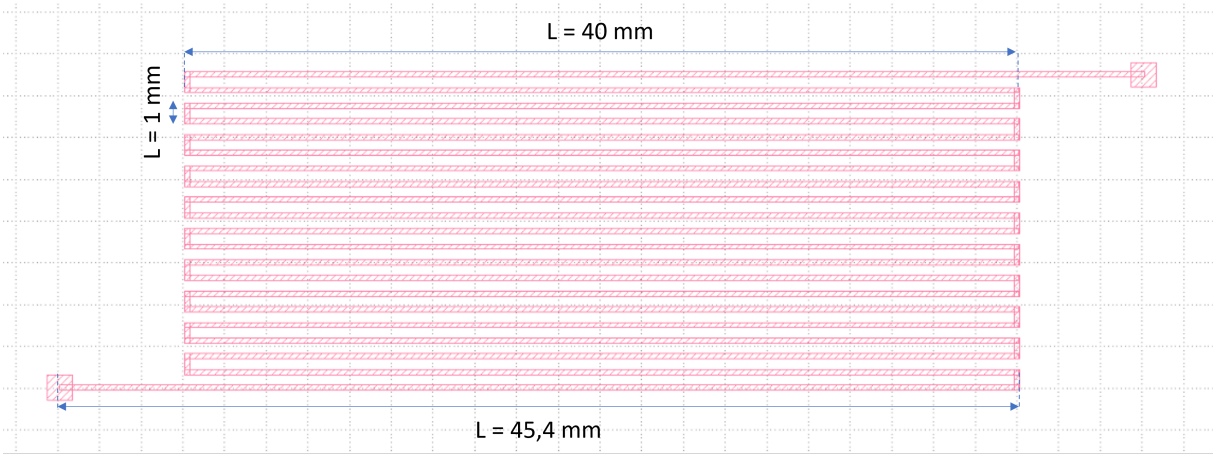

Figure 5.2: Visualisation of mask 2.

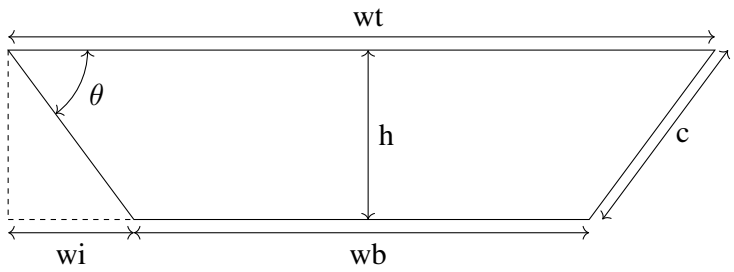

Figure 5.3: Section of a microchannel fabricated on a silicium wafer.

temperature is monitored by a thermocouple placed at the sample inlet.
The sample is affixed to an aluminum heating block via a sample holder system. This aluminum block is heated by a cylindrical heating cartridge placed at its bottom. This cartridge has a power of $P = 500$ W and can reach temperatures as high as 500°C. A 3D view of the aluminum heating block is provided in Figure 5.6. The sample wall temperature is measured using thermocouple T_p.

Remark 5.3.1. During the experiments, the thermocouple was moved at various points on the sample to assess any potential temperature gradient within the microchannels. This test revealed no temperature difference between the top, the bottom and the sides of the different samples. Consequently, it is reasonable to consider that the temperature in the sample is quite homogeneous.

Remark 5.3.2. Initially, two methods were planned to measure the heat flux transferred to the microchannel:

1. Utilizing a heat flux sensor positioned beneath the sample (CAPTEC).
2. Calculating the temperature gradient within the aluminum block using the thermocouples T_1 and T_2.

However, measures revealed that about 90% of the heat flux transferred to the silicon chip was lost either through convection above the sample or through conduction in the inlet/outlet lines. For this reason, it was not possible to measure the heat flux with an acceptable accuracy. To avoid this issue, it would be necessary to vacuum the experimental setup to cancel external convection, which was not possible in this experimental campaign. In addition, because of low temperature gradient in the aluminium block ($T_1 \approx T_2$ from Figure 5.4), it was also not possible to measure heat flux with the second method. As a result, the estimation of the heat flux transfered to the flow was deduced from bubble growth rate as presented in section 5.7.

Two methods were developed to measure the mass flow rate through the microchannel:

1. **Weighting method:** A recovery tank is initially filled with water and put on a weighting scale to measure the mass flow rate. The outlet tube is immersed into the water. Multiple tests and observations showed that the water vapour recondensates in the recovery tube, allowing for two-phase mass flow rate measures. Additionally, a layer of vegetal oil covers the water to prevent evaporation. Preliminary measures revealed that without this layer of vegetal oil, up to 10% of the water could evaporate during an experiment. A schematic view and a photograph of this setup are shown in Figures 5.7a and 5.7b.
2. **Ruler method:** In some of the experiments, the supply tank is emptied to make the liquid/air interface visible. A ruler is placed next to the inlet transparent tube to monitor the water level. Because the inlet tube is of constant diameter, it is possible to determine the mass flow rate from it. This method however suffers from a major drawback: air bubbles can be trapped in the liquid when the inlet line is filled, and between one and two hours are necessary to remove these bubbles. For this reason, we verified that the two methods give the same results, but most experiments only use the weighting method.

5.3.2 Visualization setup

Due to the small dimensions of the microchannels, visualization of the two-phase flow requires a microscope and a lighting apparatus. Additionally, a high-speed camera was employed to record the two-phase flow. The visualization setup is depicted in Figure 5.8.

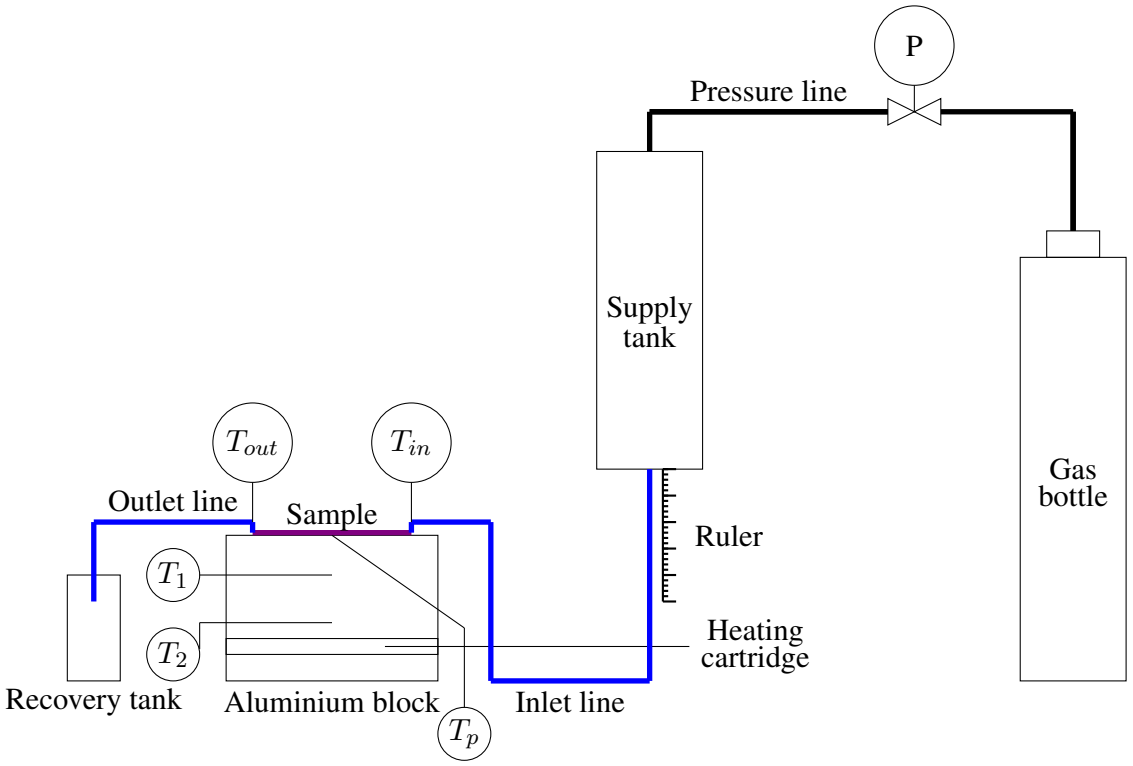

Figure 5.4: Schematic view of the experimental setup. The blue lines represent the water lines. The black line represents the pressure line. P, T_{int}, T_{out}, T_1, T_2, and T_p represent the physical measures.

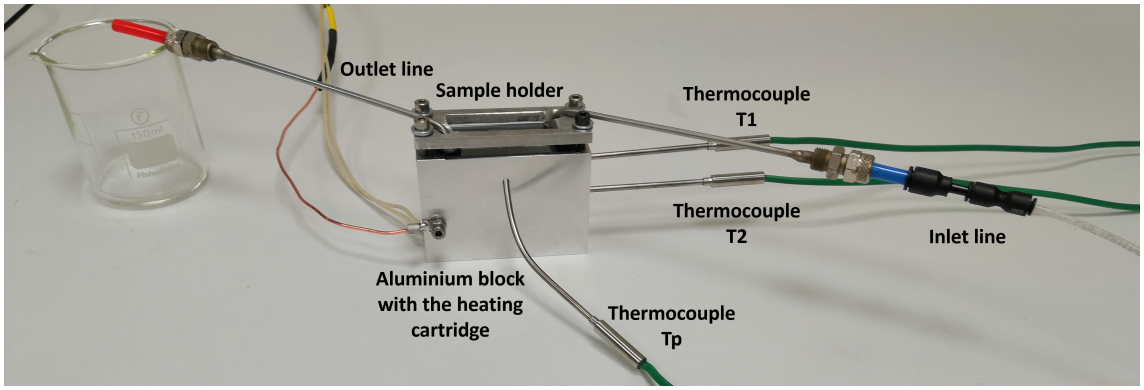

Figure 5.5: Photograph of the experimental setup. The thermocouples T_{in} and T_{out}, as well as the camera are not present in this picture.

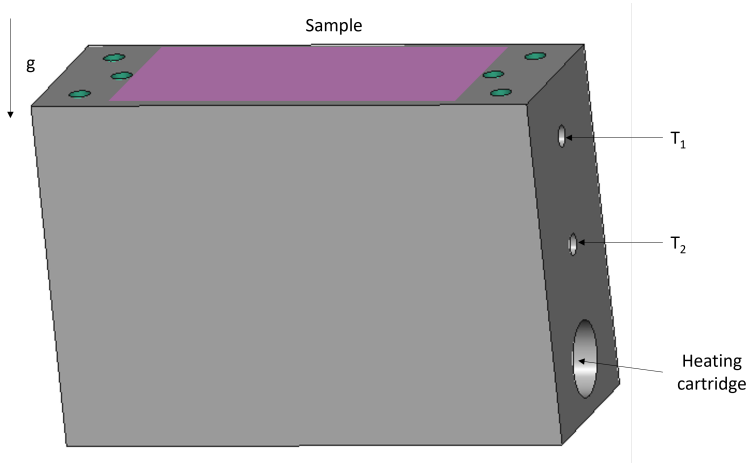

Figure 5.6: Schematic 3D view of the heating block. The sample is put at the top of it and maintained by a sample holder (not represented on this picture). The holes in the block are designed for the heating cartridge and the T_1 and T_2 thermocouples.

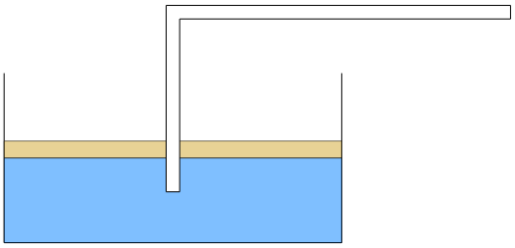

(a) Schematic view of the recovery tank. The blue volume represents liquid water, and the yellow volume represents the oil. The tube immersed in the recovery tank is the outlet line.

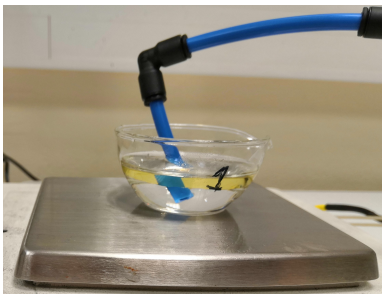

(b) Photograph of the recovery tank on the weighting scale. The volume of water, the volume of oil, and the outlet line are visible.

Figure 5.7

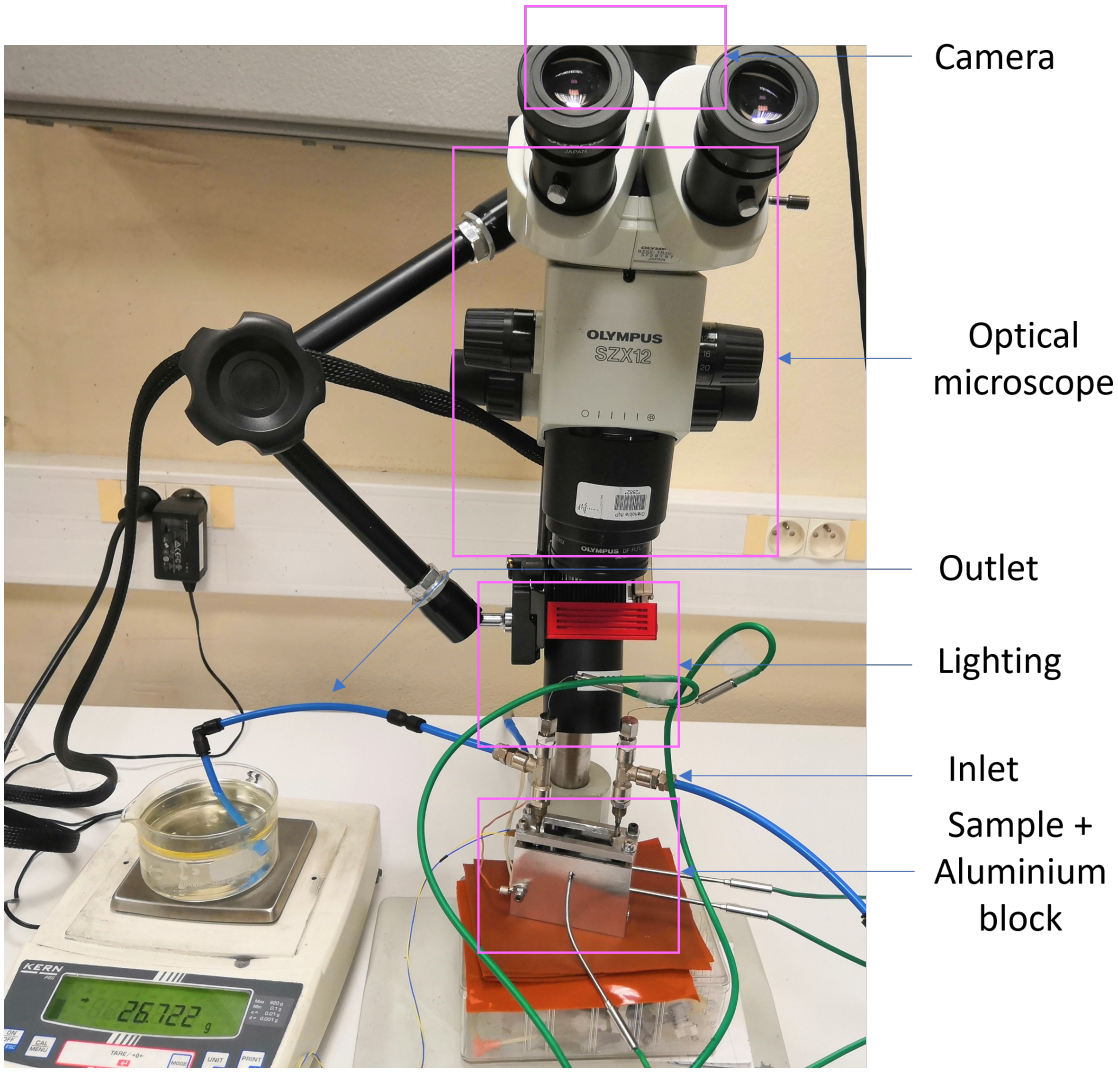

Figure 5.8: Photograph of the visualization setup.

The microscope setup consists of an Olympus SZX12 Stereo Microscope with a $\times 10$ zoom, utilized for magnification and observation. Lighting is provided by the Komi Cyclops 1 LED, delivering 20,000 lux of power at a distance of 20 cm. For capturing the flow, a Phantom VEO camera with a resolution of 2048×700 pixels is employed. In order to provide us a long acquisition time to scrutinize the flow behaviour, the camera operated between 30 and 200 fps.

5.4 Single phase pressure drop

Given the very small dimensions of the microchannels, they can easily be obstructed by dust particles, leading to a significant decrease in their hydraulic diameter. To verify the conformity of each sample, it is important to measure their hydraulic diameter experimentally. To do that, a pressure difference is applied between the inlet and the outlet of the sample, and the mass flow rate is compared to the analytical solution of Poiseuille.

Remark 5.4.1. Because of the fabrication process, the section of the microchannel is trapezoidal, as depicted in Figure 5.3. This has to be taken into account when computing the theorical head losses.

5.4.1 Theory

5.4.1.1 Hydraulic diameter

The hydraulic diameter is defined as four times the ratio between the cross-section and the perimeter of the microchannel, as in equation 5.1.

$$D_h = \frac{4A}{\mathcal{P}} \tag{5.1}$$

Using the notations of Figure 5.3, the cross section and the perimeter are equal to:

$$A = \frac{(wt + wb)h}{2} \qquad \mathcal{P} = wt + wb + 2c \tag{5.2}$$

Equation 5.3 gives the value of c. The angle θ is usually around 54°, but it can be computed more precisely as $\theta = \arctan(h/wi)$.

$$c = \frac{wi}{\cos\theta} = \frac{(wt - wb)/2}{\cos\theta} \tag{5.3}$$

5.4.1.2 Theorical pressure loss

The Darcy law (equation 5.4) gives the head losses for a channel in the general case. Using this expression, it is possible to predict the pressure loss ΔP knowing the mass flow rate $\dot{m}$, the channel length L, and the hydraulic diameter D_h, or conversely, it is possible to predict the mass flow rate knowing the pressure loss and the hydraulic diameter.

$$\dot{m} = \frac{2\rho\Delta P D_h^2 A}{\mu \,\mathrm{Po}\, L} \tag{5.4}$$

Po is the Poiseuille number. It depends on the geometry of the channel. For square channels, it is equal to $\mathrm{Po} = 56$, while for circular channels, it is equal to $\mathrm{Po} = 64$ for instance. A is the cross-section area of the channel.

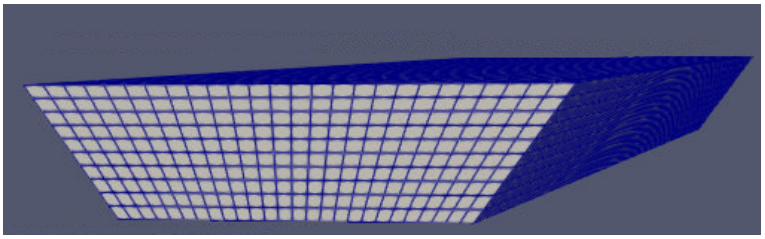

Figure 5.9: Mesh of sample B with $\Delta x = 6$ µm.

Remark 5.4.2. Mossaz et al. (2015) showed that the correlation proposed by Guyer (1989) to compute the Poiseuille number for laminar flows is also valid for trapezoidal microchannels. In this correlation, Po is computed from equation 5.5.

$$\mathrm{Po} = 96 k_1 \tag{5.5}$$

k_1 is computed by equation 5.6. χ is the aspect ratio defined as $\chi = \dfrac{h}{(wt + wb)/2}$.

$$k_1 = 1 - 1.3553\chi + 1.9467\chi^2 - 1.7012\chi^3 + 0.9564\chi^4 - 0.2537\chi^5 \tag{5.6}$$

The correlation of Mossaz was verified numerically with neptune_cfd. A single phase water flow is simulated across a trapezoidal microchannel with the same cross section as sample B ($h = 64$ µm, $wt = 267$ µm and $wb = 172$ µm) and a length $L = 1$ mm. Two meshes were used to conduct a mesh sensitivity study: a coarse mesh with $\Delta x = 6$ µm (depicted in Figure 5.9) and a fine mesh with $\Delta x = 3$ µm. There was no visible difference in the pressure drop between the two meshes, the pressure drop computed by neptune_cfd in both cases was 380,000 Pa/m. The theoretical pressure drop according to the correlation of Mossaz is 398,000 Pa/m, which corresponds to a relative difference smaller than 5%.

5.4.2 Experimental verification of the geometry

To verify the conformity of the geometry of each microchannel, a pressure difference was imposed between the inlet and the outlet of the microchannels, and the liquid mass flow rate was measured with either the weighting method, or the ruler method, or both. The experimental Poiseuille number is computed from equation 5.7. The theoretical Poiseuille number is computed from the correlation of Mossaz.

$$\mathrm{Po} = \frac{2\rho_l \Delta P D_h^2 A}{\mu_l \dot{m} L} \tag{5.7}$$

The mass flow rate was measured with pressures ranging from 1 to 12 bar, and temperatures ranging from 25°C to 100°C. The experimental conditions are given in Table 5.3, and the results are given in Figures 5.10, 5.11 and 5.12. The experimental results are within 12%, 3%, and 25% of the theoretical results for samples A, B and D respectively.

Remark 5.4.3. The experimental Poiseuille number for samples A and B deviates by no more than 12% from the theoretical Poiseuille number. However, for sample D, the error margin can reach up to 25%. While this discrepancy is within an acceptable range to consider sample D functional. For the purposes of this chapter, we will adjust the Poiseuille number from 57.4 to 50. Additionally, it is noteworthy that neptune_cfd calculated a Poiseuille number of 54, slightly smaller than the correlation proposed by Mossaz.

Measure	Sample A		Sample B		Sample D	
	ΔP (bar)	Temperature (°C)	ΔP (bar)	Temperature (°C)	ΔP (bar)	Temperature (°C)
1	4	20	1	20	1	50
2	2	20	2	20	1	50
3	3	20	3	20	1	50
4	1	85	4	20	1	50
5	1	89.5	5	20	1	50
6	1	92.5	5.75	20	1	50
7	1	97.5	8	20	1	50
8			1	10	20	50
9			1	12	1	50
10			1	12.3	1	50

Table 5.3: Operating conditions for tests with pure liquid flow.

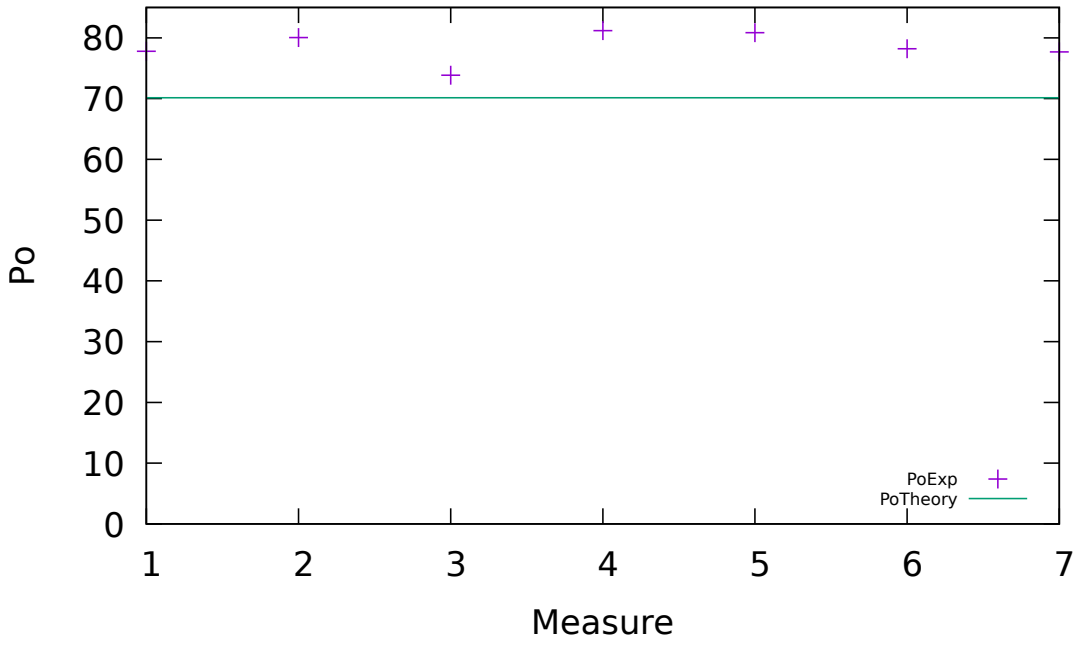

Figure 5.10: Experimental and theoretical values of the Poiseuille number for sample A.

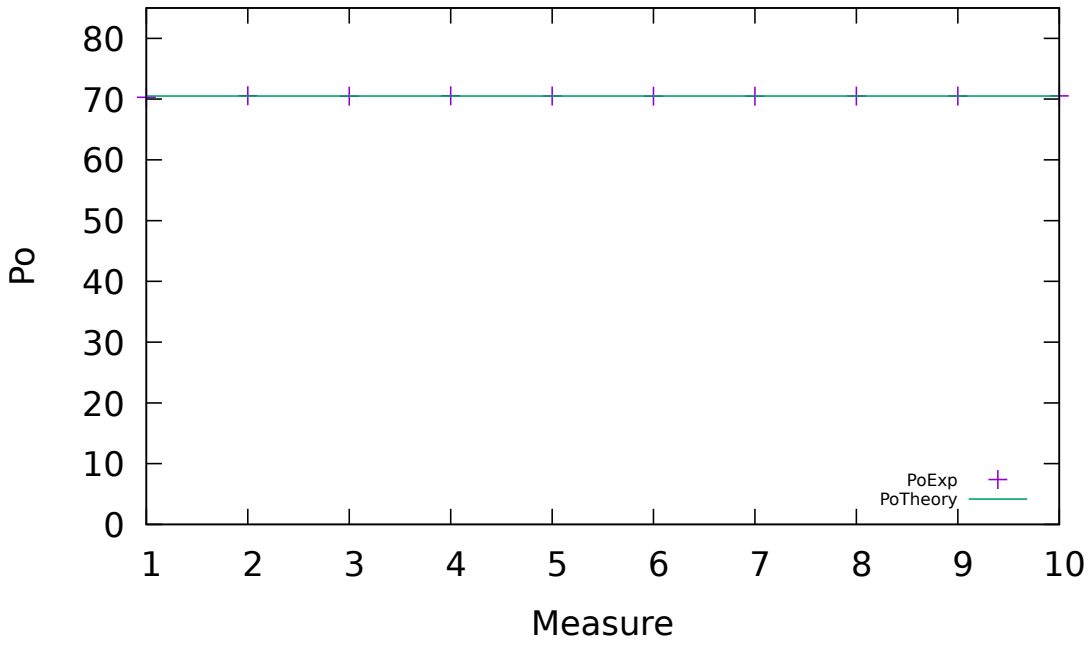

Figure 5.11: Experimental and theoretical values of the Poiseuille number for sample B.

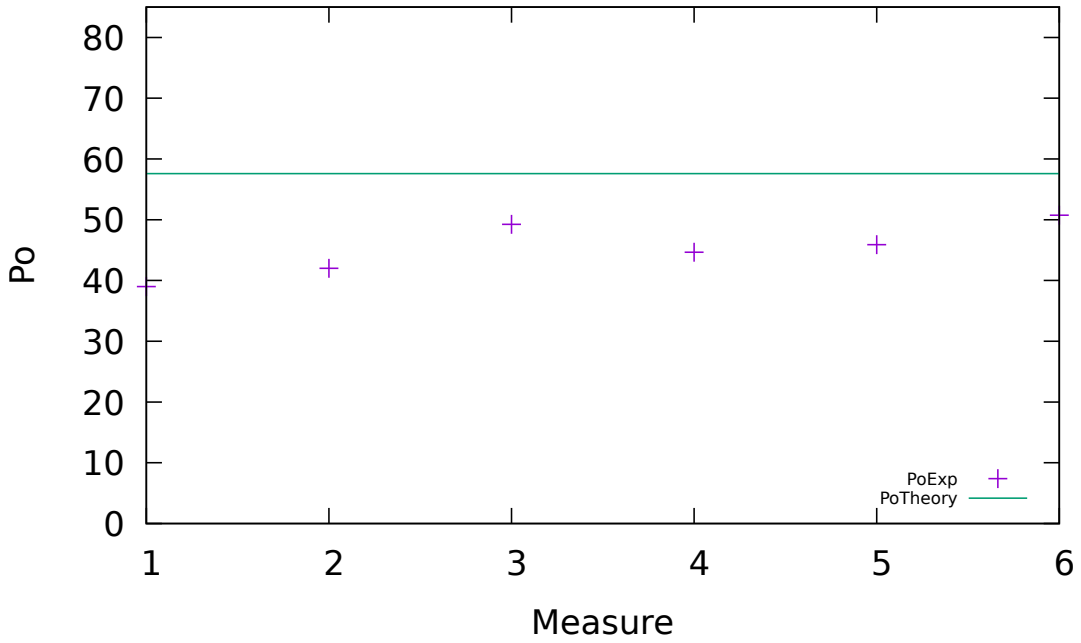

Figure 5.12: Experimental and theoretical values of the Poiseuille number for sample D.

5.5 Characterization of the flow regimes

Being able to identify the correct flow regimes in microchannels is important to determine the pressure loss. Throughout the experimental campaigns, six flow regimes were identified, as illustrated in Figure 5.13. Here are the descriptions of each regime:

- **Single-phase liquid flow:** This regime occurs when the heat flux is insufficient to induce nucleation.
- **Slug flow regime:** At sufficiently high heat fluxes, bubble nucleation occurs, leading to the formation of bubbles at the wall and the growth of vapour bubbles in the superheated liquid. This phenomenon is similar to the experiments conducted by Mukherjee (see section 4.3.3).
- **Single interface boiling:** This regime is characterized by low liquid velocities and relatively high heat fluxes. A very stable liquid/vapour interface is observed in the microchannel, where boiling at the interface balances the liquid velocity, resulting in the interface not moving. This flow regime is very rare and was not identified in the reference articles dealing with flow regimes in microchannels such as Kawahara et al. (2002) or Triplett et al. (1999).
- **Annular flow:** At high heat fluxes and gas volume fractions, vapour bubbles merge, resulting in an annular flow. In this regime, vapour flows through the core of the microchannel while a liquid film adheres to the walls.
- **Droplet/Dryout:** At very high heat fluxes, the liquid film evaporates, creating "holes" in the liquid film. This regime is characterized by a vapour flow at the core and small droplet formation and sliding on the walls.
- **Single-phase vapour flow:** When all the liquid evaporates, a single-phase vapour flow develops.

This flow regime arrangement and especially the identification of a new regime (single interface boiling) is a valuable experimental result that would have been difficult to predict with numerical simulations.

5.5.1 Slug flow regime

In the slug flow regime, bubbles nucleate with diameters similar to that of the channel width. These bubbles then grow due to the wall heat flux and pressure drop. In this regime, vapour bubbles are separated from the wall by a thin liquid film. The liquid and vapour velocities are very similar in this regime for low Capillary and Reynolds numbers.

Remark 5.5.1. For Weber numbers much smaller than 1 ($\mathrm{We}_l \approx 0.01$ in the experiments), the correlation of Aussillous and Quéré (2000) can give an estimation of the liquid film thickness δ between the two horizontal planes.

$$\frac{\delta}{D_h} = \frac{0.67\,\mathrm{Ca}^{2/3}}{1 + 3.35\,\mathrm{Ca}^{2/3}} \tag{5.8}$$

In this chapter, the order of magnitude of $\frac{\delta}{D_h}$ is 0.006. Therefore the liquid film thickness is less than 1 µm. For such a small liquid film, it is reasonable to assume that the vapour and liquid velocities are the same.

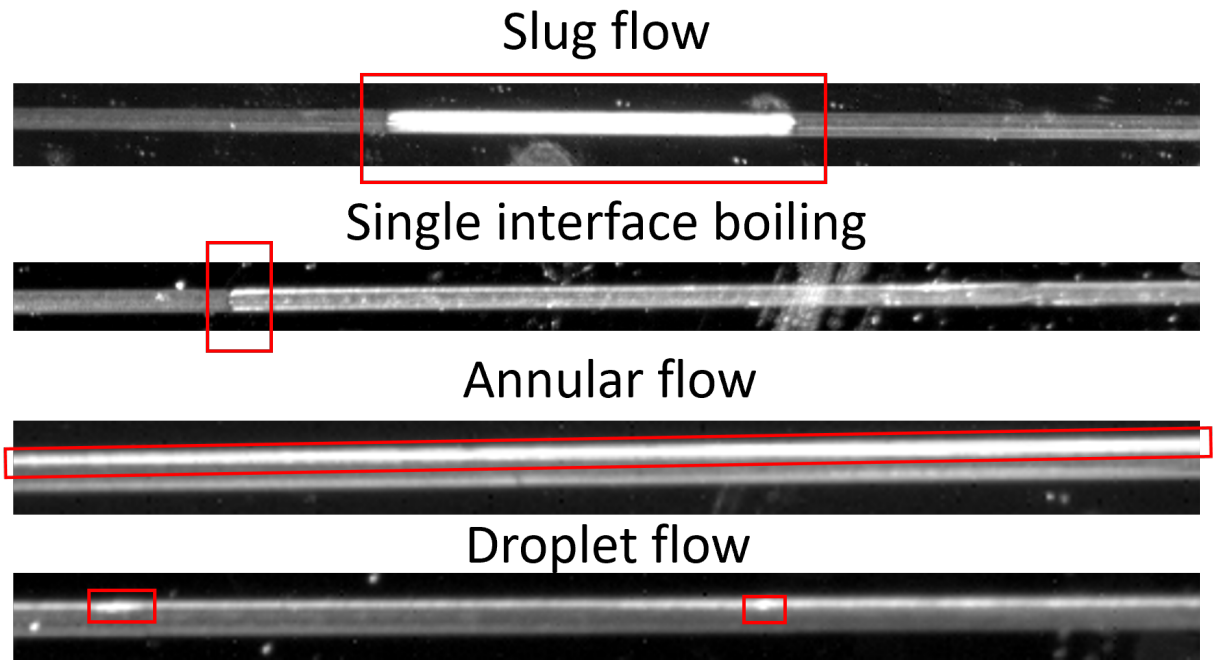

Figure 5.13: Flow regimes observed in microchannels.

5.5.2 Single interface boiling

The heat and mass transfer mechanisms involved in single interface boiling share similarities with the Sucking/Stefan problems (refer to section 3.3.1 for further details). However, in our experiments, mass transfer rates are significantly higher due to the presence of a wall heat flux and non-zero fluid velocity. To maintain a stable single interface boiling regime, the boiling velocity must be the same as the fluid velocity. If the boiling velocity is higher, the interface will move toward the inlet and the flow will eventually shift to an annular regime. If the boiling velocity is lower than the dynamic velocity, the interface will be moved toward the outlet. This will lead to the nucleation of new bubbles and the development of a slug flow regime.

5.5.3 Annular flow

In the annular flow regime, vapour flows at the core of the microchannel at a high velocity, while a liquid film flows on the walls of the channel. With the experimental setup used in this campaign, it was not possible to measure the liquid and vapour velocities. Therefore, this flow regime will not be studied quantitatively in this chapter.

5.5.4 Droplet/dry-out flow

Just before the total dry-out of the channel, a droplet flow regime is observed. It is important to distinguish this regime from the typical droplet or mist flow, where small droplets are carried by the gas in the central region of the flow. In the droplet/dry-out regime observed here, because of confinement, droplets adhere to the wall and move slowly until they completely vaporize. This behaviour is the last regime before single-phase vapour flow.

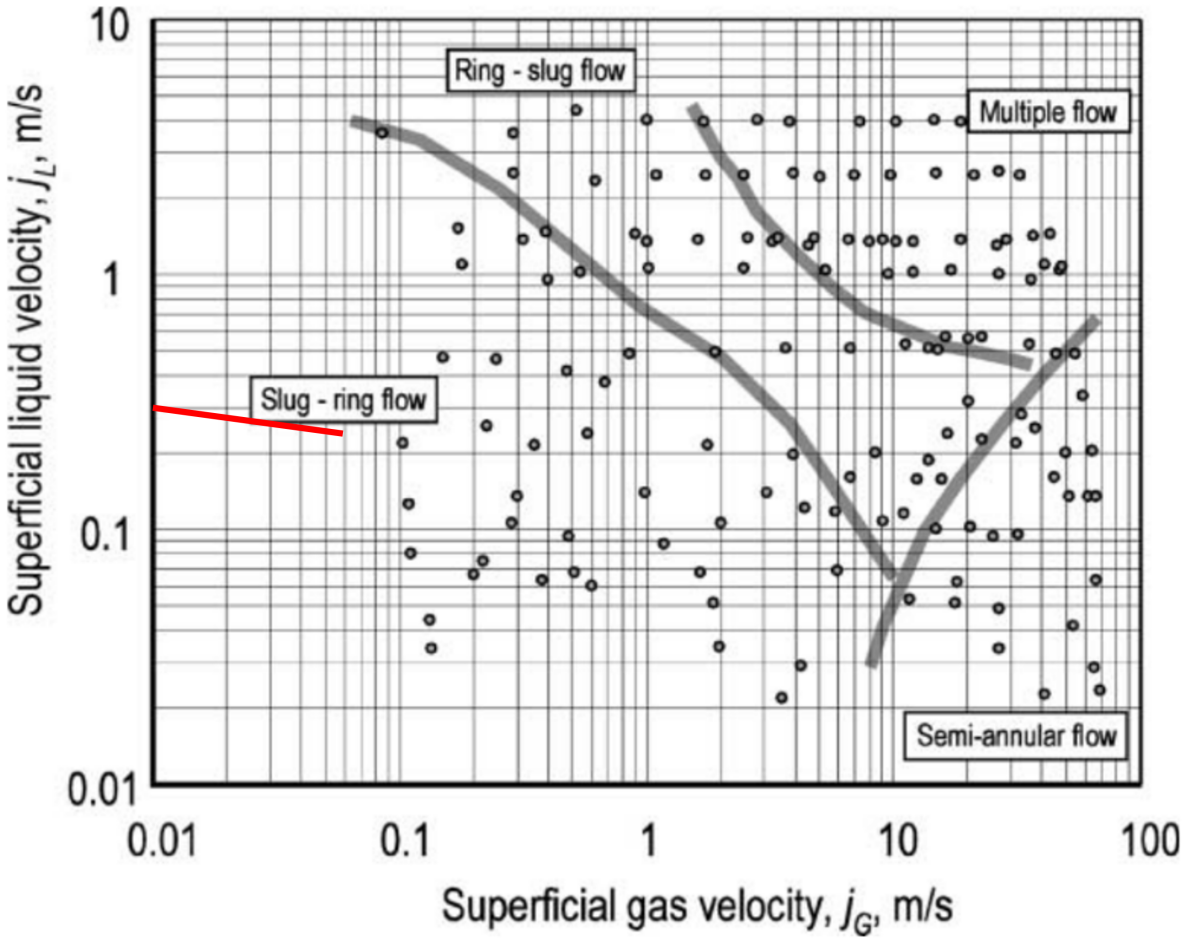

Figure 5.14: Flow regime map for a 100 µm microchannel from Kawahara et al. (2002). The red line represents the slug regimes observed during the experimental campaign.

5.5.5 Flow regime prediction

For adiabatic flows, the flow regime is determined using the superficial liquid and gas velocities j_l and j_g like in Figure 5.14. Assuming that the liquid and the gas are at the same velocity in the slug flow regime, it was possible to assess the superficial liquid and gas velocities ($j_k = \alpha_k u_k$) using equation 5.9. The red line on the map represents the range of the superficial liquid and gas velocities observed during the experiments (with a gas volume fraction between 0 and 10%).
The experimental superficial velocities closely match the flow regime map proposed by authors such as Kawahara (Figure 5.14) or Triplett (Figure 5.15). However, positioning the other flow regimes on the map was not feasible. This is due to the absence of the single interface boiling flow regime in adiabatic flows, and the difficulty to measure the experimental superficial liquid and vapour velocities in the annular flow regime.

$$\begin{cases} u_l = u_g \\ \dot{m} = (\alpha_l \rho_l u_l + \alpha_g \rho_g u_g) A \end{cases} \tag{5.9}$$

Instead, we classify the flow regimes based on the liquid velocity compared to the vaporization velocity.

Remark 5.5.2. Using the Poiseuille law at low gas volume fractions, the liquid velocity can be computed with equation 5.10.

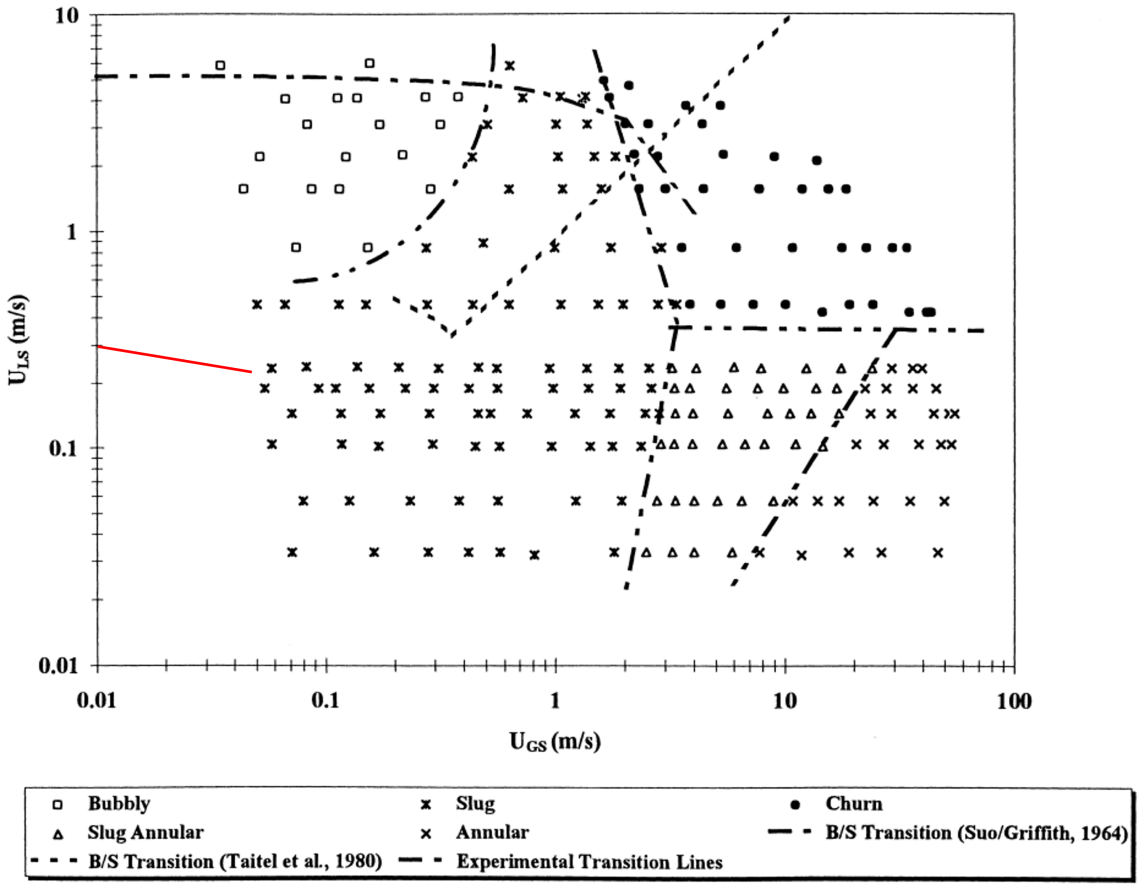

Figure 5.15: Flow regime map for a 1 mm minichannel from Triplett et al. (1999). The red line represents the slug regimes observed during the experimental campaign.

$$u_l = \frac{2\Delta P D_h^2}{\alpha_l \mu_l \, \mathrm{Po} \, L} \tag{5.10}$$

Using an energy balance equation, the boiling velocity can be computed from thermal powers P_{tot} and P_{sensi} and from latent heat h_{lat} as in equation 5.11.

$$u_{boil} = \frac{P_{tot} - P_{sensi}}{A h_{lat}} \tag{5.11}$$

P_{tot} is the total heat power transfered to the fluid. A is the channel cross section. $P_{sensi} = \dot{m} c_p (T_{out} - T_{in})$ is the sensible heat necessary to heat the fluid up to the outlet temperature.

- If $P_{sensi} < \dot{m} c_p (T_{sat} - T_{in})$, the fluid is not heated to saturation. Thus, the flow regime is a single phase liquid regime.
- Else if $u_l > u_{boil}$, boiling occurs but the vapour bubbles are carried by the liquid to the outlet, generating a slug regime.
- If $u_l \approx u_{boil}$, the interface between the liquid and the gas remains stationary, resulting in a single interface boiling regime.
- Finally, if $u_l < u_{boil}$, boiling is faster than the liquid, and a drying sequence will take place. The flow regime will be annular, droplet/dry out, and then single-phase vapour.

Remark 5.5.3. In a future experiment, it would be interesting to measure the heat flux transfered to the liquid to verify the validity of this classification.

5.6 Pressure drop

The pressure drop depends on the flow regime. For single-phase liquid and vapour flows, the Poiseuille and Muskat-Poiseuille equations are employed to calculate pressure losses. For the slug flow regime, the Kreutzer law serves as a suitable approximation for determining head losses. For the single interface boiling regime, the pressure drop can be split in two terms: the pressure loss in the single-phase liquid region before the interface, and the pressure loss in the single-phase vapour region after the interface. For the annular and droplet flow regimes, the correlations are less straightforward and will not be presented in this manuscript.

Remark 5.6.1. Silicium is an extremely wettable surface, with a contact angle close to 0°, consequently the pressure drop caused by wettability can be neglected.

5.6.1 Poiseuille laws

For single-phase liquid flows, the flow-rate/pressure formula is the Poiseuille law. It was verified in section 5.4.2, and the results are presented in Figure 5.10, 5.11, and 5.12.

$$\dot{m}_l = \frac{2\rho_l \Delta P D_h^2 A}{\mu_l \, \mathrm{Po} \, L} \tag{5.12}$$

For single-phase vapour flows, the flow-rate/pressure formula is the Muskat-Poiseuille law (Muskat (1934)), which takes the gas compressiblity into account.

$$\dot{m}_g = \frac{D_h A}{\mu_g} \frac{M}{RT} \frac{P_{in}^2 - P_{out}^2}{L} \tag{5.13}$$

Inlet pressure (bar)	Experimental mass flow rate (g/h)	Theoretical mass flow rate (g/h)
2	1.1	1.1
2.5	5.3	4.5
3	6.0	6.0

Table 5.4: Experimental and theoretical mass flow rates in single-phase vapour flow.

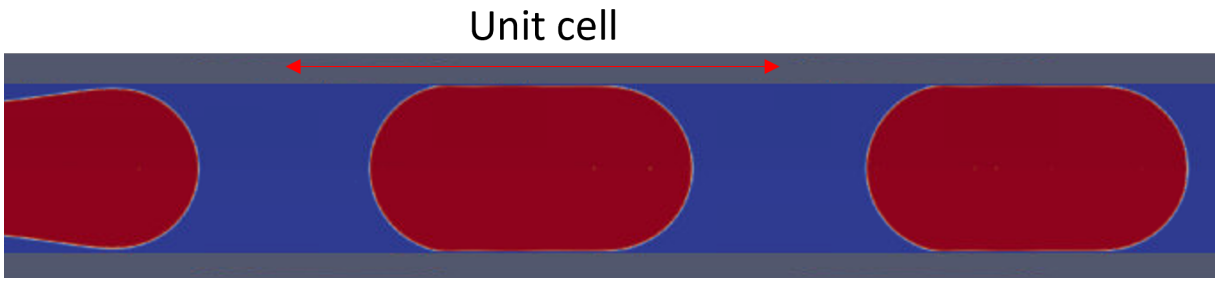

Figure 5.16: Schematic view of a unit cell. The red arrow represents the length L_l.

The Muskat-Poiseuille law was verified on sample D at a temperature $T = 200$ °C. The mass flow rate was measured using the ruler method. This high temperature was necessary to ensure a single-phase vapour flow in the microchannel. Furthermore, the Muskat-Poiseuille law could not be tested on other samples because the mass flow rate was then too small due to the smaller hydraulic diameter of the other microchannels. The measures are presented in Table 5.4, and show a good agreement with the theoretical results.

5.6.2 Kreutzer law

The Kreutzer law (equation 5.14) is a semi-analytical law used to predict pressure drop in the slug regime. It is the sum between the single-phase liquid pressure drop, and the contribution of the gas bubbles.

$$\dot{m}_{slug} = \alpha_l \rho_l \frac{2\Delta P D_h^2}{\mu_l \,\mathrm{Po}\, L(1 + 0.07 \frac{D_h}{L_l}(\frac{\mathrm{Re}}{\mathrm{Ca}})^{1/3})} A \tag{5.14}$$

A is the cross section of the microchannel. L_l is the length of the liquid slugs between the vapour bubbles, as defined in Figure 5.16.

Remark 5.6.2. The term $1 + 0.07\dfrac{D_h}{L_l}\left(\dfrac{\mathrm{Re}}{\mathrm{Ca}}\right)^{1/3}$ represents the contribution of the vapour bubble to the pressure loss. In our experimental conditions, this term is very close to 1 and can be neglected. For instance, assuming a velocity of 0.1 m/s and a liquid slug length of 10 cm, this term would be equal to 1.001. Therefore, the Kreutzer law simplifies to:

$$\dot{m}_{slug} = \alpha_l \dot{m}_l \tag{5.15}$$

where $\dot{m}_l$ can be computed from equation 5.12.

Maintaining a stable slug flow regime for at least 15 minutes to accurately estimate the mass flow rate is challenging. As a result, the mass flow rate was measured in only one experiment to verify the Kreutzer law. This experiment, involving sample D, is detailed in Table 5.5, showing an 18% discrepancy between the experimental and theoretical mass flow rates, which is within an acceptable range.

Inlet pressure (bar)	Volume fraction (-)	Experimental mass flow rate (g/h)	Theoretical mass flow rate (g/h)
1	0.1	14.3	17.55

Table 5.5: Experimental and theoretical mass flow rate in the slug flow regime with sample D.

Sample	Inlet pressure (bar)	Volume fraction (-)	Experimental velocity range (m/s)	Theoretical velocity (m/s)
A	1	0.035	[0.075- 0.08]	0.096
D	1	0.14	[0.3-0.325]	0.297

Table 5.6: Experimental and theoretical velocities in the slug flow regime with samples A and D.

An alternative approach to verifying the Kreutzer law without the need for prolonged slug flow is to compare the experimental bubble velocity, obtained through image analysis, with the theoretical Kreutzer velocity (as per equation 5.16). This method assumes that the bubble velocity matches the liquid velocity, a reasonable assumption in the slug flow regime as discussed in section 5.5.1. The results, provided in Table 5.6, indicate that the difference between the experimental and theoretical velocities is consistently under 20%. The methodology for calculating the volume fraction used in these tables is outlined in section 5.7.3.

$$u = \frac{1}{1-\alpha_g}\frac{\Delta P D_h^2}{\mu_l \,\mathrm{Po}\, L} \tag{5.16}$$

5.6.3 Single interface Boiling

Single interface boiling is the succession of a single-phase liquid flow and a single-phase gas flow as depicted in Figure 5.17. Consequently, the pressure drop in single interface boiling is the cumulative effect of head losses in both the liquid and gas phases. While there is not an explicit analytical formula for calculating these head losses, numerical methods can be employed. Specifically, a 1D model can be utilized, employing equation 5.17 to compute pressure drop in the liquid zone ($L < L_l$) and equation 5.18 in the gas zone ($L > L_l$).

$$\frac{\mathrm{d}P}{\mathrm{d}x} = \frac{\mu_l \,\mathrm{Po}\, \dot{m}_{int}}{2\rho_l A} \tag{5.17}$$

$$\frac{\mathrm{d}P}{\mathrm{d}x} = \frac{\mu_g \,\mathrm{Po}\, \dot{m}_{int}}{2\rho_g A} \tag{5.18}$$

$\rho_g = \dfrac{PM}{R_{gas}T}$ is computed using the ideal gas law.

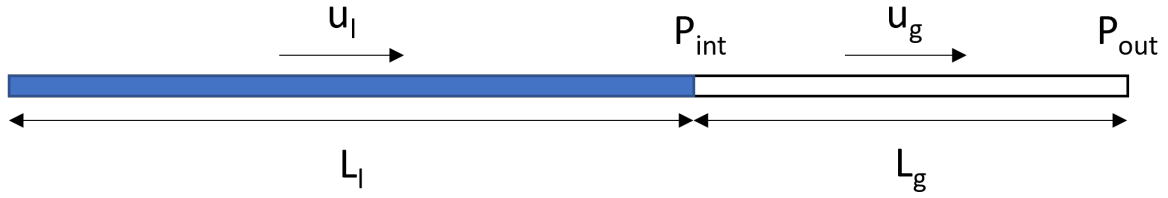

Figure 5.17: Schematic view of the single interface boiling flow regime.

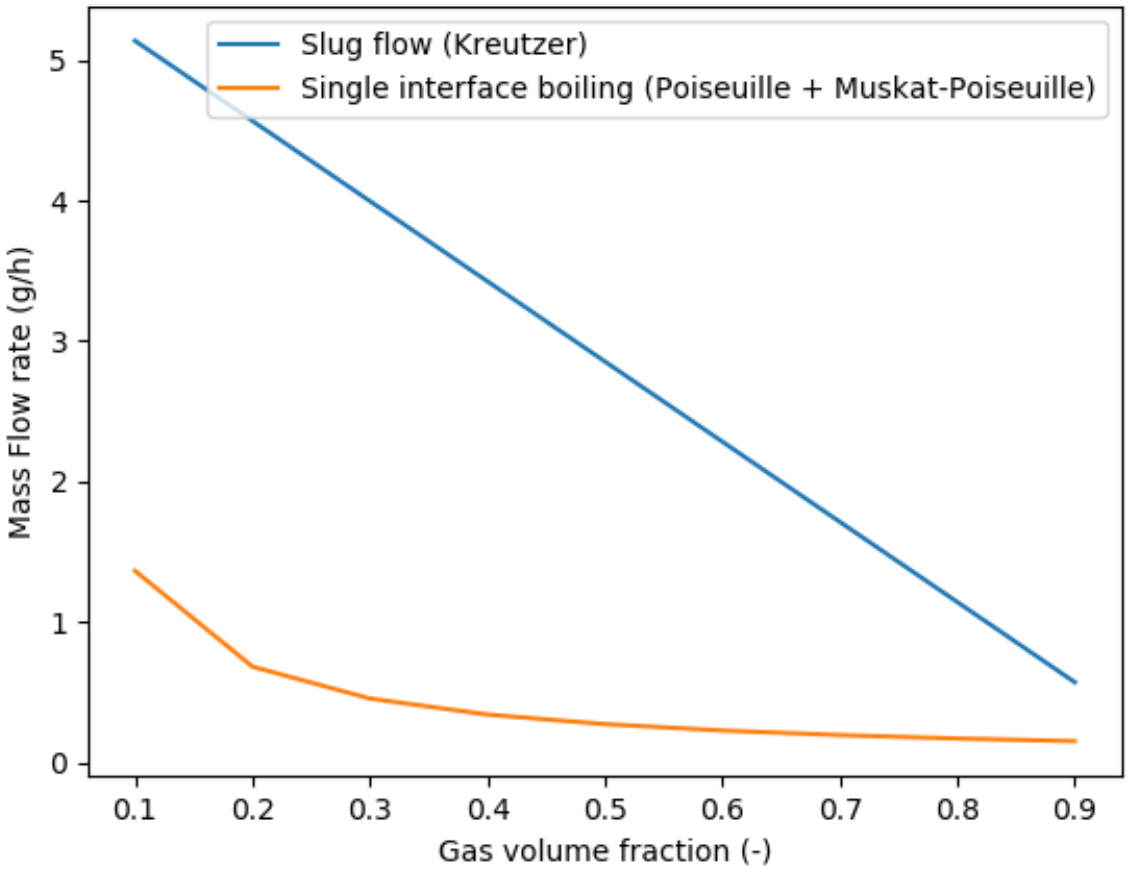

Figure 5.18: Mass flow rate estimation in slug flow and single interface boiling regime versus average gas fraction in a channel for a pressure loss of 1 bar.

5.6.4 The importance of the flow regime on pressure loss

The choice of flow regime can significantly influence pressure loss, even for the same pressure differences and volume fractions. While slug flow exhibits pressure loss similar to single-phase flow, the dynamics change notably in the single interface boiling regime. Phase change at the interface, or pure vapour flow, leads to a very high gas velocity because of the density difference between phase (the conservation of mass implies $u_g = \frac{\rho_l}{\rho_g} u_l$ in single-phase flow for instance). Additionally, phase change leads to a decrease in the fluid viscosity ($\mu_g < \mu_l$). At near-atmoshperic pressures, the pressure loss in the single-phase vapour zone ($L > L_l$) is significant and increases the total pressure loss.
The influence of flow regime becomes evident when observing the mass flow rate plotted against the gas volume fraction for channel A, under a pressure difference of $\Delta P = 1$ bar (Figure 5.18). As expected, the mass flow rate is significantly larger (by roughly a factor of 5) during slug flow compared to single interface boiling.

Remark 5.6.3. For this reason, predicting the flow regime correctly is of significant importance.

5.7 Quantitative results on heat and mass transfer in the slug flow regime

At low Reynolds numbers and moderate wall temperatures, a stable nucleation followed by a slug regime manifests. Within this regime, a bubble periodically forms at a nucleation site, and grows until the outlet, as depicted in Figure 5.19. Using image analysis, it is possible to compute the bubble growth velocity over time $\frac{dL_b}{dt}$. Under some hypothesis, it is then possible to assess a heat flux transfered from the liquid to the bubble φ_b, and a Nusselt number Nu.

5.7.1 Evaluation of the bubble position, and velocity over time

5.7.1.1 Evolution of the bubble position over time

To obtain information on the bubble growth and position, the positions marking the noze and the tail of each bubble are recorded in every frame using the Phantom High Speed software (PCC), as illustrated in Figure 5.20. These positions, initially provided as (X, Y) coordinates, are then transformed into a "1D position" coordinate through a Python script. This "1D position" ranges from 0 mm at the inlet to slightly over 800 mm at the outlet. The 1D position of the start of the bubble is denoted X_0, while the position of the tail of the bubble is denoted X_1. The bubble length L_b is computed as:

$$L_b = X_1 - X_0 \tag{5.19}$$

The bubble position is its center of gravity computed as:

$$X = \frac{X_0 + X_1}{2} \tag{5.20}$$

5.7.1.2 Computation of the bubble velocity

The bubble velocity is defined as the velocity of its center of gravity $u_g = \frac{\mathrm{d}(X_0 + X_1)/2}{\mathrm{d}t}$. However, in boiling flows, the center of gravity of bubbles moves due to two factors: the dynamic force caused by the pressure difference, and the growth of the bubble in the downstream direction. To separate these two factors, the bubble velocity can be divided into two contributions:

$$u_g = \frac{\mathrm{d}(X_0 + X_1)/2}{\mathrm{d}t} = \frac{\mathrm{d}X_0}{\mathrm{d}t} + \frac{1}{2}\frac{\mathrm{d}(X_1 - X_0)}{\mathrm{d}t} \tag{5.21}$$

Figure 5.21 shows that the evolution of X_0 over time is linear for ($t < 0.9$ s), and rather close to the theoretical single phase liquid velocity. This indicates that the velocity of the back of the bubble is the same as the liquid velocity u_l. Additionally, $X_1 - X_0$ is the bubble length, thus, equation 5.21 can be rewritten as:

$$u_g = u_l + \frac{1}{2}\frac{\mathrm{d}L_b}{\mathrm{d}t} \tag{5.22}$$

5.7.2 Experimental cases for the computation of the Nusselt number

Two experiments involving a periodic slug regime are studied in this chapter. The first one involves sample A, the second one involves sample D. In both cases the perdiodic slug regime was maintained for several minutes (5 minutes for sample A, 10 minutes for sample D), and the position and growth velocity of 15 bubbles was tracked for sample A (50 for sample D). The time interval between each frame was $\Delta t = 33$ ms, corresponding to 30 frames per second (FPS). The experimental conditions are given in Table 5.7. In sample A, the bubble velocity was measured to be around $u_b = 80$ mm/s with the method described in section 5.7.1.2. This is in good agreement with the Poiseuille velocity $u_{Poiseuille} = 100$ mm/s. In sample D, the bubble velocity was measured to be around $u_b = 300$ mm/s. This is in good agreement with the predicted Poiseuille velocity $u_{Poiseuille} = 255$ mm/s.

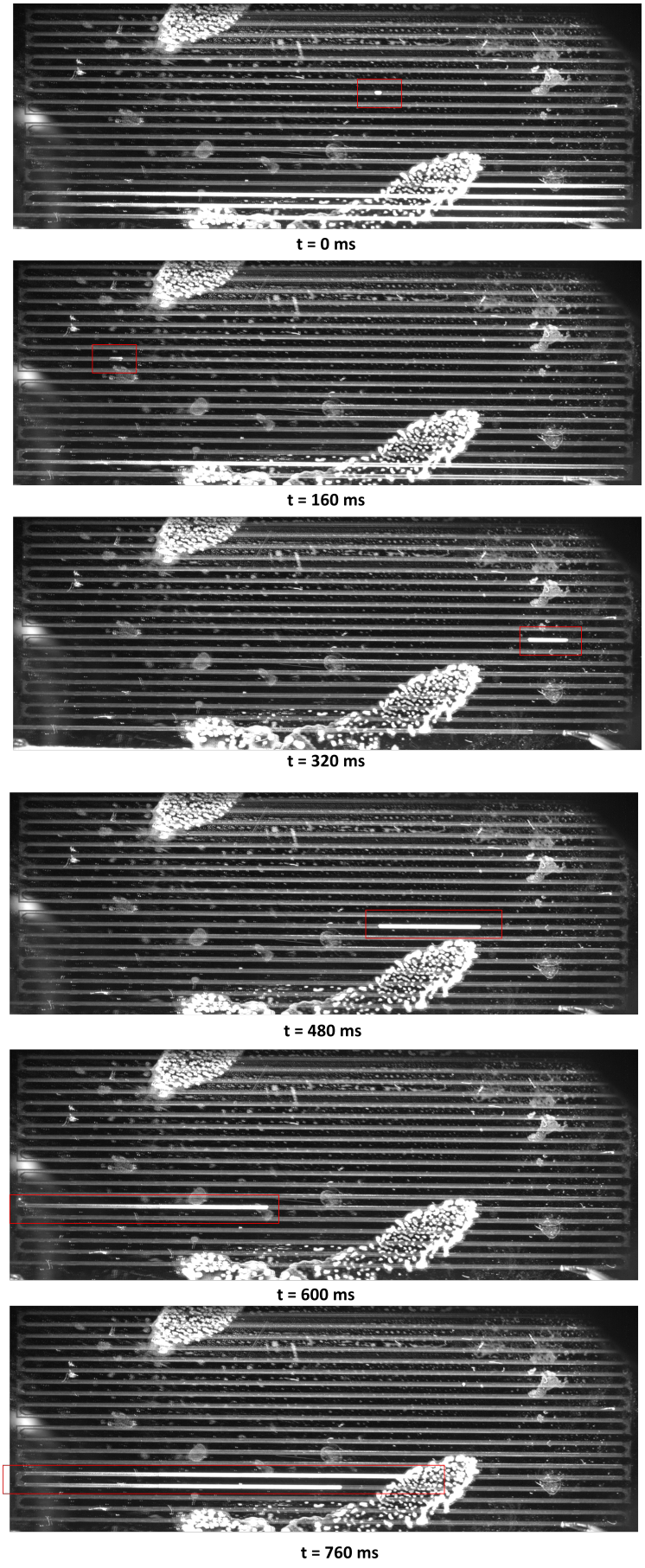

Figure 5.19: Growth of a vapour slug during the experiment (sample A). The white stains on the sample result from the anodic sealing process and, unfortunately, cannot be removed.

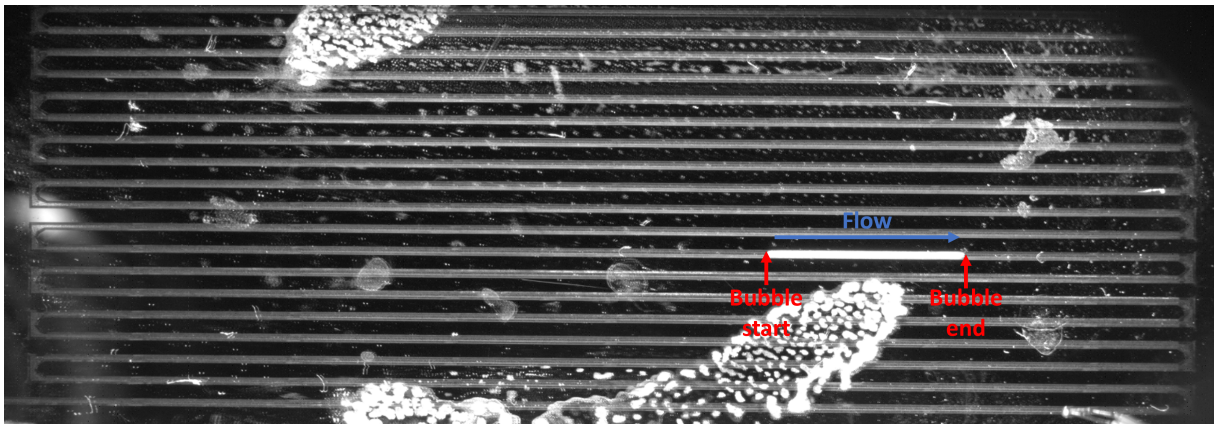

Figure 5.20: Measure of the bubble noze and bubble tail.

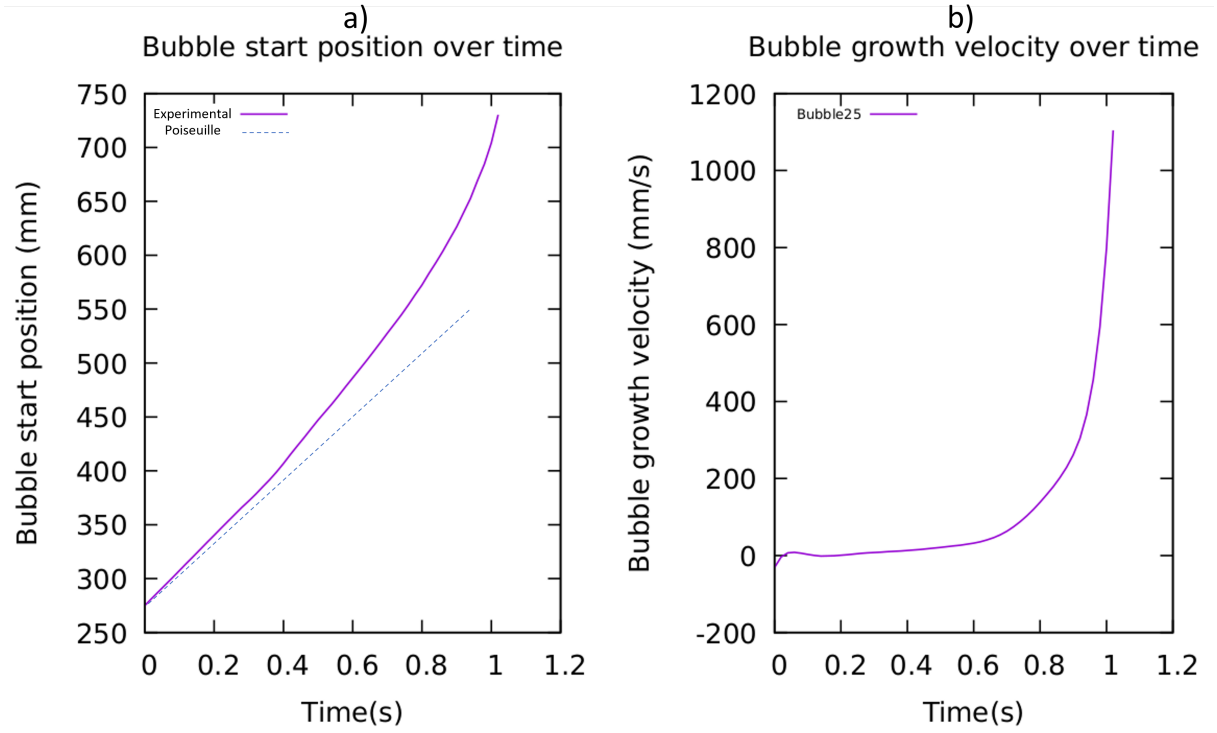

Figure 5.21: Bubble tail position (X_0) and bubble growth velocity $\left(\frac{dL_b}{dt}\right)$ over time for bubble 25 (sample D). In the left figure, the dotted line is computed using the liquid Poiseuille law (equation 5.12).

Sample	ΔP (bar)	T_w (°C)
A	1	110
D	1	109

Table 5.7: Experimental conditions for sample A and sample D in the slug regime.

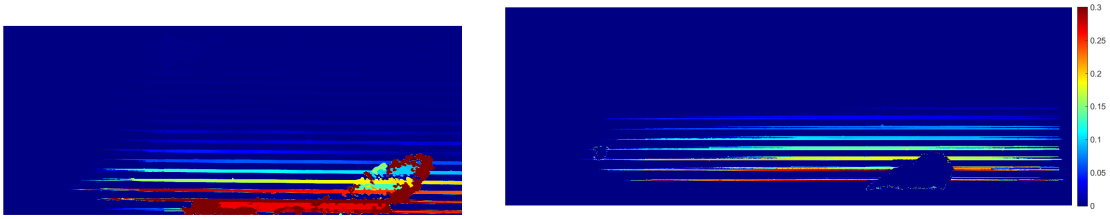

(a) Time-averaged gas volume fraction in sample A.

(b) Time-averaged gas volume fraction in sample D.

Figure 5.22

5.7.3 Volume fraction and nucleation frequency in the slug regime

To characterize the vapour distribution in the samples, volume fraction maps and profiles were extracted from image processing using Matlab (more information in Villegas et al. (2019)). First, images were binarised using a threshold on the grey level and on the object maximum aspect ratio. This step enables the detection of bubbles in some part of the images. Typically, it was difficult to detect clearly bubbles in the left and right channel bends. Then, using an image averaged over time, it was possible to measure the gas fraction distribution in the sample for slug flow regime. Estimation of the bubble frequency was also deduced from flow visualisation.

The results will be presented for sample A and sample D, with the same experimental conditions as above.

5.7.3.1 Results in sample A

The image processing was conducted on approximately 4000 images for this case, corresponding to a physical time $\Delta t = 132$ s. During this period, 83 bubbles were detected, resulting in a nucleation frequency of 0.63 bubbles/s. Figure 5.22a illustrates the average local volume fraction in the microchannel. As expected, the gas volume fraction is higher near the outlet, reaching 22% in the last subchannel. Figure 5.23a depicts the local volume fraction $\alpha_g(x)$ as a function of the vertical pixel (with 0 corresponding to the inlet and 800 to the outlet). Averaging this across all subchannels results in a volume fraction $\alpha_g = 3.5\%$ for sample A.

5.7.3.2 Results in sample D

In sample D, the image processing was conducted on about 3000 images which corresponds to a physical time $\Delta t = 100$ s. During this period, 28 bubbles were detected, resulting in a nucleation frequency of 0.28 bubbles/s. Figure 5.22b illustrates the average local volume fraction in the microchannel with $\alpha_g(x)$ increasing as we get closer to the outlet. Figure 5.23b shows the local volume fraction $\alpha_g(x)$ as a function of the vertical pixel (0 corresponds to the inlet and 800 to the outlet). Averaging this across all subchannels results in a volume fraction $\alpha_g = 4,7\%$ for sample D.

5.7.4 Computation of the Nusselt number: method 1

A method for estimating the Nusselt number was inspired from the work of Magnini and Matar (2020), which involves conducting an energy balance at the bubble scale. This approach is based on the following assumptions:

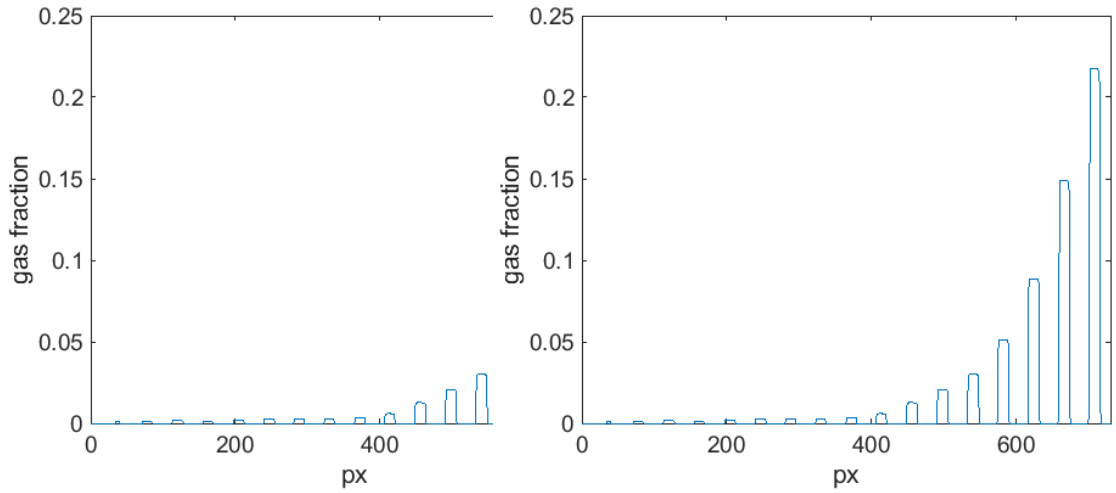

(a) Time-averaged gas volume fraction as a function of the position in microchannel A. 0 px corresponds to the inlet. 800 px corresponds to the outlet.

(b) Time-averaged gas volume fraction as a function of the position in microchannel D. 0 px corresponds to the inlet. 800 px corresponds to the outlet.

Figure 5.23

1. The heat flux at the bubble surface along its path, denoted as φ_b (W/m^2), remains constant over time and is supplied by the liquid phase.
2. There is negligible heat storage in the liquid between two bubbles.
3. The interfacial area between the bubble and the liquid is given by $A_b = \mathcal{P} \times L_b$, where $\mathcal{P}$ represents the perimeter of the microchannel and A_b is the length of the bubble. While the bubble volume variation is estimated as $\mathrm{d}V_b = A_{section}\mathrm{dL}$ with $A_{section}$ the cross section of the channel.

Under these assumptions, equation 5.23 is the energy balance at the scale of one bubble.

$$h_{lat}\mathrm{dm} = \varphi_b A_b \mathrm{dt} \tag{5.23}$$

Therefore, because of hypothesis 3.

$$h_{lat}\rho_v A_{section} dL_b = \varphi_b \mathcal{P} L_b \mathrm{dt} \tag{5.24}$$

Integrating equation 5.24 gives:

$$L_b(t) = K \exp\left(\frac{t}{\tau}\right) \tag{5.25}$$

where K is a constant, and τ is given by equation 5.26. With this formula, an approximation of τ gives a value of φ_b.

$$\tau = \frac{h_{lat}\rho_v A_{section}}{\varphi_b \mathcal{P}} \tag{5.26}$$

Assuming there is no energy storage in the liquid, it is possible to compute the power transfered to the bubble P_b as:

$$P_b = \varphi_b \mathcal{P} L_b \tag{5.27}$$

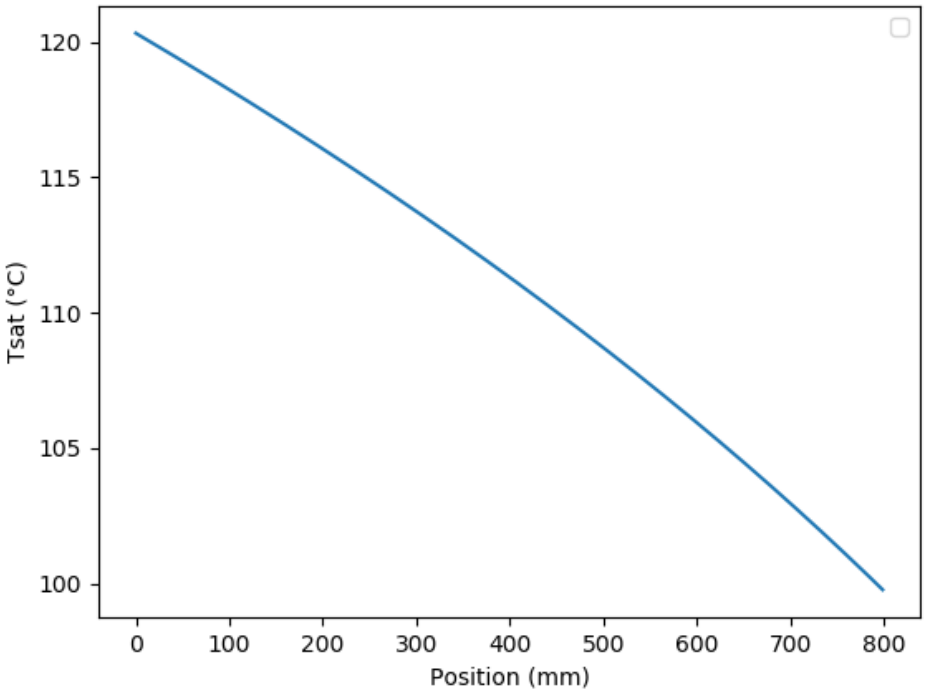

Figure 5.24: Saturation temperature as a function of the position in the microchannel. The position "0 mm" corresponds to the inlet ($P = 2$ bar). The position "800 mm" corresponds to the outlet ($P = 1$ bar).

Therefore, the heat exchange coefficient h is equal to:

$$h = \frac{P_b}{A_{ref}(T_w - T_{sat}(x))} \tag{5.28}$$

Estimating the saturation temperature $T_{sat}(x)$ in the microchannel is not straightforward because the pressure varies across the channel. To address this, we assume a linear pressure loss across the microchannel, expressed as $P(x) = P_{in} - \frac{x}{x_{max}}(P_{in} - P_{out})$. The corresponding saturation temperature, $T_{sat}(P(x))$, is then determined using thermodynamic tables. For a pressure difference $\Delta P = 1$ bar, the resulting saturation temperature profile is illustrated in Figure 5.24.
In equation 5.28, A_{ref} is the area of the surface where boiling occurs. It is equal to $A_{ref} = \mathcal{P}(x_{max} - x_i)$, where x_i is the position where $T_{sat}(x_i) = T_w$, and x_{max} the position corresponding to the end of the bubble.
Finally, the Nusselt number is defined in equation 5.29. To compute the Nusselt number, L_b is plotted as a function of the superheat ($\Delta T = T_w - T_{sat}$) estimated as in Figure 5.24.

$$\mathrm{Nu} = \frac{hD_h}{\lambda} \tag{5.29}$$

The slope of the curve is then equal to $\frac{\mathrm{Nu}(x_{max} - x_i)\lambda}{\varphi_b D_h}$.
The experimental Nusselt number will be compared to the correlation of Renksizbulut and Niazmand (2005). This correlation can be applied for fully developed single phase liquid flows in trapezoidal channels for Reynolds numbers between 0.1 and 1000. Mossaz et al. (2015) found that this correlation (detailed in equation 5.30) was accurate for microchannels as well.

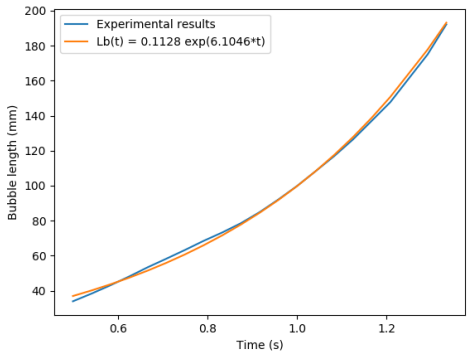

(a) Evolution of the bubble length over time for sample D (bubble 37). The blue line represents the experimental results, the orange line is an exponential fit.

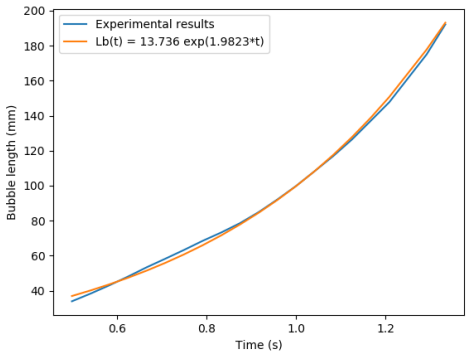

(b) Evolution of the bubble length over time for sample A (bubble 15). The blue line represents the experimental results, the orange line is an exponential fit.

Figure 5.25

$$\mathrm{Nu} = \left[2.87\left(\frac{90}{\theta}\right)^{-0.26} + 4.8\exp\left(-3.9\beta\left(\frac{90}{\theta}\right)^{0.21}\right)\right] k_2 \tag{5.30}$$

$\theta = 54.7$ is the apex angle, and $\beta = \dfrac{h}{w_b}$ is the aspect ratio (see Figure 5.3). $k_2 = 1 + 0.075(1 + \beta)\exp(-0.45\,\mathrm{Re})$ is a function of the Reynolds number.

5.7.4.1 Method 1 applied to sample D

The evolution of the bubble length over time for sample D is given in Figure 5.25a for bubble 37. An exponential function fits the bubble evolution over time well, with $1/\tau$ varying from 6.0 to 6.3 depending on the bubble. We will therefore take $\tau = 0.16$ s. Using equation 5.26, this results in a heat flux $\varphi_b = 441.6$ W/m^2. Figure 5.25a shows the evolution of the bubble length as a function of the superheat. The slope of the curve is equal to 11.2 mm/°C for ΔT between 0 and 2 °C, and 24 mm/°C for ΔT larger than 2 °C. This results in Nusselt numbers equal to $\mathrm{Nu} = 2.3 \times 10^{-3}$ and $\mathrm{Nu} = 5 \times 10^{-3}$ using equation 5.29. The correlation of Renksizbulut and Niazmand (2005) predicts a Nusselt number equal to 2.53 for a single phase liquid flow, which is significantly larger than the Nusselt number estimated with method 1.

5.7.4.2 Method 1 applied to sample A

The evolution of the bubble length over time for sample A is given in Figure 5.25b for bubble 15. An exponential function fits the bubble evolution over time well, with $1/\tau$ varying from 1.9 to 2.2 depending on the bubble. We will therefore take $\tau = 0.49$ s. Using equation 5.26, this results in a heat flux $\varphi_b = 110$ W/m^2. The slope of the curve is equal to 37.5 mm/°C, which gives a Nusselt number $\mathrm{Nu} = 1.3 \times 10^{-3}$. The correlation of Renksizbulut and Niazmand (2005) predicts a Nusselt number equal to 3.53 for a single phase liquid flow, which is significantly larger than the Nusselt number estimated with method 1.

5.7.4.3 Conclusion on method 1

Method 1 severely underpredicts the Nusselt number. This is probably caused by unreasonable hypotheses. In particular, it is likely that a large amount of heat is stored in the liquid between two bubbles. Consequently, it is wrong to assume that the interfacial area between the bubble and the liquid is $A = \mathcal{P} \times L_b$. For these reasons, method 1 will be abandonned in favour of method 2.

5.7.5 Computation of the Nusselt number: method 2

Method 2 also involves an energy balance at the bubble scale, but different hypothesis are made. For instance:

1. The heat flux at the bubble surface φ_b (W/m^2) is constant over time.
2. Boiling only occurs at the front of the bubble. Hence, the interfacial area between the bubble and the liquid is the microchannel section.

In this approach, the computation of the Nusselt number involves the following steps:

1. Energy balance at the bubble scale.
2. Computation of the heat transfer coefficient.

5.7.5.1 Energy balance at the bubble scale

Assuming that boiling only occurs at the front of the bubble, the energy required to induce a vaporization of a volume dV$_b$ (inducing a growth of a bubble on a length dL$_b$) is given by equation 5.31.

$$E = \rho_v \mathrm{dV}_b h_{lat} = \rho_v A_{section} \mathrm{dL}_b h_{lat} \tag{5.31}$$

Conversely, the interfacial energy transfered from the superheated liquid to the bubble during a time dt is given by equation 5.32.

$$E = \varphi_b A_{section} \mathrm{dt} \tag{5.32}$$

φ_b represents the heat flux transferred by the superheated liquid to the bubble, $A_{section}$ is the section of the microchannel, equal to the area of heat exchange between the front of the bubble and the superheated liquid ($A_b = A_{section}$ in method 2). Finally, dL$_b$ is the variation in bubble length due to boiling.
Using equations 5.31 and 5.32, it is possible to estimate the heat flux φ_b.

$$\varphi_b = \rho_v \frac{\mathrm{dL}_b}{\mathrm{dt}} h_{lat} \tag{5.33}$$

5.7.5.2 Computation of the heat transfer coefficient

By definition, the heat transfer coefficient is $h = \dfrac{\varphi_b}{\Delta T}$. φ_b is computed with equation 5.33. $\Delta T = T_w - T_{sat}$ is computed with the method detailed in section 5.7.4 assuming constant pressure loss. The Nusselt number is then computed using in equation 5.34.

$$\mathrm{Nu} = \frac{h D_h}{\lambda} \tag{5.34}$$

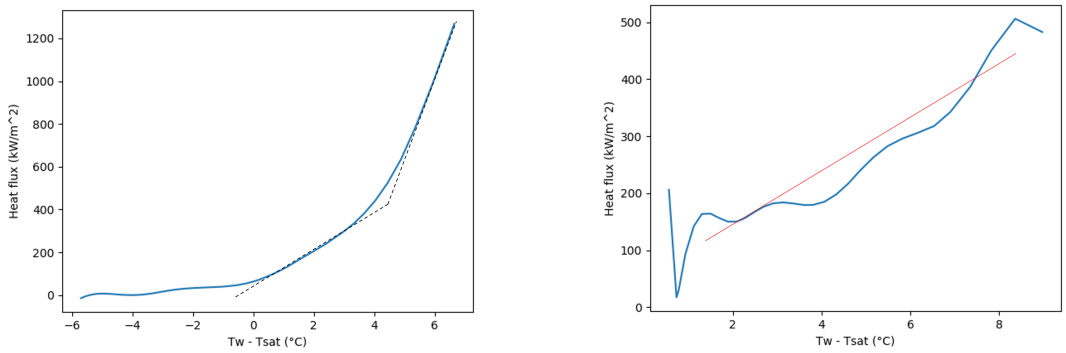

(a) Sample D: Heat flux as a function of the superheat for bubble 25.

(b) Sample A: Heat flux as a function of the superheat for bubble 12.

Figure 5.26

5.7.5.3 Method 2 applied to sample D

The evolution of the heat flux φ_b as a function of the superheat is plotted in Figure 5.26a for bubble 25 to compute the Nusselt number, as explained in the previous section.

Remark 5.7.1. Bubble 25 is representative of the behavior observed in most bubbles. Its length and position evolve particularly smoothly, making it an ideal candidate to represent the average bubble behavior.

For low superheats ($\Delta T < 3.5$°C), the heat transfer coefficient is roughly $h = 86$ kW.m^{-2}.K^{-1}, which corresponds to a Nusselt number of 16. For high superheats ($4°C < \Delta T < 6°C$), the heat transfer coefficient is around $h = 318$ kW.m^{-2}.K^{-1}, which corresponds to a Nusselt of 60. As a comparison, the correlation of Renksizbulut and Niazmand (2005) predicts a Nusselt number of 2.53 for single-phase flows. As expected, the Nusselt number for boiling flows is larger.

5.7.5.4 Method 2 applied to sample A

The evolution of the heat flux as a function of the superheat typically looks like Figure 5.26b for sample A. It is less regular than in sample D, therefore the error on the heat transfer coefficient is higher. The heat transfer coefficient is around $h = 55$ kW.m^{-2}.K^{-1}, corresponding to a Nusselt number of 8. As a comparison, the correlation of Renksizbulut and Niazmand (2005) predicts a Nusselt number of 3.53 for single-phase flows, smaller than the experimental coefficient, as expected.

5.8 Conclusion

Remark 5.8.1. In this chapter, several experiments involving boiling in 100 µm microchannels were presented. Six distinct boiling flow regimes were identified: single-phase liquid, slug, single interface boiling, annular flow, droplet/dryout, and single-phase vapour. The flow regime can be predicted by comparing the dynamic velocity to the boiling velocity.
Additionally, heat transfer was quantitatively measured in a periodic slug regime, providing information on the growth velocity of vapour slugs. Table 5.8 summarizes the order of magnitude of the dimensionless numbers observed for samples A and D.

	Sample A	Sample D
Reynolds liquid	38	150
Reynolds gas	1	4
Capillary	3×10^{-4}	10^{-3}
Jakob	15	11
Péclet	58	230
Prandtl liquid	1.8	1.8
Prandtl gas	1	1
Nusselt	8	16-60

Table 5.8: Dimensionless numbers involved in sample A and sample D in the slug flow regime.

Part III

Upscaling

Three-dimensional numerical simulations are prohibitively expensive for industrial applications, such as simulating the drying of failed fuel rods. To address this limitation, this part introduces a 1D model for boiling flows in microchannels, discussed in Chapter 6. The model is based on findings from parts I and II to predict pressure loss and phase change with reasonable accuracy for microchannels with diameters under 140 µm, Reynolds numbers below 100, and Nusselt numbers between 5 and 50. With this 1D approach, it was feasible to simulate the experiments presented in the previous section within a week.
However, even this 1D model remains computationally demanding for full-scale industrial applications. Therefore, a simplified 0D model, detailed in chapter 7, was developed to simulate the industrial scenario in under a minute, offering a practical solution and concluding this PhD research.

CHAPTER 6

1D model for boiling flows in microchannels

Summary

The 3D computations presented in Chapters 3 and 4 provide highly accurate results but require significant computational resources and time. Simulating a microchannel longer than a few centimeters using these methods is not realistic.
This chapter aims to introduce a 1D method for simulating slug flows in microchannels, using upscaling laws derived from LEGI experiments and 3D simulations. To achieve this, a pressure drop upscaling law and a phase change model are implemented.

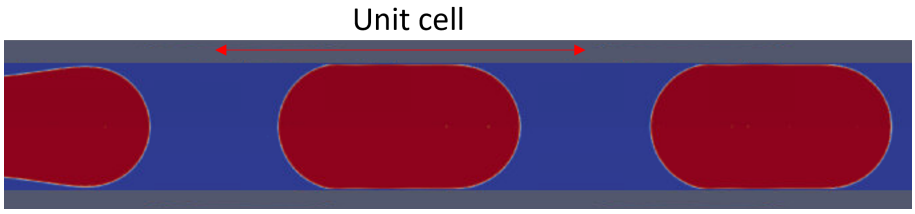

Figure 6.1: Unit cell in a slug flow. It corresponds to a gas bubble and two halves of the adjacent liquid slugs.

6.1 Pressure drop

6.1.1 The Kreutzer law

Section 0.3.3 showed that predicting head losses in microchannels using 1D empirical correlations is challenging. However, when the flow regime is known, mechanistic models can provide reasonable predictions. For example, Kreutzer et al. (2005) proposed a pressure drop correlation specifically for cylindrical microchannels, which can be adapted for rectangular microchannels as well. This correlation has been used and validated both experimentally and numerically by several research groups, including Gupta et al. (2009), Kurimoto et al. (2019), Choi et al. (2010), Fries and Rudolf von Rohr (2009), Ganapathy et al. (2013), and Walsh et al. (2009). It is now widely employed to predict pressure drops in slug flow regimes.

Remark 6.1.1. The correlation of Kreutzer provides a method to calculate the pressure loss across a "unit cell" within a microchannel flow. A unit cell, as depicted in Figure 6.1, consists of a gas bubble and two halves of the adjacent liquid slugs. According to this correlation, the total pressure drop across a unit cell, denoted as ΔP_{tot}, is the sum of the pressure drop due to the gas bubble ΔP_g and the pressure drop due to the liquid slug ΔP_l. This relationship is mathematically expressed as:

$$\Delta P_{tot} = \Delta P_l + \Delta P_g \tag{6.1}$$

The pressure drop in the liquid phase can be computed from the single phase analytical solution (equation 6.2).

$$\frac{\Delta P_l}{L_l} = 4 f_l \frac{\rho_l j_t^2}{2 D_h} \tag{6.2}$$

j_t is the total volumetric flux, and L_l is the length of the liquid phase. f_l is the friction factor for a single phase liquid flow. It is equal to $16/\,\mathrm{Re}$ for circular channels, and $14.2/\,\mathrm{Re}$ for square channels.
Adding an empirical pressure drop in the gas bubbles, Kreutzer et al. (2005) found that the total pressure drop follows equation 6.3.

$$\frac{\Delta P_{tot}}{L_{UC}} = 4 f \frac{\rho_l j_t^2}{2 D_h} \tag{6.3}$$

L_{UC} is the length of a unit cell.

Remark 6.1.2. f is the total friction factor computed by equation 6.4 with the correlation of Kreutzer.

$$f = \frac{16}{\mathrm{Re}} \left(1 + \alpha_1 \frac{D}{L_l} \left(\frac{\mathrm{Re}}{\mathrm{Ca}} \right)^{1/3} \right) \tag{6.4}$$

Figure 6.2: Water volume fraction (in blue) in the microchannel in the Gupta case. The picture is taken from Gupta et al. (2009).

The Reynolds number is computed as $\mathrm{Re} = \frac{\rho_l j_t D_h}{\mu_l}$, the capillary number as $\mathrm{Ca} = \frac{\mu_l j_t}{\sigma}$. α_1 is an empirical coefficient. Its value was determined to be 0.07.

The model of Kreutzer requires the knowledge of the slug length L_l. This parameter can be measured experimentally, computed numerically or from correlations (like (Abadie, 2013) or Yao et al. (2019) for rectangular channels).

6.1.2 Extension of the Kreutzer solution

The solution developed by Kreutzer is validated specifically for water flows in cylindrical microchannels. Recently, Kurimoto et al. (2019) extended Kreutzer's unit cell model to square microchannels and also applied it to multiple fluids. In this extended model, the pressure drop across the unit cell is calculated using equation 6.3. The friction factor, which is a critical component in determining the pressure drop, is then computed using the correlation proposed by Kurimoto et al. (2019), as described in equation 6.5.

$$f = \frac{\mathrm{Po}}{\mathrm{Re}} \left(1 + \frac{D_h}{L_l} \frac{0.25\,\mathrm{Ca}^{-1/3}}{1 + 0.744\,\mathrm{Ca}^{2/3} - 0.623\,\mathrm{We}^{0.12}} \right) \tag{6.5}$$

Po is the Poiseuille number which depends on the geometry of the microchannel. For square microchannels it is equal to 56.9. $\mathrm{We} = \frac{\rho_l j_t^2 D_h}{\sigma}$ is the Weber number.

Remark 6.1.3. For water at moderate to low velocities, the Weber term ($0.587\,\mathrm{We}^{0.131}$) is often negligible. Similarly, for water at low velocity, ($0.744\,\mathrm{Ca}^{2/3}$) is negligible. Under these conditions, equation 6.5 converges toward the solution of Kreutzer.

6.1.3 Numerical simulations

The case study from Gupta et al. (2009) was simulated as a benchmark to evaluate neptune_cfd's performance on adiabatic slug flows. This case is a very refined numerical VOF study used to validate the Kreutzer law and serves as a reference. The physical domain consists of a cylindrical channel with a diameter $d = 500$ µm and a length of $10d$. This domain was represented using a 2D axisymmetric approach with a cell size of $\Delta x = 2$ µm. In the simulation, water and air were injected into the microchannel with superficial velocities of $j_l = 0.255$ m/s and $j_g = 0.245$ m/s respectively. To ensure the formation of a single bubble separated from the wall by a liquid film, the air was injected at the center of the cylinder, while the water was injected near the wall within the last 10 micrometers. The results of the simulation include the liquid film thickness at the wall, the bubble length, the liquid slug length, and the pressure drop. A view of the flow for a mesh with $\Delta x = 5$ µm is presented in Figure 6.2.
Figure 6.3 illustrates the qualitative results obtained using neptune_cfd. However, the liquid film at the wall could not be accurately modeled using the interface sharpening approach because the interface is spread over five cells, which is equivalent to the width of the liquid film. Despite this limitation, the bubble length, liquid slug length, and pressure drop were computed with reasonable accuracy, as summarized in Table 6.1.

Figure 6.3: Air volume fraction in the microchannel at $t = 10$ ms.

Quantity	neptune_cfd	Gupta numerical	Correlation
Bubble length	$1.9d$	$2.0d$	-
Liquid length	$1.0d$	$1.3d$	-
Pressure drop (Pa/m)	125,380	70,700	107,000 (with $L_l = L_b + L_l = 2.9d$)

Table 6.1: Bubble length, slug length and pressure drop for the case of Gupta.

6.1.4 Simplification of the Kreutzer solution

The term for the bubble pressure drop is often negligible in practical scenarios. For instance, in the experiments presented in the previous chapter, the value of $\alpha_1 \frac{D}{L_l} \left(\frac{\mathrm{Re}}{\mathrm{Ca}}\right)^{1/3}$ is approximately 10^{-6}, which is significantly smaller than 1. In such cases, particularly for small gas volume fractions, the Kreutzer law simplifies to a weighted Poiseuille law, as shown in equation 6.6.

$$u = \frac{1}{1-\alpha_g} \frac{\Delta P d_h^2}{\mu_l \, \mathrm{Po} \, L} \tag{6.6}$$

This formula was validated experimentally in chapter 5 (Table 5.6 more specifically), and will be used for the upscaling.

6.2 First upscaling method

To transition from a 3D simulation to a 1D simulation, both a pressure loss model and a phase change model are necessary. In this initial approach, pressure loss is calculated using the weighted Poiseuille law (equation 6.6), while heat and mass transfer are modeled using the Mucellphage model.

6.2.1 Pressure loss

For pressure loss, the weighted Poiseuille law (equation 6.6) is implemented as a momentum source term, TS_k, in neptune_cfd.

$$\frac{\partial}{\partial t}(\alpha_k \rho_k \underline{u}_k) + \nabla.(\alpha_k \rho_k \underline{u}_k \otimes \underline{u}_k) = -\alpha_k \nabla P + \underline{I}_k + \alpha_k \underline{TS}_k \tag{6.7}$$

with $\underline{TS}_k = -\frac{\mu_l \underline{U}_k Po}{2 d_h^2}$. $\underline{U}_k = \sum_I^{ncel} \alpha_l \underline{u}_k / ncel$ is the average velocity across the whole channel. The interfacial momentum transfer term $\underline{I'}_k$ is set as an infinite drag force to get $\underline{u}_l \approx \underline{u}_g$.

6.2.2 Description of the numerical case

This initial approach was evaluated using a hypothetical test case to compare the numerical results obtained with this upscaling method against those from 3D simulations. The physical domain consists of a rectangular microchannel with a cross-sectional area of 152 µm × 100 µm, similar to sample D from the experimental campaign (chapter 5), although sample D has a trapezoidal rather than a rectangular cross-section. The simulation was conducted over a 1 mm length, as simulating a longer microchannel would be computationally prohibitive for the 3D approach.

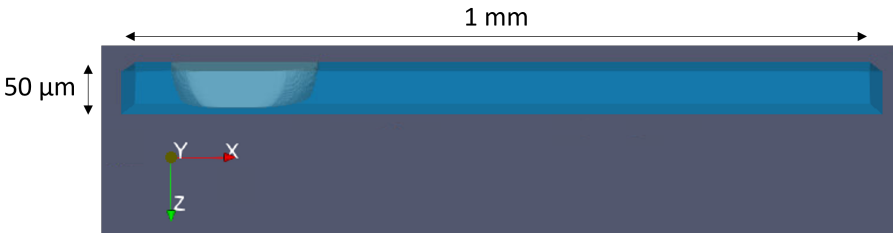

Figure 6.4: Initial conditions of the 3D case.

6.2.2.1 3D data setting

The domain is discretized using a Cartesian mesh with a uniform cell size of $\Delta x = 2$ µm. Symmetry boundary conditions are applied along the $y = 0$ and $z = 0$ planes, effectively reducing the computational domain to a quarter of the cross-sectional area, resulting in a total of 462,500 cells. Wall boundary conditions are enforced at $y = 76$ µm and $z = 50$ µm.
An inlet boundary condition is specified at $x = 0$ with a constant liquid water velocity $u_l = 0.3$ m/s and a liquid temperature $T_l = 102$°C. An outlet boundary condition is set at $x = 1$ mm, with an outlet pressure $P_{out} = 1$ bar.
The computational domain is initialized with a gas bubble in a superheated liquid. The bubble's center is positioned at (150,0,0) µm with an initial diameter of $d_0 = 200$ µm. The liquid temperature is maintained at $T_l = 102$ °C. The initial conditions are illustrated in Figure 6.4. A constant time step of $\Delta t = 10^{-7}$ s is employed throughout the simulation, and a contact angle of $30°$ is imposed at the walls.

6.2.2.2 1D data setting

In the 1D simulation, the computational domain mirrors that of the 3D simulation but is meshed only in the x direction, with 500 cells each having a size of $\Delta x = 2$ µm. The inlet and outlet boundary conditions remain consistent with those in the 3D simulation. Symmetry boundary conditions are applied along the y and z directions, as pressure loss is accounted for by a momentum source term. The same initial conditions are applied for both the liquid and gas phases as used in the 3D simulation. The 1D case is similar to a Sucking/Stefan case, with the inclusion of an inlet condition and a pressure loss correlation.

6.2.3 Numerical results

The numerical results for the 3D and 1D simulations are presented in Figure 6.5 at $t = 1$ ms. The position of the back of the bubble is the same for both simulations, indicating that the bubble velocity is identical in both the 3D and 1D cases. However, there is a notable difference in the size of the bubble: it is significantly larger in the 3D simulation compared to the 1D simulation. This discrepancy is quantitatively illustrated in Figure 6.6, where the equivalent bubble radius is approximately 10% smaller in the 1D simulation after 1 ms.
It is important to note the significant difference in computational cost between the 1D and 3D approaches. The 1D approach requires only one processor, with a computational speed of 0.04 seconds per iteration. In contrast, the 3D approach necessitates 96 processors, with a computational speed of 2.9 seconds per iteration. While the number of processors needed for a 3D study on a small length is manageable, the 3D computations are over 70 times slower.

6.3 Second upscaling approach: corrective coefficient for wettability

The previous section as well as section 4.3.3 demonstrated that wettability significantly impacts heat and mass transfer in microchannels. This is because wettability affects both the interfacial area between the

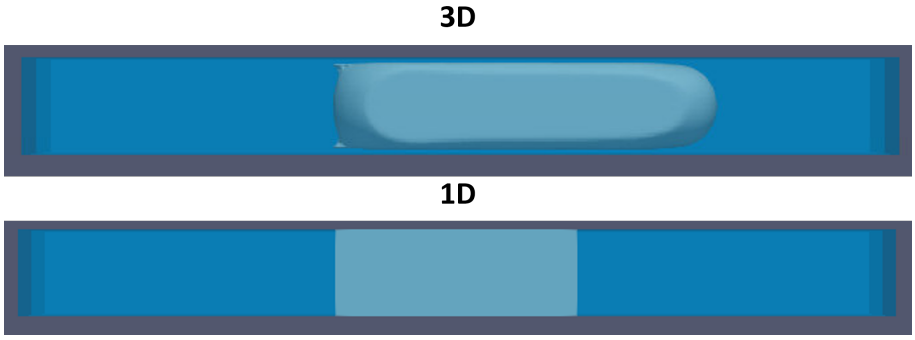

Figure 6.5: View of the bubble at $t = 1$ ms. The top picture represents the 3D simulation while the bottom picture is the 1D simulation.

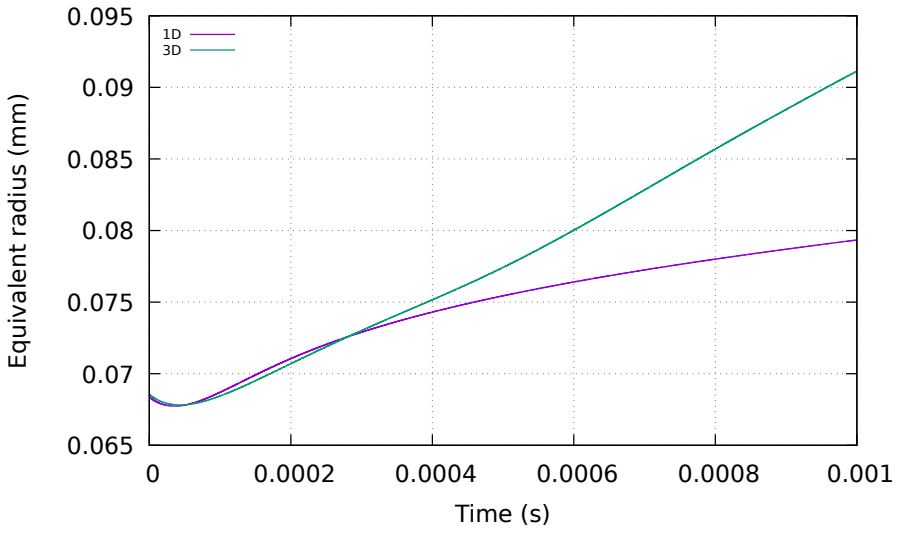

Figure 6.6: Evolution of the equivalent bubble radius over time for the 1D and 3D simulations. The equivalent bubble radius was defined in a previous section by equation 3.18.

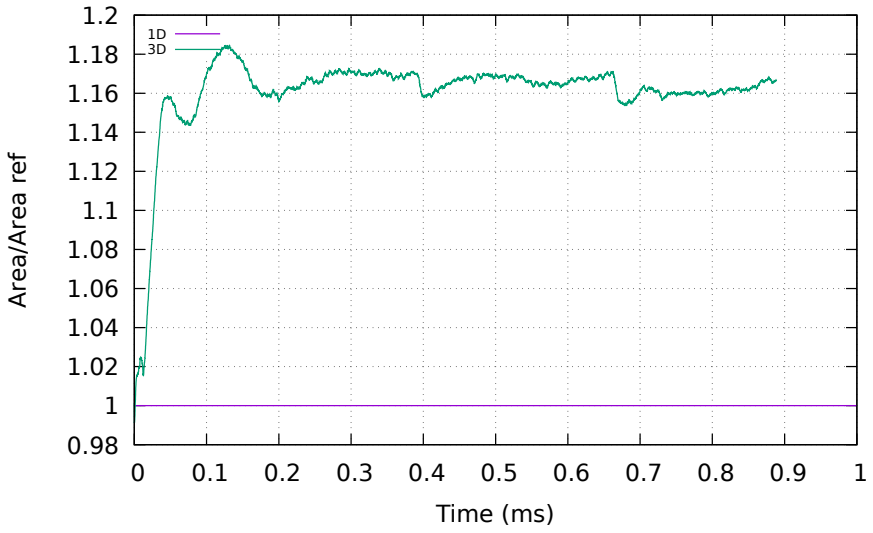

Figure 6.7: Evolution of the interfacial area over time. The reference interfacial area A_0 represents the section of the microchannel.

liquid and the bubble and the velocity around the bubble's nose. In both cases, it was shown that using a contact angle of 90° (or employing a 1D approach, which is effectively the same) instead of a contact angle of 30° led to a 100% underestimation of the boiling rate. To address this discrepancy in the second upscaling approach, a corrective coefficient K_{wet} is introduced into the mass transfer computation.

6.3.1 Heat and mass transfer in a slug bubble

One potential explanation for the difference in boiling rates between the 1D and 3D computations could be the difference in interfacial area at the bubble nose, as a curved interface typically has a greater area than a planar one. However, plotting the interfacial area over time for both the 1D and 3D cases revealed that the difference is actually quite small, approximately 20%, as shown in Figure 6.7.
Additional observations revealed that the discrepancy in boiling rates between the 1D and 3D simulations is actually due to the velocity of the water around the bubble slug. In the 1D model, both the gas and bubble velocities are constant across the microchannel, with $u_{1D} = 0.3$ m/s. In contrast, the 3D simulation captures a liquid film at the channel corners, where the velocity at the interface between the liquid and the bubble can exceed $u_{3D} = 1$ m/s. This increased local velocity significantly enhances heat and mass transfer, contributing to the observed differences.

A wetting coefficient K_{wet} was added to the Mucellphage model to account for these differences. The interfacial heat transfer term is computed using equation 6.8.

$$\Pi'_k = -K_{wet} \frac{\lambda_k \nabla T_k A_{int}}{V_{cell}} \tag{6.8}$$

Different values of K_{wet} were tested on several cases using the 1D and 3D data settings presented in section 6.2.2.2 with inlet velocities ranging between u_{in} = 0 m/s and u_{in} = 0.3 m/s. The best value of K_{wet} was found to be K_{wet} = 2. The evolution of the bubble radius over time is given for the 3D model and the 1D model with a corrective coefficient in Figure 6.8a for an inlet velocity u_{in} = 0 m/s, and in Figure 6.8b for an inlet velocity u_{in} = 0.1 m/s. The difference on the boiling mass flow rate between the 1D approach, and the 3D coefficient is less than 30%, which is acceptable.

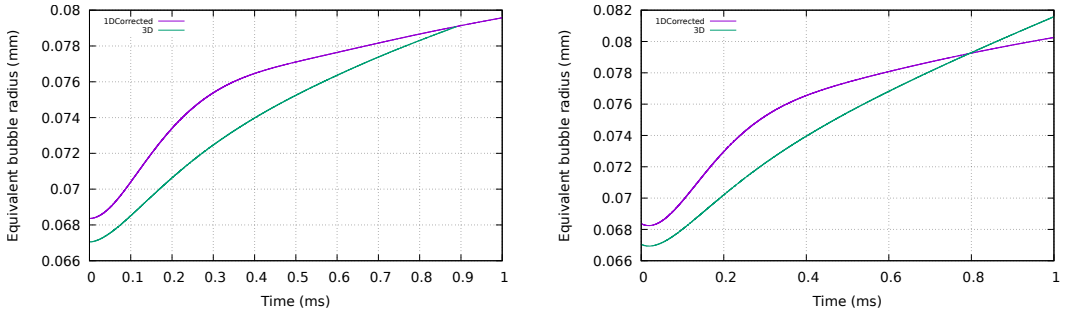

(a) Evolution of the bubble radius over time in the case $u = 0$ m/s.

(b) Evolution of the bubble radius over time in the case $u = 0.1$ m/s.

Figure 6.8

Remark 6.3.1. The coefficient $K_{wet} = 2$ presented in this section was only validated for hydraulic diameters $D_h < 100$ µm, Reynolds numbers $\mathrm{Re} < 100$ and Nusselt numbers between 5 and 50. A general coefficient would probably be a function of the Reynolds number and of the bubble length L_b. Such a coefficient would however require extensive calibration and validation.

6.3.2 Validation on a LEGI slug case

This model was tested on case D from the experimental campaign (see section 5.7.2). In this case, the pressure difference between the inlet and the outlet is $\Delta P = 1$ bar, and the wall temperature is $T_w = 109°\mathrm{C}$.

The case is simulated using a 1D channel because the cost of a 3D computation would be prohibitive. The dimensions of the channel are 750,000 µm × 128 µm × 100 µm. An inlet condition is imposed at $x = 0$ m, and an outlet condition is imposed at $x = 0.75$ m. The other boundaries are treated as walls as explained in the previous section. The grid size in the x direction is $\Delta x = 2.5$ µm.

A bubble with a length $L_b = 7$ mm is initialized at $x = 450$ mm, similar to the experimental setup. Water is initialized at its saturation temperature T_{sat} elsewhere. Saturated water is injected at a velocity of $u = 0.25$ m/s at the inlet, and the outlet pressure is set at $P_{out} = 1$ bar.

To simulate the wall heat transfer, a volume thermal source term $\varphi_v = \varphi_w A/V$ [W/m^3] was implemented, equivalent to a surface heat flux $\varphi_w = 50$ W/m^2 applied to the cells with a liquid temperature $T_l < 110°\mathrm{C}$. The methodology presented in the previous section is applied to this case, incorporating the Kreutzer law for pressure loss and the Mucellphage model with a corrective coefficient $K_{wet} = 2$. The results are presented in Figure 6.9. The points represent the experimental data, the red line represents the results of the 1D model without the corrective coefficient, and the green line represents the results of the 1D model with $K_{wet} = 2$. The results given by the 1D model with the corrective coefficient are acceptable, with an error of roughly 35% on the bubble length at the outlet. The growth rate is overestimated at the start of the microchannel and underestimated at the end of the microchannel, similar to the calibration case.

As for the presure loss, the 1D model predicts an inlet pressure $P = 1.8$ bar instead of the experimental value $P = 2$ bar.

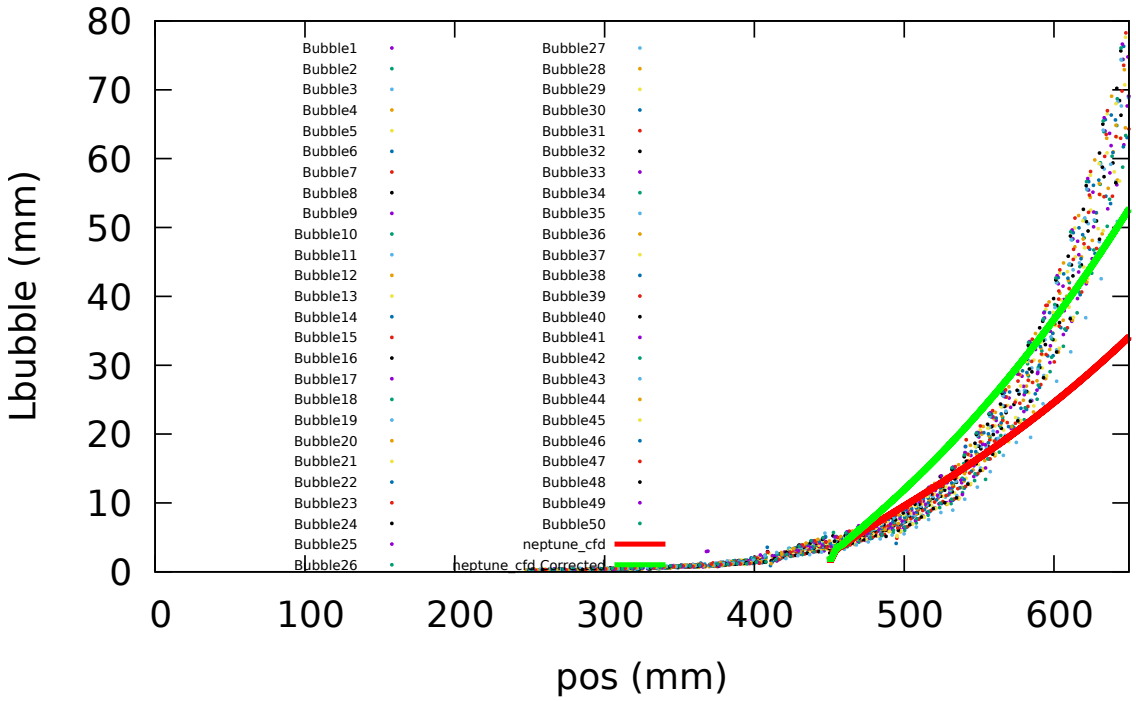

Figure 6.9: Evolution of the bubble length as a function of the position in case D. The points represent the experimental data, the red line represents the results of the 1D model without the corrective coefficient. Finally, the green line represents the results of the 1D model with $K_{wet} = 2$.

6.4 Conclusion

This chapter presented a method to transition from a 3D approach to a significantly less computationally intensive 1D approach. The method is based on the Kreutzer law to compute the pressure drop. The Kreutzer law has been shown to provide accurate results, with only a marginal loss in accuracy due to this simplification.

For heat and mass transfer, the Mucellphage model tends to underestimate phase change due to its inability to account for 3D effects like wettability. To address this, a new approach was proposed, incorporating a corrective coefficient, K_{wet}, into the interfacial enthalpy source term. We found that using $K_{wet} = 2$ provided acceptable results for microchannel flows at low Reynolds numbers, with an error of about 30% in the final bubble radius. However, his coefficient K_{wet} is only valid for the conditions $D_h < 140$ µm, $\mathrm{Re} < 100$ and $5 < \mathrm{Nu} < 50$. Future studies will be necessary to generalize the value of this coefficient.

CHAPTER 7

Industrial results

Summary

In this chapter, we demonstrate that, based on the findings from previous chapters, two-phase flow effects in the cracks of failed nuclear fuel rods are minimal. This allows for a simplified approach to modeling the fluid dynamics within these cracks, specifically by representing the flow as single-phase vapor flow. Leveraging this simplification, we have developed an efficient 0D (zero-dimensional) industrial model capable of simulating the drying process of a failed rod in under a minute.

Using this model, we constructed tables that provide estimated drying times as a function of two key parameters: the width of the crack and the residual heat power within the transport cask. These tables will be employed by the Direction du Combustible Nucléaire (DCN)—the engineering team responsible for transporting failed rods—as an operational tool to address drying and transport concerns for these components.

Sample	ΔP (bar)	T_w (°C)
A	1	125

Table 7.1: Experimental conditions in the drying case.

7.1 Two-phase effects are marginal

The goal of this section is to demonstrate that two-phase effects are negligible in the industrial scenario for heat flux applied to the cracks greater than $\varphi = 3000$ W/m^2, which corresponds to a residual transport cask heat power $Q = 10kW$. This is because water boiling in the cracks occurs rapidly, and the water exiting the rod plenum evaporates almost instantly. In section 7.1.1, we prove this result using the 1D upscaling model presented in the previous chapter. Section 7.1.2 backs this conclusion through experimental considerations. Finally, section 7.1.3 uses analytical considerations to show that the flow in the cracks of failed rods can be simplified by a single-phase vapour flow.

7.1.1 Numerical considerations: drying of a microchannel

The 1D model presented in this previous chapter was applied to a microchannel representing a crack with a width $e = 20$ µm in the uranium pellets. The computational domain has a dimension $20 \times 25,000 \times 4,000,000$ µm with a cell size $\Delta x = 5$ µm along the z axis, resulting in 800,000 cells. This cell size is probably not enough to reach mesh convergence, therefore interface boiling is underestimated. However, computations with a finer mesh were not possible for numerical stability reasons. An inlet boundary condition is defined at $x = 0$ with a mass flow rate $\dot{m} = 1$ g/d of liquid water at the saturation temperature T_{sat} of the inlet. The plane $x = 4$ m is an outlet with a pressure condition set at $P_{out} = 10$ mbar to match the industrial conditions. A symmetry boundary condition is applied to the other boundaries as explained in chapter 6. A volumic thermal source term corresponding to a heat flux $\varphi = 10$ kW/m^2 is applied in every cell to take thermal effects into account. To model pressure loss, the Muskat-Poiseuille law presented in equation 5.13 and validated for single-phase vapour flows is implemented in the momentum source term $\underline{TS}_k$ with the method described in section 6.2.1.
A liquid/vapour front is initially set at $x = 30$ cm from the inlet with $\alpha_l = 1$ if $x < 30$ cm, and $\alpha_g = 1$ else, and the computation was run for 1 ms. We observed that the liquid/vapour front moved toward the inlet, indicating the drying of the channel and a single-phase vapour flow for $x > 30$ cm.

7.1.2 Experimental considerations: drying of a microchannel

In the experimental campaign described in the previous chapter, several cases demonstrated complete drying of the microchannel. For example, under the conditions listed in Table 7.1, the channel was fully dried by the end of the first subchannel ($L = 4$ cm). A temperature difference of $\Delta T = 0.72$°C was measured between the bottom and top thermocouples (T_2 and T_1 in Figure 5.4). Given that the thermal conductivity of aluminum is $\lambda = 237$ W/m/K and the distance between the thermocouples is 18 mm, the heat flux received by the microchannel can be estimated as $\varphi = \lambda \nabla T = 9480$ W/m^2.

Remark 7.1.1. As discussed in section 5.3.2, a significant portion of the heat flux is dissipated through various mechanisms. Consequently, the actual heat flux within the microchannel is substantially lower than the estimated 9480 W/m^2.

The Reynolds number (Re) in the experiment is higher than in the industrial drying of failed rods. Additionally, the area-to-volume ratio (A/V) is smaller in the experimental setup. As a result, a heat flux of $\varphi = 10,000$ W/m^2 leads to quicker drying in the industrial scenario compared to the experimental

case. Therefore, it is reasonable to assume that the cracks in the failed rods will be fully dried after just a few centimeters.

7.1.3 Analytical considerations: drying of a microchannel

The gas volume fraction $\alpha(x,t)$ in a microcrack varies with time and position. However, as demonstrated in Figure 5.22a from the experimental chapter, it is possible to calculate a time-averaged gas volume fraction $\alpha(x)$ within the microchannel. This section proposes an analytical method to achieve this calculation, based on the following assumptions:

- The flow regime is steady, which is valid for the drying of a failed rod that occurs over several hours or days. Therefore $\dfrac{\partial \alpha_l(x)}{\partial t} = 0$.
- The liquid density ρ_l remains constant spatially and throughout the process.
- The liquid velocity u_l changes slowly in the flow direction compared to the volume fraction α_l. This implies that $\dfrac{\partial(\alpha_l u_l)}{\partial x} = u_l \dfrac{\partial \alpha_l}{\partial x}$.
- The heat flux φ is constant in the microchannel. Therefore, the mass source term can be expressed as $-\Gamma_l = -\dfrac{\Pi'}{h_{lat}} = -\dfrac{\varphi S}{V_{cell} h_{lat}}$.

These assumptions are developped in more detail and challenged in the PhD thesis of Kledy (2018).
The liquid mass balance is described by equation 7.1. Given the assumptions outlined above, this equation simplifies to equation 7.2.

$$\frac{\partial \alpha_l \rho_l}{\partial t} + \frac{\partial(\alpha_l \rho_l u_l)}{\partial x} = \Gamma_l \tag{7.1}$$

$$\frac{\partial \alpha_l}{\partial x} = -\frac{\varphi S}{V h_{lat} \rho_l u_l} \tag{7.2}$$

The total evaporation of water takes longer in larger cracks due to the reduced area-to-volume ratio. Therefore, we consider the worst-case scenario with a crack width $e = 20$ µm. In this scenario, we have:

- Heat flux $\varphi = 10000$ W/m^2
- Surface area $S = 2(eL + bL) = 0.2$ m^2
- Volume of the channel $V = ebL = 2 \times 10^{-6}$ m^3
- Mass flow rate $\rho_l u_l A_{section} = 3$ g/d, hence $\rho_l u_l = 0.07$ kg/m^2/s

This leads to the following volume fraction gradient:

$$\frac{\partial \alpha_l}{\partial x} = -10.6 \text{ m}^{-1} \tag{7.3}$$

This means the liquid volume fraction decreases from 1 to 0 within 1/10.6 meters (less than 10 cm). Consequently, two-phase flow occurs only in the first 10 centimeters of the crack, with single-phase gas flow dominating for the remaining 3.9 meters. Applying similar reasoning as detailed in Appendix B for rarefaction, it can be concluded that two-phase effects are minimal.

7.2 The 0D drying model

With the single-phase simplification, it is possible to build a 0D model to simulate the drying of failed rods in less than a minute. This section presents the 0D model and some validation of its results.

7.2.1 Presentation of the 0D model and numerical scheme

7.2.1.1 Numerical scheme

The drying process of a failed fuel rod encompasses two coupled phenomena: the boiling of liquid water in the plenum and the two-phase flow occurring within the cracks of the uranium pellets. In this model, the boiling of liquid in the plenum is addressed using a 0D approach, while the flow within the cracks is resolved with the Muskat-Poiseuille law.
Figure 7.1 is a schematic view of a failed fuel rod (plenum + crack), as modeled by the 0D model. It is defined by:

- Geometric parameters of the plenum, namely $r = 4.18$ mm the internal radius of the plenum, and h_{pl}, the height of the plenum (18.9 mm for new rods but it is usually smaller for irradiated rods).
- Geometric parameters of the cracks. As explained in section 0.2.3, a crack is defined by its equivalent width e (between 6.3 and 30 µm), by its axial length L (around 3.6 m), and by its equivalent radial length b (25 mm).
- The mass of liquid water at iteration k, m^k.
- The height of the liquid water at iteration k, h^k.
- The pressure in the plenum at iteration k, P^k.
- The number of moles of vapour in the plenum at iteration k, n^k.

Remark 7.2.1. Representing the complex network of cracks in the uranium pellets with an equivalent crack may initially raise doubts. However, in microfluidics, singular head losses, and hence tortuosity, are often negligible. This can be demonstrated by a straightforward order of magnitude analysis. Singular head losses are calculated using equation 7.4, whereas regular head losses are computed using equation 7.5.

$$\Delta P_{sing} = \Lambda \frac{\rho u^2}{2} \tag{7.4}$$

Λ is equal to 1 for an elbow.

$$\Delta P_{reg} = \frac{32 \mu L}{D_h^2} u \tag{7.5}$$

For a vapour flow at $u = 1$ m.s^{-1} in cracks with an hydraulic diameter $D_h = 40$ µm at atmospheric pressure, ΔP_{sing} = 0.3 Pa and $\Delta P_{reg} = 8 \times 10^5$ Pa. Consequently, the pressure drop induced by tortuosity is negligible, even for thousands of elbows. This finding is consistent with the results reported in Davy (2022).

The numerical scheme is presented in Figure 7.2. In the initial step, we simulate the boiling of the water between the iterations k and $k + 1$. Due to the heat flux φ_{pl}, a mass m_{ev} evaporates, causing a decrease in the mass of liquid m^{k+1} and the liquid height h^{k+1}. This mass transfer results in an increase in the amount of vapour $n_v^{k+1,i}$ and the pressure $P^{k+1,i}$.
In the second step, the head loss law for the cracks calculates the mass flow rate, determining m_{fiss}, the mass of vapour removed from the plenum during iteration $k + 1$. This vapour removal leads to a reduction in the amount of vapour n^{k+1} and a decrease in the pressure P^{k+1}. Figure 7.3 illustrates the numerical scheme of the 0D model for a single iteration.

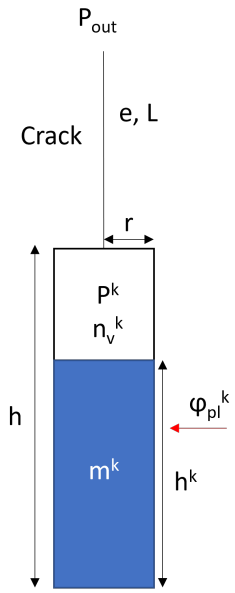

Figure 7.1: 0D modelling of a failed fuel rod.

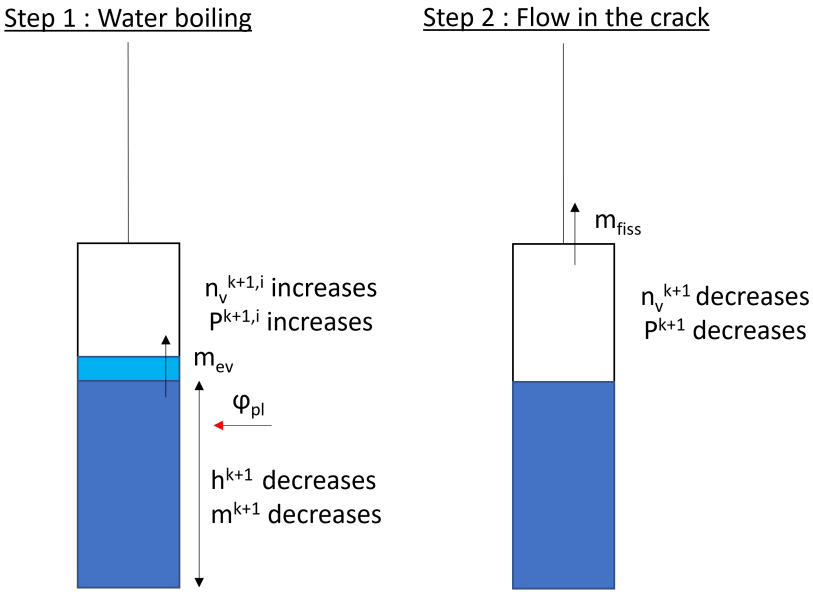

Figure 7.2: Picture of the numerical scheme of the 0D model.

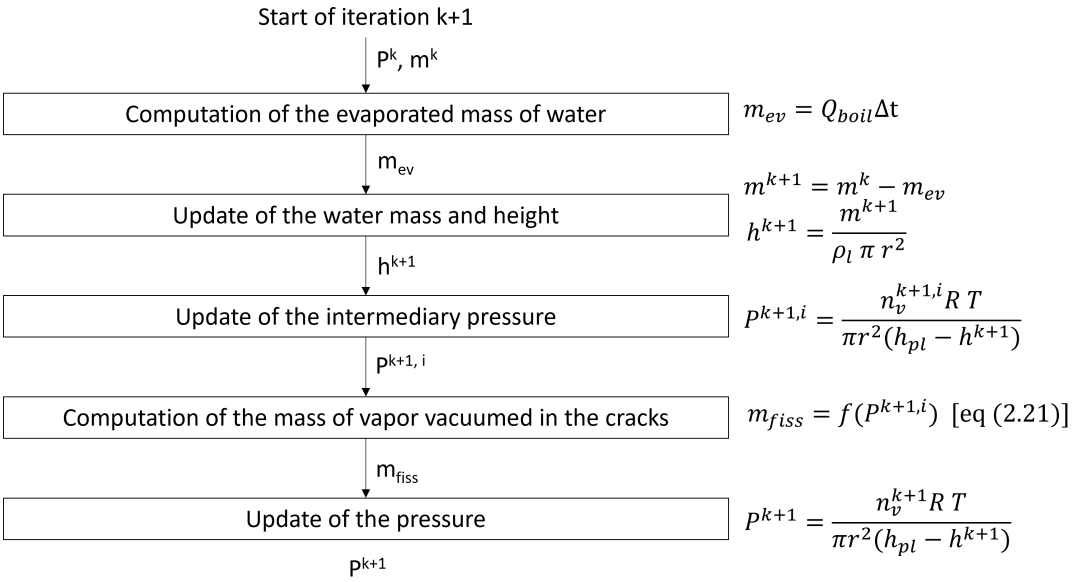

Figure 7.3: Numerical scheme of the 0D model for one iteration.

Remark 7.2.2. To update the intermediary pressure, the ideal gas law $PV = nR_{gas}T$ is used. The volume V of vapour in the plenum at iteration $k+1$ is $V = \pi r^2(h_{pl} - h^{k+1})$, hence the intermediary pressure $P^{k+1,i}$.

$$P^{k+1,i} = \frac{n_v^{k+1,i} RT}{\pi r^2 (h_{pl} - h^{k+1})} \tag{7.6}$$

The same method is applied to compute P^{k+1}.

Remark 7.2.3. The numerical scheme presented in Figure 7.3 also requires the modelling of Q_{boil} and of m_{fiss}. The computation of these two values is presented in the following sections.

7.2.1.2 Computation of Q_{boil}

Computation of φ_{pl} An industrial safety study conducted at EDF R&D by Didier Colmont in 2022 provides a correlation giving the heat flux applied to the plenum of a rod φ_{pl} [W.m^{-2}] as a function of the residual heat power of the transport cask Q [kW]. The knowledge of this heat flux is necessary to compute Q_{boil}, and presented in equation H.6.

$$\varphi_{pl} = (0.707 + 0.0129Q)(82.167 + 5.317Q - 0.0367Q^2 - T_{pl}) \tag{7.7}$$

T_{pl} is the temperature of the plenum. This correlation gives an error smaller than 10% compared to the numerical simulations for residual heat powers Q between 6 and 48 kW.

Remark 7.2.4. The correlation presented above is only valid for assemblies placed in the middle of the transport cask. Assemblies placed near the walls of the transport cask are too cold to be dried in a reasonable time. More details about how this correlation was obtained are provided in Appendix H.

Computation of Q_{boil} from φ_{pl} The computation of the boiling mass flux Q_{boil} requires additional assumptions.
A first assumption is that the liquid water inside the failed rod and the rod cladding are the same temperature. This assumption is justified through Thom's correlation (equation 7.8), which provides an approximation for the wall superheat $\Delta T = T_w - T_{sat}$ needed to initiate nucleate boiling. In the scenarios discussed in this chapter, Thom's correlation indicates that nucleate boiling occurs when the wall superheat exceeds 1°C.

Remark 7.2.5. The correlation of Thom provides the wall superheat necessary for the onset of nucleate boiling under conditions where the nucleate boiling predominates over forced convection.

$$T_w - T_{sat} = 22.5\varphi^{0.5} \exp\left(-\frac{P}{8.7}\right) \tag{7.8}$$

with φ the heat flux in MW/m^2 and P the pressure in MPa.

A second assumption is that the total heat flux on the plenum can be split in two terms: the sensitive heat flux φ_{sensi} and the latent heat flux φ_{boil}.

$$\varphi_{pl} = \varphi_{sensi} + \varphi_{boil} \tag{7.9}$$

This assumption is true for saturated pool boiling.
Under these two assumptions, we define a sensible heat flux φ_{sensi} and a liquid temperature T_l:

$$\varphi_{sensi} = \frac{\rho_l r c_p}{2\Delta t}(T_{sat} - T_l) \tag{7.10}$$

Remark 7.2.6. Δt is the numerical time step. A time step of 0.1 s is taken for the simulations presented in this chapter. It was shown that there is no time step sensitivity with this value.

1. If the liquid is below saturation at the end of the iteration ($T^{k+1} < T_{sat}$), all the heat is used to heat the liquid. Therefore $T_l^{k+1} = T_l^k + \dfrac{2\varphi_{pl}\Delta t}{\rho_l r c_p}$ and $\varphi_{boil} = 0$.
2. Else $\varphi_{boil} = \varphi_{pl} - \varphi_{sensi}$ and $T_l^{k+1} = T_{sat}$.

Finally, the boiling mass flux Q_{boil} can be written as a function of the latent heat flux. h_{lat} is the latent heat of water.

$$Q_{boil} = \frac{\pi r^2 \varphi_{boil}}{h_{lat}} + \frac{2\pi r h^k \varphi_{boil}}{h_{lat}} \tag{7.11}$$

7.2.1.3 Computation of m_{fiss}

The previous section showed that the flow in uranium cracks can be represented by a single-phase vapour flow. In these conditions, equation 7.12 describes the 4$^{\text{th}}$ step in Figure 7.3.

$$m_{fiss} = \frac{e^3 bM}{24\mu LRT}((P^{k+1,i})^2 - P_{out}^2)\Delta t \tag{7.12}$$

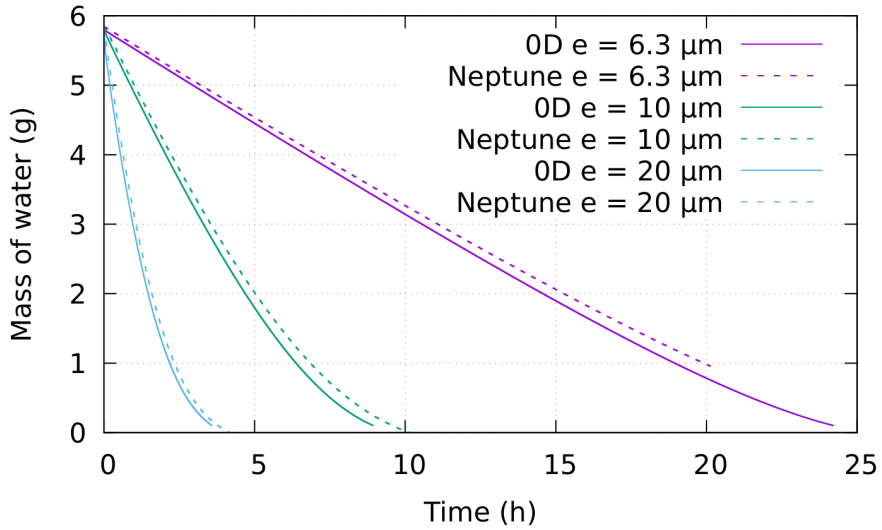

Figure 7.4: Evolution of the mass of water in the plenum and comparison of the results of the 0D model (continuous lines) with the results of neptune_cfd (dash lines).

7.2.2 Numerical results

7.2.2.1 Numerical verification of the 0D model

To validate the numerical scheme presented in the previous section, the results of the 0D model are compared to the results of neptune_cfd, a multiphase CFD code developed by EDF R&D and presented in detail in chapter 1.
In this case, a cylinder with a radius $R = 0.5$ cm and a height $h = 15$ cm is filled with $h_0 = 10.5$ cm of saturated liquid water at $P = 15$ bar. A negative inlet condition is applied at the top of the plenum to vacuum the vapour using the Poiseuille law (equation 7.12) for a crack widths e of 6.3, 10, and 20 µm, and the same heat flux as in the 0D model is applied to the walls. Figures 7.4 and 7.5 show the evolution of the mass of water and of the pressure with the 0D and CFD models. The computations with the 0D model stop when the liquid mass in the plenum is smaller than 0.1 g, while the neptune_cfd simulations either stop when the plenum is fully dried or when the computational times is greater than 3 days. The results are very similar, with differences always smaller than 5%. Therefore, the 0D model is validated and predicts the physical phenomena correctly.

Remark 7.2.7. It should be noted that the 0D model runs in less than ten seconds, while neptune_cfd needs about three days to simulate 20 hours of drying.

7.2.2.2 Sensitivity studies

Sensitivity studies were conducted with the 0D model to estimate the impact of the crack width and of the residual heat on the drying of failed rods. The plenum is modeled by a cylinder with a radius $R = 0.5$ cm and a height $h = 25.5$ cm initially filled at 90% with liquid water. This differs from the real size of the plenum ($h \approx 15$ mm) to get a total volume of 20 cm^3, which is the maximum volume of water in a failed rod. The crack width is varied from $e = 6.3$ µm to $e = 20$ µm because section 0.2.3 shows that these are the most realistic values for irradiated rods. The residual heat power of the transport cask varies from 6 to 48 kW. The evolution of the mass of water in the plenum over time is plotted in Figures 7.6 and 7.7 for different crack widths and different residual heat powers. It shows that both parameters have a very strong impact on the drying time of failed rods. For instance, the drying of a rod with a crack width

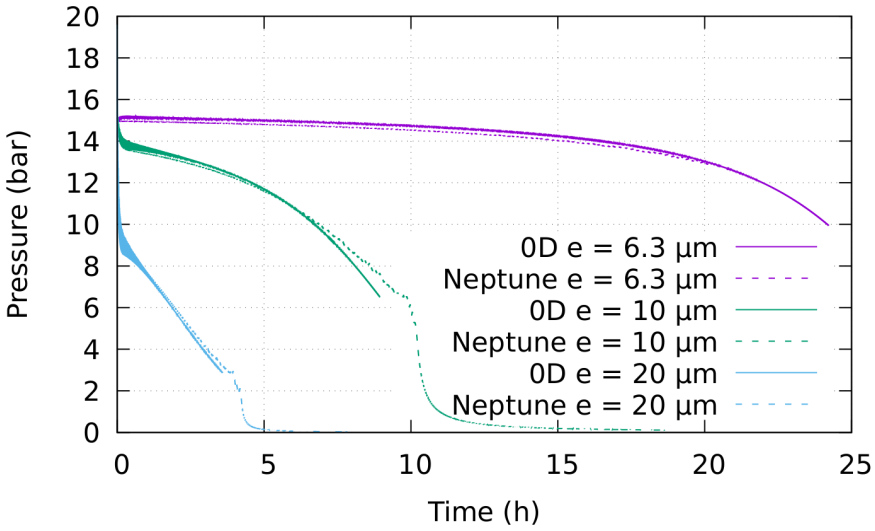

Figure 7.5: Evolution of the pressure in the plenum and comparison of the results of the 0D model (full lines) with the results of neptune_cfd (dash lines).

$e = 6.3$ µm is four times slower than the drying of a rod with a crack width $e = 20$ µm. The impact of the residual heat power Q is even more important. In a transport cask with $Q = 48$ kW, the drying is about 30 times faster than in a transport cask with $Q = 6$ kW.

Remark 7.2.8. In this chapter, the drying time is the time necessary to remove 99% of the water present initially present in a failed rod. It differs from the drying time presented in table 7.4, which is the drying time necessary to remove 95% of the water present in a failed rod.

7.2.2.3 Evaluation of the importance of the latent heat

In some of the previous studies on the drying of failed rods, the authors neglected the latent heat of the water and assumed that the pressure in the plenum P_{pl} is equal to the saturation pressure at the asymptotic temperature of the plenum $P_{sat}(T_{pl,asymptotic})$. Under this assumption, the drying time can be estimated directly from the Poiseuille law (equation 7.13), without a 0D model.

$$\Delta t = \frac{\frac{e^3 bM}{24 \mu LRT}((P_{sat}(T_{pl,asymptotic}))^2 - P_{out}^2)}{m_{liq}} \tag{7.13}$$

m_{liq} is the mass of liquid contained in the failed rod.
Table 7.2 gives the drying times for a failed rod in a transport cask with a residual power $Q = 24$ kW. The first line gives the drying time computed with the 0D model and plotted in Figure 7.6. The second line gives the drying time computed with the Poiseuille law, neglecting the latent heat of the liquid water. It shows that the second method heavily underestimates the drying time. This is especially an issue for the larger cracks, because the heat flux applied to the plenum is not sufficient to vaporize enough water to keep the pressure at its maximum level. Therefore, the latent heat of the liquid should not be neglected.

7.2.3 Conclusion

A 0D model was developed in Python to simulate the drying of failed fuel rods, several qualitative conclusions can still be drawn:

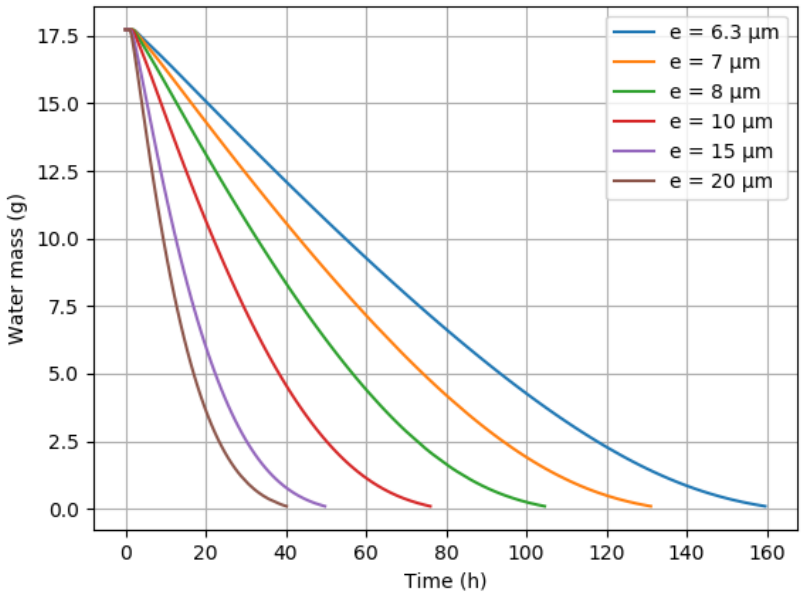

Figure 7.6: Evolution of the mass of water in the plenum over time for $Q = 24$ kW. The crack width e is varied from 6.3 to 20 µm.

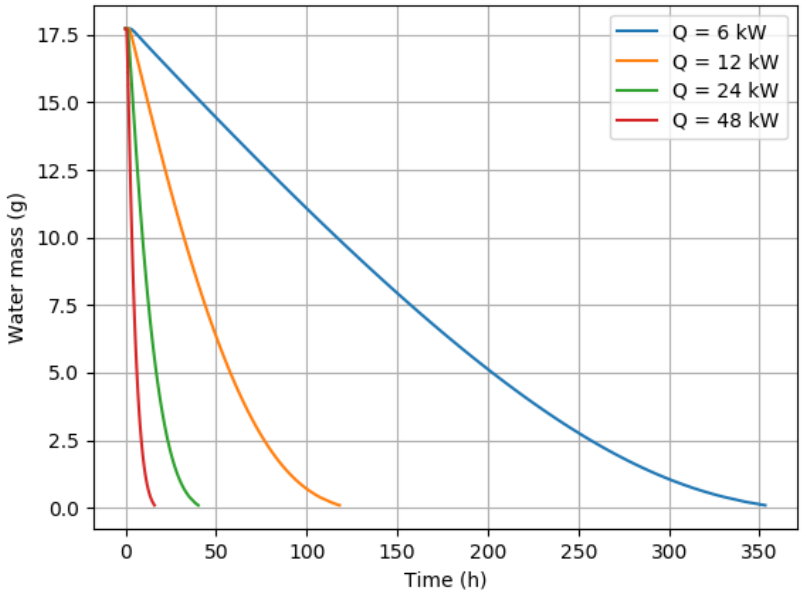

Figure 7.7: Evolution of the mass of water in the plenum over time for $e = 20$ µm. The residual heat power varies from 6 to 48 kW.

	e = 20 µm	e = 15 µm	e = 10 µm	e = 8 µm	e = 6.3 µm
Drying time with the 0D model (h)	40.2	49.8	76.0	104.6	159.6
Drying time with the Poiseuille law (h)	3.7	8.8	29.6	57.7	118.2

Table 7.2: Drying time at $Q = 24$ kW with the 0D model and with the Poiseuille law.

- The drying process is notably influenced by the width of the cracks, with drying occurring approximately four times faster in larger cracks compared to smaller ones.
- Residual heat within the transport cask significantly impacts the drying process, with drying rates approximately 30 times faster under a residual heat of 48 kW compared to 6 kW.
- Given the substantial energy required for liquid water vaporization, the latent heat of water cannot be disregarded. Consequently, a 0D model is indispensable for representing boiling in the plenum.

For orders of magnitude of mass flow rates, velocities, pressures, and temperatures, Table 7.3 provides an overview of their expected values for a single-phase gas flow.
This 0D model was presented at PATRAM22, an international conference dedicated to the transportation of radioactive materials. The conference paper can be found in Appendix I.

(e (µm), Q (kW))	(20, 48)	(20, 24)	(6.3, 24)	(6.3, 48)
Mass flow rate (g/h)	1.5	0.5	0.125	0.6
Liquid velocity (m/s)	8.0×10^{-4}	2.8×10^{-4}	2.2×10^{-4}	1.1×10^{-3}
Pressure in the plenum (bar)	10	5	12	28
Heat flux (W/m^2)	1250	625	625	1250
Temperature (°C)	180	152	188	230

Table 7.3: Order of magnitude of the properties of the flow in the cracks of failed rods.

7.3 Industrial table

This section presents a table giving the drying time of failed rod as a function of the relevant parameters from the results obtained with the 0D model. To do that, 99 simulations were performed, covering 9 reference crack widths and 11 different thermal conditions. For each crack width, drying times at 50% (t_{50}) and 95% (t_{95}) were calculated. These values represent the time required to remove 50% and 95% of the water from a failed rod, respectively. The results from these simulations are detailed in Table 7.4 and Table 7.5.
Plotting the drying time as a function of crack width and residual heat yields a surface plot. Initially, this surface was approximated using a two-variable polynomial function. However, this approach proved inadequate, with maximum relative errors reaching up to 60%. To improve accuracy, the "LinearNDInterpolator" function from Python was employed. This method constructs a piecewise linear approximation by creating triangles between adjacent data points. The resulting approximation for t_{95} is shown in Figure 7.8.

Power (kW) / Crack width (µm)	6.3	7	8	10	12	14	16	18	20
6	6188.4	4564.4	3087.0	1639.8	997.6	669.1	482.5	368.3	294.0
8	3224.9	2381.4	1631.5	886.4	554.4	383.3	285.4	224.7	184.7
12	1085.5	814.4	572.7	330.9	221.4	163.5	129.4	107.6	92.6
16	459.9	352.9	257.0	159.5	114.2	89.3	74.2	64.2	57.0
20	233.4	183.8	139.0	92.4	70.0	57.2	49.2	43.7	39.6
25	121.3	98.7	77.9	55.6	44.3	37.7	33.3	30.3	28.0
30	74.0	61.9	50.6	38.1	31.5	27.5	24.8	22.8	21.4
35	50.6	43.3	36.3	28.4	24.1	21.4	19.5	18.2	17.2
40	37.6	32.7	28.0	22.5	19.4	17.5	16.1	15.1	14.4
45	29.7	23.5	22.8	18.7	16.3	14.8	13.8	13.0	12.4
48	26.5	23.5	20.5	17.0	15.0	13.6	12.7	12.0	11.5

Table 7.4: Drying time at 95% (h) as a function of the crack width and of the residual heat power of the transport cask.

Power (kW) / Crack width (µm)	6.3	7	8	10	12	14	16	18	20
6	2822.8	2064.2	1390.1	721.9	426.6	276.6	192.1	141.1	108.5
8	1459.2	1069.8	723.8	380.9	229.2	152.0	108.5	82.0	64.9
12	479.1	354.4	243.7	134.0	85.1	59.9	45.4	36.3	30.3
16	195.9	147.2	104.0	60.7	41.2	30.8	24.7	20.7	17.9
20	95.4	73.3	53.5	33.5	24.1	19.0	15.8	13.7	12.1
25	47.2	37.5	28.6	19.3	14.8	12.2	10.5	9.3	8.4
30	27.8	22.7	18.0	12.9	10.3	8.8	7.7	7.0	6.4
35	18.4	15.5	12.6	9.5	7.8	6.8	6.1	5.5	5.1
40	13.5	11.5	9.6	7.5	6.3	5.5	5.0	4.6	4.3
45	10.5	9.1	7.8	6.2	5.3	4.7	4.3	3.9	3.7
48	9.4	8.2	7.0	5.6	4.8	4.3	3.9	3.7	3.4

Table 7.5: Drying time at 50% (h) as a function of the crack width and of the residual heat power of the transport cask.

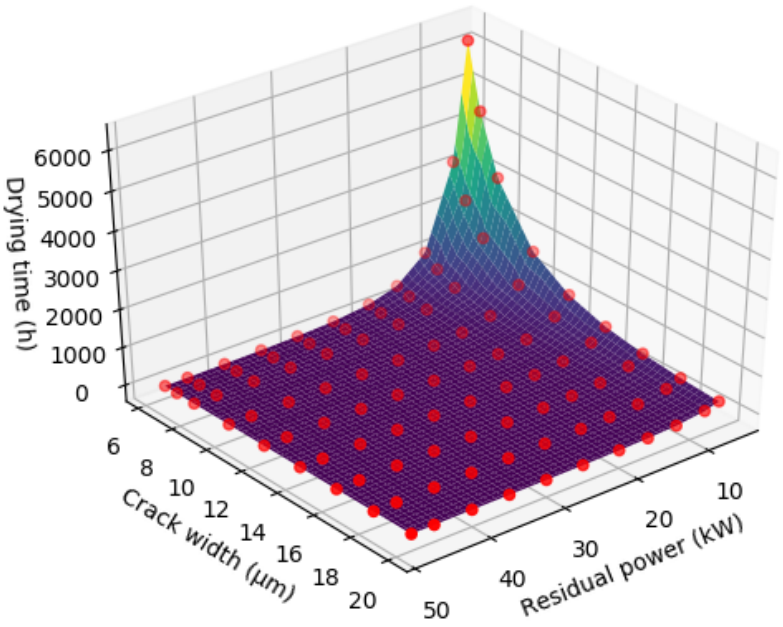

Figure 7.8: Drying time at 95% as a function of the residual heat power and of the crack width. The red dots represent the data from the 0D model. The surface was obtained with a linear interpolation by part. However, this figure is intended for illustrative purposes only. EDF operational units are advised to rely on the provided tables for practical use.

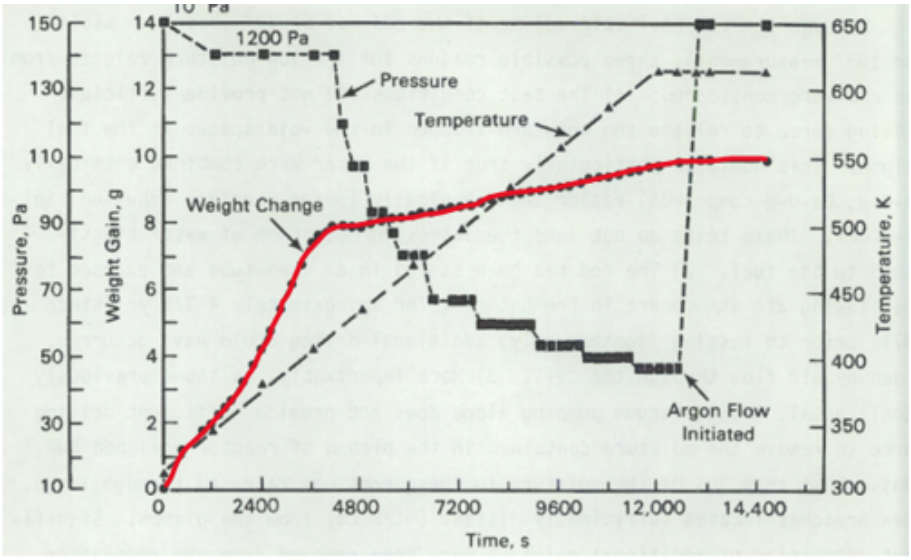

Figure 7.9: Evolution of the water gain, the temperature, and the pressure over time. The red curve represents the evolution of the mass of water removed from the failed rod. The caption is taken from Kohli (1986).

Remark 7.3.1. In a practical situation, it is more convenient for the operationals units of EDF to use the tables rather than the interpolator function to estimate the drying time. For instance, consider a failed rod with a crack width of $e = 12.6$ µm and an assembly power of $P = 32$ kW. Table 7.4 indicates that t_{95}(12.6 µm, 30 kW) = 31.5 h and t_{95}(14 µm, 35 kW) = 21.4 h. Therefore, the drying time in this specific scenario is between 21.4 h and 31.5 h.

7.4 Integral experimental validation

To date, the only experiment tracking the evolution of water mass over time during the drying of a failed fuel rod is that of Kohli (1986). In this experiment, a rod's plenum was punctured, filled with ten grams of water, sealed, and then placed inside a heated and vacuumed steel furnace tube. The pressure, temperature, and weight changes were monitored throughout. Since the rod was in a furnace rather than a transport cask, the heat transfer correlation presented in equation H.6 is not applicable; instead, a constant heat flux condition was used for simulation.
Figure 7.9 illustrates the water mass evolution in the plenum over time from Kohli's experiment, while Figure 7.10 presents the results from the 0D model under three different heat flux conditions (φ_{pl} ranging from 1000 to 2000 W/m^2). The rod's burnup was 15.6 MWd/kgU, corresponding to a crack width of approximately 40 µm (see Figure 10).
The 0D model's prediction of the water mass vacuumed over time aligns well with the experimental data, suggesting that the model effectively simulates the drying process. To draw more definitive conclusions, it would be necessary to conduct an integral experiment under the same conditions as the French industrial drying process. However, such an experiment has not yet been performed.

7.5 Conclusion

This chapter presents tables detailing the drying time as a function of two key parameters: residual heat power and crack width, derived from the 0D model. It is important to note that the model assumes the failed rod is centrally positioned within the shipping cask. This assumption is crucial for the applicability

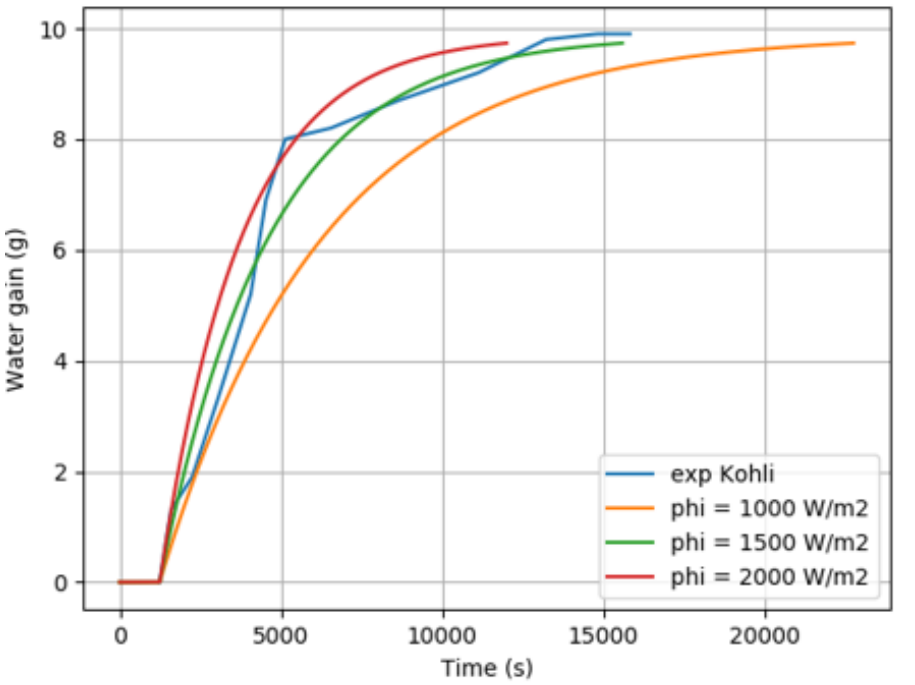

Figure 7.10: Evolution of water mass in the plenum over time, and comparison between the experimental results and the 0D results.

of the presented values. Additionally, all other assumptions in the model are conservative, meaning the actual drying time may be quicker than the predicted value.

CHAPTER 8

Conclusion and Perspectives

Summary

This chapter summarizes the key conclusions from the PhD research, highlighting both the academic and industrial results. Additionally, the perspective section outlines potential future work, particularly regarding the generalization of the Mucellphage model. While the research primarily focused on boiling flows in microchannels, where the Mucellphage model proved effective, further refinements would be required to adapt the model to more complex flow scenarios.

8.1 Conclusion

The study of the industrial drying of failed fuel rods employed a variety of approaches, including numerical models (0D, 1D, and 3D) and experimental investigations.
The introduction introduced the industrial context, highlighting the problem of fuel rods losing their watertight integrity each year within the primary circuit. Transporting these failed rods from nuclear reactors to reprocessing plants poses a significant challenge due to the risk of hydrogen generation from dissociated trapped water. Therefore, this thesis aimed to accurately assess the drying time of failed rods. The chapter also discussed the unique characteristics of boiling flows in microchannels and reviewed existing 1D and 3D models. A key observation was that none of the 1D correlations available in the literature could predict pressure loss or heat transfer in microchannels with sufficient accuracy, which has led to a growing reliance on 3D CFD studies.
Then first part of this manuscript presented resolved 3D numerical simulations of boiling flows in microchannels with the multi-field software neptune_cfd.

- Chapter 1 introduced the neptune_cfd software, a multi-field CFD code utilized throughout the PhD. It provided an overview of the general equations and specific models used.
- Chapter 2 assessed the abililty of neptune_cfd to model adiabatic flows, particularly examining spurious velocities induced by surface tension forces in a static bubble under various mesh refinements. The study found that finer meshes reduced spurious velocities. The Bhaga case, involving a rising bubble under gravity, was also simulated in 3D with excellent qualitative and quantitative results. The conclusion of this chapter is that an infinite drag force limits the spurious velocities and improves the quantitative results.
- Chapter 3 introduced the Mucellphage model, a new method based on the gradient approach for calculating heat and mass transfer across large interfaces in a multi-field CFD code. The model was rigorously tested and validated against several analytical cases (e.g., Sucking and Stefan problems, and Scriven case, which is also an experimental case) with errors below 5% compared to analytical solutions. It was also validated against the Florschuetz experiment, which involves the rise of a bubble in a superheated liquid.
- Finally, chapter 4 presented improvements to the existing wettability model, enabling more complex microchannel case simulations. For example, in the Mukherjee case, a vapour bubble's growth in a microchannel was studied. The research revealed that the bubble's growth was faster when in motion and that wettability effects, particularly the contact angle, significantly influenced the boiling velocity. An error of up to 100% in the boiling rate could occur with an incorrect contact angle.

Following this comprehensive numerical study, part II detailed two experimental campaigns conducted at LEGI. These campaigns identified several flow regimes during the drying of microchannels with diameters around 100 µm (e.g., slug flow, single interface boiling, annular flow, droplet flow). The slug flow regime was found to be the most common, justifying the previous numerical approach. The experiments also confirmed the validity of Kreutzer's law for predicting pressure drops in microchannels at low Reynolds numbers.
Part III developped two upscaling models to simulate the slug flow regime in microchannels in a reasonable time.
Chapter 6 presented an upscaling method to simulate boiling flows in microchannels using a 1D approach. This method incorporated Kreutzer's law (validated experimentally) for pressure loss calculations and the Mucellphage model for interface boiling. It was discovered that 3D effects significantly influence boiling in slug flows, necessitating a corrective coefficient to adjust for the underestimation of heat and mass transfer at the interface. While this approach allows for the simulation

of slug flow regimes in microchannels with less computational resources than 3D simulations, it is less accurate, with boiling rate errors potentially exceeding 30%. Furthermore, the computational time remains important, with simulations of real cases lasting several days.
To conclude this PhD and answer the industrial concern, chapter 7 used experimental and numerical evidence to prove that two-phase flow effects are negligible during the drying of failed fuel rods due to the rapid evaporation of water in microcracks. Subsequently, a 0D model was built to simulate boiling in the plenum and single-phase vapour flow in the uranium cracks. Tables were generated to provide drying times at 50% and 95% completion for failed rods in transport casks, considering various crack widths and residual heat power levels. These results offer practical guidance for operational teams managing the drying of failed fuel rods in an industrial context.

8.2 Perspectives

As discussed throughout this manuscript, 3D CFD simulations of boiling flows in microchannels offer high accuracy and reliability but remain prohibitively costly for complex applications. Future research should focus on reducing computational time for these methods. Two potential solutions were explored during this PhD work: implementing an Adaptive Mesh Refinement (AMR) method and integrating the Mucellphage into the Generalized Large Interface Model (GLIM). However, these methods require further validation and thus are presented here as avenues for future study rather than in a dedicated chapter of this manuscript.

8.2.1 Adaptative Mesh Refinement

Modelling bubbles and slugs with a large interface approach requires a very refined mesh for two main reasons. First, a minimum of 20 cells per bubble diameter is required to compute the surface tension force with reasonable accuracy (as explained in section 2.1). Additionally, when studying heat and mass transfer with the Mucellphage model, the size of a cell must be smaller than the linear thermal boundary layer. In 3D cases, this second condition is very demanding, and often millions of cells are required to model a single bubble. To decrease the computational cost of these scenarios, many research groups use an Adaptive Mesh Refinement method.
Adaptive Mesh Refinement (AMR) is a numerical method that involves modifying the mesh of the computational domain during a computation. For instance, it is possible to refine the mesh at the interface of a bubble as the bubble moves, while derefining the mesh far from the interface.
Adaptive mesh refinement is currently in development for neptune_cfd; therefore, it is not possible to use it for industrial cases yet. However, restarting a computation from a different mesh is possible. The variables are interpolated to the new mesh, ensuring mass, momentum, and energy conservation. By automating the restart computations and mesh generation, a "pseudo-AMR" method was implemented to illustrate the substantial computational time gain. The computational domain is initially represented by a coarse mesh with a cell size Δx, and it is modified at every restart with the following procedure:

1. Every cell at a distance smaller than $5\Delta x$ from the interface ($\alpha = 0.5$) is divided into 8 smaller cells with a size $\Delta x/2$.

2. Every cell at a distance smaller than $4\Delta x$ from the interface (including the already refined cells) is divided into 8 smaller cells. Therefore the cells at a distance smaller than $4\Delta x$ have a cell size $\Delta x/4$.

The computation is stopped each time the interface moves by more than $3\Delta x$ to ensure it stays within the refined area. The outcome of this procedure is depicted in Figure 8.1 for the case of Scriven (bubble in a superheated liquid).

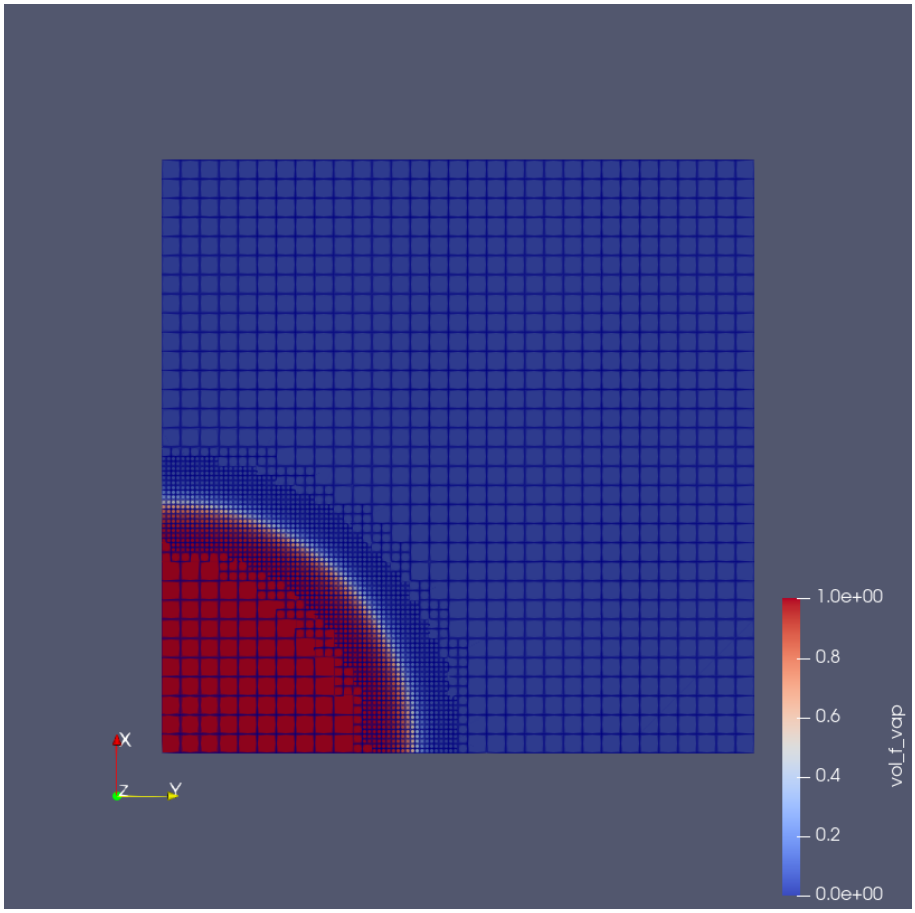

Figure 8.1: 3D bubble represented with AMR. The cell size at the interface is four times smaller than far from the interface.

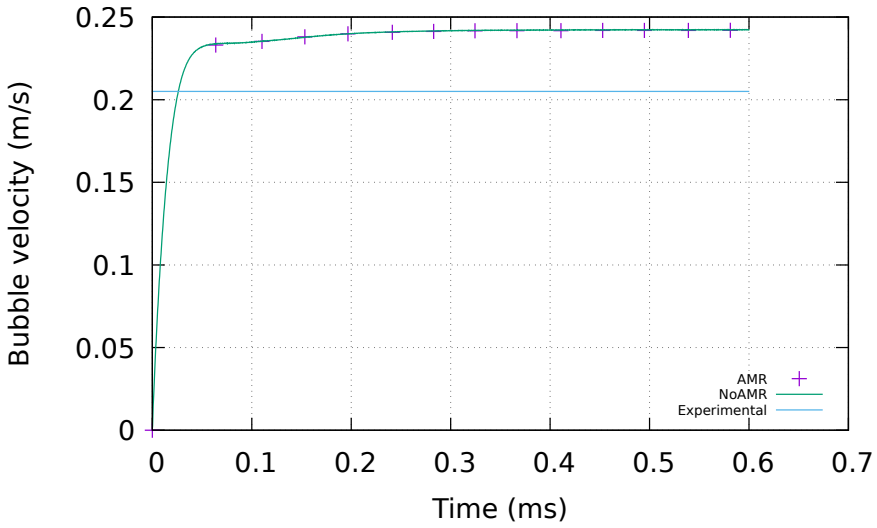

Figure 8.2: Evolution of the bubble velocity over time. The green line represents the evolution of bubble velocity without Adaptive Mesh Refinement (AMR). The purple crosses indicate the results obtained using the AMR method, showing almost no difference in the computational accuracy. The blue line denotes the asymptotic experimental velocity.

The results obtained with this pseudo-AMR method showed excellent agreement with the results obtained using a very refined mesh (uniform cell size of $\Delta x/4$), with relative errors on the evolution of the bubble radius over time smaller than 0.1% as illustrated in Figure 8.2. There was a substantial computational gain. The AMR mesh contained between 70,000 and 150,000 cells, while the very refined mesh contained over 1.9 million cells.

The same AMR approach — with 3 layers of refinement — was applied to the Bhaga case (described in section 2.2), an experiment tracking the velocity and shape of a rising bubble caused by the buoyancy effect. This case is part of the validation base of neptune_cfd with a uniformly very refined mesh. There was no visible difference in the results between the validation case and the AMR case. The validation case required 27 million cells, while the AMR case only required 500,000. The adaptative mesh used for the Bhaga case is presented in Figure 8.3.
In conclusion, Adaptive Mesh Refinement (AMR) is a viable solution to substantially decrease the computational cost of simulations involving large interfaces. It demonstrates no apparent drawbacks, maintaining result accuracy compared to a uniformly refined mesh, while potentially reducing the mesh size by a factor of nearly 100 in various 3D cases. The forthcoming integration of an AMR method into neptune_cfd holds promising prospects for advancing large interface simulations.

8.2.2 Integration of the Mucellphage in a multi-regime model

The Mucellphage mass transfer model presented in chapter 3 can predict heat and mass transfer at large interfaces with a great accuracy when the mesh is fine enough. However, in scenarios characterized by complex flows with multiple regimes and numerous droplets or bubbles, the model encounters significant limitations. First, it is unrealistic to simulate more than a few dozens of bubbles or droplets with the approach presented in part I. Aditionally, the Mucellphage model relies on the presence of an interface (isosurface α = 0.5) to calculate the heat transfer term. Consequently, it is incapable of handling processes involving the nucleation of bubbles.
Dispersed models, such as droplet or bubble models however, are capable of handling these situations by modelling subgrid droplets or bubbles but do not have the same level of accuracy as the Large Interface

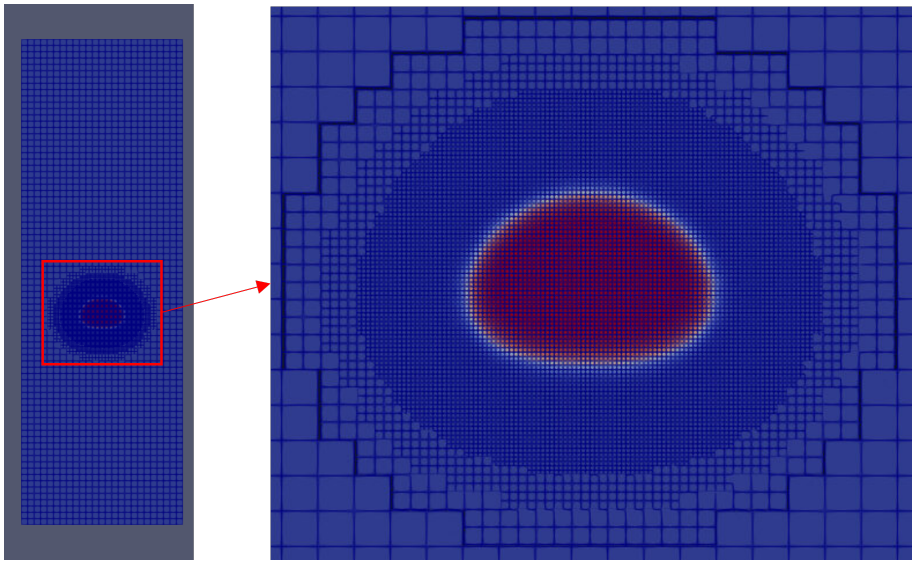

Figure 8.3: Caption from the simulation of the Bhaga case with AMR. The right picture is on the bubble from the left picture. The three layers of refinement around the moving bubble are clearly visible.

Approach. Therefore, coupling the Mucellphage with dispersed models to benefit from the accuracy of the LIM in the areas where the mesh is fine enough, while solving small droplets/bubbles with a dispersed approach would take the best out of both approaches. This type of coupling is called a multi-regime model.
This section explains why the existing multi-regime models are incompatible with the Mucellphage and discusses how the Mucellphage could be effectively coupled with a new multi-regime approach. A feasibility case is presented to illustrate the potential of this integration. However, extensive validation is required before this approach can be considered reliable. For this reason, this work is presented as a perspective rather than a fully developed chapter.

8.2.2.1 Existing multi-regime models in the litterature

Unlike single-fluid codes, two-phase CFD codes such as neptune_cfd have the capability to simulate both dispersed flows (bubbles, droplets) and large interfaces. Typically, these approaches are not employed simultaneously in various applications. For instance, modelling the spray of droplets in a nuclear containment scenario requires only a droplet model, while the growth of a single vapour bubble necessitates solely a large interface model. However, in more intricate flows, the nucleation of small bubbles may precede their growth into large bubbles. In such cases, handling the nucleation of small bubbles requires a dispersed bubble model, while the modelling of large bubbles is accomplished using a large interface approach. The challenge in developing such a method lies in accurately identifying the transition between a dispersed regime and a resolved interface.

8.2.2.2 GLIM

The standard multi-regime approach employed in neptune_cfd, known as the GLIM (Generalized Large Interface Model) and presented in Appendix J, is based on comparing the gradient of the volume fraction with the size of the cell, as illustrated in Equation 8.1. In this approach, a cell is solved with the large interface model if the volume fraction experiences a change exceeding 0.2 within the cell; otherwise, the dispersed approach is applied.

0	0.05	0.1	0.4	0.8	0.95	1

Figure 8.4: Example of the variation of the volume fraction across a large interface when interface sharpening is activated.

$$\begin{cases} \text{LIM if } \|\nabla \alpha_l\| > \dfrac{0.2}{\Delta x} \\ \text{Dispersed model else} \end{cases} \tag{8.1}$$

This method is frequently used in diverse industrial investigations to integrate neptune_cfd's standard large interface model (the LI3C) with droplet and bubble models. However, challenges arise when implementing this approach alongside interface sharpening. Figure 8.4 demonstrates a typical variation in volume fraction across a large interface when employing interface sharpening. It becomes apparent that certain cells within the large interface are treated as dispersed because the variation in volume fraction between two cells of the large interface can be smaller than 0.2.

8.2.2.3 GEMMA

The GEMMA (GEneralized Multiphase Modelling Approach), developed by De Santis et al. (2021), is another method designed to capture the transition between dispersed and large interface flow regimes. In this approach, the curvature of the interface, denoted as κ, is compared to the size of the cell. A cell is treated as a large interface if its curvature is greater than $\dfrac{1}{4\Delta x}$, as shown in Equation 8.2. The GEMMA criterion is almost always met for large interfaces since their curvature radius is large compared to the size of a cell. However, GEMMA quite often identifies large interfaces in the middle of dispersed flows because the computation of curvature does not make physical sense in these areas.

$$\begin{cases} \text{LIM if } \kappa > \dfrac{1}{4\Delta x} \\ \text{Dispersed model else} \end{cases} \tag{8.2}$$

8.2.2.4 Explicit interface identification

To overcome the limitations of the GLIM and GEMMA approaches, an explicit identification method could be employed to locate large interfaces and integrate the Mucellphage in a multiregime approach. A preliminary implementation of this method is presented in this section as a perspective for this PhD, but it would require more work and extensive validation before it can be used industrially. This method initially identifies cells containing the isosurface $\alpha = 0.5$. Subsequently, it assumes that all cells within $5\Delta x$ of this isosurface are large interfaces, while the remaining cells are considered dispersed. This process is summarized by equation 8.3.

$$\begin{cases} \text{LIM if the cell is within } 5\Delta x \text{ of the isosurface } \alpha = 0.5 \\ \text{Dispersed model else (see chapter 1 or Appendix J for more information on the dispersed models).} \end{cases} \tag{8.3}$$

A case similar to the "bubble column" case of Hänsch et al. (2012) is used to evaluate the explicite interface identification method. In this demonstration case, vapour is injected at the bottom of the domain and rises due to initial velocity and gravity. This method distinguishes between dispersed bubbles and larger bubbles: smaller vapour bubbles are handled as dispersed bubbles, while larger bubbles are

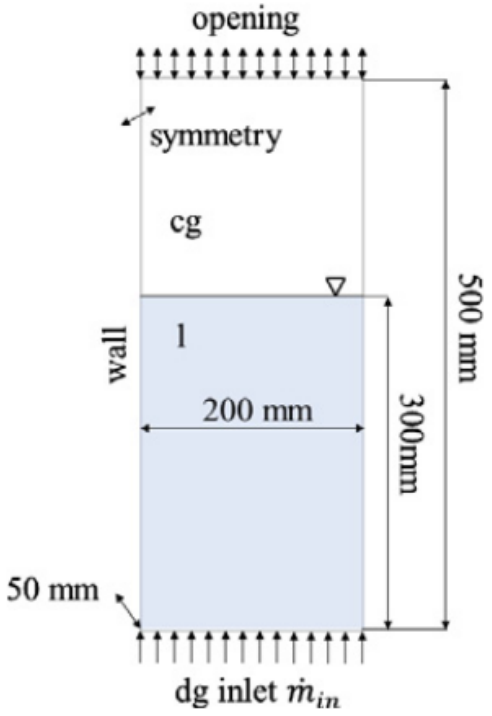

Figure 8.5: Schematic view of the computational domain. The Figure is taken from Hänsch et al. (2012).

	Liquid	Vapour
ρ (kg.m^{-3})	678	55.5
μ (Pa.s)	8.6×10^{-5}	2.2×10^{-5}
c_p (J.K^{-1}.kg^{-1})	6380	7000
h_{lat} (J.kg^{-1})	1.32×10^6	
T_{sat} (K)	584.1	

Table 8.1: Physical properties of water at 100 bar.

modeled using a Large Interface approach.

The domain for the evaluation case is a $50 \times 400 \times 500$ mm cuboid. Two different constant cell sizes are used: $\Delta x = 5$ mm for the coarse mesh and $\Delta x = 2.5$ mm for the fine mesh. Figure 8.5 provides a schematic view of this domain. By utilizing these two mesh resolutions, we can assess the performance and accuracy of the method under different computational conditions, similar to the approach used in the "bubble column" case by Hänsch et al. (2012).
Water is initialized for $z < 300$ mm at a pressure $P = 100$ bar and a temperature $T = T_{sat} + 4 = 588$ K. Saturated vapour is initialized for $z > 300$ mm. The pressure at the outlet is fixed at $P = 100$ bar, and the walls are adiabatic. At the inlet, a parabolic velocity profile is imposed with a maximum velocity of $u = 0.1$ m/s. The vapour is injected at the saturation temperature. The physical properties of water at 100 bar are managed using the CATHARE tables, which closely match those presented in Table 8.1.
A view of the bubble column is presented in Figure 8.6. The left image shows the results on the coarse mesh, while the right picture shows the results on the fine mesh. Large interfaces, particularly large bubbles, are represented in red, while dispersed bubbles, solved with a subgrid model, are represented in light blue. A comparison between the two meshes reveals that the finer mesh identifies significantly more large interfaces, as expected. The results of this model provide good qualitative results in

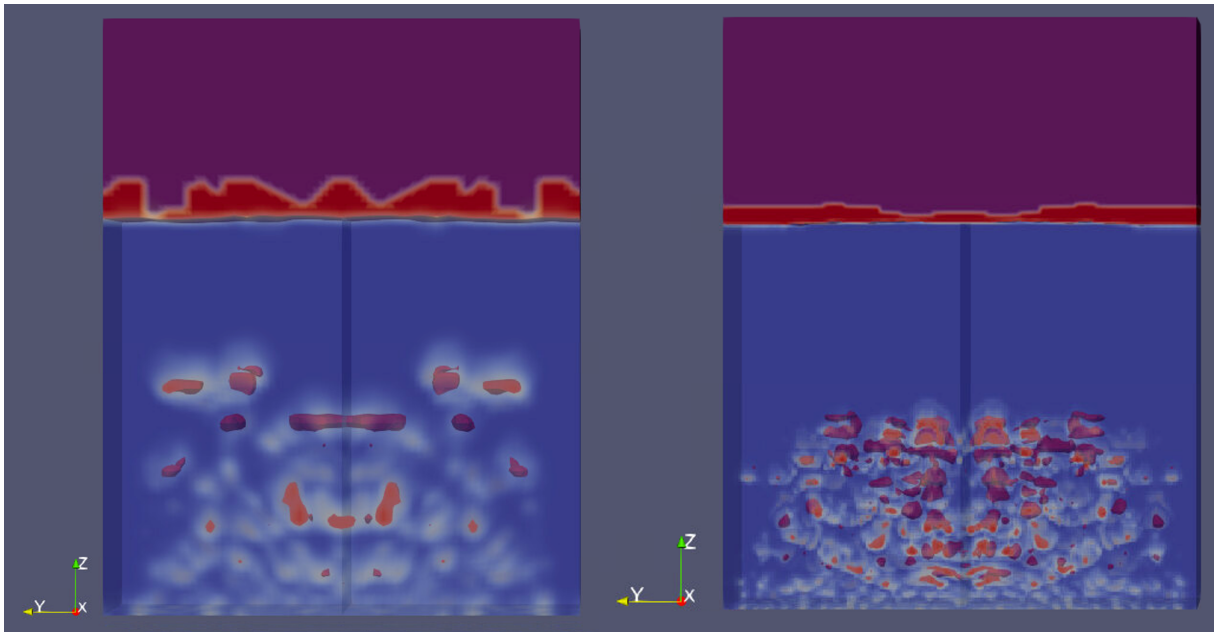

Figure 8.6: View of the flow at $t = 0.4$ s for the coarse and the fine mesh. The red bubbles represent the bubbles solved with a large interface model. Light blue represents dispersed bubbles, and dark blue represents water.

this demonstration case and illustrate how the Mucellphage model can be effectively implemented in a multiregime approach. However, extensive validation is still necessary before this model can be considered reliable for broader applications.

8.2.3 Other applications

The cases presented in this manuscript focused specifically on the drying of failed fuel rods. However, boiling flows in microchannels are a topic of interest for several other industrial applications, and the approach presented in this manuscript could also be used in the following fields:

- Microelectronics
- Sap flows in trees
- Boiling flows in the steam generator of SMR
- Hydrogen fuel cells
- Water desalination

The models developed and presented in this manuscript will be used in future projets and PhD works. Notably, the Mucellphage model is used in the PhD work of Adrien Fayet (CADIOU et al. (2024)) to model critical heat flux in a confined configuration.

8.2.4 Industrial perspectives

Currently, no integral experiment has been conducted on the drying of failed fuel rods under the French industrial process. To enhance the reliability of the conclusions drawn from this PhD —such as the assumption that two-phase effects in microcracks can be neglected and that several small cracks can be considered equivalent to one larger crack — an integral experiment would be essential. One potential

approach for this experiment would involve injecting water into a cracked rod specifically designed to simulate the structure of a failed fuel rod and applying a heat flux similar to that in a shipping cask. Key data, including the evolution of water mass over time, pressure, temperature, and heat flux in the plenum, should then be collected and compared with the methods and findings presented in this manuscript. This comparison would provide a critical validation of the theoretical and numerical models developed in this work.

APPENDIX A

The double gas expansion test

The double gas expansion test is the standard test to measure the free volume of irradiated rods. This section details how it is conducted.

Remark A.0.1. The double gas expansion test is designed for unfailed irradiated rods only. It is assumed that the rod is filled with gas (with no liquid), and that the gas is trapped in the irradiated rod (no leak).

A.1 Presentation of the experimental apparatus

Figure A.1 provides a schematic representation of a typical double expansion apparatus, which consists of two main volumes:

1. V_{de}, the double expansion volume. This is the primary volume used in the test where the gas initially expands after the valve is opened.
2. V_d, the dead volume. This is the volume that contains the irradiated rod during the test.

Both volumes are connected by a valve, and the pressure in both volumes in monitored by pressure sensors.
The free volume in the irradiated rod is denoted V_{free}. The pressure in the irradiated rod is denoted P_{rod}.

A.2 Experimental protocol

Before the start of the experiment, both the dead volume containing the failed rod (V_d) and the double expansion volume (V_{de}) are evacuated to create a vacuum. It is assumed that the initial pressure in these two volumes is $P_d = P_{de} = 0$ Pa. The experiment proceeds in two steps:

- **Rod puncturing measure:** In this step, the irradiated rod is punctured, allowing the gas trapped inside the rod to expand into the dead volume V_d. The pressure in V_d is then measured.
- **Second Expansion Measure:** In the second step, the valve between V_d and V_{de} is opened, allowing the gas to further expand into the double expansion volume V_{de}. After the gas has fully expanded and reached equilibrium, the pressure is measured again.

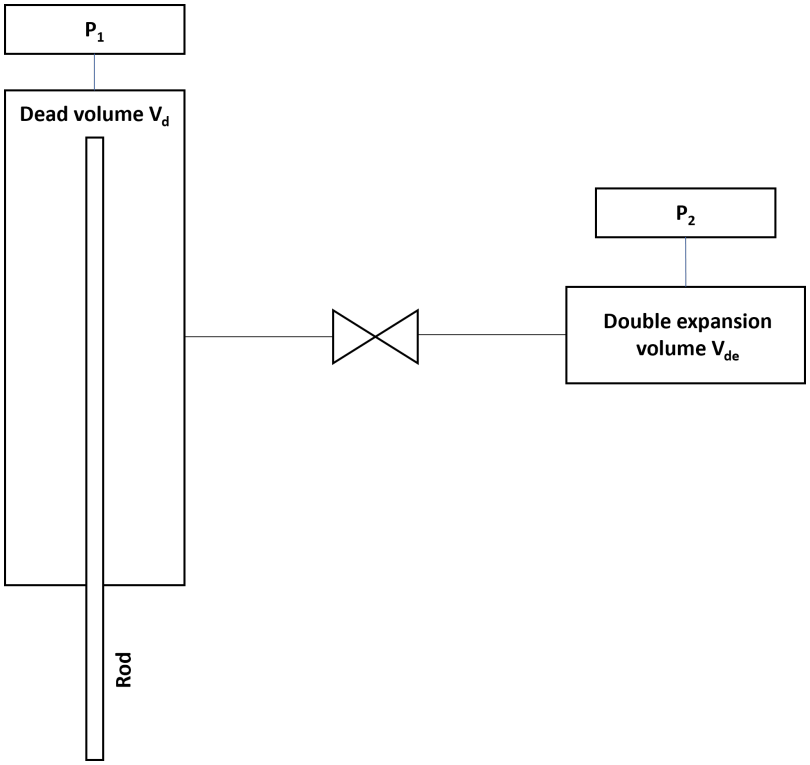

Figure A.1: Schematic view of a standard double expansion apparatus.

A.2.1 Rod puncturing

At $t = 0$, the irradiated rod is punctured, causing the gas inside the rod to rapidly expand into the dead volume (V_d). This expansion leads to a pressure increase in V_d. Over time, as the gas continues to disperse and reach equilibrium, the pressure stabilizes at an asymptotic value, P_1. This process typically takes around 2 hours, by which time the gas inside the rod has been completely released into the dead volume.
The ideal gas law states that the product between the pressure and the volume is constant. Hence, it is possible to link P_1 and the free volume V_{free}.

$$P_{rod}V_{free} = P_1(V_{free} + V_d) \tag{A.1}$$

A.2.2 Second expansion

At $t = t_1$, the valve between the dead volume V_d and the volume of double expansion V_{de} is opened. This allows the gas that had previously expanded into V_d to further expand into the combined volume $V_d + V_{de}$. After sufficient time has passed, the pressure stabilizes at a new asymptotic value, P_2. The ideal gas law gives:

$$P_1(V_{free} + V_d) = P_2(V_{free} + V_d + V_{de}) \tag{A.2}$$

A.3 Conclusion

Remark A.3.1. Using equations A.1 and A.2, the free volume V_{free} of a failed rod can be calculated as follows:

$$V_{free} = \frac{V_{de} P_2}{P_1 - P_2} - V_d \tag{A.3}$$

APPENDIX B

The rarefaction phenomenon

The Navier-Stokes equations assume that a fluid can be described by macroscopic properties such as density or viscosity. However, for gas flows in microchannels, especially at low pressures when the mean free path of gas molecules is not small compared to the diameter of the channel, this assumption is not always valid.
This phenomenon, known as the rarefaction effect, has been studied since the end of the 19th century (Maxwell (1878)) and continues to be the subject of research by various groups (Nicolas et al. (2018), Ramdane (2021), Tchekiken (2014)). Studies have shown that the Navier-Stokes equations remain valid far from the wall if the Knudsen number is sufficiently small. Near the wall, a velocity slip boundary condition combined with a temperature jump can reasonably model the rarefaction effect.
During the vacuum drying of failed fuel rods, vapour flows through cracks with widths of a few micrometers, and the pressure can drop to values as low as 10 mbar. In these conditions, rarefaction effects become significant.

B.1 Mean free path

To determine whether rarefaction effects need to be considered or can be neglected, the mean free path (λ), defined as the average distance traveled by a molecule before colliding with another molecule, must be calculated.

Remark B.1.1. The two most common correlations to calculate the mean free path are the correlation of Bird (1994), and the correlation of Sharipov and Seleznev (1998). Under the assumption of perfect gas, and spherical molecules, Bird (1994) found an analytical expression of the mean free path:

$$\lambda = \frac{k_B T}{\sqrt{2}\pi d^2 P} \tag{B.1}$$

where k_B is Boltzmann's constant, T the gas temperature, d the diameter of the molecule, and P the pressure of the gas.
Because the diameter of the molecule is not always easy to measure, a more macroscopic expression was suggested by Sharipov and Seleznev (1998) involving the viscosity μ.

$$\lambda = \frac{\mu}{P}\sqrt{\frac{\pi R T}{2M}} \tag{B.2}$$

The gas flow in failed fuel rods, typically has the following characteristics :

- T = [300,500] K depending on the superheat. We will pick $T = 370$ K to get a good order of magnitude
- $d = 0.4$nm (diameter of a molecule of water)
- $\mu = 10^{-5}$ Pa.s (water vapour at low pressure)
- $M = 0.018$ kg/mol
- $P =$ [10, 1000] mbar

Using these values, the formula of Bird (1994) gives $\lambda = 7.0$ μm at 10 mbar. The formula of Sharipov gives $\lambda = 5.0$ μm at 10 mbar

B.2 Rarefied flow regimes

Remark B.2.1. The Knudsen number is the dimensionless number used to determine whether the mean free path is negligible compared to the characteristic length, or not. It is defined as:

$$\mathrm{Kn} = \frac{\lambda}{L} = \sqrt{\frac{\gamma\pi}{2}}\frac{Ma}{Re} \tag{B.3}$$

L is the characteristic dimension (the crack width in the case of failed rods), γ the isentropic coefficient, Ma the Mach number, and Re the Reynolds number.

The rarefied flow regimes can be characterized as follows according to Nicolas et al. (2018):

- If $\mathrm{Kn} < 10^{-2}$, the mean free path is negligible compared to L. Thus the flow is continuous and can be fully solved by the Navier-Stokes equations with a no-slip boundary condition at the wall (hydrodynamic regime).
- If $10^{-2} < \mathrm{Kn} < 10^{-1}$, the flow can be considered continuous far from the wall. However, close to the wall, at a distance smaller than a few λ from the wall (in the "Knudsen layer"), the equilibrium is not reached, and the usual wall law models cannot be used. This is called the slip-flow regime.
- If $10^{-1} < \mathrm{Kn} < 10$, λ and L have similar dimensions, this is the transition regime.
- If $\mathrm{Kn} > 10$, the gas molecules interact more often with the wall than with other molecules, this is the free-molecular regime. It must be solved with the Boltzmann equations or molecular dynamics.

Figure B.1 shows the evolution of the Knudsen number according to the pressure in a failed fuel rod. It shows that the slip-flow regime is reached in failed rods when the pressure is sufficiently small.

B.3 The slip-flow regime

In the slip-flow regime, the Navier-Stokes equations are valid far from the walls but not in the Knudsen layer. Within this layer, molecules interact more with the wall than with other molecules, resulting in a velocity slip and a temperature jump. The width of the Knudsen layer is typically λ.

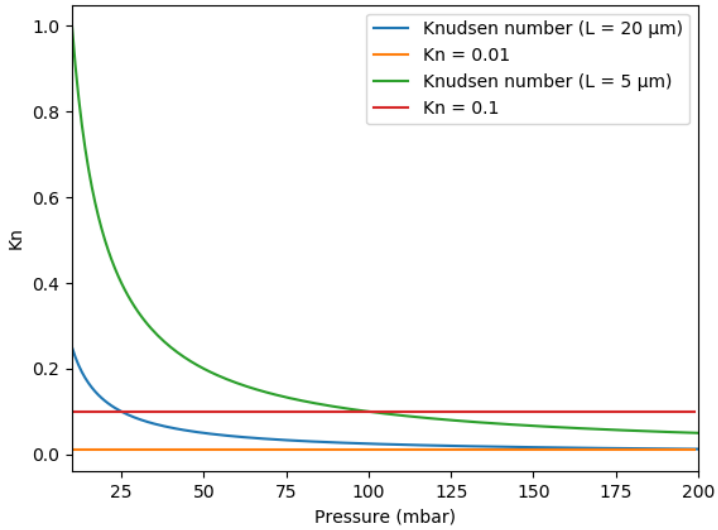

Figure B.1: Evolution of the Knudsen number according to pressure for a failed fuel rod with a crack width $e = 5$ µm, and for a failed fuel rod with a crack width $e = 20$ µm.

B.3.1 Velocity at the wall

In the slip-flow regime, the gas velocity at the wall is not zero, as illustrated in Figure B.2. To account for this effect, Navier (1827) and Maxwell (1878) suggested that the slip velocity u_g in the Knudsen layer is proportional to the normal gradient of the velocity and the mean free path λ (Equation B.4). This boundary condition at the wall replaces the usual no-velocity-slip boundary condition.

$$u_g = \lambda \nabla u.\underline{n} \tag{B.4}$$

B.3.2 Temperature jump at the wall

Similarly, rarefaction implies a temperature jump condition near the wall. This condition is proportional to the normal temperature gradient as in equation B.5.

$$T_g - T_w = 2\xi_T \lambda \nabla T.\underline{n} \tag{B.5}$$

T_g is the temperature of the gas close to the wall, T_w the wall temperature. The coefficient ξ_T is defined as $\xi_T = \dfrac{2\gamma}{Pr(\gamma+1)}$, with γ the isentropic coefficient and Pr the Prandtl number.

B.4 Rarefaction in failed rods

Rarefaction is involved at two places during the drying of failed rods: in the functional gap between the basket and the shielding of the transport casks as explained in section H.3.3, and in the pellet cracks at low pressure as explained in section B.2.
In the first case, the rarefaction effects cannot be neglected, and are taken into account in the thermal model to compute the heat flux on the failed rod. This section focuses on the gas flow in the UO_2 cracks.

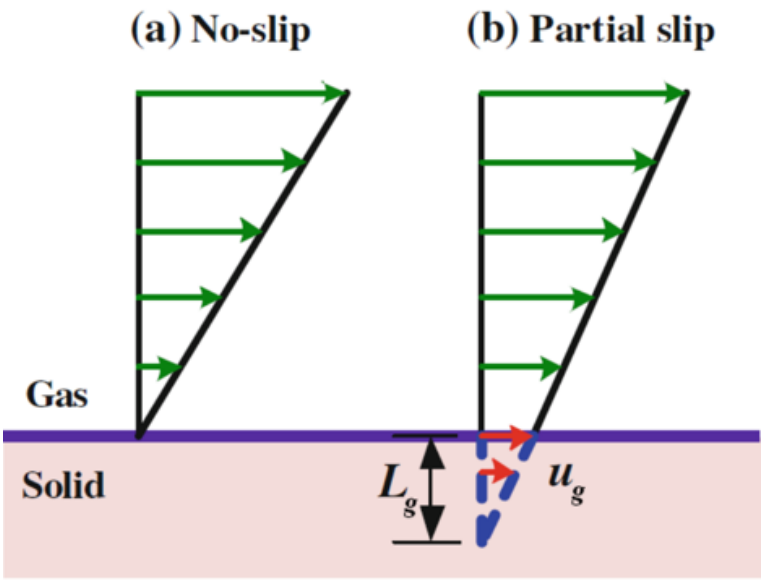

Figure B.2: Velocity profile with, and without a slip boundary condition (from Tchekiken (2014)).

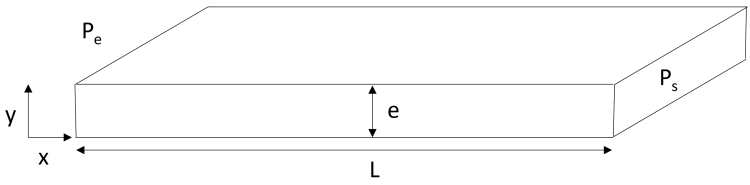

Figure B.3: Schematic drawing of a Poiseuille flow between two planes.

B.4.1 Poiseuille flow with slip boundary conditions

One method to evaluate the significance of the rarefaction effect is by comparing the analytical solution for a Poiseuille flow with a no-slip boundary condition to the solution for a Poiseuille flow with slip boundary conditions. For this comparison, two infinite planes defined by $(y = 0)$ and $(y = e)$ are considered, as depicted in Figure B.3. At $x = 0$, a pressure P_e is applied, and at $x = L$, a pressure P_s is applied.
One way to assess the importance of the rarefaction effect is to compare the analytical solution for a Poiseuille flow with no slip boundary condition with the solution for a Poiseuille flow with slip boundary conditions.
For this, two infinite planes defined by $(y = 0)$ and $(y = e)$ are considered as in Figure B.3. At $x = 0$, a pressure P_e is applied. At $x = L$, a pressure P_s is applied.

Remark B.4.1. Under the following assumptions, Poiseuille found an analytical formulation of the velocity profile (equation B.6).

- single-phase flow
- laminar flow
- low compressibility
- flow between two planes

- no velocity slip at the wall

$$u(x,y) = \frac{1}{2\mu}\frac{dP}{dx}((y-\frac{e}{2})^2 - \frac{e^2}{4}) \tag{B.6}$$

After integration, an analytical formulation of the mass flow rate can also be found.

$$\dot{m} = \frac{e^2}{12}\frac{M}{\mu RT}(P_e^2 - P_s^2)A \tag{B.7}$$

with A the area crossed by the flow.

The slip boundary condition defined by equation B.4 modifies the velocity profile in the Poiseuille problem, and the new solution is given by equation B.8. More details about the analytical demonstration of this equation can be found in Tchekiken (2014).

$$u(x,y) = \frac{1}{2\mu}\frac{dP}{dx}((y-\frac{e}{2})^2 - \frac{e^2}{4} - \lambda e) \tag{B.8}$$

The integration of equation B.8 gives an expression of the mass flow rate:

$$\dot{m} = \frac{e^2}{12}\frac{M}{\mu LRT}(P_e^2 - P_s^2)A(1 + 6\frac{2-\sigma_u}{\sigma_u}\,\mathrm{Kn}) \tag{B.9}$$

Remark B.4.2. The term $(1 + 6\frac{2-\sigma_u}{\sigma_u}\,\mathrm{Kn})$ in the mass flow rate equation, known as the Poiseuille factor, indicates that the mass flow rate is higher in rarefied flows due to the slip condition. For example, with a Knudsen number $\mathrm{Kn} = 0.1$, the mass flow rate is 1.6 times larger when considering the rarefaction effects.

B.4.2 Numerical resolution of Poiseuille in 1D

The previous section demonstrated that rarefaction effects are locally significant in areas of failed rods where the pressure is low. However, this analysis doesn't provide quantitative information on the total pressure loss, considering the entire rod, including regions where the pressure is high and rarefaction effects are negligible.

To assess this global pressure drop, let's consider a failed rod with a crack length $L = 3.6$ m, a crack width $e = 6.3$ µm. A Poiseuille flow of liquid vapour with a mass flow rate $\dot{m} = 18.7$ g/d is imposed and a pressure $P_{out} = 10$ mbar is applied. The pressure in the plenum P_{pl} is computed using a 1D Python program, employing either equation B.7 (neglecting the velocity slip), or equation B.9 (taking the velocity slip into account).
The results are plotted in Figure B.4. The right picture demonstrates that the rarefaction effects play a role when the pressure is low, near the outlet. However, these head losses are totally negligible when considering the full crack length.

Remark B.4.3. Based on the 1D analysis, it is decided to neglect rarefaction effects in the cracks of failed rods.

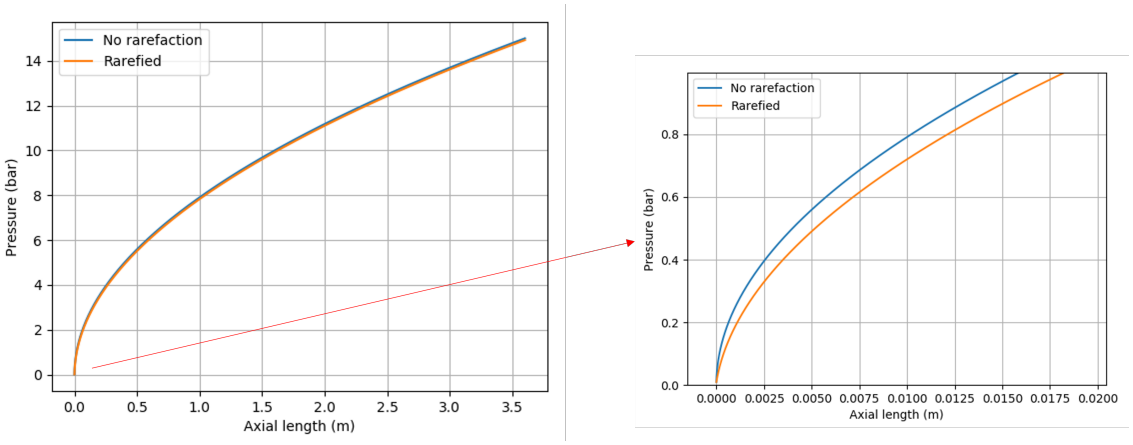

Figure B.4: Pressure profile in a failed rod under a Poiseuille gas flow. The orange curve represents the pressure profile when rarefaction effects are taken into account. The blue curve represents the pressure profile when the rarefaction effects are neglected.

APPENDIX C

From Navier-Stokes to multifield equations

The Navier-Stokes equations include mass balance, momentum balance and energy balance.
Mass balance equation:

$$\frac{\partial \rho}{\partial t} + \nabla(\rho \underline{u}) = 0 \tag{C.1}$$

Momentum balance equation:

$$\frac{\partial}{\partial t}(\rho \underline{u}) + \nabla.(\rho \underline{u} \otimes \underline{u}) = -\nabla P + \underline{\underline{\mu S}} + \rho \underline{g} \tag{C.2}$$

Energy balance equation:

$$\frac{\partial}{\partial t}(\rho H) + \nabla.(\rho H \underline{u}) = \nabla.(\lambda \nabla T) + \nabla.(\underline{\underline{\mu S}}.\underline{u}) + \frac{\partial P}{\partial t} + \rho \underline{g}.\underline{u} \tag{C.3}$$

C.1 Fixed grid approaches

To obtain the two-fluid equations on a fixed grid, we define a phase indicator function χ_k equal to 1 in phase k, 0 otherwise. This function has the following properties:

$$\sum_k \chi_k = 1 \tag{C.4}$$

$$\chi_m \chi_n = \delta_{nm} \chi_m \tag{C.5}$$

where δ is the Dirac function.

$$\nabla \chi_k = -\underline{n_k^{int}} \delta^{int} \tag{C.6}$$

n_{int} is the Dirac function centered at the interface, n_k^{int} is the normal at the interface.

$$\frac{\partial \chi_k}{\partial t} = u^{int} n_k^{int} \delta^{int} \tag{C.7}$$

u^{int} is the interface velocity.
In the two-fluid approach, each local quantity Φ (density, velocity, pressure, temperature etc) becomes $\chi_k \Phi_k$. Therefore, the Navier-Stokes equations can be rewritten:
Mass balance:

$$\frac{\partial \chi_k \rho_k}{\partial t} + \nabla(\chi_k \rho_k \underline{u_k}) = \chi_k \rho_k (\underline{u}^{int} - \underline{u_k}).\underline{n}_k^{int} \delta_{int} \tag{C.8}$$

Momentum balance:

$$\frac{\partial}{\partial t}(\chi_k\rho_k\underline{u_k})+\nabla.(\chi_k(\rho_k\underline{u_k}\otimes\underline{u_k}+P_k\underline{\underline{I_d}}-\mu_k\underline{\underline{S_k}}))-\chi_k\rho_k\underline{g}=(\rho_k\underline{u_k}\otimes(\underline{u}^{int}-\underline{u_k})-P_k\underline{\underline{I_d}}+\mu_k\underline{\underline{S_k}}).\underline{n}_k^{int}\delta^{int} \tag{C.9}$$

where $\underline{\underline{I_d}}$ is the identity matrix.

Energy balance:

$$\begin{aligned}\frac{\partial}{\partial t}(\chi_k\rho_k H_k)+\nabla\cdot(\chi_k(\rho_k H_k\underline{u_k}-\mu_k\underline{\underline{S_k}}\cdot\underline{u_k}-P_k\underline{u_k}+\lambda_k\nabla T_k))&\\ -\frac{\partial\chi_k P_k}{\partial t}-\chi_k\rho_k\underline{g_k}\cdot\underline{u_k}&\\ =(\rho_k H_k+P_k)(\underline{u^{int}}-\underline{u_k})\cdot\underline{n_k^{int}}\delta^{int}&\\ +(\mu_k\underline{\underline{S_k}}-\lambda_k\nabla T_k)\cdot\underline{n_k^{int}}\delta^{int}&\end{aligned} \tag{C.10}$$

The mass transfer Γ_k at the interface is defined as in equation C.11. This represents the mass jump condition.

$$\Gamma_k=\rho_k(\underline{u}^{int}-\underline{u_k}).\underline{n}_k^{int}\delta_{int} \tag{C.11}$$

C.2 Two-fluid model

In the two-fluid model, a volumetric averaging is used. $<\Phi>$ is the average of Φ on a volume Ω.

$$<\Phi>_k=\frac{1}{\Omega_k}\int_{\Omega_k}\Phi d\Omega=\frac{1}{\Omega_k}\int_{\Omega}\chi_k\Phi d\Omega \tag{C.12}$$

The volume fraction α_k is the average volume of the indicator function:

$$\alpha_k=<\chi_k>=\frac{1}{\Omega}\int_{\Omega}\chi_k d\Omega=\frac{\Omega_k}{\Omega} \tag{C.13}$$

Therefore, it is possible to write:

$$<\chi_k\Phi>=\alpha_k<\Phi>_k \tag{C.14}$$

Using these properties on the equations presented in the previous sections give the two-fluid balance equations (equation 1.1 for mass balance, equation 1.2 for momentum balance, and equation 1.3 for energy balance).

APPENDIX D

The Mucellphage implementation

Two sources were modified to implement the Mucellphage model in neptune_cfd: nc_ws_enthalpy_source_terms.c, the source where the heat and mass transfer terms are computed, and cal_surf.c, a new source to compute the geometrical parameters necessary in the Mucellphage. neptune_cfd is not an open source code, therefore an algorithmic description will be given instead of the source code.

D.1 nc_ws_enthalpy_source_terms.c

In this source, the variable "tst" is computed. This variable corresponds to the heat transfer rate on phase k (W/m^3).

$$tst_k = \alpha_k \Pi'_k = \alpha_k \frac{\varphi_k A_{int}}{V_{cell}} = -\alpha_k \frac{\lambda_k \nabla T_k S_{int}}{V_{cell}} \tag{D.1}$$

$\varphi_k = -\lambda_k \nabla T_k$ is the heat flux through an interface. A_{int} is the area of the interface in the cell considered, and V_{cell} is the volume of the cell.
The implementation of the Mucellphage function in this function represents 134 lines of code in neptune_cfd.

D.1.1 I/ Computation of the geometric parameters of each cell

The Mucellphage model requires the knowledge of several geometrical parameters to identify the interface, and reconstruct the interface plane. More specifically:

- **sommets:** this table contains the index of the 8 vertexes for each hexaedral cell. sommets[8*c_id + k] returns the index of the kth vertex of cell c_id.
- **coordsommets:** this 3 dimension table stores the (x, y, z) coordinates of the 8 vertexes for each hexaedral cell. For instance, coordsommets[8*c_id + k][0] returns the x coordinates of the kth vertex of cell c_id.
- **alphavertex:** this table stores the value of the gas volume fraction α_g for each vertex. alphavertex[inod_] returns the value of α_g at the vertex inod_.
- **cellvertex:** this table stores the index of the cells adjacent to a vertex. cellvertex[8*inod_ + k] returns the index of the k^{th} cell adjacent to vertex inod_.

The functions _calc_sommets and _calc_aretes are called at the beginning of the function to compute these tables. These functions are described in section D.2.5.

D.1.2 II/ Identification of the interface cells

A cell contains the interface (the iso-surface $\alpha = 0.5$), if at least one of its vertexes has a gas volume fraction smaller than 0.5, and at least one of its vertexes has a gas volume fraction greater than 0.5.
The variables inf05 and sup05 state whether a cell has a vertex with a volume fraction α_g smaller or greater than 0.5 respectively. All the vertexes are tested, and if at least one vertex has a volume fraction smaller/greater than 0.5, then inf05/sup05 is set to 1. The variables node1 and node2 store the index of a vertex with a volume fraction smaller/greater than 0.5.

D.1.3 III/ Identification of a point in the interface

As explained in section 3.2.2.3, the interface is approximated by a plane in each cell. This plane is constructed from a point and a normal vector. Given that $\alpha_{node1} < 0.5$ and $\alpha_{node2} > 0.5$, it is possible to interpolate the coordinates of the interface point x_{int} from x_1 and x_2 the coordinates of node1 and node2:

$$x_{int}[i] = x_1[i] + \frac{0.5 - \alpha_1}{\alpha_2 - \alpha_1}(x_2[i] - x_1[i]) \tag{D.2}$$

The coordinates of this point are stored in the 3 dimension variable ptint.

D.1.4 IV/ Construction of the interface plane

A plane is defined by its cartesian equation:

$$Ax + By + Cz + D = 0 \tag{D.3}$$

A, B, and C are the coordinates of the normal vector to the interface $\vec{n} = (A, B, C) = \frac{\vec{\nabla}\alpha_l}{\|\vec{\nabla}\alpha_l\|}$. The interface point verifies the cartesian equation of the plane, therefore D is equal to:

$$D = -Ax_{int} - By_{int} - Cz_{int} \tag{D.4}$$

The 4 dimension variable "plan" stores the values (A, B, C, D) and defines the interface plane.

D.1.5 V/ Computation of the area of the interface plane in the cell

The area of the interface plane in the cell S_{int} is computed in the function cal_surf. This function is described in section D.2.7.

D.1.6 VI/ Identification of the normal cell to the interface

As explained in section 3.2.2.2, the normal cell J to the interface is identified by minimizing the angle between the normal vector to the interface $\vec{n}$ and the vector linking the cells $\vec{IJ}$. This is done by maximizing the scalar product:

$$\vec{n}.\vec{IJ} \tag{D.5}$$

The index of the normal cell to the interface is stored in the variable pos.

D.1.7 VII/ Distance between the normal cell and the interface

The absolute distance d between a plane (A, B, C, D) and a point (x_{pos}, y_{pos}, z_{pos}) is computed by injecting the coordinates of the the point in the cartesian equation of the plane.

$$d = |Ax_{pos} + By_{pos} + Cz_{pos} + D| \tag{D.6}$$

D.1.8 VIII/ Computation of the temperature gradient

The temperature gradient is defined as:

$$\nabla T = \frac{T_{pos} - T_{sat}}{d} \tag{D.7}$$

D.1.9 IX/ Computation of enthalpy source term

The enthalpy source term is computed as:

$$tst = -\alpha\lambda\nabla T S_{int}/V_{cell} \tag{D.8}$$

D.2 Algorithm

```
I/ Computation of the geometric parameters
_calc_sommets
_calc_aretes
II/ Identification of the interface cells
for (all cells iel in the mesh)
  for (all vertexes inod of the cell iel)
    if (alphavertex(inod) < 0.5)
      inf05 = 1 and node1 = inod
    else
      sup05 = 1 and node2 = inod
III/ Identification of a point in the interface
  if (inf05 == 1 and sup05 == 1)
  /* if the cell is crossed by the interface */
    for (0 <= i <= 3)
      ptint[i] = coord(node1)[i]
      + (0.5 - alpha(node1)))/(alpha(node2)-alpha(node1)) * coord(node2)[i]
IV/ Construction of the interface plane
    for (0 <= i <= 3)
      normalvector[i] = grad(alpha(iel))[i] / norm(grad(alpha(iel))[i])
      plan[i] = normalvector[i]
    plan[3] = - (plan[0]*ptint[0] + plan[1]*ptint[1] + plan[2]*ptint[2])
V/ Computation of the area of the interface plane in the cell
    Sint = cal_surf
VI/ Identification of the normal cell to the interface
    for (all cells J sharing a vertex with iel)
      for (0 <= i <= 3)
        IJ[i] = coord(J)[i] - coord(iel)[i]
      Prodscal_J = scalarproduct(normalvector, IJ)
      if (Prodscal_J = max)
        pos = J
VII/ Distance between the normal cell and the interface
    d = |plan[0]*coord(pos)[0] + plan[1]*coord(pos)[1]
    + plan[2]*coord(pos)[2] + plan[3]|
VIII/ Computation of the temperature gradient
    gradT = (Temp(pos) - Tsat(iel)) / d
IX/ Computation of enthalpy source term
    tst(iel) = -alpha(iel)*lambda(iel)*gradT*Sint/volume(iel)
```

D.2.1 cal_surf.c

The routine cal_surf.c was entirely developed during the PhD to compute the geometrical parameters of a cell (such as the indexes of its edges and vertexes), and to compute the area of the intersection between a plane and a cell. It consists of the following functions:

- **position_plan**
- **cal_surf_triangle**
- **tri_point_face**
- **calc_sommets**
- **calc_aretes**
- **cal_surf**

This routine contains 710 lines of code

D.2.2 position_plan

This function computes the relative position between a point and a plane by injecting the coordinates of the point in the cartesian equation of the plane :

$$relativepos = Ax_{pt} + By_{pt} + Cz_{pt} + D \tag{D.9}$$

It returns the real relativepos. If relativepos is positive, the point is "above" the plane, else the point is "below" the plane. position_plan is used in the function cal_surf to determine the intersection between the interface plane and the edges of the cell.

```
position_plan(plan, pt):
  return(plan(0)*pt(0) + plan(1)*pt(1) + plan(2)*pt(2) + plan(3))
```

D.2.3 cal_surf_triangle

This function computes the area of a triangle using the coordinates of 3 points A, B, and C. The area A of a triangle ABC is computed as:

$$A = 0.5\|\vec{AB} \wedge \vec{AC}\| \tag{D.10}$$

cal_surf_triangle is called in cal_surf to compute the area of triangles.

```
cal_surf_triangle(x1, x2, x3):
  for (0 <= i <= 3)
    AB[i] = x2[i] - x1[i]
    AC[i] = x3[i] - x1[i]
  vecABC = prodvec(AB, AC)
  return(0.5*norm(vecABC))
```

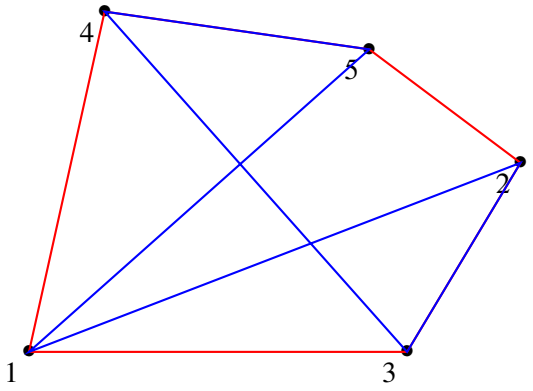

Figure D.1: Blue line: 5 points randomly linked - red line: convex polygon from 5 points.

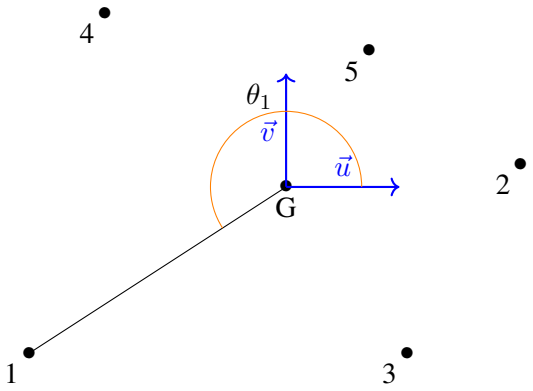

Figure D.2: Computation of the angle θ. G is the gravity center of the polygon, $(\vec{u}, \vec{v})$ is a basis of the plane.

D.2.4 tri_point_face

The intersection between the interface plane and a cell is a convex polygon made of the intersection between the interface plane and the edges of the cell (see Figure 3.5b for an example). Constructing a polygon numerically from a list of points is however not as straightforward as it may seem, because the points need to be in the correct order to get a convex polygon. Figure D.1 shows that linking the points randomly (blue line) does not give a polygon, they need to be ordered correctly (red line). The goal of this function is to "sort" a list of points to get a convex polygon.
To do that, the angle θ_i between a vector $\vec{u}$ of the plane, and the vector constructed by linking each point to the center of gravity of the polygon is computed as illustrated in Figure D.2. The points are then sorted by their angle θ_i to get the convex polygon.
The function tri_point_face takes Lpoint, a list of points, and plan, the 4 parameters (A, B, C, D) of the cartesian equation of the plan as inputs. It returns Lpoint_tri, the sorted list of points. The function follows the following steps:

1. **Computation of ($\vec{u}$, $\vec{v}$).** two orthonormal vectors of the plane are computed. Assuming that C (from the plane equation) is not zero, $E = (0, 0, -D/C)$ and $F = (1, 1, -(A + B + D)/C)$ are two points of the plane. $\vec{u} = \frac{\vec{EF}}{\|\vec{EF}\|}$ is a vector of the plane, and $\vec{v} = \vec{n} \wedge \vec{u}$ is an orthonormal vector of the plane. If $C = 0$, a similar procedure is used with A or B.
2. **Computation of G.** The gravity center of the polygon is computed as $G[i] = \sum Lpoint[k][i]/n_{point}$.
3. **Computation of the angle between $\vec{OP_i}$ and $\vec{u}$.** For each point P_i of the list, the scalar product $\vec{OP_i}.\vec{u}$ is computed. By definition $\vec{OP_i}.\vec{u} = \|\vec{OP_i}\| \cos(\theta_i)$. Hence, if $\vec{OP_i}.\vec{u} > 0$, $\theta_i = \text{acos}\left(\frac{\vec{OP_i}.\vec{u}}{\|\vec{OP_i}\|}\right)$, else $\theta_i = 2\pi - \text{acos}\left(\frac{\vec{OP_i}.\vec{u}}{\|\vec{OP_i}\|}\right)$
4. **List sorted by θ_i.** The list of points is sorted by a semi-naive substitution algorithm.

```
tri\_point\_face(Lpoint, plan):
I/ Computation of (u,v)
E(0) = E(1) = 0
F(0) = F(1) = 1
/* Assuming that C is not 0 */
E(2) = -plan(3) / plan(2)
F(2) = -(plan(0) + plan(1) + plan(3) / plan(2)
for (0 <= i <= 3)
  u(i) = F(i) - E(i)
u /= norm(u)
v = prodvec(u, (plan(0), plan(1), plan(2))
II/ Computation of G
for (0 <= i <= 3)
  G[i] = 0
for (all points k in Lpoint)
  for (0 <= i <= 3)
    G[i] += Lpoint[k][i] / len(Lpoint)
III/ Computation of the angle (OP_i, u)
ALLOC angle(len(Lpoint))
for (all points k in Lpoint)
  for (0 <= i <= 3)
    GP[i] = Lpoint[k][i] - G[i]
  GPdotu = ProdScal(GP, u)
  if (ProdScal(GP, v) >= 0)
    angle[k] = acos(GPdotu/||GP||)
  else
    angle[k] = 2*pi - acos(GPdotu/||GP||)
IV/ List sorted by theta
for (1 <= k <= len(ListeTri))
  j = k
  while (j > 0 and angle[j-1] > angle[j])
    tmpangle = angle[j]
    angle[j] = angle[j-1]
    angle[j-1] = tmpangle

    tmppt = Lpoint_tri[j]
    Lpoint_tri[j] = Lpoint_tri[j-1]
    Lpoint_tri[j-1] = Lpoint_tri[j]
```

D.2.5 calc_sommets

Unfortunately, neptune_cfd does not have a function which returns the 8 vertexes of a cell. Consequently, getting the 8 vertexes of a cell requires looping through all the vertexes, finding the 4 adjacent faces, looping through all the faces, finding the adjacent cells, then linking the vertex to the cell and finally running a unicity test to avoid having 4 times the same vertex linked to a cell. The implementation of this algorithm is easy but long, and will not be detailed in this manuscript.
The function calc_sommets returns the following tables:

- **sommets.** A list containing the index of the 8 vertexes for each cell iel. sommets[8*iel + k] returns the index of the kth vertex of cell iel.
- **alphavertex.** A list containing the volume fraction at the vertexes. The volume fractions in the vertexes are interpolated from the volume fractions in the cell center. alphavertex[inod] returns the volume fraction of the vertex inod.
- **cellvertex.** A list containing the 4 adjacent cells to a vertex. cellvertex[4*inod+k] returns the kth cell adjacent to vertex inod.

D.2.6 calc_aretes

This function returns the table aretes. This table contains information on the 12 edges for each cell. Each edge is characterized by two vertexes of the cell. aretes[24*iel + 2*k] and aretes[24*iel + 2*k + 1] return the two vertexes characterizing the kth edge of cell iel. To build this list, the following steps are followed:

1. **Construction of the face planes.** For each face, their plane equation is determined. The parameters of the cartesian equation (A, B, C, D) are stored in the variable 'plan'.
2. **Construction of the edges.** Each face is made of 4 vertexes. These vertexes are sorted using the function tri_point_face to build the 4 edges from the 4 vertexes.
3. **Construction of the table aretes.** The edges are shared between two faces. Consequently, unicity needs to be checked before adding the edges to the table aretes.

```
I/ Construction of the face planes
for (all faces ifac in the mesh)
  plan[0] = normalvector[ifac][0]
  plan[1] = normalvector[ifac][1]
  plan[2] = normalvector[ifac][2]
  k = 0
  for (all vertex inod in the face)
    for (0 <= i <= 3)
      Lsommets[k][i] = coord(inod)[i]
      k+=1
  plan[3] = - (plan[0]*Lsommets[0][0] + plan[1]*Lsommets[0][1]
  + plan[2]*Lsommets[0][2])
II/ Construction of the edges
  Lsommets_tri = tri_point_face(Lsommets)
  for (0 <= j <= 4)
    aretesface[2*j] = Lsommets_tri[j]
    aretesface[2*j + 1] = Lsommets_tri[j+1]
III/Construction of the table aretes
  I = cell adjacent to ifac
```

```
l = 0 /* Edge number */
for (0 <= j <= 4)
  if ((aretesface[2*j], (aretesface[2*j+1]) is not in aretes[24*I])
    aretes[24*I + 2*k] = aretesface[2*j]
    aretes[24*I + 2*k + 1] = aretesface[2*j + 1]
    l += 1
```

D.2.7 cal_surf

This function computes the area of the interface in a cell. To do that, the algorithm follows these steps:

- The intersection between the interface plane and each edge of the cell is determined if it exists.
- A convex polygon is built from these points.
- This polygon is split into triangles.
- The area of the interface in the cell is the sum of the area of the triangles.

This process is described in Figures 3.5a, 3.5b, 3.5c.

D.2.7.1 I/ Identification of the intersection between the interface plane and the cell edges

An edge is cut by a plane if one of the vertex is below the plane, and the other is above the plane. Mathematically, this is equivalent to the condition:

$$\text{position\_plan(plan, node1)} \times \text{position\_plan(plan, node2)} < 0 \tag{D.11}$$

If this condition is verified, the intersection point between the plane and the edge is computed. The plane is defined by its cartesian equation (equation D.12) and the line (AB) is defined by its parametric equation (equation D.13).

$$Ax + By + Cz + D = 0 \tag{D.12}$$

$$\begin{cases} x = x_A + (x_B - x_A)t \\ y = y_A + (y_B - y_A)t \\ z = z_A + (z_B - z_A)t \end{cases} \tag{D.13}$$

Injecting equation D.13 in equation D.12 gives the value of t corresponding to the intersection between the plane and the line:

$$t = -\frac{Ax_A + By_A + Cz_A + D}{A(x_B - x_A) + B(y_B - y_A) + C(z_B - z_A)} \tag{D.14}$$

The intersection point is finally added to the list PointIntersection.

D.2.7.2 II/ Sorting of the intersection points to build a convex polygon

The intersection points are sorted using the function tri_point_face to build a convex polygon.

D.2.7.3 III/ Split of the polygon into triangles

The n-polygon is split into n-2 triangles. To do that, a reference point is arbitrarily chosen. Then, this point is linked to the k^{th} and $k+1^{th}$ points of the polygon to build triangles.

D.2.7.4 IV/ Computation of the area of the triangles

The area of each triangle is computed with the function cal_surf_triangle. The area of the interface of the cell is the sum of the area of the triangles.

D.2.7.5 Code

```
I/ Identification of the intersection between
the interface plane and the cell edges
nbintersection = 0
for (all edges k of the cell iel)
  pointarete1 = aretes[24*iel + 2*k]
  pointarete2 = aretes[24*iel + 2*k + 1]

  coupe = _position_plan(plan, pointarete1)
      *_position_plan(plan, pointarete2)

  if (coupe < 0)
    a = coord(pointarete2)[0] - coord(pointarete1)[0]
    b = coord(pointarete2)[1] - coord(pointarete1)[1]
    c = coord(pointarete2)[2] - coord(pointarete1)[2]
    t = - _position_plan(plan,pointarete1)
    / (plan[0]*a + plan[1]*b + plan[2]*c)

    PointIntersection[nbintersection][0] = pointarete1[0] + a*t
    PointIntersection[nbintersection][1] = pointarete1[1] + b*t
    PointIntersection[nbintersection][2] = pointarete1[2] + c*t
    nbintersection += 1
II/ Sorting of the intersection points to build a convex polygon
PointIntersection_tri = _tri_point_face(PointIntersection)
III/ Split of the polygon into triangles
for (0 <= j <= nbintersection-1)
  triangle[3*j] = PointIntersection_tri[0]
  triangle[3*j+1] = PointIntersection_tri[j]
  triangle[3*j+2] = PointIntersection_tri[j+1]
IV/ Computation of the area of the triangles
  surface += _cal_surf_triangle(triangle[3*j],
  triangle[3*j+1], triangle[3*j+2])
return(surface)
```

APPENDIX E

The analytical solution of Scriven

The first analytical solution for the growth of a bubble in a superheated liquid was obtained and compared to experimental results by Plesset and Zwick (1954). However, Scriven (1958) showed that the approximations made in Plesset and Zwick (1954) are only valid over a restricted ranged of pressure and superheat, and proposed a more general solution. This section will detail quickly the analytical solution of Scriven as well as its hypothesis. For a more detailed demonstration, the reader is referred to Scriven (1958).

E.1 Balance equations

Because of the geometry of the problem, spherical coordinates are used in this demonstration (r, θ, ϕ). The bubble is in an infinite liquid, which means that the problem is isotropic. Therefore, the derivatives according to θ and ϕ are equal to zero ($\frac{\partial}{\partial\theta} = \frac{\partial}{\partial\phi} = 0$). Additionally, the velocities and flux are only considered in the radial direction ($u = u_r$). Therefore, the expression of the divergence of the velocity is:

$$div(u) = \frac{1}{r^2}\frac{\partial r^2 u}{\partial r} \tag{E.1}$$

E.1.1 Mass balance equation

Using spherical coordinations for an incompressible liquid, the mass balance equation is given by equation E.2.

$$\frac{1}{r^2}\frac{\partial}{\partial r}(r^2 u_l(r,t)) = 0 \tag{E.2}$$

Hence, $r^2 u_l(r,t)$ is only a function of time. Given that at $r = R$, $u_l(R,t) = \dot{R}$, this gives equation E.3.

$$u_l r^2 = \dot{R}R^2 \tag{E.3}$$

E.1.2 Energy balance equation

The energy balance equation in spherical coordinates is given by equation E.4.

$$\frac{\partial T}{\partial t} + u_l \frac{\partial T}{\partial r} = \chi_l (\frac{\partial^2 T}{\partial r^2} + \frac{2}{r}\frac{\partial T}{\partial r}) \tag{E.4}$$

After the substitution of u_l by the expression found in equation E.3, we get equation E.5.

$$\frac{\partial T}{\partial t} = \chi_l (\frac{\partial^2 T}{\partial r^2} + \frac{2}{r}\frac{\partial T}{\partial r}) - \frac{R^2 \dot{R}}{r^2}\frac{\partial T}{\partial r} \tag{E.5}$$

E.2 Initial and boundary conditions

The resolution of the system given by equations E.3 and E.5 requires some initial and boundary conditions.

- The initial temperature is uniform and equal to T_0. This gives equation E.6.

$$T_l(r, 0) = T_0 \tag{E.6}$$

- Far from the interface, at infinity, the temperature is constant and equal to T_0, hence equation E.7.

$$T(\infty, t) = T_0 \tag{E.7}$$

- At the interface between the liquid and the gas, both fluids are at saturation, therefore equation E.8.

$$T(R, t) = T_{sat} \tag{E.8}$$

- At the bubble interface, energy conservation states that the latent heat (heat inducing mass transfer) is equal to the difference between the sensible heat of the liquid and the sensible heat of the gas as in equation E.9

$$\frac{4}{3}\pi R^3 \rho_g (h_{fg} + c_{p,g}(T(R, t) - T_0)) + \rho_l c_{p,l} \int_R^\infty 4\pi r^2 (T(r, t) - T_0) \mathrm{dr} = 0 \tag{E.9}$$

E.3 Solution

Using the results from the previous section, the problem can be summarized by the following set of equations.

$$\begin{cases} T(r, 0) = T(\infty, t) = T_0 \\ (R, t) = T_{sat} \\ \dfrac{\partial T}{\partial t} = \chi_l (\dfrac{\partial^2 T}{\partial r^2} + \dfrac{2}{r}\dfrac{\partial T}{\partial r}) - \dfrac{R^2 \dot{R}}{r^2}\dfrac{\partial T}{\partial r} \\ \dfrac{4}{3}\pi R^3 \rho_g (h_{fg} + c_{p,g}(T(R, t) - T_0)) + \rho_l c_{p,l} \displaystyle\int_R^\infty 4\pi r^2 (T(r, t) - T_0) \mathrm{dr} = 0 \end{cases} \tag{E.10}$$

To simplify the equations of this system, Scriven introduced the following dimensionless parameters:

$$X = \frac{T - T_\infty}{T_\infty} \tag{E.11}$$

$$\tau = \frac{T_\infty - T_{sat}}{T_\infty} \tag{E.12}$$

$$\zeta = \frac{\rho_g h_{fg}}{\rho_l c_{p,l} T_\infty} \tag{E.13}$$

$$\omega = \frac{\rho_g}{\rho_l} \tag{E.14}$$

$$\nu = \frac{c_{p,l} - c_{p,g}}{c_{p,l}} \tag{E.15}$$

System (E.10) then gives:

$$\begin{cases} X(r,0) = X(\infty,t) = 0 \\ X(R,t) = -\tau \\ \dot{X} = \chi_l (X_{rr} + 2r^{-1} X_r) - r^{-2} R^2 \dot{R} X_r \\ X_r(R,t) = \chi_l^{-1} \dot{R} (\zeta + \omega\nu\tau) \end{cases} \tag{E.16}$$

Scriven assumed on dimensional grounds the solution $X(r,t) = X(s)$. β is the dimensionless growth constant, a new parameter of the problem.

$$r = 2\beta\sqrt{\chi_l t} \tag{E.17}$$

$$s = \frac{r}{2}\sqrt{\chi_l t} \tag{E.18}$$

X_{ss} can be expressed using the third equation in (E.10).

$$X_{ss} = 2X_s(-s - s^{-1} + \beta^3 s^{-2}) \tag{E.19}$$

After two integrations, the following expression of X is found with A a constant of integration

$$X = -A \int_s^\infty x^{-2} \exp(-x^2 - 2\beta^3 x^{-1}) \mathrm{dx} \tag{E.20}$$

Finally, the fourth equation in System (E.10) is used to determine this constant:

$$X = -(\zeta + \omega\nu\tau) 2\beta^3 \exp(3\beta^2) \int_s^\infty x^{-2} \exp(-x^2 - 2\beta^3 x^{-1}) \mathrm{dx} \tag{E.21}$$

The second equation in System (E.10) gives an equation for the growth constant β.

$$\frac{\tau}{\zeta + \omega\nu\tau} = 2\beta^3 \exp(3\beta^2) \int_s^\infty x^{-2} \exp(-x^2 - 2\beta^3 x^{-1}) \mathrm{dx} \tag{E.22}$$

Thus, the solution of this problem is:

$$\begin{cases} R = 2\beta\sqrt{\chi_l t} \\ \dfrac{\tau}{\zeta + \omega\nu\tau} = 2\beta^3 \exp(3\beta^2) \displaystyle\int_s^\infty x^{-2} \exp(-x^2 - 2\beta^3 x^{-1}) \mathrm{dx} \end{cases} \tag{E.23}$$

The growth constant β, can either be determined numerically from equation (E.22), or from a correlation. Scriven proposed the following correlation when β is large:

$$\beta = \sqrt{\frac{3}{\pi}} \frac{\rho_l c_{p,l} \Delta T}{\rho_g h_{fg}} \tag{E.24}$$

For water at atmospheric pressure, this correlation is valid for moderate and high levels of superheat (typically $\Delta T > 3°\mathrm{C}$). At higher pressure, this approximation is often incorrect. In this manuscript, β was computed from equation E.22 to get an accurate analytical solution.

APPENDIX F

More validation of the Mucellphage model

In this section, the validation of the Mucellphage model is extended to the following cases:

- Condensation
- Condensation with the presence of non condensable gases
- Boiling with fluids other than water
- Phase change on non cubic hexaedra

F.1 Condensation with the Mucellphage model

The Mucellphage model is also validated against the Stefan model with condensation. The boiling Stefan case was presented in section 3.3.2 where vapour was in contact with a superheated wall, inducing boiling at the vapour/liquid interface. In the condensation version of the Stefan problem, water is in contact with a subcooled wall, leading to condensation at the liquid/vapour interface as shown in Figure F.1.

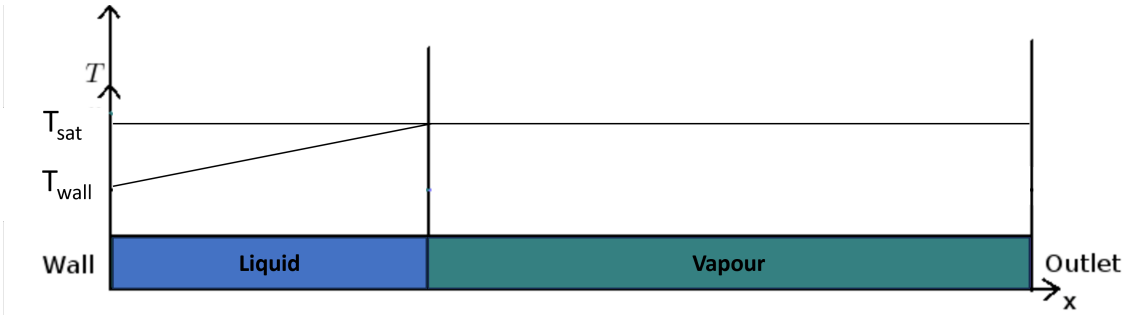

Figure F.1: Description of the Stefan condensation problem.

The position of the interface is described by equation F.1.

$$X(t) = 2\beta\sqrt{\chi_l t} \tag{F.1}$$

where β is the solution of equation F.2. erf is the error function defined as $erf(z) = \frac{2}{\pi}\int_0^z e^{-t^2}\,\mathrm{dt}$.

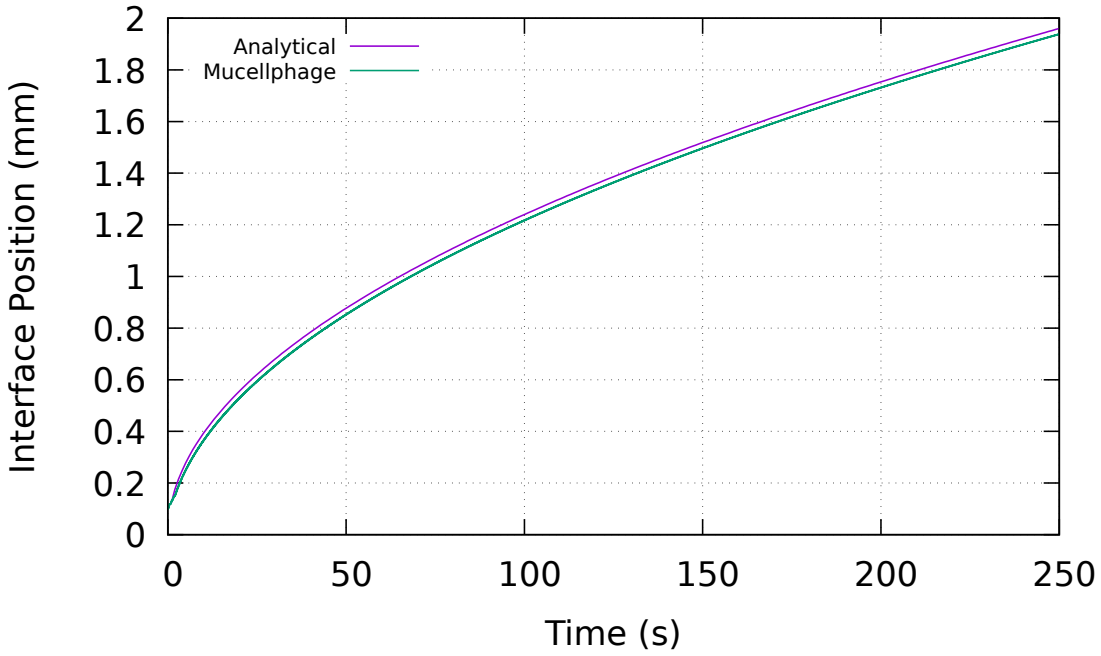

Figure F.2: Evolution of the interface position over time for the condensation Stefan problem. The purple curve represents the analytical results. The green curve represents the results with neptune_cfd.

$$\beta \exp(\beta^2)\text{erf}(\beta) = \frac{c_{p,l}(T_{max} - T_{sat})}{\sqrt{\pi} h_{lat}} \tag{F.2}$$

In this section, the 1D domain is 3 mm long, with a cell size $\Delta x = 0.003/200$ m. The liquid/vapour interface is initially at a position $7\Delta x$ from the wall. The wall temperature is $T_{wall} = T_{sat} - 25 = 348$ K. A linear interpolation is used to initialize the liquid temperature between the wall (T_{wall}) and the interface (T_{sat}). Figure F.2 shows the evolution of the interface over time. The agreement between the analytical and the Mucellphage solution is excellent.

F.2 Condensation with the presence of non condensable gases

neptune_cfd also handles the presence of non condensable gases such as air or hydrogen when modelling phase change. The Stefan problem was validated with the presence of air in Davy (2022) with the Fleau model. The use of the Mucellphage model instead of the Fleau model changes the convergence speed, but does not change the convergence toward the analytical solution.

F.3 Boiling with fluids other than water

In Magnini (2012), the author simulated the Scriven case with multiple fluids including R134a. The physical propertiers of R134a are given in Table F.1. In this case, a bubble with a radius R_0 = 100 µm is initialized at atmospheric pressure in an infinite liquid at a temperature $T_0 = T_{sat} + 5$. We employ a 2D axisymmetric mesh, using a domain that constitutes $1/180^{th}$ of a cylinder with a radius 500 µm and a height 500 µm. Outlet boundary conditions are applied at the top and at the right boundaries. The cell sizes used in the simulations are 4 µm, 2 µm, and 1 µm.

	Liquid	Gas
ρ (kg.m^{-3})	1366	5.3
c_p (J.kg^{-1}.K^{-1})	1288	794
λ (W.m^{-1}.K^{-1})	0.102	0.0093
h_{lat} (kJ.kg^{-1})	217	
T_{sat} (°C)	-26.3	

Table F.1: Physical properties of R134a.

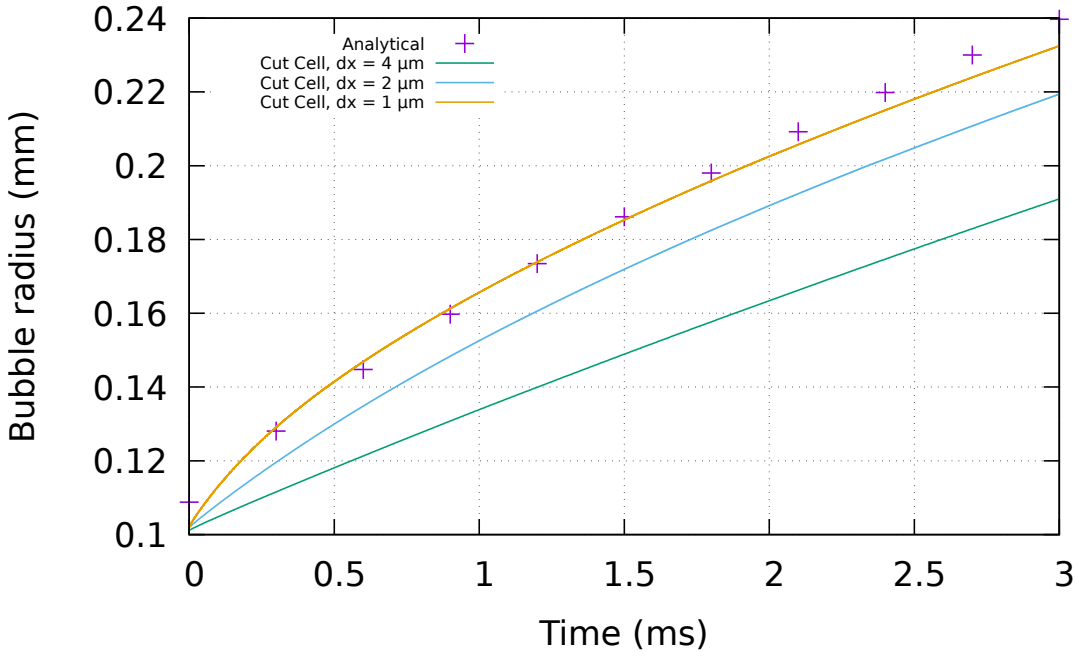

Figure F.3: Evolution of the bubble radius over time with several 2D axisymmetric meshes on the R134a case.

Remark F.3.1. Because of the physical properties of R134a, the approximation of Scriven (equation 3.17) is slightly inaccurate. The analytical results presented in this section are taken from equation F.3, solved with a python script.

$$\begin{cases} R = 2\beta\sqrt{\chi_l t} \\ \dfrac{\tau}{\zeta + \omega\nu\tau} = 2\beta^3 \exp(3\beta^2) \displaystyle\int_s^\infty x^{-2} \exp(-x^2 - 2\beta^3 x^{-1}) \mathrm{dx} \end{cases} \tag{F.3}$$

Figure F.3 shows the evolution of the bubble radius over time. The results with the finest mesh is within 5% of the analytical solution, which is acceptable. A finer mesh and a smaller time step would grant more accurate results, but be more computationally intensive.

F.4 Phase change on non cubic hexaedra

The Scriven case presented in section 3.3.3 was simulated on a $150 \times 100 \times 50$ mesh to assess the ability of the Mucellphage to predict phase change on non cartesian meshes. The evolution of the bubble radius over time is represented in Figure F.4. It shows that the $150 \times 100 \times 50$ mesh gives roughly the same

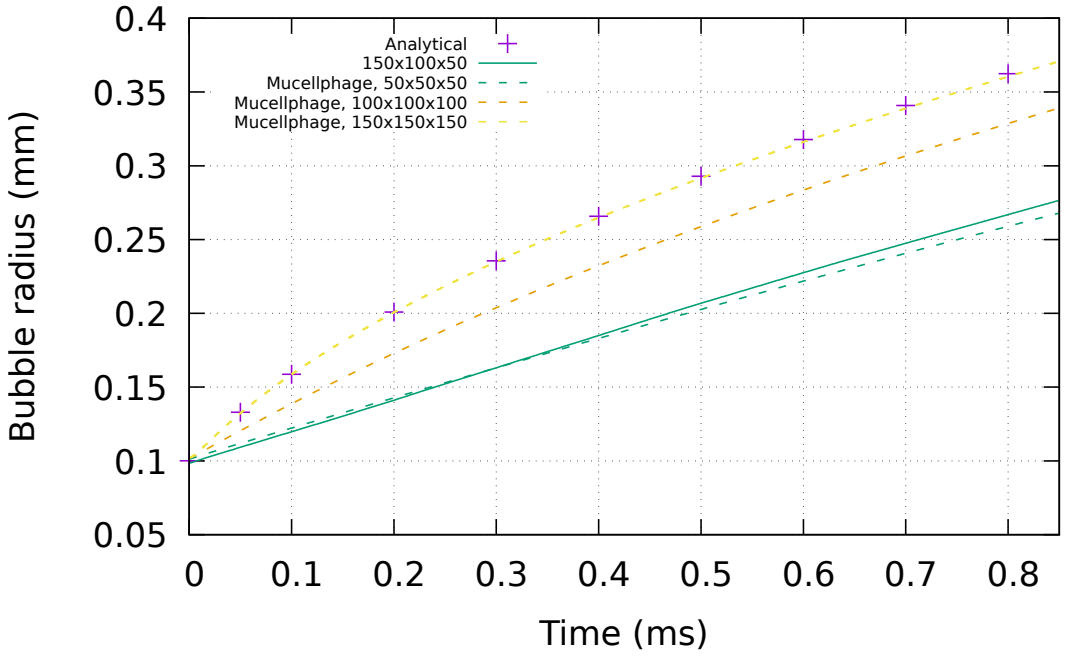

Figure F.4: Evolution of the bubble radius over time on the Scriven case. The full line represents the results with a non cubic mesh, while the dotted line represent the evolution with the cartesian mesh.

results as the $50 \times 50 \times 50$ mesh, which was expected because heat transfer is limited by the coarser side of the mesh.